ABSTRACT

Title of Document: ADAPTIVE MAGNETORHEOLOGICAL SEAT
SUSPENSION FOR SHOCK MITIGATION.

Harinder Jit Singh
Doctor of Philosophy, 2014

Directed By: Norman M. Wereley
Minta Martin Professor and Chair
Department of Aerospace Engineering

This research focuses on theoretical and experimental analysis of an adaptive seat suspension employing magnetorheological energy absorber with the objective of minimizing injury potential to seated occupant of different weights subjected to broader crash intensities. The research was segmented into three tasks: (1) development of magnetorheological energy absorber, (2) biodynamic modeling of a seated occupant, and (3) control schemes for shock mitigation.

A linear stroking semi-active magnetorheological energy absorber (MREA) was designed, fabricated and tested for intense impact conditions with piston velocities up to 8 m/s. MREA design was optimized on the basis of Bingham-plastic model (BPM model) in order to maximize the energy absorption capabilities at high impact velocities. Computational fluid dynamics and magnetic FE analysis were

conducted to validate MREA performance. Subsequently, low-speed cyclic testing (0-2 Hz subjected to 0-5.5 A) and high-speed drop testing (0-4.5 m/s at 0 A) were conducted for quantitative comparison with the numerical simulations.

Later, a nonlinear four degrees-of-freedom biodynamic model representing a seated 50th percentile male occupant was developed on the basis of experiments conducted on Hybrid II 50th percentile male anthropomorphic test device. The response of proposed biodynamic model was compared quantitatively against two different biodynamic models from the literature that are heavily implemented for obtaining biodynamic response under impact conditions. The proposed biodynamic model accurately predicts peak magnitude, overall shape and the duration of the biodynamic transient response, with minimal phase shift. The biodynamic model was further validated against 16 impact tests conducted on horizontal accelerator facility at NAVAIR for two different shock intensities. Compliance effects of human body were also investigated on the performance of adaptive seat suspension by comparing the proposed biodynamic model response with that of a rigid body response.

Finally, three different control schemes were analyzed for maximizing shock attenuation using semi-active magnetorheological energy absorber. High-speed drop experiments were conducted by dropping two rigid payloads of 240 and 340 lb mass from heights of 35 and 60 inch to simulate different impact intensities. First control scheme called constant stroking load control offered inflexible stroking load irrespective of varying impact severity or occupant weight. The other two control schemes: terminal trajectory control and optimal control adapted stroking load as per

the shock intensity. The control schemes were compared on the basis of their adaptability and ease of implementation.

These tools can serve as the basis for future research and development of state-of-the-art crashworthy seat suspension designs that further enhance occupant protection compared to limited performance of existing passive crashworthy concepts.

ADAPTIVE MAGNETORHEOLOGICAL SEAT SUSPENSION FOR SHOCK
MITIGATION

By

Harinder Jit Singh

Dissertation submitted to the Faculty of the Graduate School of the
University of Maryland, College Park, in partial fulfillment
of the requirements for the degree of
Doctor of Philosophy
2014

Advisory Committee:
Professor Norman Wereley, Chair/Advisor
Professor Sung Lee
Professor James Baeder
Professor Amr Baz
Professor Shapour Azarm

Dedication

This dissertation is dedicated to my parents, Raj Pal Singh and Rajinder Kaur, and my

elder brother, Deepinderjit Singh, who always motivated me to pursue my dreams.

Acknowledgements

I am extremely thankful to my advisor, Dr. Norman Wereley, for his wonderful guidance and motivation at different levels during my Master and Doctoral research. The opportunities while working with him were immeasurable. His strong encouragement led me to conduct quality research, participate in various research conferences and student competitions. The positive environment that he always maintains was conducive for me to reach the Ph.D. finishing line.

I would also like to thank my doctoral committee for their invaluable guidance, teaching and contributions. Dr. Sung Lee, Dr. James Baeder, Dr. Shapour Azarm and Dr. Amr Baz enriched my learning by teaching great academic courses and for providing deep insights into academics and industrial experiences.

My gratitude to Mr. William Glass at NAVAIR for supporting my research during my MS and Ph.D. His enormous support during the challenging times goes beyond measure. The efforts that he put for scheduling full-scale testing at NAVAIR are commendable.

Thank you to Dr. Joseph Pellettiere at FAA for his kind guidance, support and invitations to various technical conferences. His knowledge and guidance shaped my research successfully.

I am grateful to Dr. Wei Hu and Dr. Young Tai Choi for helping me learn about experimental design, fabrication and testing with MR devices in a very friendly manner. They always welcomed me whenever I had doubt regarding my research. I consider myself fortunate to work with Dr. Curt Kothera (InnoVital Systems, Inc.)

Table of Contents

List of Tables

List of Figures

Nomenclature

A_c = effective coil gap cross-section area

A_d = effective MR valve cross-section area

A_p = area of piston

C = damping constant

C_{eq} = equivalent damping constant

d = MR valve thickness

d_c = coil gap thickness

D_h = hydraulic diameter in MR valve

$D_{h_{eff}}$ = hydraulic diameter in coil gap

D_b = effective MR valve diameter

D_p = piston diameter

D_{in} = inner diameter of MREA cylinder

D_r = diameter of piston rod

DR = dynamic range

E_D = energy dissipated by MREA

f = Darcy friction factor in MR valve

f_c = Darcy friction factor inside coil gap

F_D = MREA stroking load

F_{D_L} = MREA limit load

F_{FR} = frictional forces

F_{MR} = MREA yield force

F_V = MREA off-state viscous force

g = acceleration due to gravity

H = drop height

H_f = H-field of MR fluid

H_S = H-field of piston

I = current input

K_{acc} = spring stiffness of accumulator

K_{FB} = coefficient for flow bending

K_{GC} = coefficient for gradual contraction

K_{GE} = coefficient for gradual expansion

K_{SC} = coefficient for sudden contraction

K_{SE} = coefficient for sudden expansion

K_{entry} = coefficient for entry effect

K_{exit} = coefficient for exit effect

$K.E.$ = kinetic energy of payload

L_a = active length of single MR valve

L_c = length of single coil

M = mass

n = number of electromagnetic coils

N = number of wire-turns per coil

P^{HC} = compressive strength of honeycomb

R_c = radius of curvature of bent pipe

Re	=	Reynolds number in MR valve
Re_{eff}	=	Reynolds number in coil gap
S	=	MREA stroke
v_o	=	sink rate
V_c	=	average fluid velocity in coil gap
V_d	=	average fluid velocity in MR valve
V_P	=	piston velocity
V^{HC}	=	crushed volume of honeycomb
$z(t)$	=	displacement
$\dot{z}(t)$	=	velocity
$\ddot{z}(t)$	=	acceleration
α_{GE}	=	central divergent angle
α_{GC}	=	central convergent angle
α_{FB}	=	bend angle
Γ	=	stroking threshold level
ΔP_{coil}	=	viscous pressure drop in coil gap
ΔP_E	=	pressure drop due to entry and exit
ΔP_{MR}	=	MR yield stress pressure drop
ΔP_{ml}	=	pressure drop due to minor losses
ΔP_η	=	viscous pressure drop in MR valve
τ_{MR}	=	MR yield stress
ρ	=	density of MR fluid

η = viscosity of MR fluid

$\in$ = average pipe wall roughness

ε = constraining parameter

Chapter 1

Introduction

1.1. Motivation

The objective of this research is to develop an adaptive crash protection system that minimizes the injury potential to seated occupants varying from 5th percentile female to 95th percentile male exposed to a wide crash spectrum. In the event of hard landing or crash of a helicopter, mine-blast of armored vehicle or automobile crash, tremendous shock loads are transmitted to operators and crew, which is a major cause of concern because high intensity loads may result in severe pelvic or spinal injuries. Therefore, minimizing the potential for injury is a key issue to consider when designing a crashworthy seat suspension. The injury potential can be significantly moderated by employing state-of-the-art crashworthy seat suspensions that control the transmission of impact loads to the seated occupant by applying stroking load appropriate to the occupant weight and crash intensity.

1.2. Crashworthy Seat Design Concepts

Generally, crashworthy systems for shock mitigation employ energy absorbers (EAs) such that the impact energy is dissipated and moderation of shock is achieved (Hiemenz *et al.*, 2007; Rakheja *et al.*, 1994; Swinbanks *et al.*, 2005; Mao *et*

al., 2014). There exist various passive, semi-active and active crashworthy seat suspensions for shock mitigation. Out of these, majority of crashworthy systems are of passive nature and are designed to operate for a narrow shock spectrum. Passive EA based seat suspensions cannot accommodate variation in occupant mass and impact severity in order to maintain good or comparable level of protection. Therefore, it is necessary for a crashworthy system to have adaptability such that all occupants (light or heavy) undergoing impact (low or high) are well protected. This led to the evolution of adaptive crashworthy systems with active or semi-active control.

1.2.1. Passive Crashworthy Systems

The stroking load offered to the seated occupant subjected to crash by the passive energy absorbers based seat suspensions are not adaptive and for the same reason they are called fixed load energy absorbers (FLEAs) (Rakheja et al., 1994). With this consideration, the passive crashworthy systems employing FLEAs are designed for only a single occupant weight and impact severity. For instance, FLEAs employed in crashworthy helicopter seats are designed mainly for 50th percentile male occupant without any consideration towards lighter or heavier occupant such as 5th percentile female or 95th percentile male (Desjardins, 2003). Different designs based on passive EAs were developed that add little flexibility in the stroking load profile of EA called variable load energy absorbers (VLEAs) (Desjardins, 2003). In such devices, the stroking load profile is manually adjusted by the operator *a priori* on the basis of predetermined occupant weight.

Various shock mitigation techniques exist for passive EAs based crashworthy systems such as plastic deformation of the material, hydraulic EAs etc. Energy absorption by crushing a tube or column made from aluminum or paper honeycomb is one simple but non-adaptive method for shock mitigation (Desjardins, 2003). Inversion tubes developed by General Motors Research Laboratories dissipated shock energy by inverting the metal tubing inside out under shock loads as shown in Figure 1.1 (Jackson et al., 2004; Kroell, 1962). The performance of inversion tubes is repeatable with good reliability and applied to crashworthy seats of UH-60 Blackhawk shown in Figure 1.2 (Desjardins, 2003). Similarly wire-bending is a mechanism in which a metal wire is plastically deformed under impact by forcing through series of rollers (Campbell, 1982). Figure 1.3 shows foldable trooper seats installed in UH-60 Blackhawk that use wire-bending shock mitigation mechanism. The rollers positions can be adjusted manually to induce variation in the stroking load profile of a wire bender as shown in Figure 1.4. The variation in the rollers setting gives slight adaptability but not to a great extent. If the rollers were too close, the wire has to bend sharply causing stroking load to increase and vice versa. Metal cutting and slitting mechanisms using single point tool are also used as a shock absorption concept in landing gears (Desjardins, 2003). Figure 1.5 and 1.6 show the metal cutting mechanism and the crashworthy seat employing such technique. There are many other concept utilizing plastic deformation such as deformable link, tube and die EA, tube flaring etc. (Desjardins, 2003).

The crashworthy seat suspensions employing plastic deformation of material are tuned to a single stroking load corresponding to $14.5g$ times the effective weight

of 50th percentile male occupant. The threshold of $14.5g$ is based on the maximum permissible load that a 50th percentile male occupant exposed to crash could sustain with 20% risk of injury as per cadaveric testing based on U.S. Army Aviators (Coltman *et al.*, 1989). However, the stroking load tuned to $14.5g$ times effective weight of 50th percentile male (180 lb) is too large for a lighter occupant (5th percentile female with 120 lb weight) and too low for a heavier occupant (95th percentile with 220 lb weight).

On the other hand, passive hydraulic EAs are devices in which a piston pushes the fluid through a small channel (orifice) inside a hydraulic cylinder and are a common approach for energy dissipation. Applications of hydraulic EAs range from vibration isolation/shock mitigation in automobiles and aircrafts to guns with large recoil forces. The variation in the stroking load of a passive hydraulic EA can be achieved by integrating mechanical moving parts that change the orifice area. Smaller the orifice area, larger is the energy dissipation force provided by hydraulic EA. Hajihosseinloo *et al*. (1989) used such variable orifice area based hydraulic EA for minimization of gun recoil forces. Chen and Macagno (1979) analyzed the performance of hydraulic energy absorbers with variable orifice area mechanism that included the contribution on frictional forces.

1.2.2. Active Crashworthy Systems

The lack of adaptability of passive EAs led to the evolution of fully controllable or active EA based crashworthy seat suspensions. An active seat suspension was developed by Swinbanks *et al.* (2005) for a marine platform with a look-ahead detection system. The look-ahead detection system employed downward

looking sensors for predicting the intensity of the upcoming shock and adjusting the stroking load accordingly. Stein (1991) simulated electro-hydraulic active vibration control system (AVCS) for off-road vehicles. The AVCS system helped improve the vibration absorption as much as 3 times when compared with the passive seat suspensions but had a major drawback of large energy consumption. Later on, Stein (1995) studied the electro-pneumatic active vibration control system (AVCS) that employed a pneumatic spring with transducers.

The major disadvantages of active seat suspensions are the requirements of large energy consumption and complicated control algorithms. Also the shock event is a short duration impact of 30-50 ms and therefore active EA based seat suspensions employing feedback and digital signal manipulation induces time delay that may render them unsuitable for shock mitigation. Such time delays impose restrictions on active systems and limit active EAs towards low-amplitude vibration isolation.

1.2.3. Semi-Active Crashworthy Systems

Crashworthy systems employing semi-active energy absorbers such as electrorheological (ER) and magnetorheological (MR) EAs combine the best features of both passive and active EAs. One such way is to design a semi-active energy absorber for a particular occupant weight based on the passive nature of an EA and then actively adapting the stroking load for other occupants. In this manner a fail-safe mechanism is developed such that in the event of failure of active component, a minimal passive stroking load is always available. ER and MR based EAs operate similarly to a passive hydraulic EA but utilize smart fluids. The

apparent viscosity of smart fluids can be controlled easily with electric or magnetic field for ER and MR based EAs respectively. MR fluid based EAs (MREAs) offer better control over stroking load with faster response times compared to ER.

1.3.   Magnetorheological Energy Absorber Based Seat Suspensions

Semi-active crashworthy seats with magnetorheological energy absorbers (MREAs) are capable of providing adaptive stroking load dependent on the impact severity and occupant weight. There exist various designs of MREA varying from simple (Hiemenz *et al.*, 2010) and easy to fabricate to more complicated designs (Bai *et al.,* 2012). An MREA operates in a similar fashion as a conventional passive EA in that a fluid is displaced through an orifice due to piston motion in a hydraulic cylinder as shown in Figure 1.7 (Cook *et al*., 2007; Mao *et al*., 2014). MREAs make use of MR fluid that consists of ferromagnetic particles in a non-magnetizable carrier fluid (typically a hydrocarbon based carrier fluid). The piston of an MREA houses a series of electromagnets that generate magnetic field when fed with current input. These electromagnets are generally copper wire windings and their magnetic field intensity can be easily controlled by selecting number of copper wire turns per electromagnet, number of electromagnets and the current input. The magnetic field generated by the current carrying coil causes magnetic induction among ferromagnetic particles, which form MR chains as shown in Figure 1.8 and apparent change in viscosity is observed. MR fluids typically consisting of 0.3-10 micrometer diameter ferromagnetic particles suspended in carrier fluid (Guo *et al*., 2012). Therefore, thick chains formed by the ferromagnetic particles under magnetic field choke the fluid flow through the orifice. The strength of magnetic chains grows

6

stronger with magnetic field and that enhances the energy absorption capability of the MR based devices until the saturation of magnetic particles.

The controllability of magnetic induction between iron particles provides adaptive stroking load which can be manipulated electronically, rapidly and reversibly, therefore, making it suitable for varying shock conditions.

1.3.1. Magnetorheological Devices

The stroking load of MREA has two components: passive viscous force due to Newtonian behavior of MR fluid under no-field conditions and controllable yield force due to magnetic induction. The extent of control authority using MREA is determined by a metric known as the dynamic range, DR. The dynamic range of an MREA is defined as the ratio of maximum achievable stroking load (i.e. stroking load at maximum current input/magnetic field) to the passive viscous force (Mao *et al.*, 2014).

$$DR = \frac{F_D}{F_V} = \frac{F_V + F_{MR}}{F_V} = 1 + \frac{F_{MR}}{F_V}$$
(1.1)

where F_D is the MREA stroking load, F_V is the passive viscous force and F_{MR} is the controllable yield force.

The dynamic range is inversely proportional to the passive viscous force which grows sharply as the piston velocity increases. In order to achieve large dynamic range of MREA, it is desirable to achieve low viscous forces with simultaneous high yield forces. Unconventional MREA designs have been proposed working in different modes of operation that aim to reduce the viscous forces and

increase the dynamic range (Bai *et al.*, 2012; Hiemenz *et al.*, 2010). There are mainly three different modes of operation in which MREA devices operate:

Flow Mode

Flow mode operates on the basis of pressure gradient that forces the MR fluid to flow through the gap or orifice where magnetic induction takes place. Flow mode is also known as Poisseulle flow between two stationary parallel plates as shown in Figure 1.9a. The magnetic field intensity across the parallel plates strengthens the MR chains and therefore restricts the fluid flow. Flow mode based MREAs have been utilized in landing gear for aircraft (Batterbee *et al.*, 2007), automobile suspensions (Carlson *et al.*, 1996), lag dampers for helicopter rotors (Hu and Wereley, 2005) and crashworthy seat suspensions for armored vehicles exposed to mine blasts (Choi and Wereley, 2005) and for helicopters (Hiemenz *et al.*, 2007).

The stroking load profile of the MREA is directly dependent on the flow channel design. Forcing the fluid flow through a complicated channel produces nonlinear behavior of the stroking load characterized by the Reynolds number. Mao *et al.* (2014) showed that the stroking load profile of a linearly stroking MREA was strongly dependent on minor losses such as sharp entrance and exit effects and that the viscous forces were proportional to the square of piston velocity i.e. $F_V \propto V_P^2$.

Shear Mode

Shear mode has linear or rotational relative translation between two parallel plates forming a flow channel. Shear mode operates as Couette flow and does not involve any pressure gradient across the fluid flow gap. The viscous forces are developed only due to relative motion between the parallel plates by shearing the

fluid and linearly proportional to the piston velocity i.e. $F_V \propto V_P$. Therefore, the viscous forces are of lower magnitude when compared to flow mode, which is conducive in achieving higher dynamic range. Another major advantage of shear mode based energy absorbers is that the design is relatively simple since the volume remains constant inside the hydraulic cylinder due to piston motion when under shear. In flow mode, the volume of shaft translating inside the hydraulic cylinder has to be accommodated by installing a high pressurized accumulator.

Shear mode based devices include rotary clutches and brakes (Dong-won *et al.*, 2009) and rotary dampers for crashworthy seats (Hiemenz *et al.*, 2010).

Squeeze Mode

Squeeze mode operates by changing the fluid flow gap parallel to the magnetic field as shown in Figure 1.9c. The squeezing of the MR chains formed under magnetic field leads to reorganization of ferromagnetic particles and higher yield force is attained for lower gaps. Squeeze modes are suitable for low stroke applications such as variable stiffness isolators, engine mounts (Zhang *et al.*, 2011) and rotating shafts (Wang *et al.*, 2005).

Mixed Mode

Mixed mode based MR devices are designed when the primary modes of operation are combined. Brigley *et al.* (2007) designed a mixed mode damper that employed all three modes of operation i.e. flow, shear and squeeze modes. The strengthening of MR chains can be enhanced to achieve large stroking loads by combining different modes. For instance, by squeezing the MR chains in squeeze

mode the particles form strong aggregated chains that are more robust to shear under magnetic field (Tang *et al.*, 2000).

1.4. Biodynamic Modeling

Design analysis of crashworthy seats for helicopters, armored vehicles and automobiles is conducted through high-speed impact testing in laboratory or full-scale crash testing with differently sized and types of seated anthropomorphic test devices (ATDs). The main purpose of such impact or full-scale crash testing is to determine spinal/lumbar loads that an occupant may incur, which is a prime factor in injury assessment and survivability. Therefore, it is essential to conduct test on ATDs with state-of-the art instrumentation that helps in predicting accurate lumbar loads occupants experience when under crash. The impact tests on ATDs are conducted in different manners such as vertical drop testing (Polanco and Littell, 2011), drop tests of ATDs installed in a subsection of vehicle/aircraft (Fasanella and Jackson, 2004), full-scale crash testing of entire vehicle/aircraft fitted with ATDs (Jackson *et al.*, 2004).

Polanco and Littell (2011) conducted series of vertical impact tests on Hybrid II 50th percentile and Hybrid III 50th percentile ATD based on different spinal configurations. Hybrid III was configured with a curved lumbar spine compared to Hybrid II with straight section lumbar spine. Two different impact conditions were generated by using different type of honeycomb blocks in the drop tower and lumbar responses of both ATDs were compared. Beeman *et al.* (2013) quantified kinetic and kinematic data based on testing on post mortem human surrogates (PMHS) and Hybrid III 50th percentile male ATD for high-speed frontal automotive collisions.

Hybrid III ATD's limitations were explored under loading conditions when compared to PHMS responses. In earlier study, Beeman *et al.* (2012) tested on five human volunteers of approximately 50th percentile weight and height, Hybrid III 50th percentile male ATD and three male PMHS for low-speed frontal impacts.

Modeling a real crash situation equipped with advanced instrumentation and state-of-the-art ATDs representing seated occupants is quite expensive. In order to reduce experimentation costs, researchers have developed computational means to assess biodynamic response of occupant under crash using finite-element models, multi-body models and lumped parameter models.

1.4.1. Finite Element Based Biodynamic Models

A finite-element model discretizes the human body into small elements and model the human body properties such as stiffness, damping and mass. For a very accurate finite element based biodynamic model, the number of discretized elements can increase substantially and require complicated modeling as well as computational time. Fasanella and Jackson (2004) compared the responses of finite element model with that of vertical drop test of two 50th percentile male Hybrid II dummies as shown in Figure 1.10. Whiplash injuries were evaluated for a 50th percentile male cervical spine resulting from vehicle crash scenarios using finite element modeling techniques (Fice and Cronin, 2012).

In order to determine the response of internal organs Toyota has developed a virtual human model, known as Total Human Model for Safety (THUMS). Various occupants have been modeled such as a 5th percentile adult female, as well as a 50th and 95th percentile adult male as shown in Figure 1.11. THUMS includes details of

bone structure, ligaments etc. and the internal organs were modeled based on CT-scans (JSOL Corporation) as shown in Figure 1.12.

1.4.2. Multi-body Models

Multi-body dynamic models employ several rigid bodies that are connected by pins or ball and socket joints depending on the degrees of freedom required. Huang (1998) developed a three dimensional multi-body model with fifteen rigid bodies as shown in Figure 1.13. Linder (2000) implemented a mathematical model of the neck for a low-velocity rear-end impact using a multi-body system program, MADYMO 2D, for soft-tissue injuries that excluded deformation of structures. Teng *et al.* (2008) explored the dynamic response of the human body in a frontal crash collision and assessed the injuries to occupant's pelvis, chest and head.

1.4.3. Lumped Parameter Based Biodynamic Models

Lumped parameter models represent the human body by connecting different lumped masses through springs and dampers that can be either linear or nonlinear. When compared to FE and multi-body models, the numerical implementation of the lumped parameter model is simple and easy to integrate with the seat suspension dynamics. One major limitation is that lumped models become complicated if multi-directional analysis is required for assessing vertical, lateral or side loads. Therefore, most biodynamic lumped parameter models are limited to unidirectional analyses.

The lumped parameter models can range from as simple as one degree-of-freedom (DOF) linear model to multi-DOF nonlinear models. Suggs *et al.* (1969) developed a two DOF lumped parameter model on the basis of experiments using a

mechanical simulator providing vibrations to the seated occupant. A four-DOF nonlinear biodynamic model was developed by Liu *et al*. (1998) based on dynamic tensile testing as shown in Figure 1.14. The model was studied by Zong and Lam (2002) to evaluate the biodynamic response of a seated occupant subjected to ship shock. Patil *et al*. (1977) modified a six-DOF biodynamic model by adding another degree of freedom corresponding to seat pan and simplified the model by neglecting internal frictional forces as shown in Figure 1.15. Qassem *et al*. (1994) studied the biodynamic response of an occupant subjected to horizontal as well as vertical vibrations by developing an eleven-DOF lumped parameter model. Liang and Chiang (2006) studied the biodynamic response for variety of biodynamic lumped parameter models exposed to vertical vibration excitations with as simple as one-DOF model to eleven-DOF biodynamic model of a pregnant woman developed by Qassem and Othman (1996) as shown in Figure 1.16.

A suitable lumped parameter based biodynamic model for crash conditions is not yet explored since all of the lumped models were developed for low amplitude vibration isolation.

1.5.   Dissertation Outline

This research is focused on the design analysis, fabrication and testing of an adaptive crashworthy system for enhanced occupant protection when exposed to crash or harsh environments. The crashworthy system incorporates semi-active MREA with a dynamic range large enough to accommodate different occupants varying form 5th percentile female to 95th percentile male seated occupants. Finally, the adaptive nature of crashworthy seat suspension is shown via experiments.

Chapter 2 deals with optimization based design analysis, fabrication and testing of MREA with large dynamic range. MREA characterization is performed via MTS cyclic testing and high-speed drop tests using a 12 ft high drop stand. The experiments are conducted for varying current inputs/magnetic field and piston velocities. Passive viscous forces and magnetic yield forces are evaluated on the basis of computational analysis and compared with analytical models based on pressure drops that fluid experiences while flowing through the gap. Refinements to the analytical model is also detailed.

Chapter 3 discusses the limitation of existing biodynamic model when used in context with crash testing and development of a nonlinear four-DOF lumped parameter model. The model is developed on the basis of experimental observations on Hybrid II 50th percentile male occupant ATD used in Sikorsky ACAP experiment (Jackson *et al.*, 2004). The model is validated against another high-speed crash experiment.

Chapter 4 elaborates the influence of occupant compliance on the performance of semi-active EA based crashworthy system. The biodynamic responses are compared with an equivalent single-DOF rigid body. Three different control schemes are discussed with their shock mitigation capabilities. The first scheme is based on constant stroking load control similar to the operation of existing passive crashworthy seat suspensions. The other two control schemes are based on optimally adapting the stroking load based on the impact severity. Injuries to the seated occupant are assessed by comparing responses with established injury criteria for vertical shocks.

Chapter 5 details the in-lab testing of the control schemes using 12 ft high drop tower at Alfred Gessow Rotorcraft Center, University of Maryland. The control schemes are based on tuning of MREA stroking load: (1) constant stroking load, (2) terminal trajectory control and (3) optimal control. As will be shown, terminal trajectory control performs better because of noise-free response without any time delay. MREA theoretical viscous and yield force models are also validated on the basis of three characteristics: energy dissipation, peak MREA load and loading pulse duration.

Chapter 6 discusses impact testing of 50th percentile male occupant for two shock intensities and biodynamic model (derived in chapter 3) validation against the experimental observations. The validation is carried out for theoretical and experimental lumbar loads for 16 impact tests.

Chapter 7 summarizes the original contributions of the research and identifies area for future work in improving the crashworthy system and expanding the biodynamic models to other occupants.

References

Bai X-X, Wereley N M, Hu W and Wang D-H, 2012 A Bidirectional Controllable Magnetorheological Energy Absorber for Shock and Vibration Isolation Systems *ASME Conference on SMASIS* doi:10.1115/SMASIS2012-8250.

Batterbee D C, Sims N D, Stanway R and Rennison M 2007 Magnetorheological Landing Gear: Validation Using Experimental Data *Smart Materials and Structures,* Vol. 16, No. 6, pp. 2441-52.

Beeman S M, Kemper A R, Madigan M L, Franck C T and Loftus S C 2012
Occupant Kinematics in Low-Speed Frontal Sled Tests: Human Volunteers,
Hybrid III ATD, and PMHS *Accident Analysis and Prevention*, Vol. 47, pp.
128-139.

Beeman S M, Kemper A R, Madigan M L and Duma S M 2013 Kinetic and
Kinematic Responses of Post Mortem Human Surrogates and the Hybrid III
ATD in High-Speed Frontal Sled Tests *Accident Analysis and Prevention*,
Vol. 55, pp. 34-47.

Brigley M, Choi Y-T, Wereley N M and Choi S B 2007 Magnetorheological
Isolators Using Multiple Fluid Modes *Journal of Intelligent Material
Systems and Structures,* Vol. 18, No. 12, pp. 1143-48.

Campbell R F 1982 Vehicle Crashworthy Seat *US Patent* 4,358,154.

Carlson J D, Catanzarite D M and St. Clair K A 1996 Commercial
Magnetorheological Fluid Devices *International Journal of Modern Physics
B*, Vol. 10, No. 23, pp. 2857-65.

Chen C J and Macagno E O 1979 Fluid and thermodynamic characteristics of
compressible recoil mechanisms Report DAAG 29-78-G-0120, US Army
Research Office by Energy Division, Iowa Institute of Hydraulic Research,
Iowa University.

Choi Y-T and Wereley N M 2005 Mitigation of Biodynamic Response to Vibratory
and Blast-induced Shock Loads Using Magnetorheological Seat Suspensions
*Proceedings of the Institution of Mechanical Engineers Part D: Journal of
Automobile Engineering,* Vol. 219, No. 6, pp. 741-53.

Coltman J W, Van Ingen C, Johnson N B and Zimmerman R E 1989 Aircraft Crash Survival Guide Vol. II-Aircraft Crash Design Impact Conditions and Human Tolerance *Aviation Applied Technology Directorate,* USAAVSCOM TR89-D-22B, pp. 29-87.

Cook E, Hu W and Wereley N M 2007 Magnetorheological Bypass Damper Exploiting Flow Through a Porous Channel *Journal of Intelligent Material Systems and Structures,* Vol. 18, No. 12, pp. 1197-1203.

Desjardins S P 2003 The Evolution of Energy Absorption Systems for Crashworthy Helicopter Seats *59th Annual AHS Forum*, Phoenix, AZ, May 6-8.

Dong-won Y, Young-su S, Hee-chang P and Sang-kyu C 2009 Design of Novel MR Rotary Brake *World Congress on Computer Science and Information Engineering,* Los Angeles, CA, IEEE.

Fasanella E L and Jackson K E 2004 Impact Testing and Simulation of a Crashworthy Composite Fuselage Section with Energy-Absorbing Seats and Dummies *Journal of the American Helicopter Society,* Vol. 49, No. 2, pp. 140-148.

Fice J B and Cronin D S 2012 Investigation of Whiplash Injuries in the Upper Cervical Spine Using a Detailed Neck Model *Journal of Biomechanics*, Vol. 45, No. 6, pp. 1098-1102.

Guo C, Gong X, Xuan S, Zong L and Peng C 2012 Normal Forces of Magnetorheological Fluids Under Oscillatory Shear *Journal of Magnetism and Magnetic Materials,* Vol. 324, No. 6, pp. 1218-1224.

Huang S-C 1998 Analysis of Human Body Dynamics in Simulated Rear-End Impacts *Human Movement Science*, Vol. 17, No. 6, pp. 821-838.

Hajihosseinloo M A, Hooke CJ, and Walton D 1989 Gun recoil system performance-measurement and prediction*Proc. IMechE Part C: J. Mech. Eng. Sci.*, Vol. 203, pp. 85-92.

Hiemenz G J, Choi Y T and Wereley N M 2007 Semi-Active Control of Vertical Stroking Helicopter Crew Seat for Enhanced Crashworthiness *AIAA Journal of Aircraft*, Vol. 44, No. 3, pp. 1031-1034.

Hiemenz G J, Hu W, Ngatu G, and Wereley N M, 2010, Rotary vane magnetorheological energy absorber U.S. Patent US2010/0300819 A1.

Hu W and Wereley N M 2005 Magnetorheological Fluid and Elastomeric Lag Damper for Helicopter Stability Augmentation *International Journal of Modern Physics B*, Vol. 19, No. 7, pp. 1471-77.

Jackson K E, Fasanella E L, Boitnott R, McEntire J, and Lewis A, 2004 Occupant Responses in a Full-Scale Crash Test of the Sikorsky ACAP Helicopter *Journal of the American Helicopter Society*, Vol. 49, No. 2, pp. 127-139.

JSOL Corporation Total Human Model for Safety (THUMS), http://ls-dyna.jsol.co.jp/en/thums/modelDetail.html Last accessed: Mar 24, 2014.

Kroell C K 1962 A Simple, Efficient, One Shot Energy Absorber *Bulletin No. 30 Shock Vibration and Associated Environments,* Part III, General Motors Research Laboratory, Warren, MI.

Liang C C and Chiang C F 2006 A Study on Biodynamic Models of Seated Human Subjects Exposed to Vertical Vibration *International Journal of Industrial Ergonomics*, Vol. 36, pp. 869-890.

Linder A 2000 A New Mathematical Neck Model for a Low-Velocity Rear-End Impact Dummy: Evaluation of Components Influencing Head Kinematics *Accident Analysis and Prevention*, Vol. 32, No. 2, pp. 261-269.

Liu X X, Shi J, Li G, Le X, Zhao B, Yue M, Liu J, Bai G and Ke W 1998 Biodynamic Response and Injury Estimation of Ship Personnel to Ship Shock Motion Induced by Underwater Explosion *Proceedings of the 69th Shock and Vibration Symposium, Shock and Vibration Information Analysis Center*, Richmond, VA, Vol. 18,pp. 1–18.

Mao M, Hu W, Choi Y T, Wereley N M, Browne A L, and Ulicny J, 2014, Experimental validation of a magnetorheological energy absorber design analysis, *Journal of Intelligent Material Systems and Structures*, 25(3):352-363.

Patil M K, Palanichamy M S and Ghista D N 1977 Dynamic Response of Human Body Seated on a Tractor and Effectiveness of Suspension Systems *Society of Automobile Engineers,* No. 770932, pp.755-792.

Polanco M A and Littell J D 2011Vertical Drop Testing and Simulation of Anthropomorphic Test Devices *67th AHS Annual Forum,* Virginia Beach, VA.

Qassem W, Othman M O and Abdul-Majeed S 1994 The Effects of Vertical and Horizontal Vibrations on the Human Body *Medical Engineering Physics*, Vol. 16, pp. 151-161.

Qassem W and Othman M O 1996 Vibration Effects on Sitting Pregnant Women-Subjects of Various Masses *Journal of Biomechanics*, Vol. 29, No. 4, pp. 493-501.

Rakheja S, Afework Y and Sankar S 1994 An Analytical and Experimental Investigation of the Driver Seat Suspension System *Vehicle System Dynamics*, Vol. 23, No. 3, pp. 501-524.

Stein G J 1991 Active Vibration Control System for the Drivers Seat for Off-road Vehicles *Vehicle System Dynamics,* Vol. 20, No. 2, pp. 57-78.

Stein G J 1995 Results of Investigation of an Electropneumatic Active Vibration Control System for a Drivers Seat *Proceedings IMechE Part D: Journal of Automobile Engineering,* Vol. 209, No. 3, pp. 227-234.

Suggs C W, Abrams C F and Stikeleather L F 1969 Application of a Damped Spring-Mass Human Vibration Simulator in Vibration Testing of Vehicle Seats *Ergonomics*, Vol. 12, No. 1, pp. 79-90.

Swinbanks M A, Simon D E, Holford J M and Napoletano JR. F M 2005 Active Suspension for a Marine Platform *US Patent Application Publication* US 2005/0278094 A1

Tang X, Zhang X, Tao R and Rong Y 2000 Structure Enhanced Yield Stress of Magnetorheological Fluids *Journal of Applied Physics,* Vol. 87, No. 5, pp. 2634-38.

Teng T L, Chang F A, Liu Y S and Peng C P 2008 Analysis of Dynamic response of Vehicle Occupant in Frontal Crash Using Multibody Dynamics Method *Mathematical and Computer Modeling*, Vol. 48, No. 11-12, pp. 1724-1736.

Wang J, Meng G, Feng N and Hahn E J 2005 Dynamic Performance and Control of Squeeze Mode MR fluid Damper-Rotor System *Smart Materials and Structures,* Vol. 14, No. 4, pp. 11.

Zhang X J *et al.* 2011 Dynamic Testing and Modeling of an MR squeeze Mount *Journal of Intelligent Material Systems and Structures,* Vol. 22, No. 15, pp. 1717-28.

Zong Z and Lam K Y 2002 Biodynamic Response of Shipboard Sitting Subject to Ship Shock *Journal of Biomechanics,* Vol. 35, No. 1, pp. 35-43.
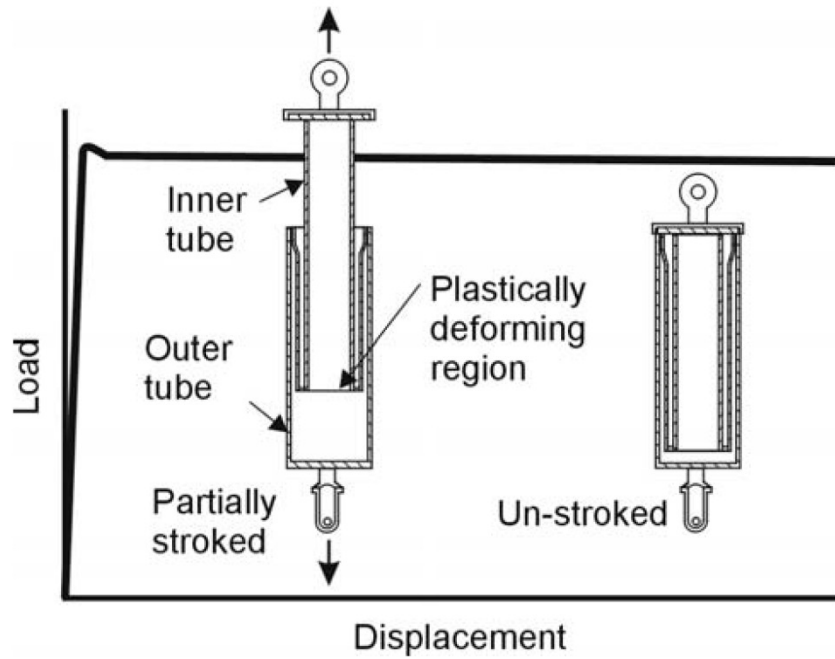
Figure 1.1. Inversion tube energy absorber concept (Desjardins, 2003).
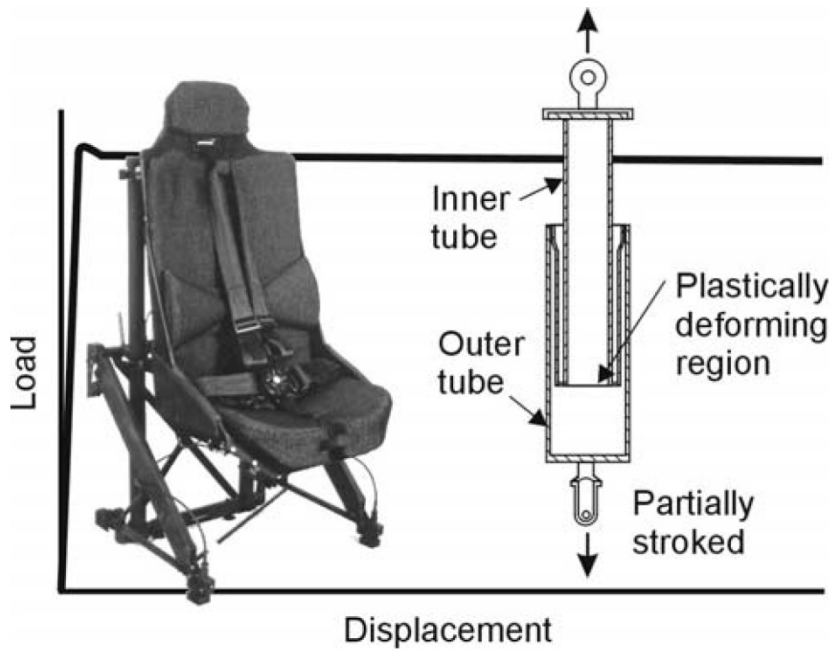
Figure 1.2. UH-60 Blackhawk crew seat employing inversion tube concept

(Desjardins, 2003).
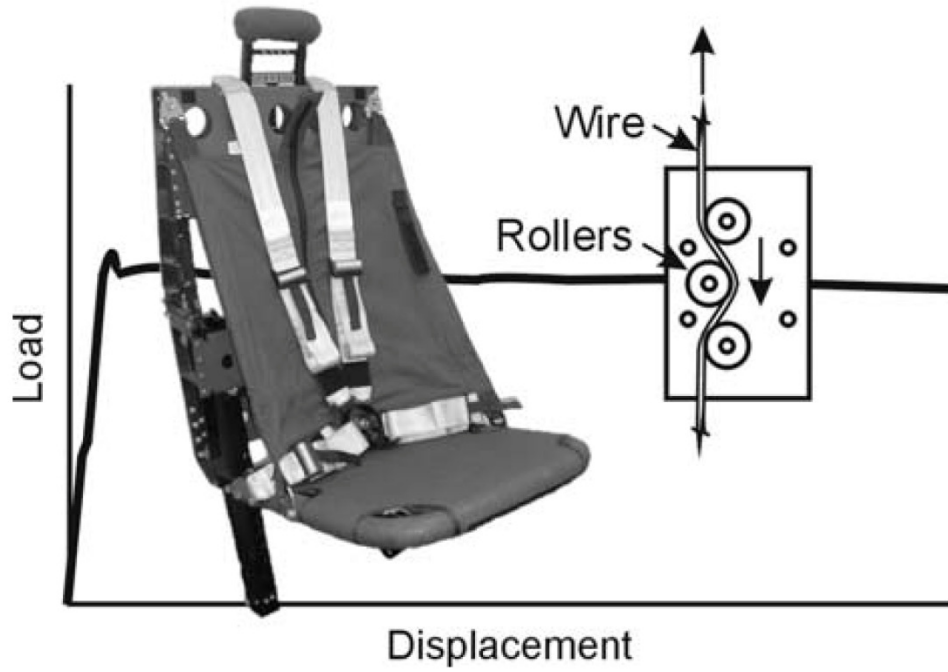
Figure 1.3. EH101 Foldable troop seat with wire bender EA (Desjardins, 2003).
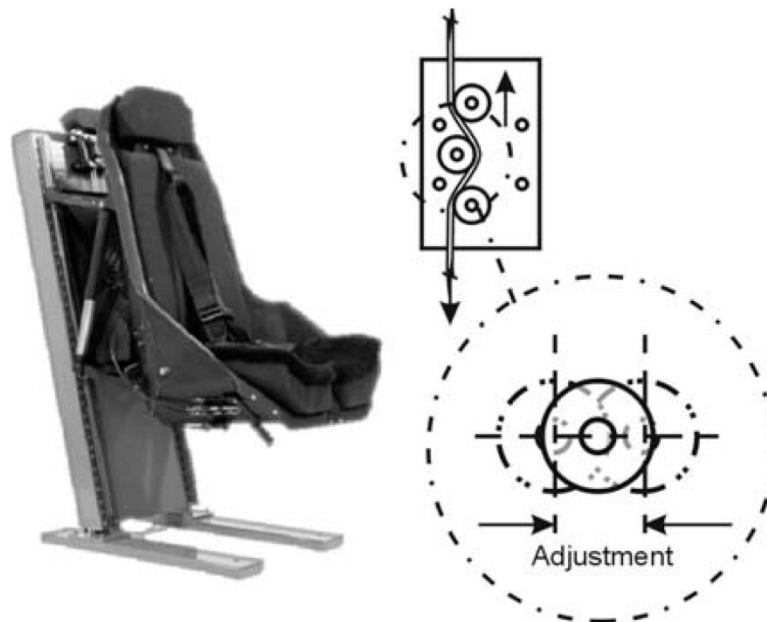
Figure 1.4. V-22 Osprey crew seat with variable load energy absorber using wire

bender (Desjardins, 2003).
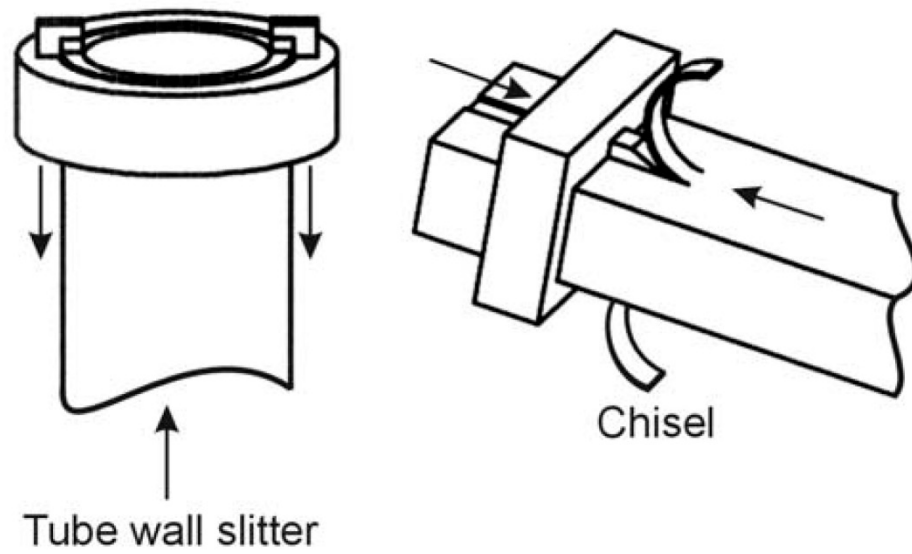
Figure 1.5. Metal cutting and slitting energy absorption concept (Desjardins, 2003)
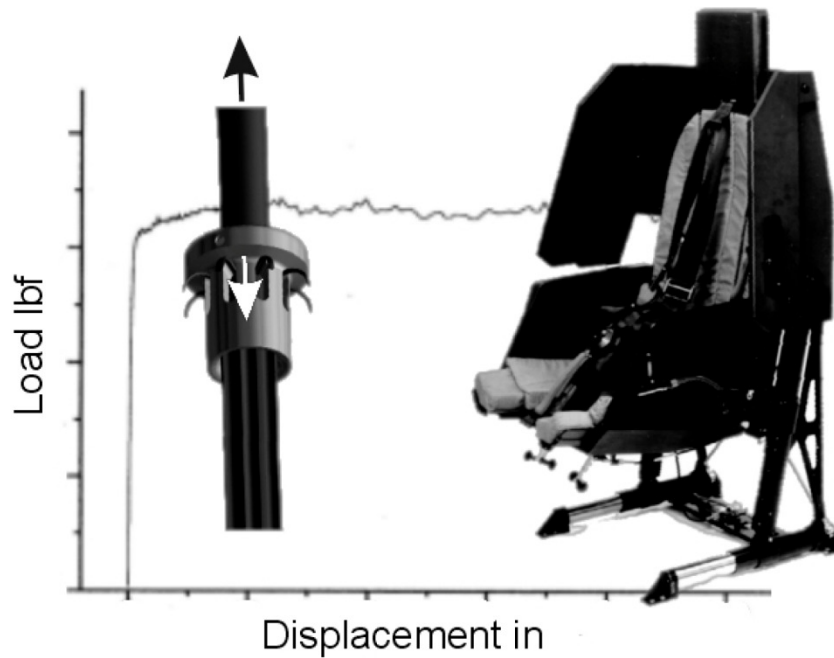
Figure 1.6. French/German Tiger armored crew seat with metal cutter EA

(Desjardins, 2003).
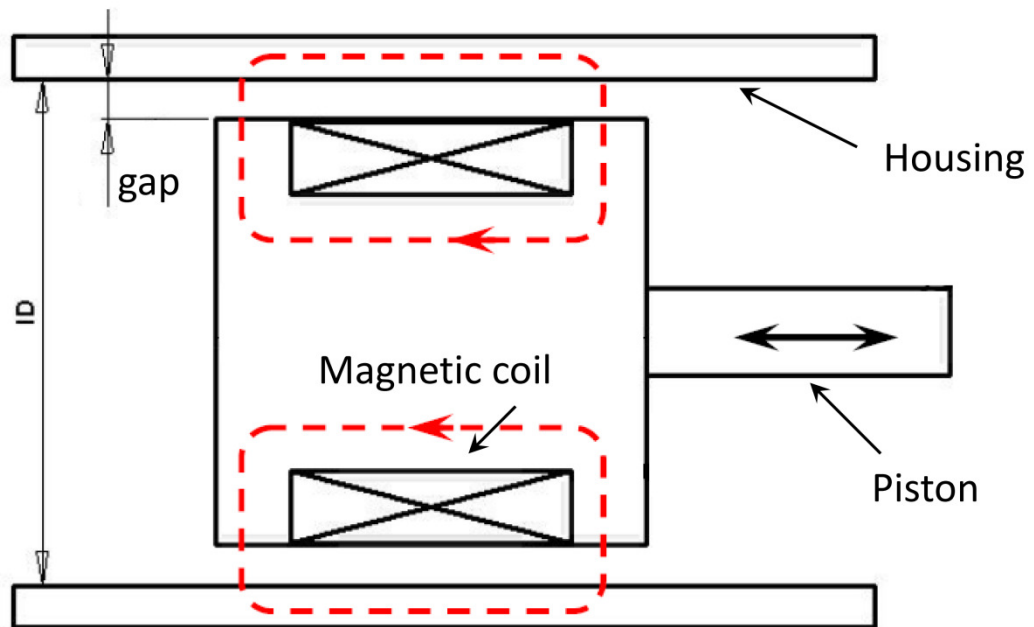
Figure 1.7. Schematic of magnetorheological energy absorber (MREA) with

magnetic circuit.
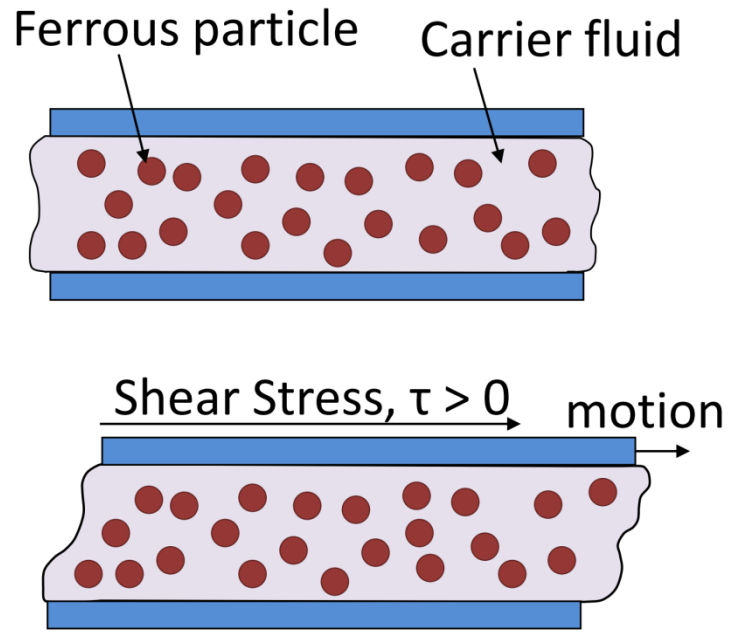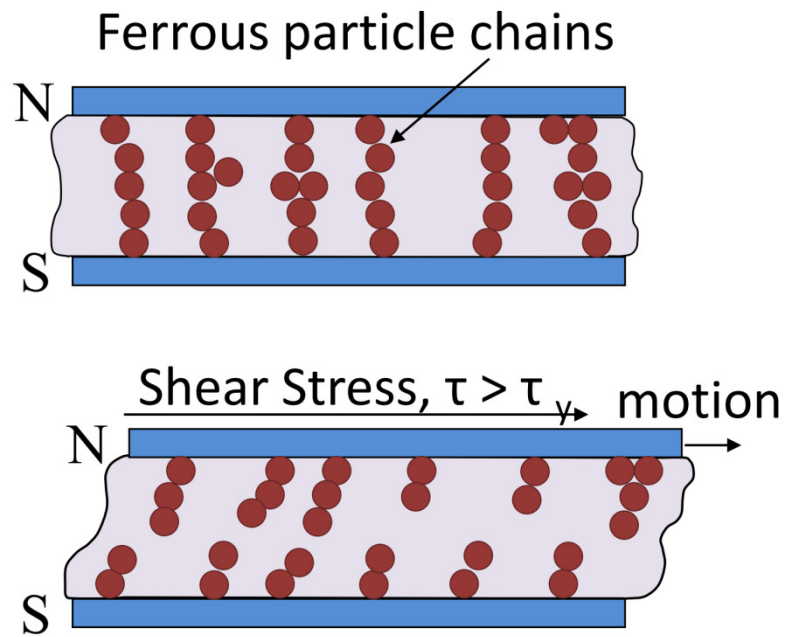
Figure 1.8. Magnetorheological fluid under shear stress for (a) no-magnetic and (b) magnetic field.
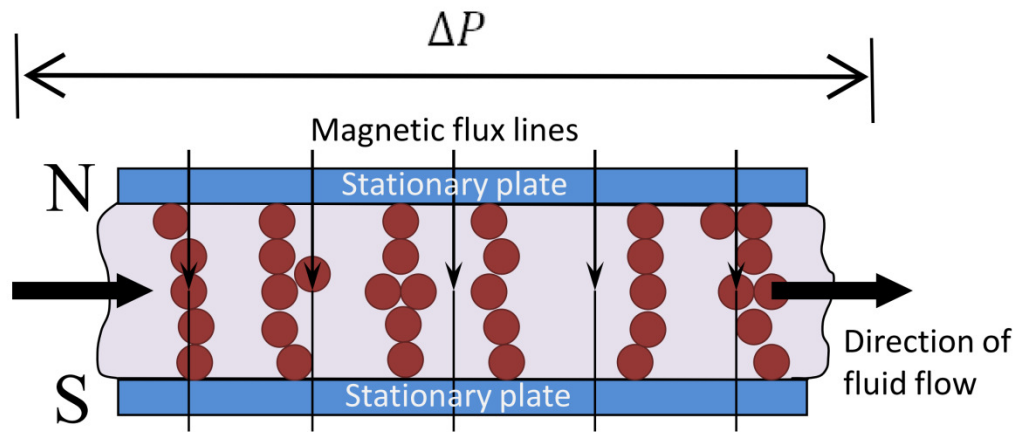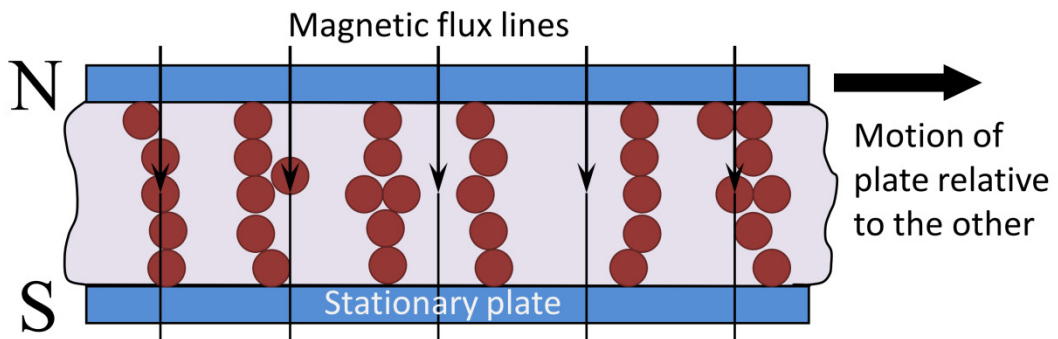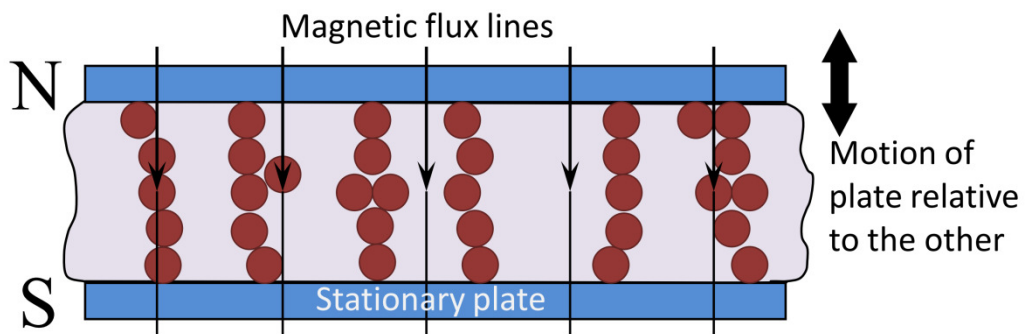
Figure 1.9. Modes of operation of MR fluid in (a) flow mode, (b) shear mode and (c) squeeze mode.
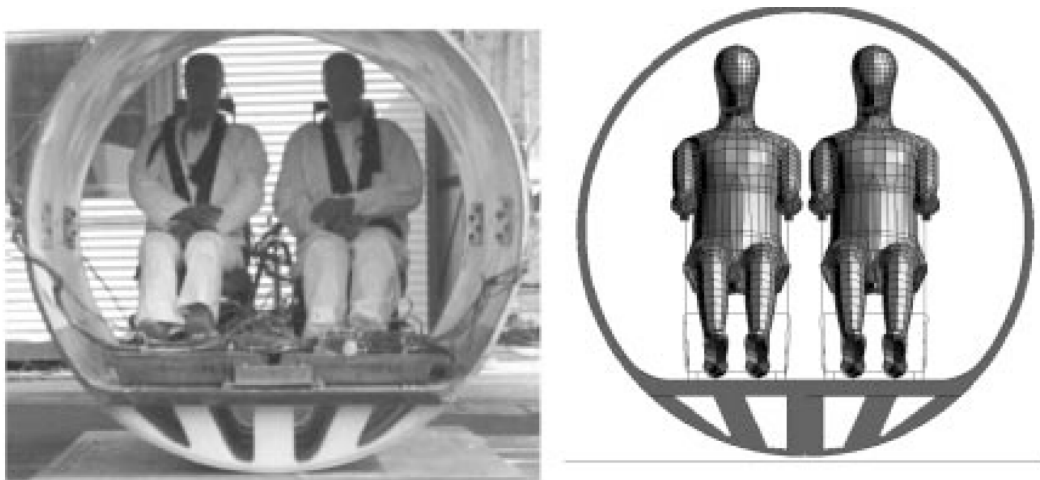
Figure 1.10. Crashworthy composite fuselage testing set-up and the related FE model (Fasanella and Jackson, 2004)

AM95   AM50   AF05
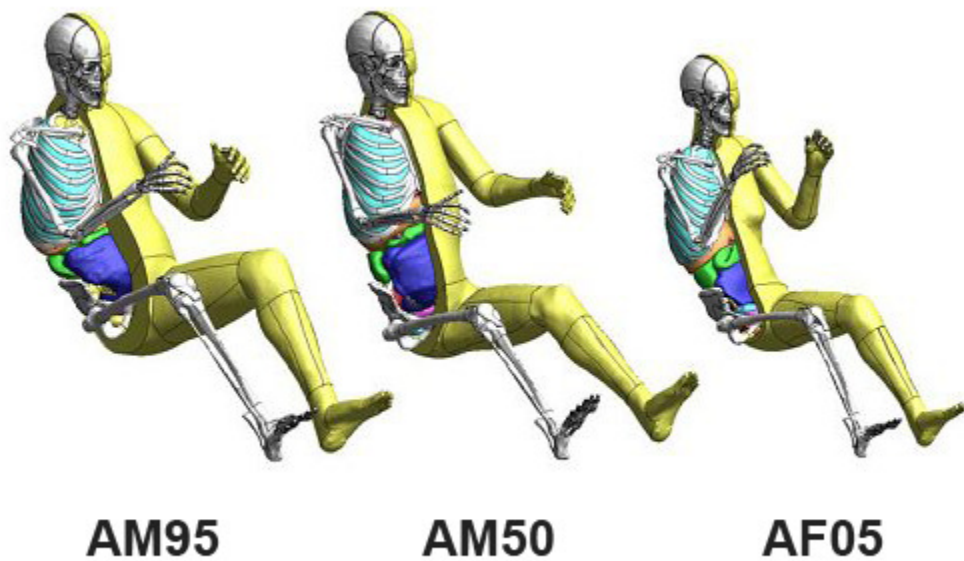
Figure 1.11. Total Human Model for Safety (THUMS) from 5th percentile female to 95th percentile male (JSOL Corporation).

Last accessed on Mar 24, 2014; http://ls-dyna.jsol.co.jp/en/thums/img/img02_03.png
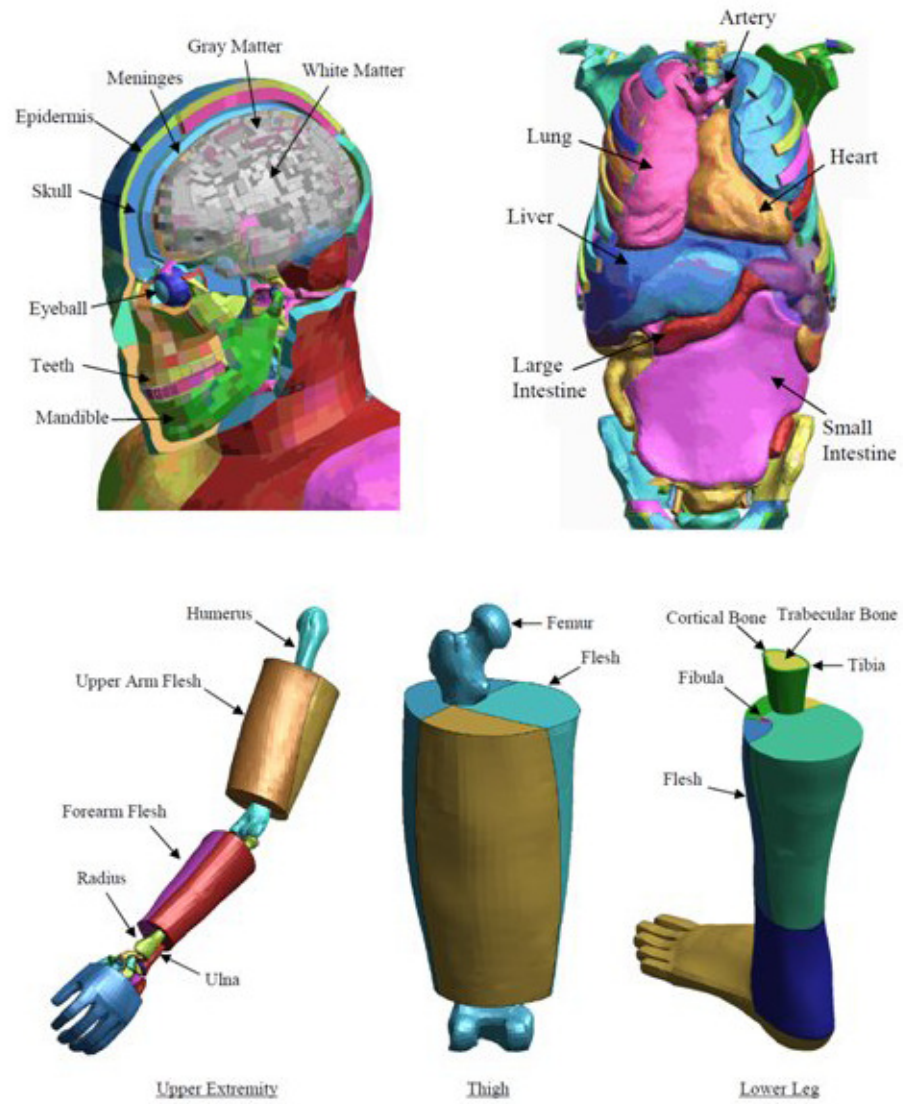
Figure 1.12. Modeling of components and bone structure in THUMS (JSOL Corporation).

Last accessed on Mar 24, 2014; http://ls-dyna.jsol.co.jp/en/thums/img/img02_01.png
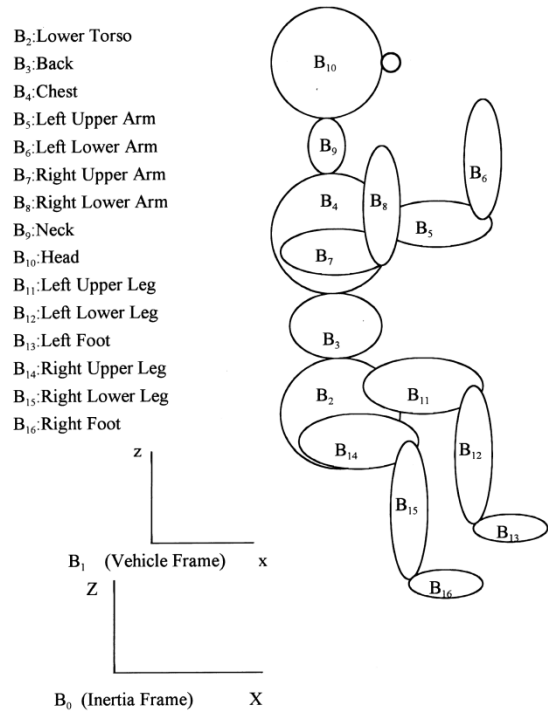
Figure 1.13. Multi-body model of a seated occupant (Huang, 1998).
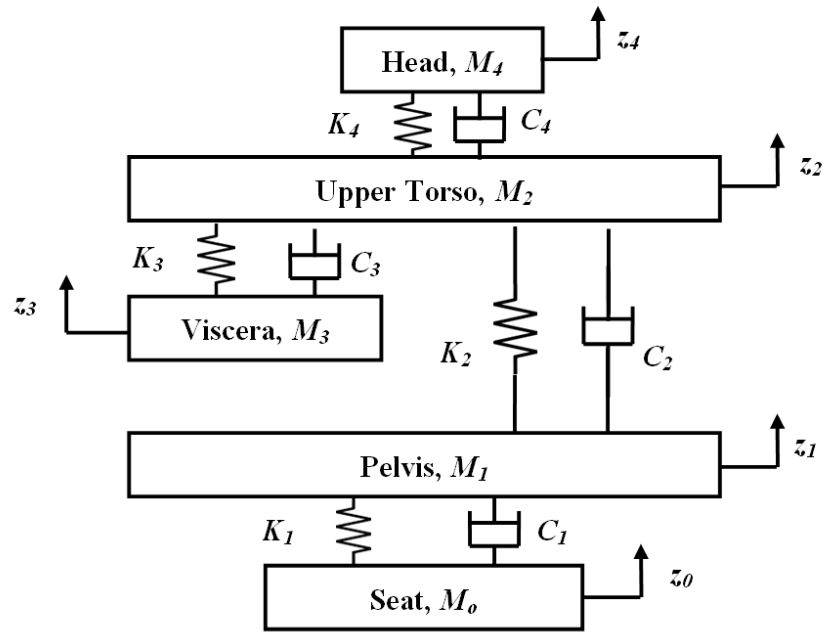
Figure 1.14. Four-DOF lumped biodynamic model of a seated occupant (Liu *et al.*, 1998).
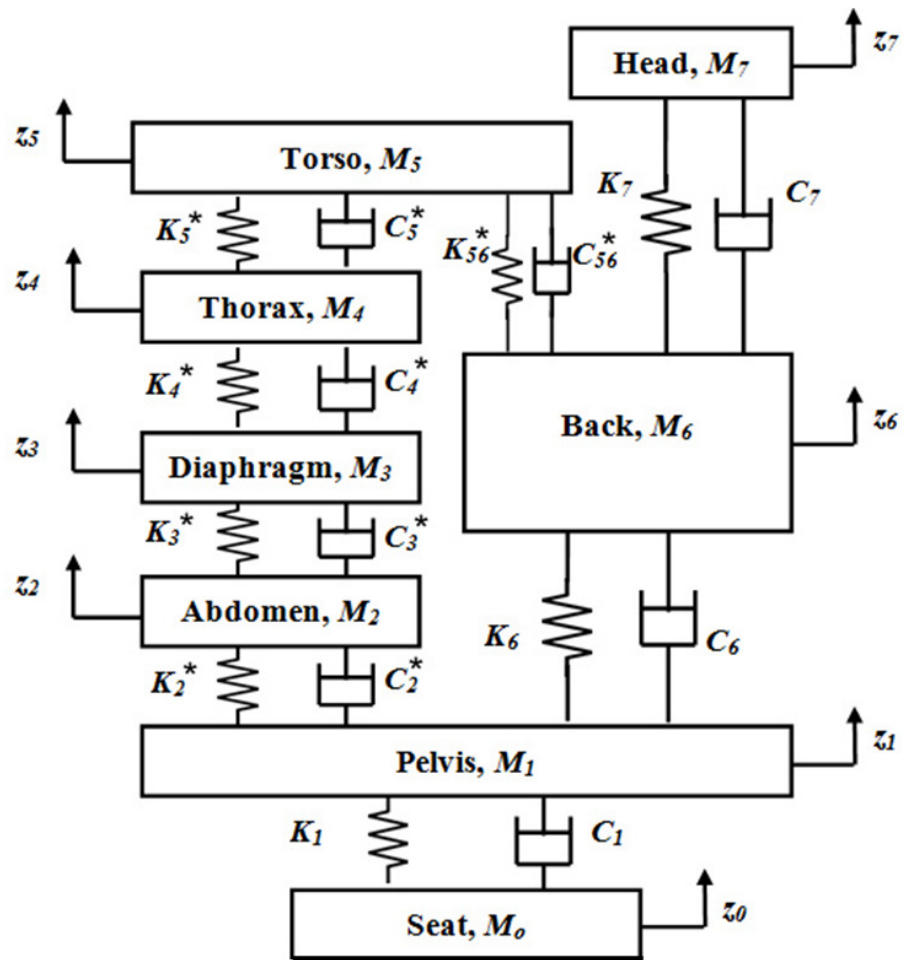
Figure 1.15. Seven-DOF lumped biodynamic model of a seated occupant developed by Patil *et al.* (1977).
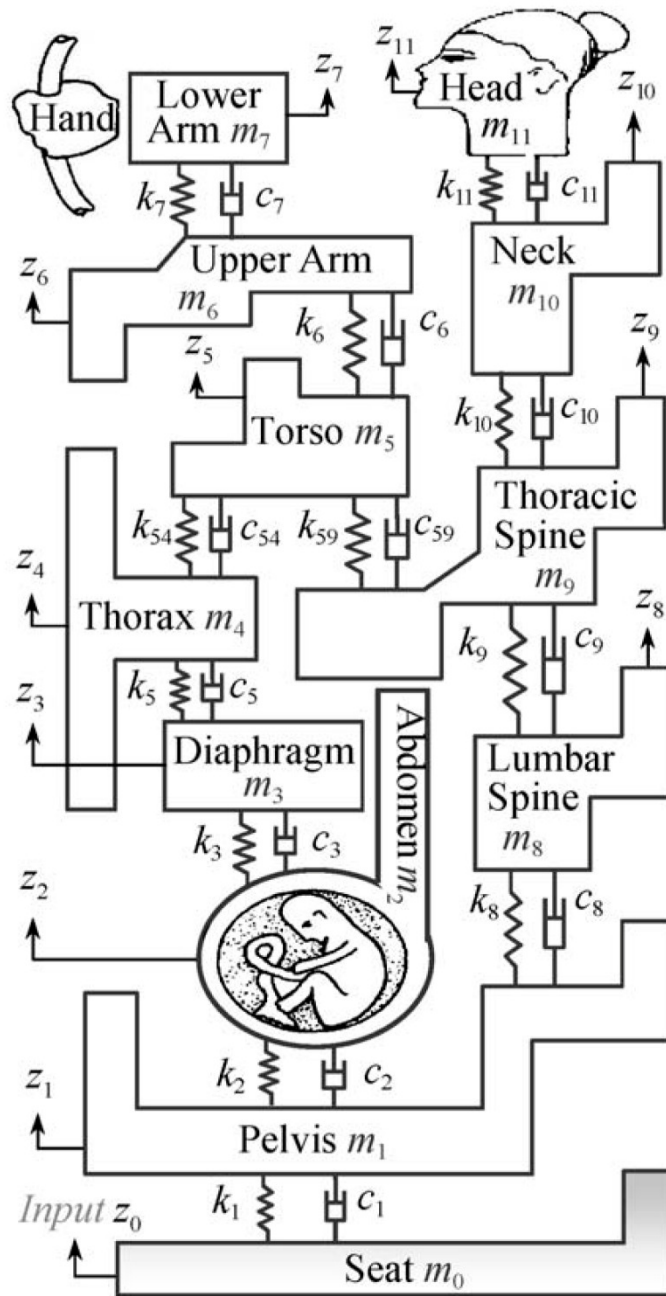
Figure 1.16. Eleven-DOF lumped biodynamic model of a seated pregnant female developed by Qassem and Othman (1996), (Liang and Chiang, 2006).

Chapter 2

Design Optimization and Experimental Validation of Magnetorheological Energy Absorber with Large Dynamic Range

2.1. Abstract

A linear stroking adaptive magnetorheological energy absorber (MREA) was designed, fabricated and tested for intense impact conditions with piston velocities up to 8 m/s. The performance of the MREA was measured by using a metric known as dynamic range, which is the ratio of maximum on-state MREA force to the off-state MREA force. Design optimization techniques were employed in order to maximize the dynamic range at high impact velocities such that MREA maintained good control authority. MREA geometrical parameters were optimized by evaluating MREA performance on the basis of Bingham-plastic model incorporating minor losses (BPM model). Computational fluid dynamics and magnetic FE analysis were conducted to verify the performance of passive and controllable MREA force respectively. Subsequently, low-speed cyclic testing (0-2 Hz subjected to 0-5.5 A) and high-speed drop testing (0-4.5 m/s at 0 A) were conducted for quantitative comparison with the numerical simulations. Refinements to the nonlinear analytical BPM model were carried out for improved forecasting of MREA performance.

33

2.2.   Introduction

Adaptive energy absorbers such as magnetorheological energy absorbers (MREAs) have been proposed as potential candidate for shock mitigation applications in automobiles, fast boats and helicopters (Choi and Wereley, 2005a; Choi and Wereley, 2005b; Hiemenz *et al.*, 2007; Singh and Wereley, 2013; Wereley *et al.*, 2011). MR recoil absorbers or dampers have also been applied in controlling the recoil dynamics subjected to large impacts (Ahmadian and Poyner, 2001; Ahmadian *et al.*, 2002; Chen and Wereley, 2004; Li and Wang, 2012). An MREA is similar to a conventional passive hydraulic energy absorber (EA) in that the fluid is pushed through an orifice as the piston moves through the hydraulic cylinder (Cook *et al.*, 2007; Mao *et al.* 2014). The orifice is typically integrated with an electromagnet housed in the piston. MREA employ smart MR fluids that are a fluidic composite in which 0.3-10 micron diameter carbonyl iron particles are suspended in a hydrocarbon-based carrier fluid (Cha *et al.*, 2010; Jeon and Koo, 2012). When current is applied to the electromagnet, the magnetic field in the orifice develops, which in turn builds the yield stress of the MR fluid and the corresponding stroking load. By controlling the current supplied to the electromagnet, the controllable component of MREA force can be adjusted in response to a command from the controller. Consequently, the load-stroke profile of the MREA can be electronically, reversibly, and rapidly adjusted, making it desirable for varying impact conditions (Choi and Wereley, 2005a). In the event of exigency such as power failure, MREAs are capable of providing limited shock absorption owing to the Newtonian behavior

of the MR fluid (i.e. no current input) like passive hydraulic EAs. A fail-safe behavior of MREA increases their suitability for crashworthiness applications.

The adaptive nature of MREA with a fixed available stroke is necessary to accommodate widely varying occupant/payload weights subjected to a large shock spectrum (Wereley *et al.*, 2011). General design guidelines govern off-state MREA stroking load to accommodate smallest occupant/payload and maximum on-state MREA stroking load for largest weight. The wide controllability of MREA is quantified by using dynamic range (Mao *et al.*, 2007). The dynamic range is defined as the ratio of maximum on-state MREA stroking load to the off-state MREA force. Various analytical and experimental studies have been conducted that show sharp drop in dynamic range as the impact velocities were increased. For an MREA to be suitable for crashworthiness applications that experience high impact velocities, a large dynamic range should be maintained to have large control authority. For instance, a helicopter could undergo hard landing between 20-22 ft/s to crash landing with impact velocities varying between 38-42 ft/s (Hiemenz *et al.*, 2007). Ahmadian and Norris (2004) studied the performance of double-ended MREA exposed to impact velocities around 6.6 m/s. The achievable dynamic range at impact velocity of 2.2 m/s was around 2.75. As the impact velocities were increased to 6.6 m/s, the dynamic range dropped to 1 signifying poor control authority at high speed impacts. Browne *et al.* (2009) impact tested MREA for velocities varying between 1-10 m/s and found similar trends of drop in dynamic range for increased impact velocities. Mao *et al.* (2007) designed a bifold MREA on the basis of Bingham-plastic nonlinear flow model for piston velocities as high as 6.75 m/s. Based on the

simulated observations, the dynamic range attained a value around 2 for piston velocities up to 6.67 m/s. The trend of decreasing dynamic range with piston velocity was also observed similar to previous studies. The reason for drop in dynamic range is connected to the variation in Reynolds number, Re. At high impact velocities, the fluid flow transitions from laminar to turbulent regime characterized by high Reynolds number. Such transition energizes the fluid flow and results in higher viscous MREA forces, further causing reduction in control authority or dynamic range. A large orifice diameter helps in maintaining low Reynolds number but that significantly weakens the magnetic flux intensity and related performance of MREA. Nevertheless, new design concepts are proposed that promise high dynamic range at large piston velocities (Hiemenz *et al*., 2010; Yazid *et al.*, 2014).

In this study, a design methodology is developed using design optimization techniques for an MREA with large dynamic range operating at piston velocities up to 8 m/s. Bingham-plastic model that included the effects of minor losses (BPM model) developed by Mao *et al.* (2014) was integrated with the optimization algorithm to determine the geometrical parameters of MREA subjected to practical constraints. The MREA geometrical parameters were finalized on the basis of numerical simulations such as computational fluid dynamics (CFD) analysis for off-state or passive viscous forces and magnetic FE analysis for controllable MREA yield forces. Subsequently, MREA was fabricated and experiments were conducted using low-speed cyclic testing and high-speed drop testing for different piston velocities and current inputs. A quantitative and qualitative comparison between analytical models and experiments was carried out.

2.3. Magnetorheological Energy Absorbers (MREAs)

A linear stroking double-ended configuration of the MREA was selected for the design analysis using a nonlinear model known as Bingham-plastic model that includes minor effects such as fluid flow experiencing sudden expansion and contraction (Mao *et al*., 2014). The double-ended configuration considers piston shafts at both ends of the piston such that the motion of the piston inside the hydraulic cylinder does not affect the fluid volume. Further, the piston consisted of multi-stage electromagnetic coils that generate magnetic field as shown in Figure 2.1.

The energy absorber (EA) forces were evaluated by estimating the pressure drops occurring inside the hydraulic cylinder due to fluid flow because of motion of piston. The schematic of geometric fluid circuit with the regions of pressure drop for a 3-electromagnetic coil configuration is shown in Figure 2.2. The pressure drops resulted because the fluid experienced the following phenomena:

- Fluid entrance from region 1-2.

- Sudden expansion from region 2-3, 4-5 and 6-7.

- Sudden contraction from region 3-4, 5-6, 7-8.

- Fluid exit from region 8-9.

- Viscous Darcy friction losses in coil gap 3, 5 and 7.

- Viscous Darcy friction losses in MR valves 2, 4, 6 and 8.

- Losses due to MR effect in MR valves 2, 4, 6 and 8.

2.3.1. Design Analysis

A detailed single-stage electromagnetic coil of piston is shown in Figure 2.3. The main parameters that define the geometry of single-stage are as follows:

- L_a active length of a single-stage (MR effect region)

- L_c coil length of a single-stage

- d MR valve thickness

- d_c coil gap thickness

- D_{in} inner diameter of hydraulic cylinder

- D_p piston diameter

- D_b effective MR valve diameter

The pressure drops of a single-stage configuration were estimated first and then extrapolated to evaluate pressure drops for a multi-stage electromagnetic coil. The pressure drops occurring due to fluid motion determine two components of MREA force: the passive viscous or off-state forces and controllable MR yield force.

The pressure drop due to MR effect, ΔP_{MR}, for a single coil is given as

$$\Delta P_{MR} = \frac{2L_a \tau_{MR}}{d}$$

$$(2.1)$$

where τ_{MR} is the MR yield stress, an inherent property of the MR fluid.

The MREA yield force, F_{MR}, for n-stage electromagnetic coil configuration was calculated as

$$F_{MR} = n\Delta P_{MR} A_p$$

$$(2.2)$$

The passive viscous or off-state pressure drop is a combination of pressure drop due to viscous losses along the MR valve, ΔP_η, pressure drop due to minor losses (sudden expansion and contraction), ΔP_{ml}, and pressure drop due to viscous losses induced by coil gap, ΔP_{coil}. These pressure drops are dependent on square of velocity and given as

$$\Delta P_\eta = \frac{\rho}{2} V_d^2 \frac{f L_a}{2d} \tag{2.3}$$

$$\Delta P_{ml} = \frac{\rho}{2} V_d^2 (K_{SC} + K_{SE}) \tag{2.4}$$

$$\Delta P_{coil} = \frac{\rho}{2} V_c^2 \frac{f_c L_c}{2d_c} \tag{2.5}$$

where, ρ is the density of MR fluid, V_d and V_c are the average fluid velocities in MR valve and coil gap respectively, which are given as

$$V_d = \frac{A_p V_p}{A_d} = \frac{A_p V_p}{\pi D_b d} \ ; \ V_c = \frac{A_p V_p}{A_c} \tag{2.6}$$

with A_p, A_d and A_c as the areas of piston, MR valve cross-section and coil gap cross-section respectively and V_p is the velocity of piston.

$$A_p = \frac{\pi}{4} \left(D_p{}^2 - D_r{}^2 \right) \tag{2.7}$$

$$A_c = \pi (r_o{}^2 - r_i{}^2) \tag{2.8}$$

$$r_o = \frac{D_{in}}{2} \ ; \ r_i = \frac{D_{in}}{2} - d_c \tag{2.9}$$

where, D_r is the diameter of piston rod.

The coefficients of sudden expansion, K_{SE}, and sudden contraction, K_{SC}, are obtained using empirical formulae (White, 1998).

$$K_{SE} = \left(1 - \frac{A_d}{A_c}\right)^2 \; ; \; K_{SC} = 0.42\left(1 - \frac{A_d}{A_c}\right)$$

(2.10)

The Darcy friction factor, f, was determined in a piecewise manner and was dependent on Reynolds number, Re, hydraulic diameter, D_h, and average pipe wall roughness, $\in$.

$$f = \beta \quad if \quad Re \leq 2000$$

(2.11)

$$f = (1-\alpha)\beta + \frac{\alpha}{\left\{1.8\log_{10}\left[\left(\frac{\in/D_h}{3.7}\right)^{1.11} + \frac{6.9}{4000}\right]\right\}^2} \quad if \quad 2000 < Re < 4000$$

(2.12)

$$\frac{1}{f^{\frac{1}{2}}} \approx -1.8\log_{10}\left[\left(\frac{\in/D_h}{3.7}\right)^{1.11} + \frac{6.9}{Re}\right] \quad if \quad Re \geq 4000$$

(2.13)

with

$$\beta = \frac{96}{Re}; \; \alpha = \frac{Re - 2000}{4000 - 2000}; \; Re = \frac{\rho V_d D_h}{\eta}; \; D_h = 2d$$

(2.14)

where, η is the viscosity of MR fluid.

The Darcy friction factor for the coil gap, f_c, was obtained by using an annular duct model similar to Darcy friction factor for MR valve by replacing β, Re and D_h with β_{eff}, Re_{eff} and $D_{h_{eff}}$ respectively.

$$\beta_{eff} = \frac{64}{Re_{eff}}$$

(2.15)

$$Re_{eff} = \frac{\rho V_c D_{h_{eff}}}{\eta} \qquad (2.16)$$

$$D_{h_{eff}} = \frac{2(r_o - r_i)}{\zeta} \qquad (2.17)$$

$$\zeta = \frac{(r_o - r_i)^2 (r_o{}^2 - r_i{}^2)}{r_o{}^4 - r_i{}^4 - (r_o{}^2 - r_i{}^2)^2 / ln(r_o/r_i)} \qquad (2.18)$$

Using the above equations, the passive viscous or off-state force, F_V, of n-stage electromagnetic coil based MR damper were obtained as

$$F_V = A_p[n(\Delta P_\eta + \Delta P_{ml} + \Delta P_{coil}) + \Delta P_E] \qquad (2.19)$$

The pressure drop arising from MR fluid undergoing a single entrance and exit effect, ΔP_E, was empirically estimated (Mao *et al.*, 2014; White, 1998).

$$\Delta P_E = \frac{\rho}{2} V_d{}^2 (K_{entry} + K_{exit}) \qquad (2.20)$$

The coefficients K_{entry} and K_{exit} were obtained in a similar fashion as for K_{SC} and K_{SE} respectively.

$$K_{entry} = 0.42\left(1 - \frac{A_d}{A_p}\right); \ K_{exit} = \left(1 - \frac{A_d}{A_p}\right)^2 \qquad (2.21)$$

The summation of passive viscous, F_V, and controllable MREA yield force, F_{MR}, results in total MREA stroking load, F_D.

2.4. Magnetorheological Energy Absorber Optimization

MREAs are capable of providing adaptive stroking load and the extent of adaptability is determined by the ratio of maximum achievable MREA stroking load

(i.e. stroking load at maximum current input), F_D, to the stroking load at off-state condition (i.e. stroking load at no current input), F_V. This ratio is defined as dynamic range, *DR* (Ahmadian and Norris, 2004; Browne *et al*., 2009).

High impact conditions result in large piston velocities and the corresponding Reynolds number, *Re,* in the MR valve and coil gap may approach a value corresponding to that of turbulent regime. The off-state or passive viscous forces, which are dependent on velocity square as discussed earlier and are uncontrollable, become large and significantly reduce the dynamic range. The sharp increase in uncontrollable force of the MREA reduces the dynamic range at large velocities. For an MREA to maintain good adaptability over the entire range of piston velocities for a given shock spectrum, it should maintain a good dynamic range. Therefore, an optimization methodology was formulated in order to expand the load-stroke profile or, equivalently, the dynamic range of MREA.

2.4.1. Optimization Formulation

The dynamic range or the load-stroke profile of MREA can be extended if the MREA stroking load at maximum magnetic field is increased with low off-state forces i.e. a trade-off between controllable and passive force. In other words, the optimized MREA should be able to provide high MREA yield force with low viscous forces for the range of operating piston velocities.

Cost Function

The dynamic range for the MREA is given as

$$DR = \frac{F_D}{F_V} = \frac{F_{MR} + F_V}{F_V} = 1 + \frac{F_{MR}}{F_V}$$

$$(2.22)$$

A typical MREA load-stroke profile with MREA stroking load at maximum magnetic field and off-state condition evaluated using the Bingham-plastic model with minor losses is presented in Figure 2.4. Increasing the dynamic range by maximizing the MREA yield force and minimizing the off-state forces is equivalent to increasing the gap between the curves corresponding to forces at maximum field and off-state or no-field. Therefore, the alternative multi-objective problem can be considered that was evaluated at peak piston velocities.

$$Max : F_{MR}$$

$$Min : F_V$$

$$(2.23)$$

There are numerous ways to interpret a multi-objective problem. Among these, the weighting method and ε-constraint method are most widely used because they can provide multiple solutions (trade-off design solutions). In the ε-constraint method, only one objective function is considered as a cost function while the other objective function is constrained using a parameter (Mavrotas, 2009). The variation of constraining parameter leads to multiple optimization problems and results in generation of multiple solutions. Therefore, the current multi-objective problem can be formulated alternatively as:

$$Max : F_{MR}$$

$$(2.24)$$

with the second objective function constrained as

$$F_V \leq \varepsilon$$

$$(2.25)$$

where ε is the constraining parameter, the variation of which results in multiple design solutions.

Design Variables

Six design variables were involved with the optimization of dynamic range or load-stroke profile of MREA that determined the geometry of the MREA and number of current carrying wire-turns in each electromagnetic coil. These are defined as follows:

1. L_a active length of a single-stage (MR effect region)

2. L_c coil length of a single-stage

3. d MR valve thickness

4. d_c coil gap thickness

5. D_{in} inner diameter of hydraulic cylinder

6. N number of wire-turns per coil

Constraints

The constraints were based on maximum allowable off-state or viscous MREA force, geometric constraints and magnetic properties of the fluid.

<u>***Constraint on Off-state MREA Force***</u>: A constraint was established on the off-state force because off-state force should not exceed the maximum permissible stroking load for lightest occupant/payload. The threshold on maximum allowable passive viscous or off-state MREA force was limited to 15 kN at peak piston velocity of 8 m/s. Since a constraining parameter corresponding to passive viscous MREA force was already assigned to the optimization problem, the constraining parameter was

varied from 12 to 18 kN with a step of 0.25 kN to obtain multiple design points. Though the maximum permissible off-state force was limited to 15 kN, the optimization was conducted up to 18 kN in order to determine the shape of Pareto frontier.

Constraint on Fluid Gap: The piston of MREA consisted of multiple electromagnetic coils comprising copper wire wrapped in the piston grooves. For a given number of wire-turns per coil, the copper wire occupies finite space. Generally, the grooves in the piston are designed slightly deeper (i.e. large coil gap, d_c) to accommodate the wire-turns comfortably because coil gap smaller than MR valve chokes the fluid flow under the motion of piston.

$$d \leq d_c$$
(2.26)

Constraint based on Magnetic Circuit: The amp-turns (NI) were determined based on Kirchoffs's law of magnetic circuits and yielded an equality constraint that involved MREA geometrical parameters.

$$NI = \oint H . dl$$
(2.27)

$$NI = H_f(2d) + H_s\left(2L_a + 2L_c + D_p\right)$$
(2.28)

where H_f and H_s are the H-field of fluid, and piston and hydraulic cylinder material, typically 12L14 steel.

***Bounds on Design Variables*:** In addition to the above mentioned constraints there were upper and lower bounds on the design variables selected on the basis of practical limitations and are mentioned in Table 2.1.

2.4.2. Optimized MREA

Optimization of MREA was executed using an inbuilt optimization methodology in MATLAB (R2010b) known as *Multistart* method. A major advantage of *Multistart* method was that it generated multiple initial design points and operated the basic optimization algorithm to find multiple local optima. Using this technique, the possibility of capturing the global optimum or the best feasible design point increased significantly. The probability of capturing the global optimum was mainly dependent on the number of initial design points being generated. However, selecting too many initial design points was also not desirable because of large computational costs. The distinct multiple local minima were then arranged in a particular order based on objective function value, the first local optimum being the best solution.

The optimization of load-stroke profile of MREA was carried out for different cases with 3-5 electromagnetic coils based piston configuration. The MREA was optimized at operating H-field of 12L14 steel and MR fluid for all configurations. The parameters used for MREA optimization are given in Table 2.2. The *Multistart* method utilized the basic optimization algorithm known as interior-point based *fmincon.* The first initial point was selected as the upper bound of the design variables as given in Table 2.1 for the optimization algorithm to commence. 25 random initial design points were generated using the *Multistart* methodology for

46

maximizing the load-stroke profile of an MREA. The multiple optimum solutions (also known as Pareto optimal solutions) corresponding to different values of constraining parameter evaluated at peak piston velocity of 8 m/s are presented in Figure 2.5. As can be seen that increased number of electromagnetic coils resulted in larger controllable MREA yield force for a given constraining parameter value. The variation of Pareto optimal solutions for a given piston configuration shows conflicting behavior between two objectives under consideration i.e. with increased MREA yield force, the passive viscous MREA force also increases. Pareto optimal solutions depict a continuous frontier for different configurations. The threshold for the passive viscous force was limited to 15 kN and therefore, only the design points satisfying this constraint were selected.

The best optimum solutions for different electromagnetic coil configurations are tabulated in Table 2.3. It is to be noticed that the active length, coil length and the number of wire-turns converged to respective upper, lower and upper limits of the design variables. Moreover, the coil gap and MR valve gap were exactly same and remained constant with varying electromagnetic coils from 3-5. Same MR valve gap and coil gap eliminated the sudden compression and expansion losses contributing to passive viscous forces. The increased electromagnetic coils resulted in decrease in the inner diameter of the MREA and the geometry of the MREA transformed from low to high aspect ratio with increased electromagnetic coils. The main reason for such a variation was that with increase in electromagnetic coils, the piston length increased and the corresponding Darcy friction losses contribution to viscous forces increased. In order to accommodate such an increment in the viscous forces, the

MREA diameter decreased resulting in lower pressure drop due to single sharp entry and exit losses and their contribution to viscous forces. Such variation resulted in maintaining the threshold of passive viscous force enforced by constraining parameter for varying electromagnetic coil configurations.

The optimized load-stroke profile of the MREA for all configurations is presented in Figure 2.6. The increase in electromagnetic coils resulted in expansion of the load-stroke profile, however, the passive viscous or off-state forces remained same due to the decreased inner diameter of MREA as explained. The optimized MREA with 5 electromagnetic coils with piston length of 8 inches provided maximum MREA yield force of 12.9 kN and was selected as design point for fabrication.

2.5.   Numerical Simulation of MREA Forces

The optimized design of 5-electromagnetic coils based MREA was modeled using computer-aided design (CAD) program, SolidWorks, to analyze the physical implementation as shown in Figure 2.7. The stroke requirement of MREA was around 16 inches (i.e. shaft length) and the selected MREA piston had a length of around 8 inches, total amounting to 24 inches of length that the MREA hydraulic cylinder should accommodate. When the MREA was fully compressed, the probability of piston impacting the inside of hydraulic cylinder was high for off-axis loads at high impact velocities. The configuration of piston shaft assembly under such a situation is similar to a long cantilever beam with heavy mass at the free end. In order to avoid the impact of piston with the hydraulic cylinder, a piston guide was proposed such that perfect longitudinal motion was maintained under all conditions

as shown in Figure 2.7. However, the addition of piston guide affected the fluid flow and the corresponding pressure drops, further affecting the MREA load-stroke profile. The quantification of variation in MREA stroking load was very critical and therefore numerical simulations were conducted. The simulations were decoupled such that passive viscous flow for different piston velocities under no-field condition (i.e. 0 A) was simulated separately to magnetic FE simulation for different current inputs with no fluid flow motion (i.e. piston velocity of 0 m/s) to predict controllable MREA yield force.

2.5.1. Viscous Flow Simulation

The numerical simulations were conducted using a commercial computational fluid dynamics package FLUENT 14.5 to estimate the passive viscous forces due to the Newtonian behavior of the MR fluid. A 2-dimensional non-uniform structured grid was created due to axi-symmetric geometry of the MREA as shown in the Figure 2.8. The mesh geometry was designed corresponding to a double-ended MREA configuration because an accumulator that accommodates volume change inside the hydraulic cylinder due to shaft motion was not modeled for the simulations. The size of the cells near walls was smaller and gradually increased when moving away from walls. The boundary conditions are illustrated in the Figure 2.8. The total pressure drop due to fluid flow was estimated at the locations upstream and downstream of the piston. These locations were approximately half the piston length. If the locations were taken too far apart then the additional losses due to viscous flow along the wall would have augmented the total pressure drop. A realizable K-epsilon turbulence model with enhanced wall treatment was also

employed with 10% turbulence intensity to predict viscous forces in the turbulent regimes arising from high piston velocities. The fluid properties were taken as listed in Table 2.2 corresponding to Lord-132DG MR fluid. Quasi-steady simulations were conducted for piston velocities varying from 1-8 m/s.

After the solver was converged for a given case, the grid was adapted for refinements using Hanging Node method to reduce the y^+ values less than 1 in order to capture accurate boundary layer effects that determine the viscous losses as shown in Figure 2.9. This led to increase in number of cells from 28,499 to 504,791. The parameters that define the MREA geometry and the piston guide were adjusted until the peak viscous force of 15 kN was achieved at piston velocity of 8 m/s. The velocity contours for the case of 8 m/s piston velocity are shown in the Figure 2.10. The total pressure drops were obtained for the piston velocities varying form 1-8 m/s and then multiplied by the piston area to obtain passive viscous or off-state MREA forces.

2.5.2. Magnetic FE Simulation

The controllable MREA yield force was estimated by conducting magnetic FE analysis using commercial package ANSYS. The adjusted parameters were used to model a rectangular body MREA for a quasi-steady analysis for a stationary piston (i.e. 0 m/s). Quasi-steady analysis resulted in a simplified MREA force analysis and had contribution only from magnetic forces. The material for piston and hydraulic cylinder were heat-treated 12L14 steel and 1018 steel respectively. The MREA shaft was made from hardened 52100 steel and had relatively large distance from the

hydraulic cylinder to form a magnetic flux circuit, hence, it was not modeled in the analysis as shown in Figure 2.11.

Few MREA parameters were more critical than others in the analysis: the number of wire-turns in a single electromagnetic coil, number of electromagnetic coils, current input and the MR valve gap, d. The analyses were conducted for current carrying copper wire (24 AWG) with currents varying from 0.5-5.5 A. The B-field obtained for a particular case of 5.5 A is shown in Figure 2.12. As can be seen, the B-field around the electromagnetic coil length and outside the hydraulic cylinder are close to zero. Similarly, the H-field in the flow channel for 5.5 A is plotted in Figure 2.13 with piston represented from 1-9 inch length. For the regions where there were electromagnetic coils, the H-field dropped when compared to H-field along the active lengths of piston where MR effect took place. The average H-field along the length of piston in the MR valve was considered to determine the yield stress for Lord-132DG MR fluid from Figure 2.14. After the estimation of MR yield stress, the MREA yield force was obtained from Eqs. (2.1) and (2.2).

The topology of the MREA after adjustments of parameters such that viscous force threshold of 15 kN was maintained at piston velocity of 8 m/s along with large MREA yield force is presented in Figure 2.15. The adjusted MREA parameters and the co-ordinates are tabulated in Tables 2.4 and 2.5 respectively.

2.6.   Experiments

The MREA was fabricated after numerical modeling based estimation of MREA yield force and off-state viscous force. The electric resistance of 5-electromagnetic coil (24 AWG) based MREA was around 12 Ω. The current carrying

copper wire inside the electromagnetic coils was isolated from MR fluid by employing Lord 310A/B high performance epoxy to avoid short circuiting conditions. The piston-shaft-guide assembly and fully assembled MREA are shown in Figure 2.16. Fully extracted MREA had length of approximately 54 inches.

2.6.1. Cyclic Testing

The MREA performance was evaluated by conducting low speed cyclic testing on a hydraulically powered MTS machine. The set up is shown in Figure 2.17. MREA was cycled with $\pm$ 1.5 inch amplitude for frequencies ranging from 0.5-2 Hz and currents varying from 0-5.5 A. The accumulator of MREA was charged with compressed nitrogen gas to 450 psi such that when the MREA was compressed the accumulator accommodated the volume change due to shaft motion inside the hydraulic cylinder. The MREA operated in two phases: (1) push phase when shaft moves inside the hydraulic cylinder and (2) pull phase when shaft moves out of the hydraulic cylinder. These two phases are illustrated in the schematic in Figure 2.18. Accumulator pressure was of critical essence when operating in push phase. An accumulator with low pressure would get compressed easily under the piston motion and the MR fluid would fill up the space. Such phenomenon results in low MREA forces because the fluid would not be pushed entirely through the MR valve. On the other hand, the MR fluid is always pushed through the MR valve during pull phase and due to this the accumulator pressure had little effect in pull phase.

An analytical model was fitted to the experimental observations to quantify and validate the numerical simulations using the equation given as

$$F_D = K_{acc}z(t) + C_{eq}\dot{z}(t) + [F_{FR} + F_{MR}]sgn(\dot{z}(t)) \tag{2.29}$$

where K_{acc} is the stiffness due to compressed nitrogen gas in accumulator, C_{eq} is the equivalent damping constant by MREA, F_{FR} is the friction in the system, $z(t)$ and $\dot{z}(t)$ are displacement and velocity of MREA piston respectively. The least squares were minimized between model predictions and experiments in order to extract the parameters using the *Multistart* method.

$$er(F_D) = \sqrt{\sum_{i=1}^{N_D}\left(F_D^i - \widehat{F_D^i}\right)^2} \tag{2.30}$$

where ($\widehat{}$) represents experiment observation and N_D is the number of data points obtained experimentally.

Figure 2.19 shows the MREA force varying with piston displacement for two different frequencies of 0.5 and 2 Hz with varying current inputs. It is to be noticed that during the pull phase, the model fits relatively better to the experiment than for push phase for both frequencies. The reason for such behavior revolves around the fact that the pressure in the accumulator (450 psi) was not sufficient. The low accumulator pressure led to easy compression and the motion of piston pushed the MR fluid into the accumulator space rather than through the MR valve causing drop in the MREA force. Overall, increased current inputs led to more dissipation of energy as it can be correlated to area increase between MREA force and displacement for higher current inputs.

The MREA force variation with piston velocity for 0.5 and 2 Hz frequency with different current inputs are plotted in Figure 2.20. For a given cyclic frequency,

increase in current input resulted in area increase i.e. hysteresis mainly due to increased MREA yield force. Similar observation was noticeable when the frequency was increased from 0.5 to 2 Hz resulting in increased velocity-dependent MREA viscous force for a given current input. Therefore, the minimum and maximum hysteresis correspond to the case of 0.5 Hz at 0 A and 2 Hz at 5.5 A respectively.

2.6.2. High Speed Drop Testing

The objective of MREA was to maintain good dynamic range at a velocity as large as 8 m/s. The cyclic testing using MTS was limited to a frequency of 2 Hz with low piston velocities around 0.5 m/s and therefore MREA was tested at a 12 ft tall high-speed drop test facility at Alfred Gessow Rotorcraft Center (AGRC), University of Maryland as shown in Figure 2.21a. The drop test facility had a carriage on which dead weights were installed and dropped from different heights to obtain varying impact conditions. The MREA set up on the drop test facility is shown in Figure 2.21b. MREA was mounted on the load cell installed on a base plate. At the other end of the shaft, a crown stand was mounted where either a thin honeycomb or a rubber pad was placed to avoid metal-to-metal contact that may cause ringing in the load cell. A linear variable differential transformer (LVDT) was mounted on one side of the MREA to measure displacement and velocity of the piston. Large cinder blocks beside MREA were deployed in order to arrest the drop weight to avoid end-stop impact resulting from over-utilizing the MREA stroke that may cause damage to the MREA. The height for dropping payload was varied from 12 to 60 inches and maximum permissible drop weight was restricted to 440 lbs with MREA stroke limited to 10 inches because of maximum LVDT displacement measurement of 10

inches. The drop tests were conducted for off-state conditions (i.e. 0 A) with accumulator pressurized to 450 psi.

Experimental data using load cell and LVDT were recorded at a sampling rate of 2 kHz. The LVDT data were differentiated using data acquisition system in order to obtain piston velocity. During the post processing, the recorded data were filtered by using CFC 60 (100 Hz cut-off frequency) for load cell and CFC 180 (300 Hz cut-off frequency) for LVDT (Huang, 2002).

The displacement, velocity and MREA viscous force (off-state) are presented in Figure 2.22. With increased drop height from 20 to 60 inches, the stroke utilized increased due to increase in kinetic energy of the payload. It can be noticed from the displacement plot that after the impact event was over, there was a rebound. The rebound came into play due to pressurized accumulator which was compressed due to shaft motion inside the hydraulic cylinder and expanded after the impact was over. Peak MREA forces were extracted corresponding to peak piston velocities and compared with the numerical simulations. Peak piston velocity attained at the drop test facility was close to 4.5 m/s. Velocities higher than 4.5 m/s were not possible due to limitations to the drop height and weight.

2.7.   Comparison

Qualitative comparison of MREA viscous force (off-state) and yield force between BPM model, numerical FE simulations and experiments is presented in this section. Figure 2.23 shows the comparison of two components of the MREA force. Since the MTS cyclic tests were low speed tests, majority of the MREA viscous forces were determined by high-speed drop tests. CFD simulations were conducted

55

up to piston velocities of 8 m/s and shows that CFD predicted MREA viscous forces are contained within 15 kN threshold. Drop tests were limited to 4.5 m/s piston velocity due to drop height restrictions. As can be seen from Figure 2.23a that CFD simulations conducted in FLUENT matched well with experimental observations up to the piston velocities of 4.5 m/s. The BPM model actually under-predicted the viscous forces by about 33% with the adjusted MREA parameters. Few reasons for such under-prediction are based on the fact that BPM model did not include the effects of piston guide. Therefore, refinements to the BPM model were also considered as will be described later. Overall, the CFD and experiments match well.

The magnetic FE simulations predicted MREA yield forces considerably accurate when compared to those obtained from testing for currents varying from 0-5.5 A as shown in Figure 2.23b. MREA yield forces were mainly determined by cyclic testing because of low piston velocities resulted in low viscous forces that did not contribute significantly toward total MREA stroking load. Peak experiment-based MREA yield force was around 11.6 kN at a current input of 5.5 A.

2.8.   Modifications to BPM Model

Few things were considered in order to refine BPM model and to further understand the reason behind large under-prediction when compared to CFD estimations for the MREA viscous forces. The BPM model previously used assumed a rectangular geometry of MREA piston without any interference from piston guide. However, the fluid channel length increased with the fluid bending through the piston guide and that particular component complemented the Darcy friction losses as can be seen from the topology of MREA shown in Figure 2.15. Also, the addition

56

of piston guide choked the fluid flow and augmented the overall pressure drop and corresponding MREA viscous forces. In addition to these, few components were considered that led to increased pressure drop due to:

2.8.1. Gradual Contraction

As can be seen from Figure 2.15 that there were some regions in which the fluid experienced gradual contraction. For example, fluid flow between section 1-2 and section 5-6 represent gradual contraction. Semi-empirical formulae related to gradual contraction in pipes were utilized from Idelchik (2001a). A schematic of gradual contraction in pipe is presented in Figure 2.24a. Equivalent annulus areas were calculated and used in the semi-empirical formula to obtain coefficient of gradual contraction given as follows:

$$K_{GC} = K_{GC}{'} \left(1 - \frac{A_0}{A_1}\right)$$

(2.31)

where $K_{GC}{'}$ is dependent on flow central convergent angle, α_{GC}, and the hydraulic diameter, D_h and obtained from tables provided in Idelchik (2001a). The areas A_0 and A_1 represent areas of narrowest and widest cross-section of the annulus.

2.8.2. Gradual Expansion

Similar to gradual contraction, gradual expansion formulae were employed for the region when the fluid leaves the piston guide (between section 7-8) as shown

in Figure 2.15. A schematic for gradual expansion is presented in Figure 2.24b. The coefficient of gradual expansion is evaluated as follows:

$$K_{GE} = K_{GE}' \left(1 - \frac{A_0}{A_1}\right)^2 \qquad (2.32)$$

where K_{GE}' is dependent on flow central divergent angle, α_{GE}, and the area ratio, A_0/A_1, and can be estimated from tables provided in Idelchik (2001b).

2.8.3. Flow Bending

The pressure drop due to fluid flow bending was also investigated. Majority of flow bending pressure drop occurred when the fluid was pushed through the piston guide (section 5-8). The flow bending was dependent on the radius of curvature, R_C, and the bend angle, α_{FB}, as per schematic presented in Figure 2.24c. The coefficient for flow bending, K_{FB}, was estimated from pipe bending formula by Idelchik (2001c).

$$K_{FB} = A_{FB} B_{FB} \qquad (2.33)$$

where

$$A_{FB} = \begin{cases} 0.9 \sin(\alpha_{FB}) & \text{if} \quad \alpha_{FB} \leq 70^\circ \\ 1 & \text{if} \quad \alpha_{FB} = 90^\circ \\ 0.7 + 0.35 \dfrac{\alpha_{FB}}{90^\circ} & \text{if} \quad \alpha_{FB} \geq 100^\circ \end{cases} \qquad (2.34)$$

and

$$B_{FB} = \begin{cases} \dfrac{0.21}{(R_C/D_h)^{2.5}} & \text{if} \quad 0.5 \leq \dfrac{R_C}{D_h} \leq 1 \\[4mm] \dfrac{0.21}{\sqrt{R_C/D_h}} & \text{if} \qquad \dfrac{R_C}{D_h} > 1 \end{cases} \tag{2.35}$$

For MREA geometry, the radius of curvature, R_C, was much larger than hydraulic diameter, D_h.

2.8.4. Darcy Friction Factor for Rough Surfaces

The effect of Darcy friction factor was also investigated if it had any major role in large under-prediction of MREA viscous forces. The piecewise modeling of Darcy friction factor given by Eqs. (2.11)-(2.13) was segmented for different flow regimes such as laminar, transition and turbulent flow regime. The turbulent flow regime equation was based on Haaland's approximation with surface roughness of $\epsilon \leq 0.05$ mm (Genic *et al*., 2011). However, the application of Lord 310A/B epoxy on the electromagnetic coil increased the surface roughness significantly. The average surface roughness for regions where epoxy was applied was around $\epsilon = 0.2$ mm approximately. Therefore, the Darcy friction factor formula for rough surface was implemented. Due to increased roughness, the viscous forces become negligible compared to inertial forces and the Darcy friction factor, f, becomes independent of Reynolds number, Re given by the following formula (Moody, 1944).

$$\frac{1}{\sqrt{f}} = 2 \log_{10}\left(\frac{3.7}{\epsilon/D_h}\right) \tag{2.36}$$

Incorporating the pressure drops due to fluid flow experiencing gradual contraction, gradual expansion and flow bending along with refinement of Darcy friction factor for rough surface led to a better matching of modified BPM model with experiments as shown in Figure 2.25. It is observable that drop tests, CFD and modified BPM model match well up to the piston velocities of 4.5 m/s. For large velocities, the predictions from modified BPM model are close to CFD estimations.

2.9.   MREA Load-Stroke Profile

The load-stroke profile for MREA under consideration subjected to current inputs varying from 0-5.5 A and for different piston velocities are presented in Figure 2.26. The experimental observations were compared with numerical simulations (CFD and magnetic FE analysis) and modified BPM model. The theoretical MREA stroking loads at non-zero current were obtained by adding model based MREA yield force (Figure 2.23b) to both CFD and modified BPM model based predictions at 0 A (Figure 2.25).

One important observation to be noticed is that the maximum kinetic energy of the payload was limited because of payload weight and drop height restrictions. Hence, when the current input was increased, the MREA yield force increased significantly and led to a large MREA stroking load offering large resistance and resulting in lower piston velocities. Due to the transformation of MREA to a very rigid EA at high current inputs, lower piston velocities were obtained. Such rigid behavior led to large ringing noise in the load cell and LVDT data for large current inputs. Therefore MTS cyclic testing results were utilized for current inputs of 4 and

5.5 A. Experiment based MREA yield force was around 11.6 kN at maximum current feed of 5.5 A.

The variation of dynamic range of MREA with its piston velocity is presented in Figure 2.27. Dynamic range is inversely proportional to the passive viscous or off-state MREA force as given in Eq. (2.22). With increased piston velocities, the off-state forces increased significantly because of dependence on square of velocity and led to drop in dynamic range as can be seen in the Figure 2.27. CFD and modified BPM model based dynamic ranges were around 1.73 at peak piston velocity of 8 m/s. Experiment, CFD and modified model based dynamic ranges were around 2.93, 3.14 and 3.36 respectively at peak piston velocity of 4.5 m/s.

2.10. Conclusions

The design methodology of magnetorheological energy absorber (MREA) with large load-stroke profile or the dynamic range was developed. MREA dimensions were obtained by maximizing the dynamic range at peak piston velocity of 8 m/s via design optimization techniques. The maximization of dynamic range required a key trade-off between controllable MREA yield force and passive viscous or off-state force. The most important constraint on the design methodology of MREA was the maximum permissible viscous force of 15 kN at piston velocity of 8 m/s. Practical considerations led to modifications in the design geometry, which were assessed by numerical simulations for both passive viscous forces and controllable MREA yield forces. MREA was fabricated after fine-tuning the geometrical parameters on the basis of CFD and magnetic FE analysis. Low speed

cyclic testing and high speed drop testing were conducted for piston velocities up to 4.5 m/s and currents in the range 0-5.5 A. Experiment based MREA performance was evaluated and validated with respect to the analytical model based observations. Model based maximum MREA yield force was around 11.3 kN at 5.5 A and passive viscous force was around 15 kN at piston velocity of 8 m/s providing the dynamic range of 1.73. The dynamic range based on experiments was around 2.93 at piston velocity of 4.5 m/s operated at maximum current of 5.5 A. The limitations of Bingham-plastic model with minor losses (BPM model) were explored and refinements were carried out. Surface roughness of flow channel proved to be a critical factor in the BPM model refinement.

References

Ahmadian M, and Poynor J C, 2001, An evaluation of magneto-rheological dampers for controlling gun recoil dynamics *Shock and Vibration*, Vol. 8, pp. 147-155.

Ahmadian M, Appleton R, and Norris J A, 2002, An analytical study of fire out of battery using magneto-rheological dampers *Shock and Vibration*, Vol. 9, pp. 129-142.

Ahmadian M, and Norris J A, 2004, Rheological controllability of double-ended MR dampers subjected to impact loading *Proceeding of SPIE*, 5386:185-194.

Browne A L, McCleary J, Namuduri C S, Webb S R, 2009, Impact performance of magnetorheological fluids *Journal of Intelligent Material Systems and Structures*, Vol. 20, pp. 723-728.

Cha G, Ju Y S, Ahure L A, and Wereley N M, 2010, Experimental characterization of thermal conductance switching in magnetorheological fluids *Journal of Applied Physics,* Vol. 107, No. 9, 09B505.

Chen P C, and Wereley N M, 2004, Magnetorheological damper and energy dissipation method U.S. Patent 6,694,856. Filed: Feb. 22, 2002. Issued: Feb. 24, 2004.

Choi Y T and Wereley N M 2005a Mitigation of Biodynamic Response to Vibratory and Blast-induced Shock Loads Using Magnetorheological Seat Suspensions *Proc. IMechE Part D: Journal of Automobile Engineering*, Vol. 219, pp. 741-753.

Choi Y T and Wereley N M 2005b Biodynamic Response Mitigation to Shock Loads Using Magnetorheological Helicopter Crew Seat Suspensions *AIAA Journal of Aircraft*, Vol. 42, No. 5, pp. 1288-1295.

Cook E, Hu W, and Wereley N M, 2007, Magnetorheological bypass damper exploiting flow through a porous channel *Journal of Intelligent Material Systems and Structures*, Vol. 18, No. 12, pp. 1197-1203.

Desjardins S P, Zimmerman R E, Bolukbasi A O and Merritt N A 1989 Aircraft Crash Survival Design Guide *Aviation Applied Technology Directorate*, USAAVSCOM TR 89-D-22D, Fort Eustis, VA.

Genic S, Arandjelovic I, Kolendic P, Jaric M, Budimir N, and Genic V, 2011, A review of explicit approximations of Colebrook's equation *FME Transactions,* Vol. 39, pp. 67-71.

Hiemenz G J, Choi Y T and Wereley N M 2007 Semi-Active Control of Vertical Stroking Helicopter Crew Seat for Enhanced Crashworthiness *AIAA Journal of Aircraft*, Vol. 44, No. 3, pp. 1031-1034.

Hiemenz G J, Hu W, Ngatu G, and Wereley N M, 2010, Rotary vane magnetorheological energy absorber U.S. Patent US2010/0300819 A1.

Huang M, 2002, Vehicle crash mechanics *CRC Press*, Dearborn, MI.

Idelchik I E, 2001a, Handbook on Hydraulic Resistance: Stream intake in pipes and channels (resistance coefficients of inlet sections), Third Edition, CRC Begell House.

Idelchik I E, 2001b, Handbook on Hydraulic Resistance: Smooth velocity variation (resistance coefficients of diffusers), Third Edition, CRC Begell House.

Idelchik I E, 2001c, Handbook on hydraulic resistance: Variation of stream direction, Third Edition, CRC Begell House.

Jeon J, and Koo S, 2012, Viscosity and dispersion state of magnetic suspensions *Journal of Magnetism and Magnetic Materials,* 324(4), pp. 424-429.

Li Z C, and Wang J, 2012, Gun recoil system employing a magnetorheological fluid damper *Smart Mater. Struct.* 21105003 doi:10.1088/0964-1726/21/10/105003

Mao M, Hu W, Choi, Y T and Wereley N M 2007, A magnetorheological damper with bifold valves for shock and vibration mitigation *J. Intell. Mater. Syst. Struct.*18 1227-1232.

Mao M, Hu W, Choi Y T, Wereley N M, Browne A L, and Ulicny J, 2014, Experimental validation of a magnetorheological energy absorber design analysis, *Journal of Intelligent Material Systems and Structures*, 25(3):352-363.

Mavrotas G 2009 Effective implementation of the epsilon-constraint method in multi-objective mathematical programming problems *Applied Mathematics and Computation*, 213455-465.

Moody L F, 1944, Friction factors for pipe flow *Transactions of the ASME*, 66(8), pp. 671-684.

Singh H J and Wereley N M 2013c Adaptive Magnetorheological Shock Isolation Mounts for Drop-induced Impacts *Smart Materials and Structures*, Vol. 22, 122001.

The Mathworks Inc., MATLAB, R2010b.

Wereley N M, Choi Y T and Singh H J 2011 Adaptive Energy Absorbers for Drop-Induced Shock Mitigation *Journal of Intelligent Material Systems and Structures,* Vol. 22, No. 6, pp. 515-519.

White F M 1998 Fluid mechanics: Viscous flow in ducts Fourth Edition, McGraw-Hill.

Yazid I I M, Mazlan S A, Kikuchi T, Zamzuri H, and Imaduddin F, 2014, Design of magnetorheological damper with a combination of shear and squeeze modes *Materials and Design*, 54(2014), pp. 87-95.

Table 2.1. Bounds on MREA design variables

Design Variable	Lower Bound	Upper Bound
L_a	0.4 inch	1.2 inch
L_c	0.4 inch	1.2 inch
d	0.1 mm	5 mm
d_c	0.1 mm	5 mm
D_{in}	2 inch	5 inch
N	200	400

Table 2.2. MREA parameters

Parameter	Value
MR fluid Density (ρ)	3080 kg/m^3
MR fluid viscosity (η)	0.112 Pa-s
Operating MR yield stress (τ_{MR})	45 kPa
Operating MR magnetizing field (H_f)	200 kA/m
Operating steel magnetizing field (H_s)	1.4 kA/m
Average pipe wall roughness (ε)	0.01 mm

Table 2.3. Global optimum solution for MREA

Design Variables	3 coils	4 coils	5 coils
L_a	1.2 inch	1.2 inch	1.2 inch
L_c	0.4 inch	0.4 inch	0.4 inch
d	3.5 mm	3.5 mm	3.5 mm
d_c	3.5 mm	3.5 mm	3.5 mm
D_{in}	3.12 inch	3.06 inch	3 inch
N	400	400	400

Table 2.4. Adjusted MREA parameters

Design Variables	5 coils
L_a	1.2 inch
L_c	0.4 inch
d	2.6 mm
d_c	2.6 mm
D_{in}	2.414 inch

Table 2.5. Co-ordinates of MREA topology w.r.t. origin

Section	Lower coordinates [x,y] (inch)	Upper coordinates [x,y] (inch)
0	[0.000, 0.500]	[0.000, 1.207]
1	[0.189, 0.800]	[0.189, 1.207]
2	[0.382, 1.105]	[0.382, 1.207]
3	[0.509, 0.980]	[0.509, 1.207]
4	[0.807, 0.980]	[0.807, 1.207]
5	[8.587, 1.105]	[8.587, 1.207]
6	[9.088, 0.595]	[9.088, 0.907]
7	[9.581, 0.595]	[9.581, 0.907]
8	[9.839, 0.500]	[9.839, 1.207]
9	[10.250, 0.500]	[10.250, 1.207]
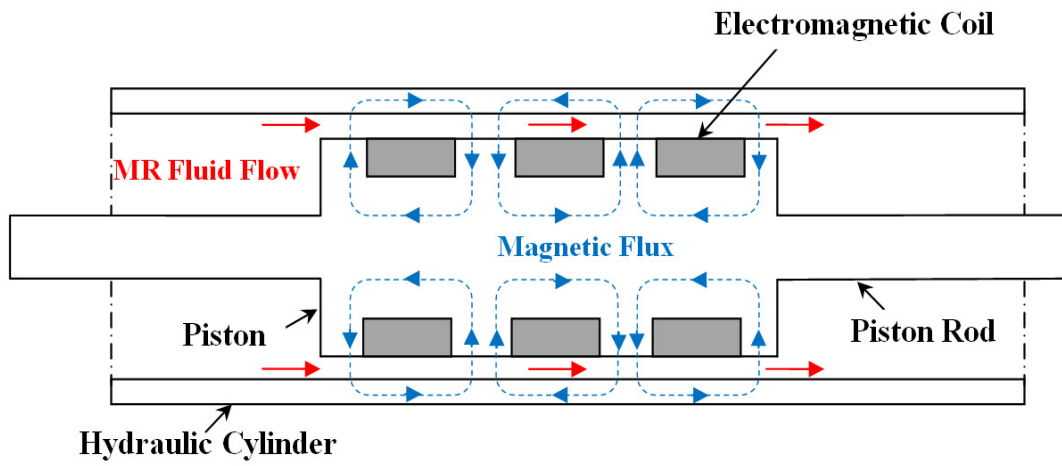
Figure 2.1. Schematic of a double-ended magnetorheological energy absorber (MREA) configuration with multi-stage electromagnetic coils.
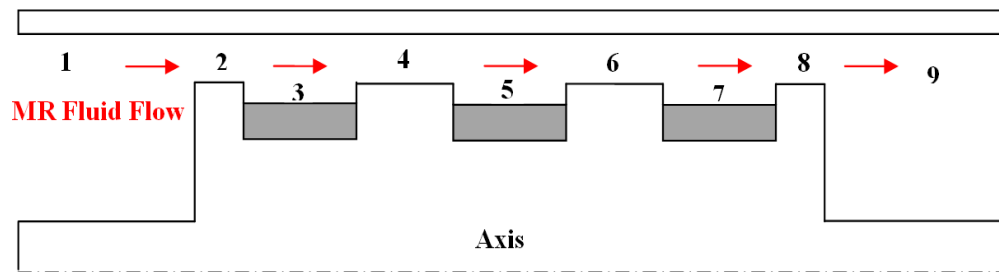
Figure 2.2. Schematic of pressure drop flow regions.
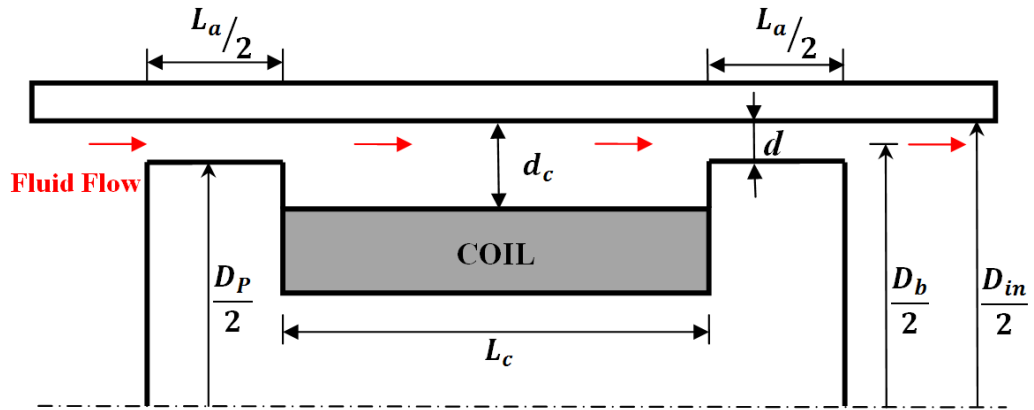
Figure 2.3. Geometric fluid circuit of a single-stage electromagnetic coil.
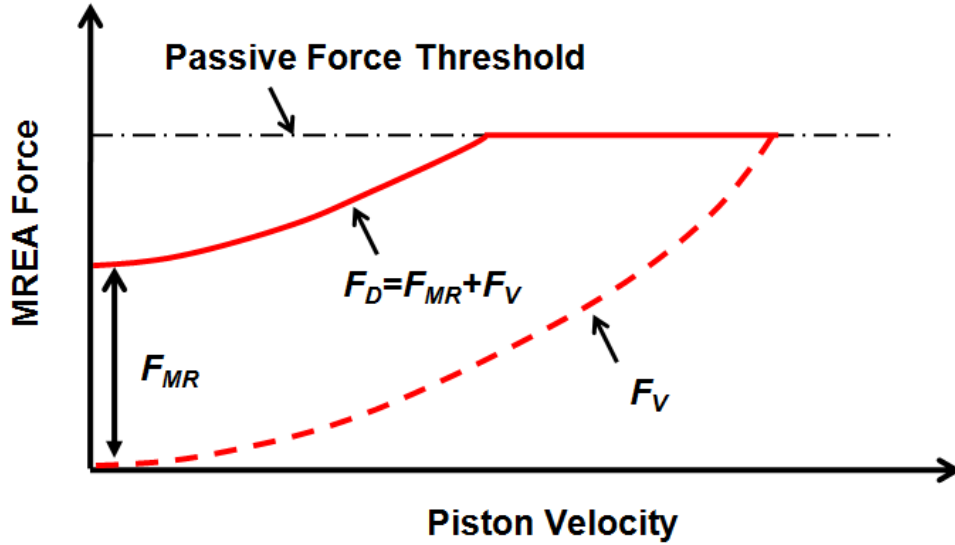
Figure 2.4. Schematic of load-stroke profile of MREA.
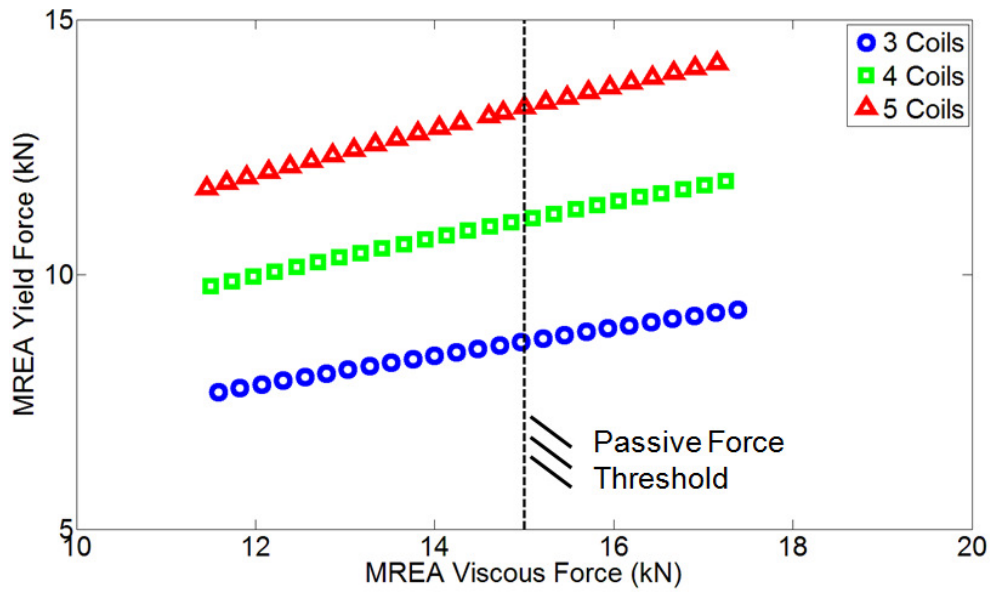
Figure 2.5. Pareto optimal solutions for different MREA configurations.
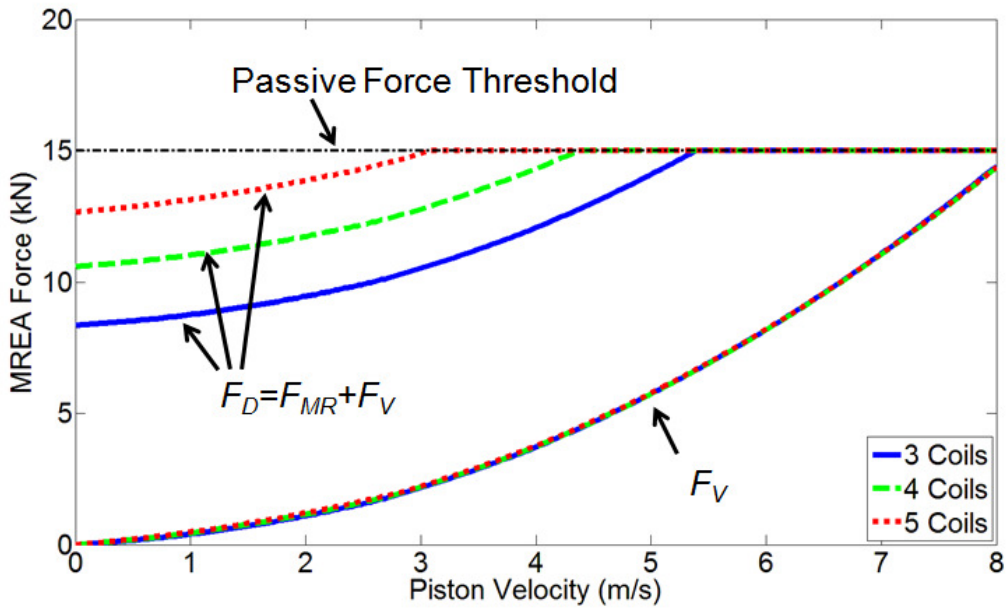
Figure 2.6. Optimized load-stroke profile for different MREA configurations.
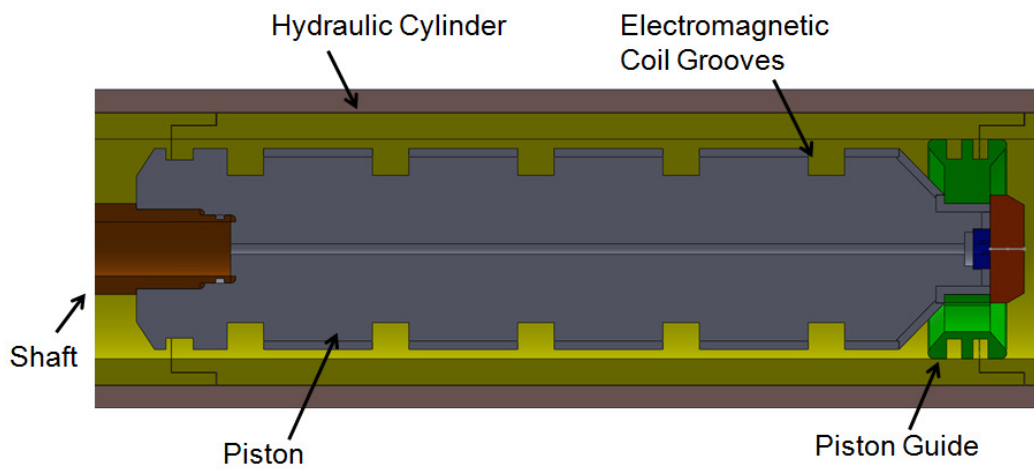
Figure 2.7. CAD model of the MREA with a piston guide.
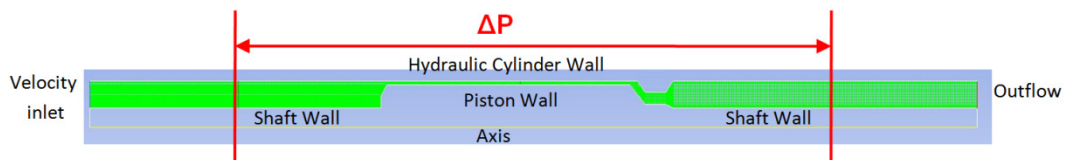
Figure 2.8. Non-uniform structured mesh for numerical simulations in FLUENT.

71
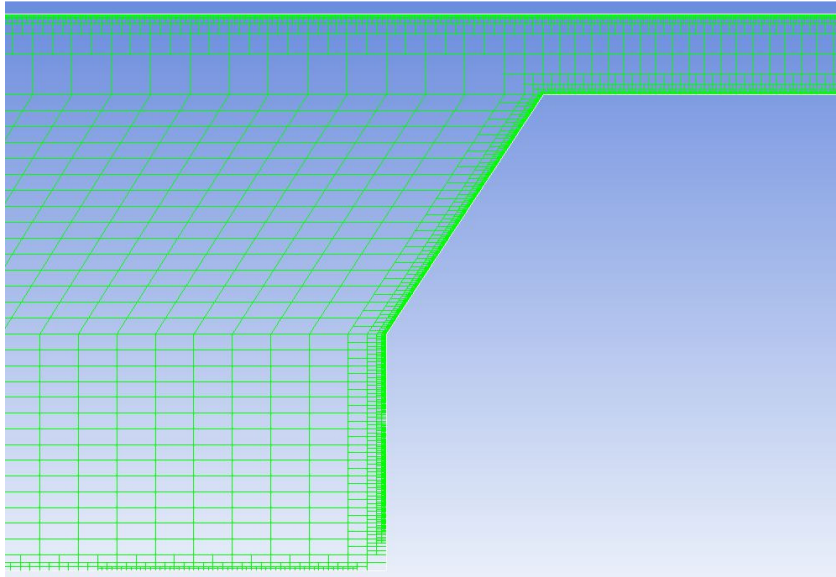
(a)
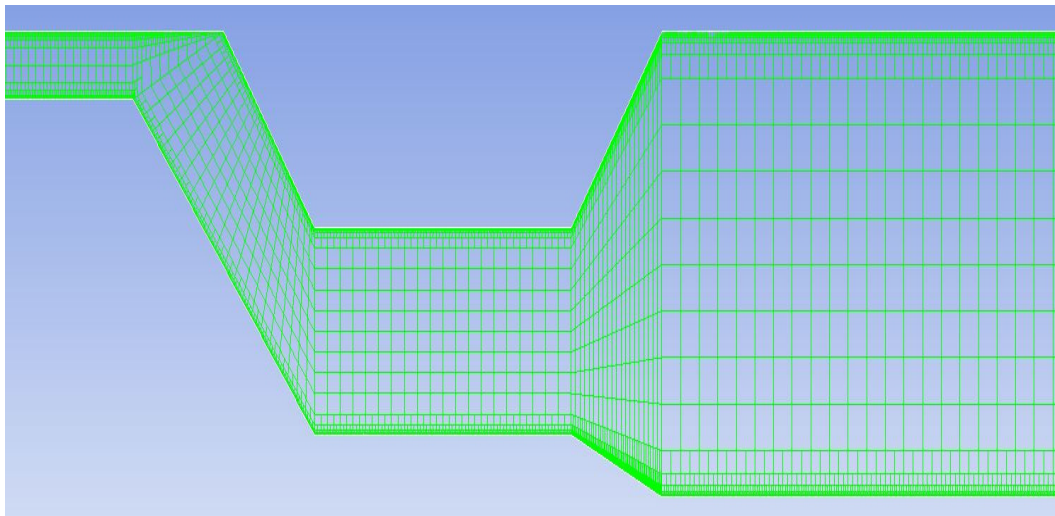
(b)

Figure 2.9. Mesh adaptation near the wall boundaries for precise boundary layer effects for (a) shaft-end and (b) piston guide of MREA.
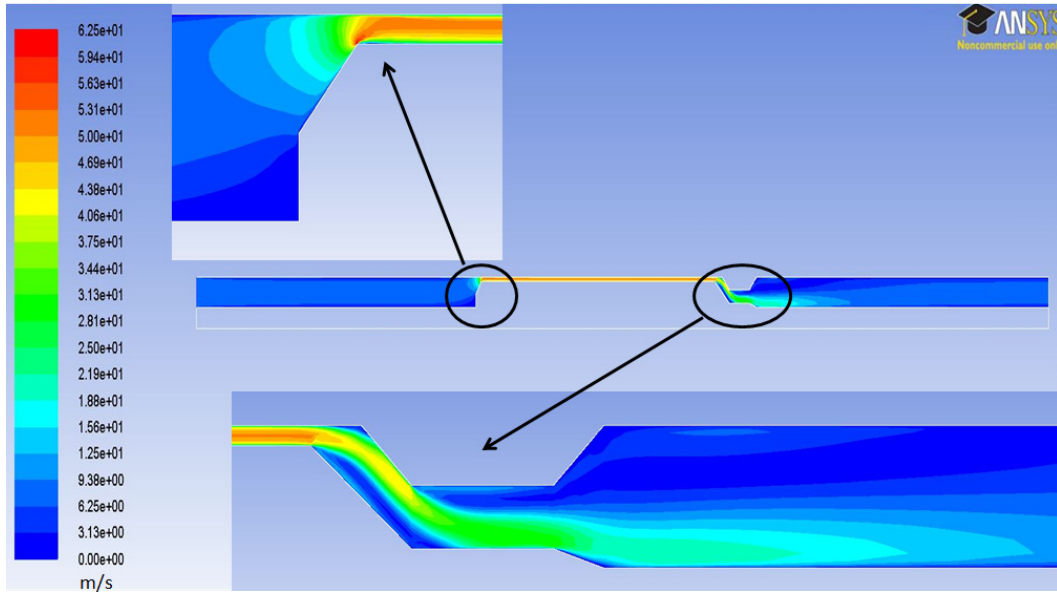
Figure 2.10. Velocity contours show recirculation regions for piston velocity of 8 m/s.
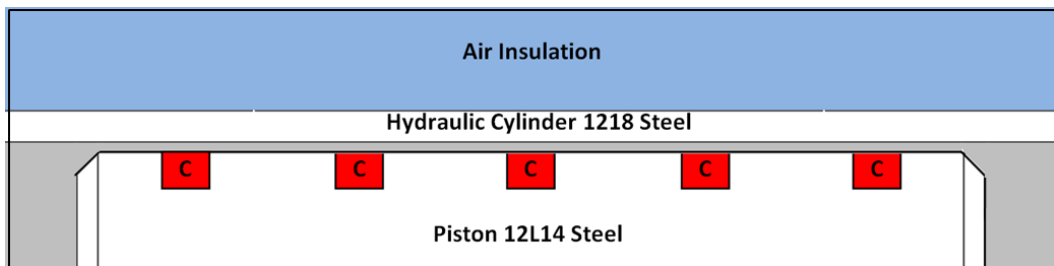
Figure 2.11. Schematic of MREA with material properties modeled for magnetic FE analysis.
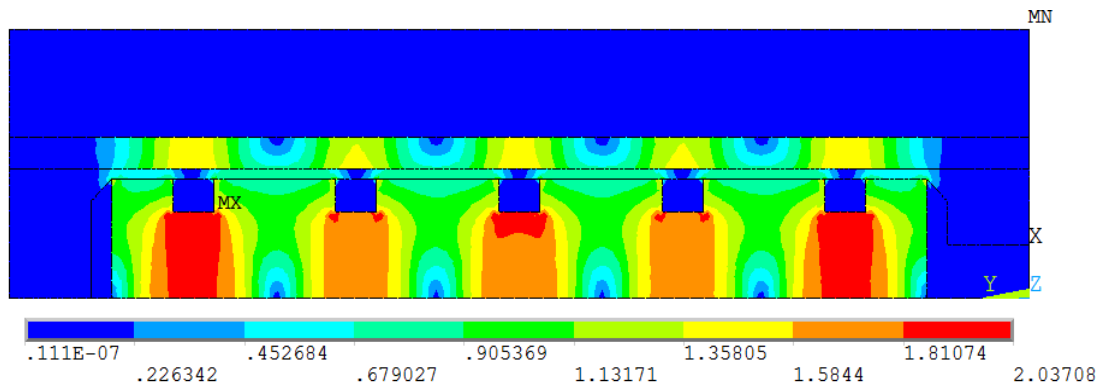
Figure 2.12. B-field obtained from magnetic FE analysis for current input of 5.5 A.
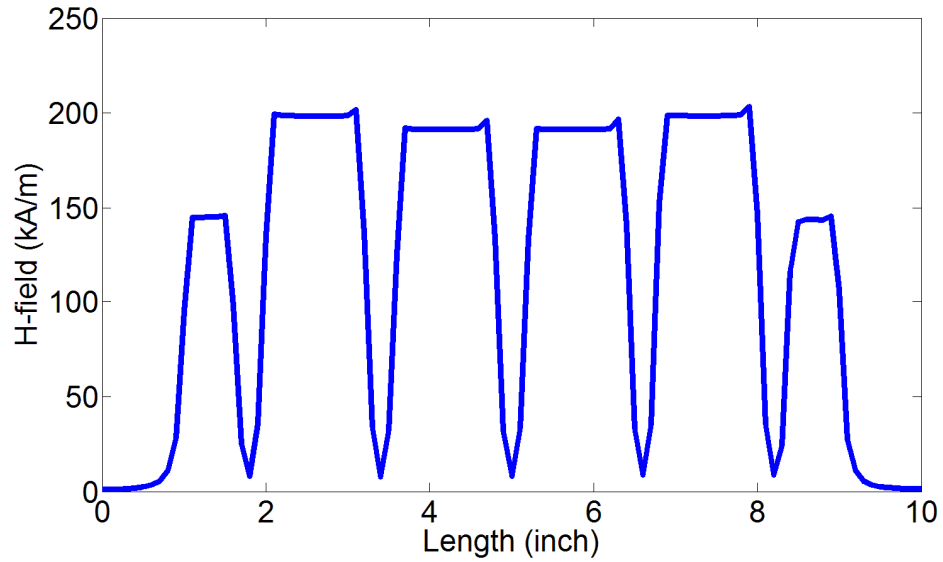
Figure 2.13. H-field in the MR valve obtained from magnetic FE analysis for current input of 5.5 A.
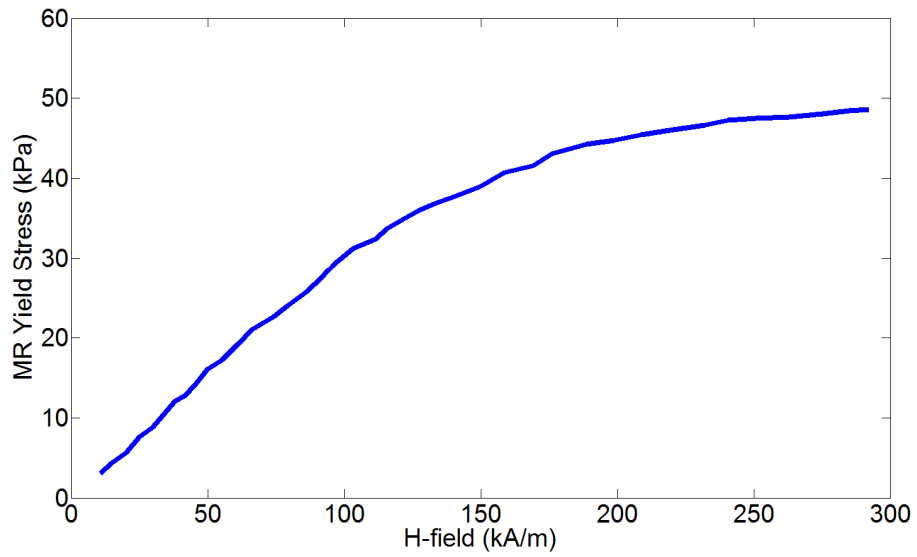
Figure 2.14. MR yield stress variation with H-field for Lord-132DG MR fluid.
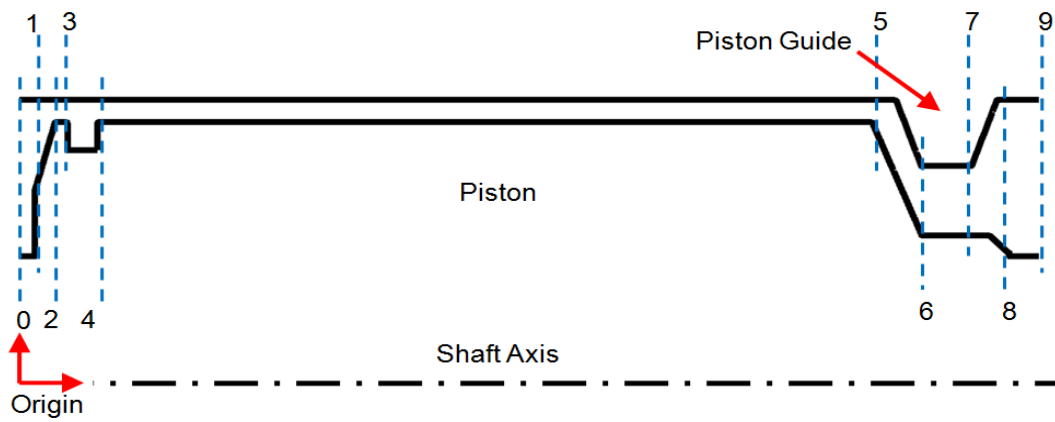
Figure 2.15. Axi-symmetric topology of MREA with respect to shaft axis.

(a)

4-ft ruler

(b)
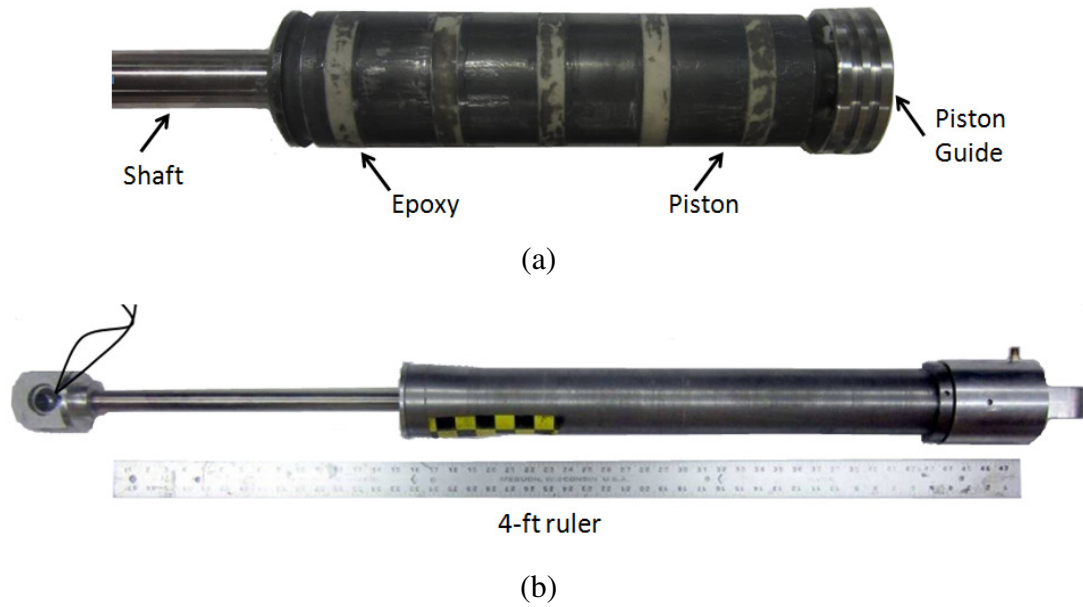
Figure 2.16. Fabricated (a) piston-shaft-guide assembly and (b) fully assembled MREA.
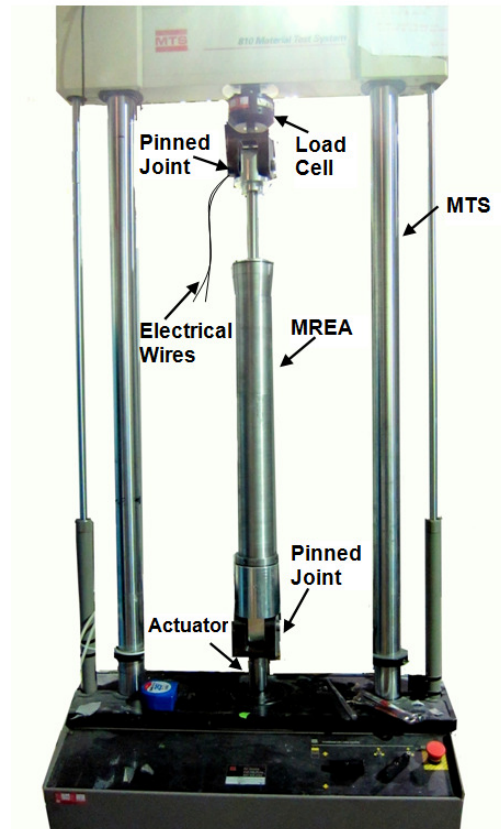
Figure 2.17. MREA set up for cyclic testing on MTS machine.
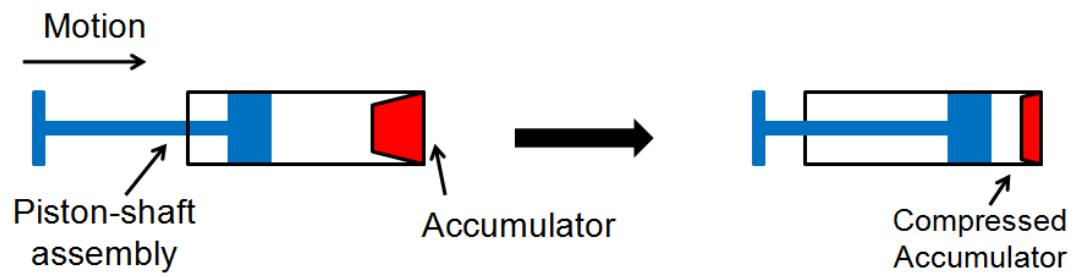
(a)
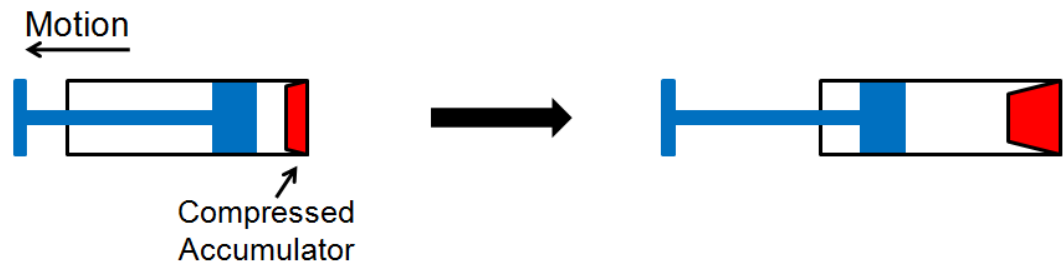
(b)

Figure 2.18. Schematic of MREA operation in (a) push and (b) pull phase.
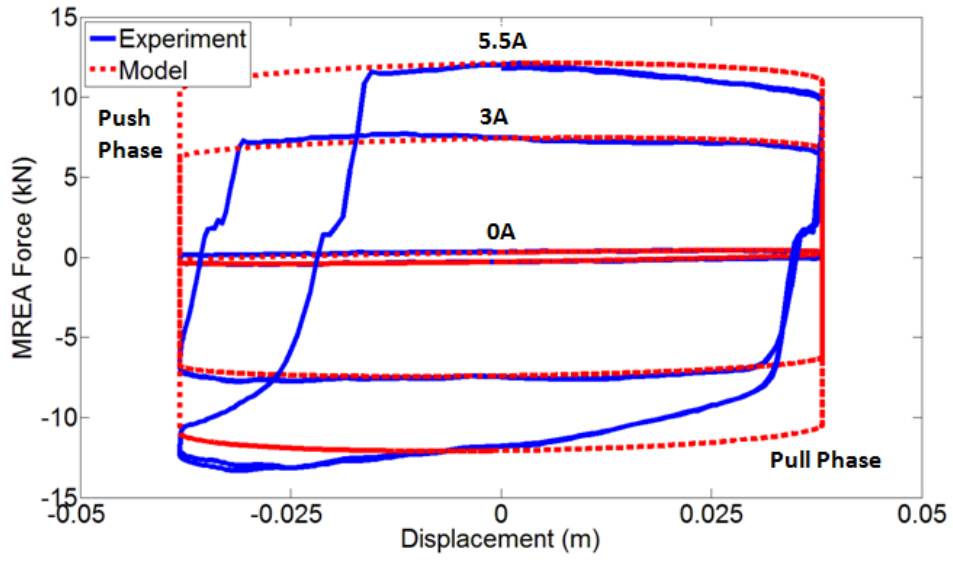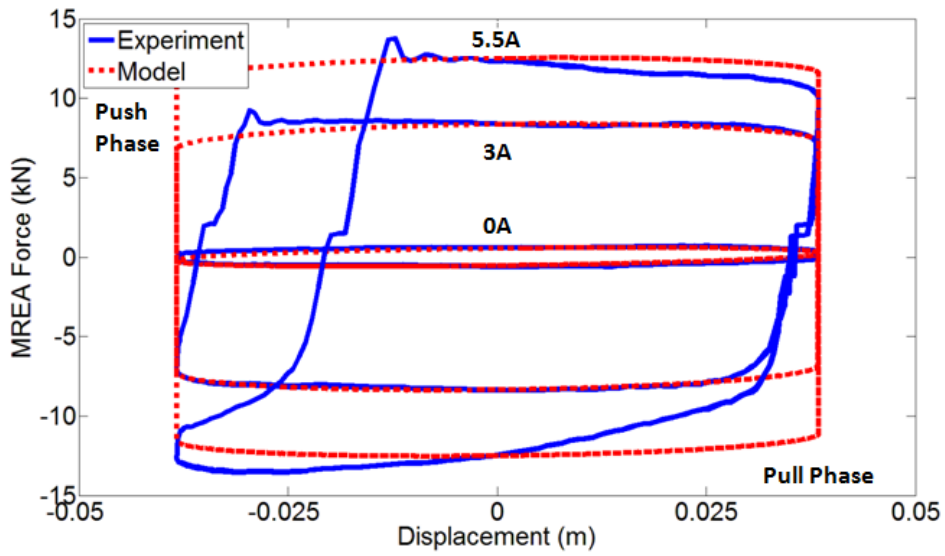
Figure 2.19. MREA force with displacement for varying currents for (a) 0.5 Hz and (b) 2 Hz cyclic frequency.
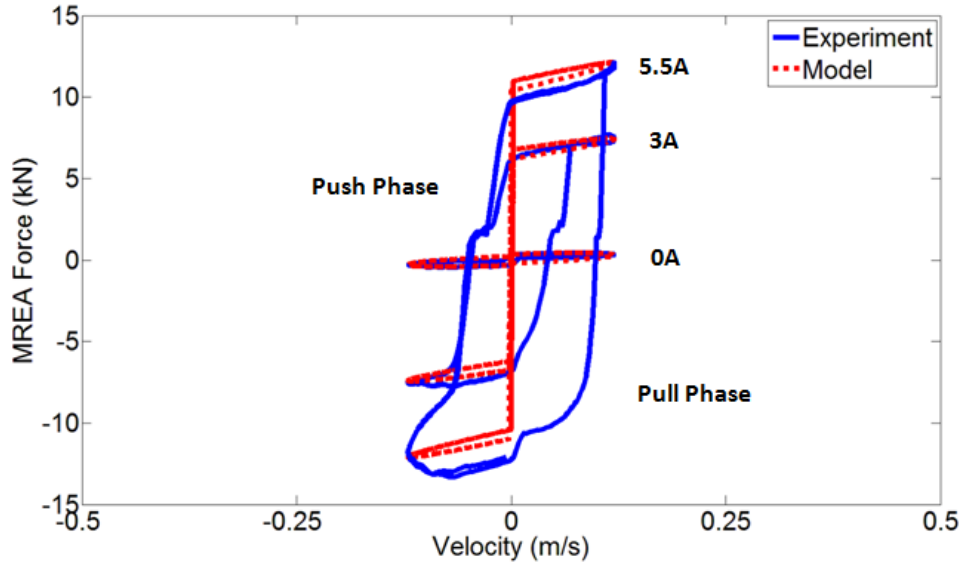
(a)
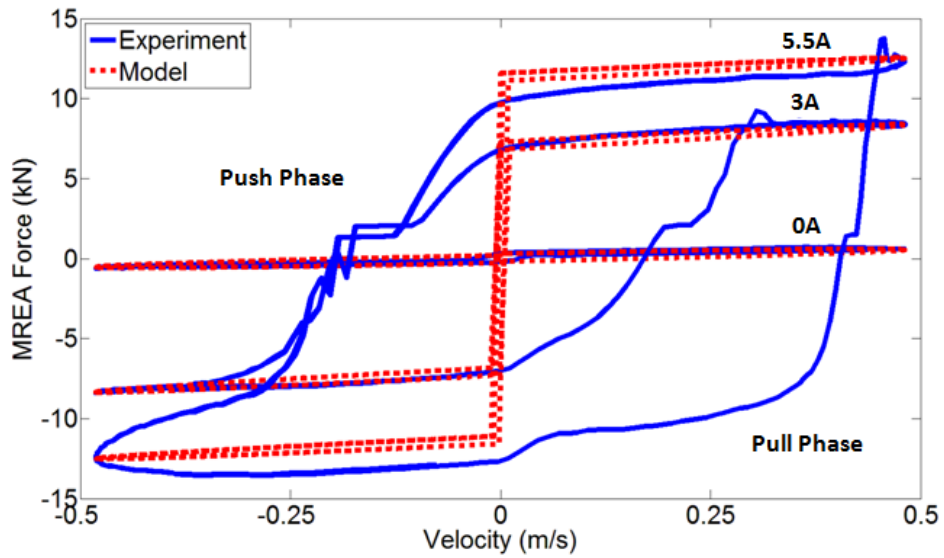
(b)

Figure 2.20. MREA force with velocity for varying currents for (a) 0.5 Hz and (b) 2 Hz cyclic frequency.
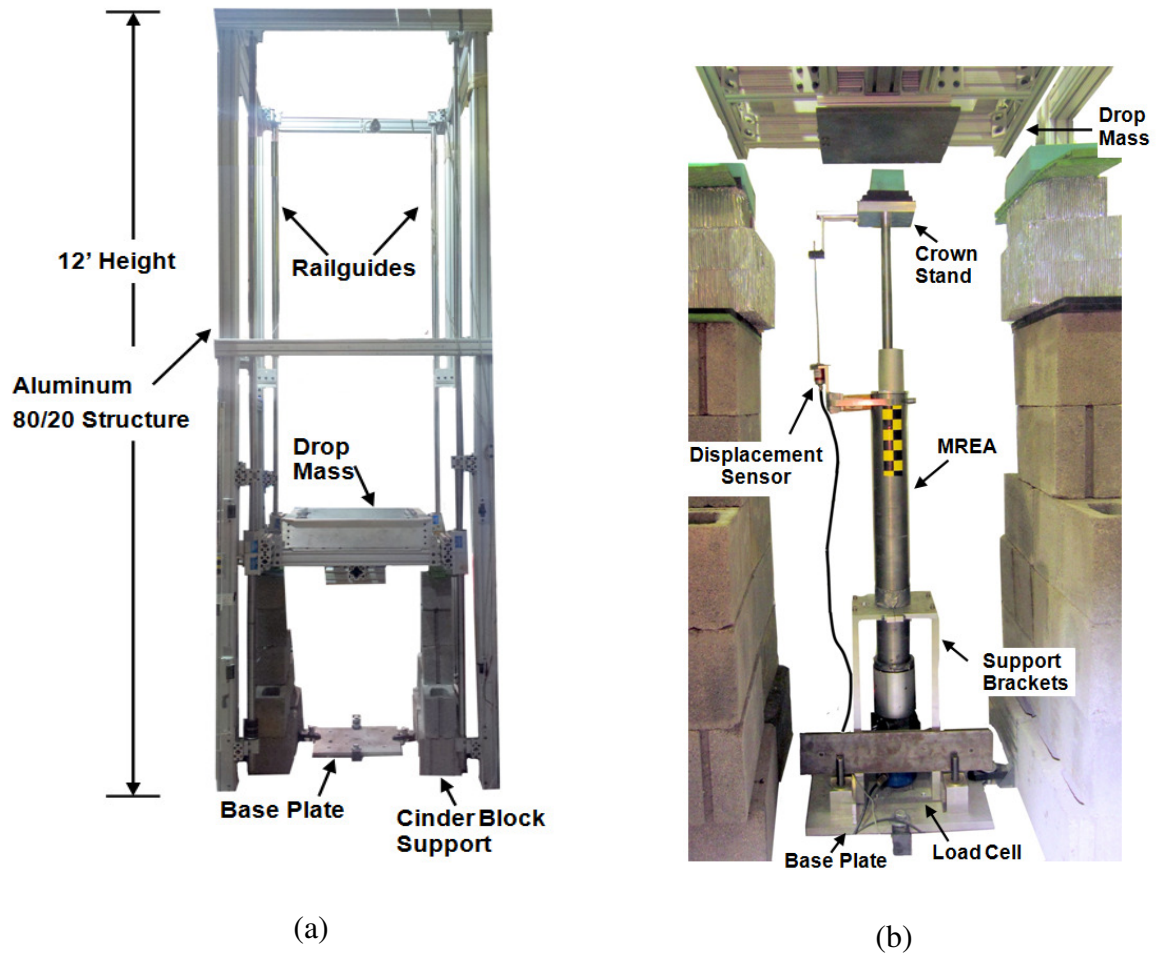
Figure 2.21. High-speed drop test facility at University of Maryland (a) test rig and (b) MREA set up.
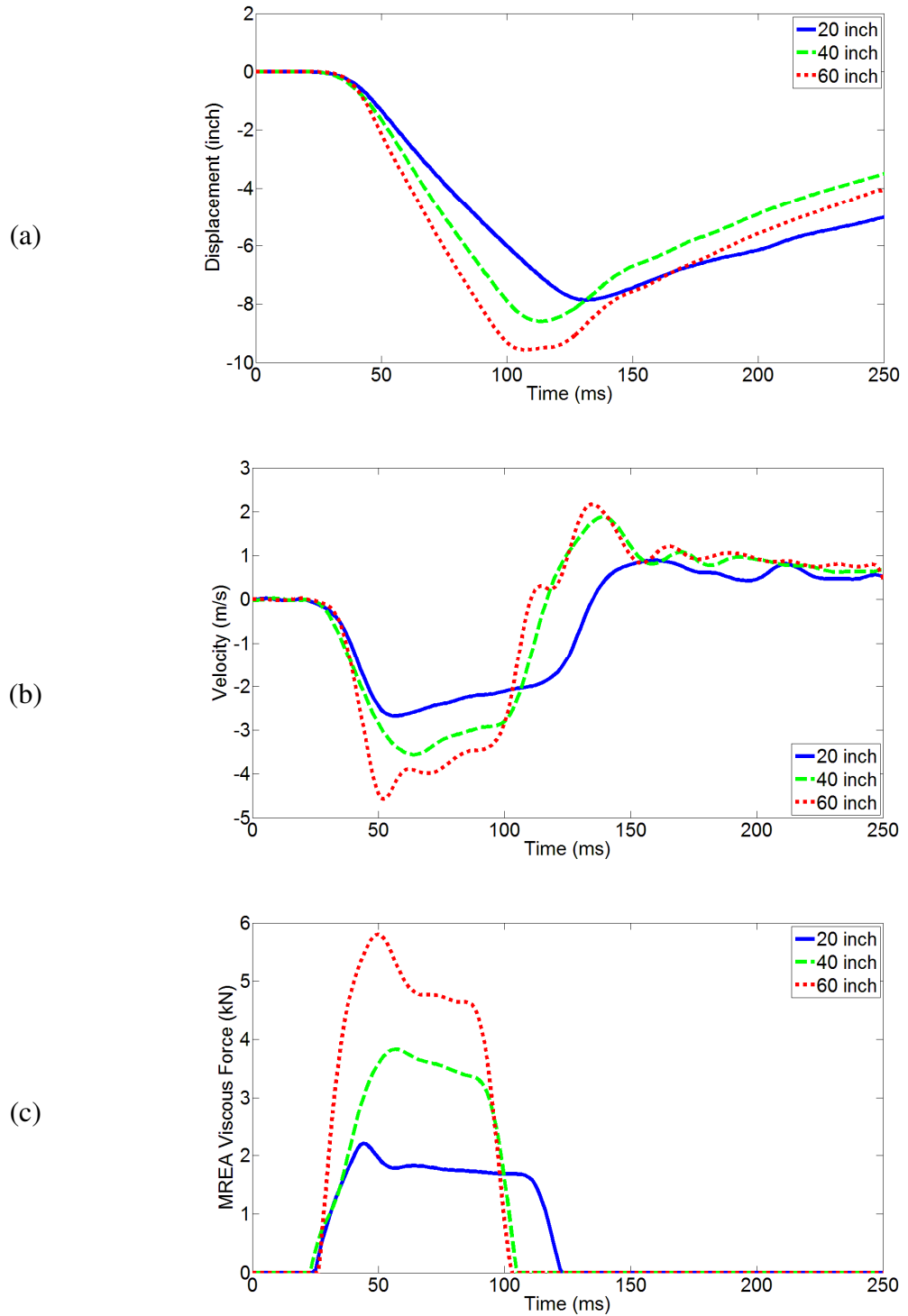
Figure 2.22. Drop test based (a) displacement, (b) velocity and (c) MREA viscous forces for drop heights varying from 20-60 inches.
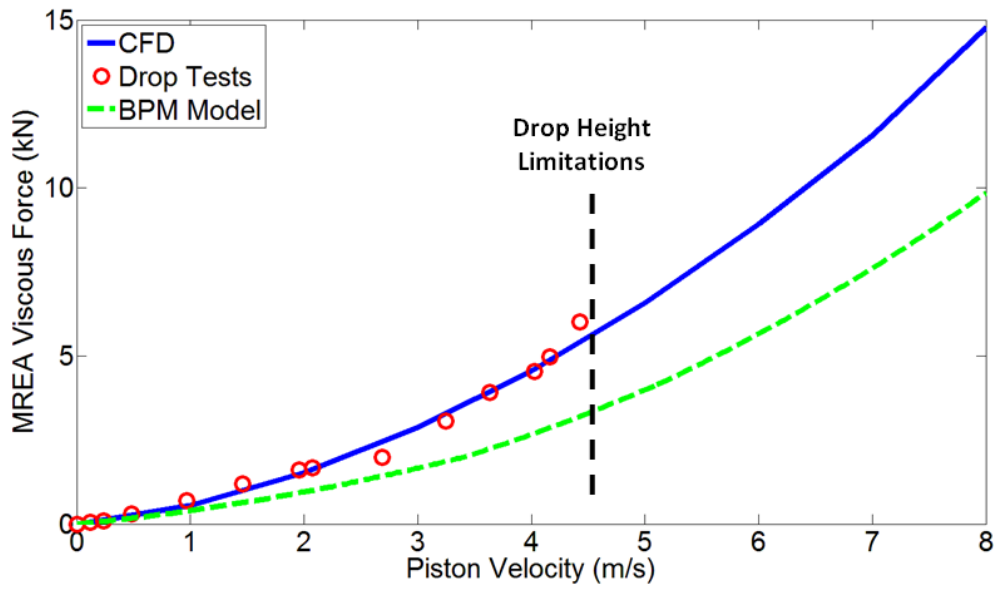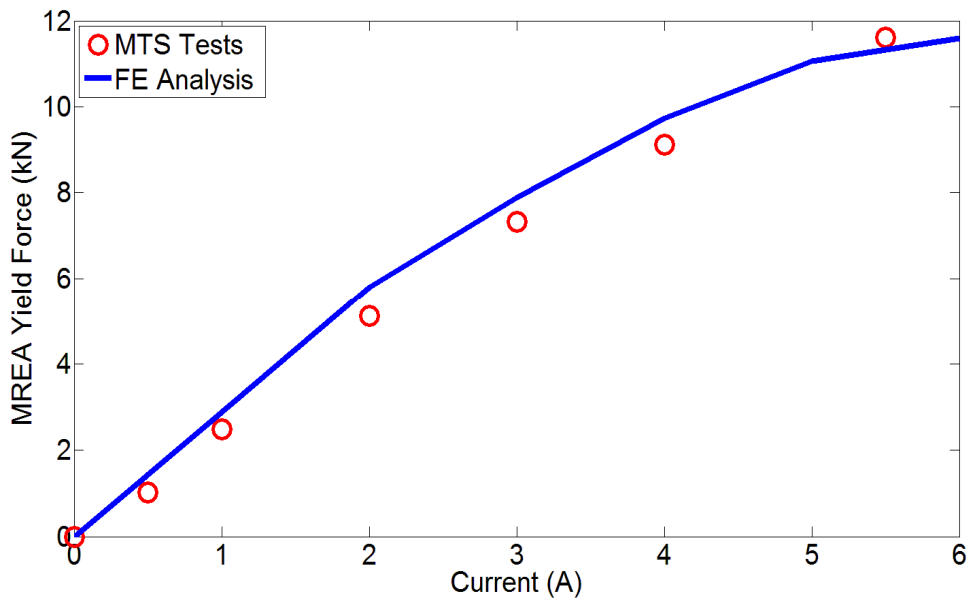
Figure 2.23. Comparison of analytical model with experiments for MREA (a) viscous force and (b) yield force.
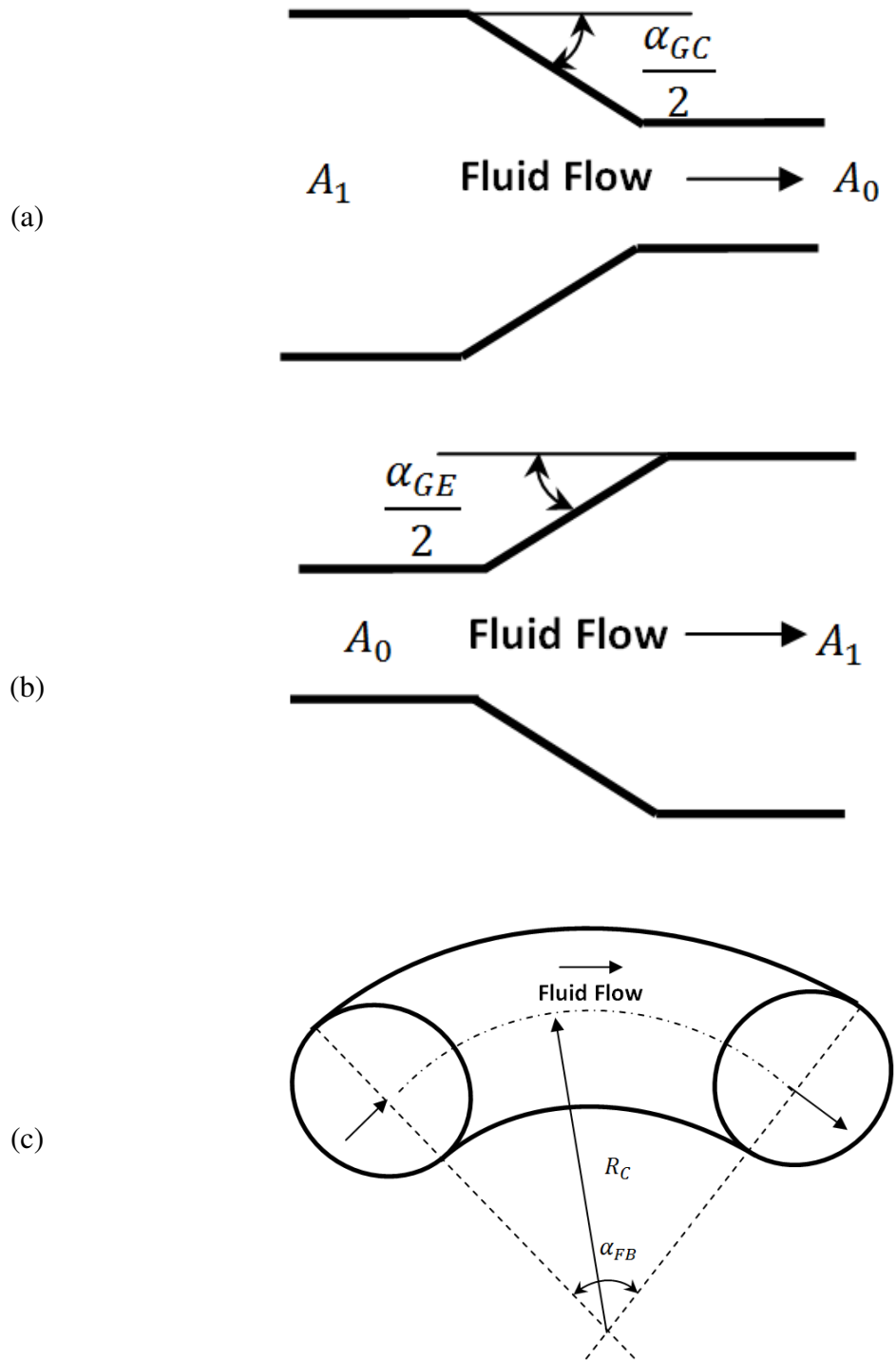
Figure 2.24. Schematic for (a) gradual contraction, (b) gradual expansion and (c) flow bending.
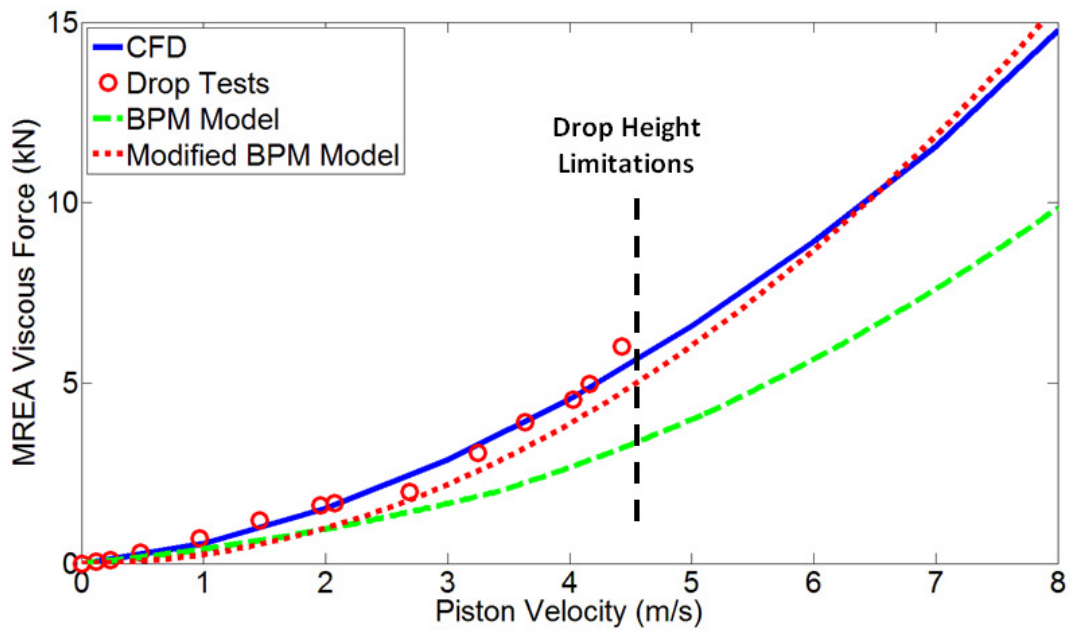
Figure 2.25. MREA viscous force variation with piston velocity incorporating modified BPM model.
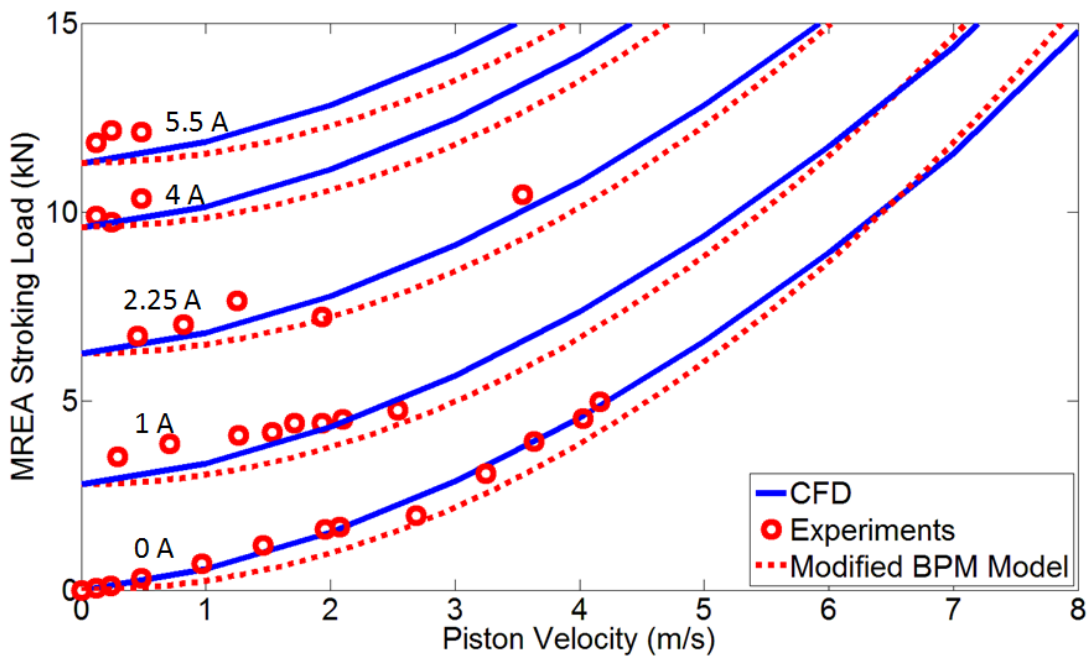
Figure 2.26. Load-stroke profile of MREA for different current inputs.
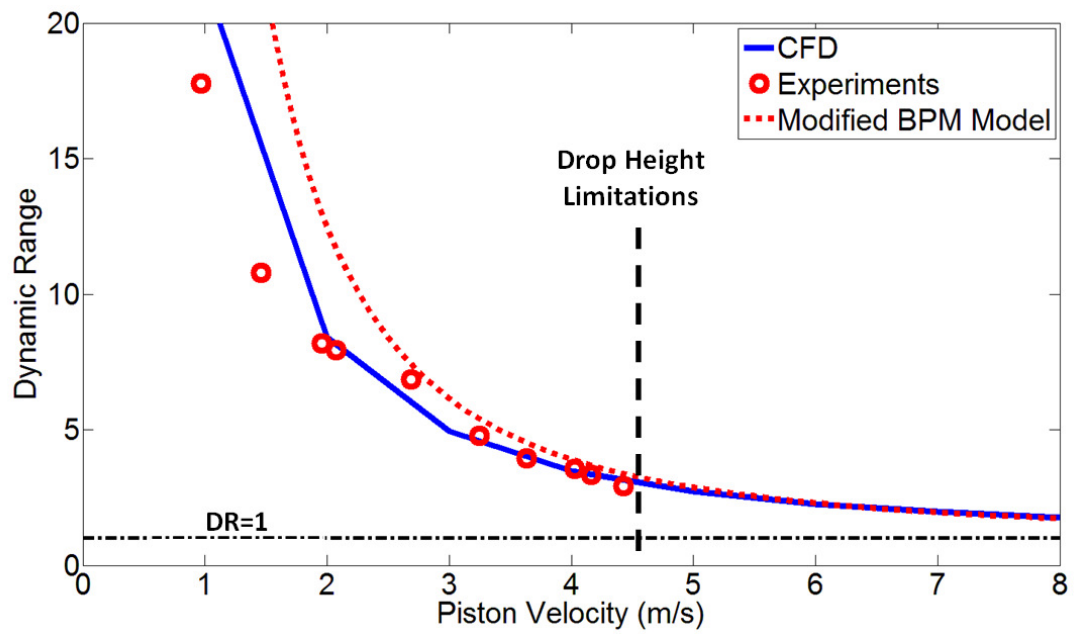
Figure 2.27. Dynamic range variation with piston velocity.

Chapter 3

Biodynamic Model of a Seated Occupant Exposed to Intense Impacts

3.1.   Abstract

Quantitative comparison of biodynamic responses, simulated using Patil's and Liu's lumped parameter models, was carried out with respect to experimental anthropomorphic test dummy (ATD) response data obtained from the Sikorsky Advanced Composite Airframe Program (ACAP) helicopter crash test (Jackson *et al.*, 2004). The biodynamic responses obtained from these models were characterized by large offsets from the experimental peak magnitudes, large perturbations in biodynamic displacements and delayed response. The inability to accurately predict biodynamic response using either model led us to develop a new four degree-of-freedom nonlinear biodynamic model corresponding to a Hybrid II 50th percentile male occupant, the parameters of which were identified by minimizing the least square error between simulated and ACAP experimental responses. The new model accurately predicts peak magnitude, overall shape and the duration of the biodynamic transient response, with minimal phase shift. The biodynamic model was further validated using data from the Crashworthy Composite Fuselage (CCF) drop experiment conducted by Fasanella and Jackson (2004).

3.2. Introduction

Several biodynamic models representing seated human subjects have been developed in order to theoretically predict the biodynamic response as accurately as possible for high-amplitude vertical, frontal, rear and side impacts, and low-amplitude vibrations (Fasanella and Jackson, 2004; Huang, 1998; Suggs *et al.*, 1969). These biodynamic models can be broadly classified into three different categories according to the type of modeling technique: finite element models, multi-body dynamic models and lumped parameter models.

Biodynamic models based on finite elements are capable of simulating the multi-directional shock loads and vibration excitations with precision. The finite element approach discretizes the human body into numerous small elements and, therefore, exact size, shape and other properties can be modeled using such techniques. For a very accurate finite element based biodynamic model, the number of discretized elements can increase substantially and require complicated modeling as well as computational time. Fasanella and Jackson (2004) correlated experimental drop test responses against crash simulated responses of finite element based seated 50th percentile Hybrid II dummies seated in Jungle Aviation and Radio Service (JAARS) energy absorber seats assembled in a crashworthy composite fuselage. Another experiment analyzed the response of a three year old Hybrid III dummy in forward and rearwards facing child restraint seats for frontal collisions (Kapoor *et al.*, 2006). The response of a 50th percentile Hybrid III dummy was investigated by Potula *et al.* (2012) for side impact vehicle collisions when the occupant was in-position and out-of position. Large scale finite element simulations were conducted

by Xingqiao et al. (2013) to evaluate head injuries arising from side curtain airbag impact. Whiplash injuries were evaluated for a 50th percentile male cervical spine resulting from vehicle crash scenarios using finite element modeling techniques (Fice and Cronin, 2012).

Multi-body dynamic models employ several rigid bodies that are connected by pins or ball and socket joints depending on the degrees of freedom required. Huang (1998) developed a three dimensional multi-body model with fifteen rigid bodies to analyze rear-end impact conditions. Linder (2000) implemented a mathematical model of the neck for a low-velocity rear-end impact using a multi-body system program, MADYMO 2D, for soft-tissue injuries that excluded deformation of structures. Teng *et al.* (2008) explored the dynamic response of the human body in a frontal crash collision and assessed the injuries to occupant's pelvis, chest and head. A multi-body model was developed for human head and neck by Lopik and Acar (2007) with refinements in the properties of soft tissues and the geometry of the vertebrae. The cervical spine model was validated by experimental measurements from actual human cervical spine specimens.

Lumped parameter models have been extensively utilized for theoretical studies in high-speed crash conditions. Lumped parameter models represent the human body by connecting different lumped masses through springs and dampers that can be either linear or nonlinear. The numerical implementation of the lumped parameter model is, therefore, simple in comparison with finite element based and multi-body models. However, if the occupant is subjected to vertical as well as variety of side loads then the analyses with lumped parameter model can become

extremely complicated. Therefore, most biodynamic lumped parameter models are limited to unidirectional analyses. Suggs *et al.* (1969) developed a two degree-of-freedom (DOF) lumped parameter model on the basis of experiments using a mechanical simulator providing vibrations to the seated occupant. A four-DOF nonlinear biodynamic model was developed by Liu *et al.* (1998) based on dynamic tensile testing. The model was further implemented by Zong and Lam (2002) to evaluate the biodynamic response of a seated occupant subjected to ship shock. Muskian and Nash (1974) developed six-DOF nonlinear lumped parameter models in which damping coefficients depended on vibration frequency. This model also included internal frictional forces representing forces between different body parts arising from relative sliding and muscle contraction. Patil *el al.* (1977) modified the six-DOF lumped parameter by adding another degree of freedom corresponding to seat pan and simplified the model by neglecting internal frictional forces. Qassem *et al.* (1994) studied the biodynamic response of an occupant subjected to horizontal as well as vertical vibrations by developing an eleven-DOF lumped parameter model. Liang and Chiang (2006) studied the biodynamic response for variety of biodynamic lumped parameter models exposed to vertical vibration excitations with as simple as one-DOF model to eleven-DOF biodynamic model of a pregnant woman.

An accurate biodynamic response is a critical element of the design process for state-of-the-art crashworthy seat suspension development, especially from the perspective of assessing the potential for injury. In this study, the biodynamic model, which is used to predict biodynamic response to impact loads, is also focused towards lumped parameter models. The responses of two different biodynamic

89

lumped parameter models: Patil's model (Patil *et al.*, 1977) and Liu's model (Liu *et al.*, 1998), are compared with the experimental response of a Hybrid II 50th percentile male anthropomorphic test dummy (ATD) obtained from full-scale crash testing under the Sikorsky Advanced Composite Airframe Program (ACAP) helicopter (Jackson *et al.*, 2004). The drawbacks of these two lumped parameter models when exposed to high-amplitude crash loads are quantified accordingly, because these biodynamic lumped parameter models were experimentally validated in the context of low amplitude vibration isolation and not shock loads. Moreover, a biodynamic lumped parameter model is lacking that is appropriate for intense shocks such as a vertical crash.

Therefore, in this study, the objective is to develop a biodynamic model for a 50th percentile male that is appropriate when analyzing the response of an occupant subjected to vertical crash loads. Two existing models from the literature by Patil *et al.* (1977) and Liu *et al.* (1998) that have been used in this context are analyzed. A new model is proposed where the biodynamic model parameters are identified using data from the Sikorsky Advanced Composite Airframe Program (ACAP) helicopter (Jackson *et al.*, 2004). All three models are compared in the context of predicting ATD response measured in the ACAP study. Subsequently, our biodynamic model is also validated against crash response data obtained from the Crashworthy Composite Fuselage (CCF) experiment (Fasanella and Jackson, 2004). We show that our four-DOF model more accurately represents ATD response for the ACAP data, as well as representing the CCF data with acceptable accuracy.

3.3. Anthropomorphic Test Dummy Response

Experimental occupant responses data from a full-scale crash testing of the Sikorsky Advanced Composite Airframe Program (ACAP) helicopter was selected to identify the parameters of the biodynamic model (Jackson *et al.*, 2004). The helicopter experienced 11.58 m/s (38 ft/s) vertical and 9.91 m/s (32.5 ft/s) horizontal velocity along with 6.25^0 nose-up pitch and 3.5^0 left-down roll during the impact. In addition, a 9.6^0/s nose-up pitch angular velocity was also induced by the pendulum swing used in the experiment to simulate crash. The helicopter was outfitted with four anthropomorphic test device (ATDs) representing pilot, copilot and two troop occupants. Pilot ATD was a 50th percentile male Hybrid II dummy with accelerometers located in head, chest, pelvis and load cell to measure spinal lumbar loads. Pilot ATD was not equipped with a helmet and had no modifications when compared to fully-equipped copilot ATD and therefore the pilot ATD's biodynamic responses had no interference resulting from additional weights. Accordingly, pilot ATD response was selected as the basis for comparison. The pilot seat employed two inversion tube energy absorbers which dissipated the shock energy when under impact. However, the stroking load profiles of inversion tubes were not described in the experiment. Therefore, the seat pan response of the lumped parameter model was simulated using pilot's measured seat pan data as shown in Figure 3.1 and corresponding biodynamic responses were observed.

3.4. Liu's Biodynamic Lumped Parameter Model

Liu *et al.* (1998) modeled a seated occupant consisting of four main lumped body parts: pelvis, upper torso, viscera and head. These body parts are developed as

nonlinear mechanical models with mass M_i, spring stiffness K_i, and passive damping constant C_i, for i=1- 4. The values of lumped masses, spring stiffnesses and damping constants are listed in Table 3.1. The displacements of seat, pelvis, upper torso, viscera and head are defined by coordinate z_i, for i=0-4 respectively, where z_i is defined positive upwards. The lumbar spine was not described in the model as a separate lumped mass segment. However, it is a fair assumption that the spinal loads are represented by the nonlinear spring and damper connecting upper torso and pelvis. All the lumped masses are assumed to be descending at the same velocity, v_0=11.58 m/s, before the impact.

The governing equations of motion for the biodynamic lumped parameter model of the occupant are given as

$$M_1 \ddot{z}_1(t) = -F_{K_{1,0}} - F_{C_{1,0}} + F_{K_{2,1}} + F_{C_{2,1}} \tag{3.1}$$

$$M_2 \ddot{z}_2(t) = -F_{K_{2,1}} - F_{C_{2,1}} + F_{K_{3,2}} + F_{C_{3,2}} + F_{K_{4,2}} + F_{C_{4,2}} \tag{3.2}$$

$$M_3 \ddot{z}_3(t) = -F_{K_{3,2}} - F_{C_{3,2}} \tag{3.3}$$

$$M_4 \ddot{z}_4(t) = -F_{K_{4,2}} - F_{C_{4,2}} \tag{3.4}$$

where

$$F_{K_{i,j}} = K_i \left(z_i(t) - z_j(t) \right) \tag{3.5}$$

$$F_{C_{i,j}} = C_i \left(\dot{z}_i(t) - \dot{z}_j(t) \right) \tag{3.6}$$

with the initial conditions given as

$$z_i(0) = 0; \; \dot{z}_i(0) = -v_0 \quad \forall \, i = [0 - 4] \tag{3.7}$$

The stiffness of the pelvis and upper torso is obtained as given by Liu *et al.* (1998). The spring connecting upper torso and pelvis, K_2, was defined for positive compression only. For the relative extension between upper torso and pelvis, a constant value was assumed by evaluating K_2 at zero relative displacement as given by Eq. (3.9).

$$K_1 = \begin{cases} 8.1075e7(z_0 - z_1)^2 & \text{if} \quad (z_0 - z_1) > 0 \\ 0 & \text{if} \quad (z_0 - z_1) \leq 0 \end{cases} \tag{3.8}$$

$$K_2 = \begin{cases} 3780 & \text{if} \quad (z_1 - z_2) < 0 \\ 3780 + 1.09e7(z_1 - z_2) - 2.69e7(z_1 - z_2)^2 & \text{if} \quad 0 \leq (z_1 - z_2) \leq 0.04 \\ 77043 & \text{if} \quad (z_1 - z_2) > 0.04 \end{cases} \tag{3.9}$$

The damping constants, C_i with i= 1-4, corresponding to lumped parameter body parts are determined using dynamic tensile tests (Liu *et al.*, 1998) are given as

$$C_i = 2\zeta_i \sqrt{M_i K_i} \tag{3.10}$$

3.4.1. Liu's Biodynamic Model Response

The seat pan of the biodynamic model shown in Figure 3.2 was excited exactly as the seat pan of the ACAP pilot's ATD plotted in Figure 3.1. The corresponding biodynamic response was obtained from Liu's biodynamic model as shown in Figure 3.3. As can be seen, the response for pelvis and lumbar spine (i.e. spring and damper loads between pelvis and upper torso) were characterized by large

discontinuities. These discontinuities in the pelvic and lumbar loads arise from the fact that the spring stiffness between pelvis and upper torso was discontinuous. Overall, the biodynamic model significantly over-predicted the peak values when compared with the experimental observations. From the Figure 3.3b, the lumbar loads experienced by ACAP pilot's ATD due to spinal compression was around 8.46 kN whereas Liu's biodynamic model predicted the lumbar loads around 18.61 kN in compression, an offshoot of 120%. The biodynamic model also predicted a delayed response when compared to experimental observations. This is due to the fact that there was negative deceleration of seat pan for up to around 90 ms as shown in Figure 3.1, which caused an extension between pelvis and seat pan. Since for such an extension, the spring stiffness between pelvis and seat pan attained a value of zero as per Eq. (3.8). When the deceleration became prominently positive, the relative displacement between pelvis and seat was large enough for the biodynamic lumped parameters to undergo decelerations instantaneously as shown in Figure 3.4.

The relative displacement between upper torso and pelvis shows significant variation up to 160 mm causing the spring stiffness, K_2, to fluctuate between two extreme values as shown in Figure 3.4. The maximum spinal compression obtained from Liu's model was around 163 mm. This fluctuation in K_2 was prominent in the pelvic decelerations as well because when the spinal stiffness was dropped to a sudden low, in other words the spine becomes relatively more compliant, the lumped mass corresponding to pelvis experienced less resistance in motion that caused sudden jump in the pelvic deceleration. Figure 3.5 shows the discontinuity in time history of spring stiffness connecting upper torso with pelvis. The spring stiffness

between pelvis and the seat pan was continuous and attained zero value for the relative extension.

3.5. Patil's Biodynamic Lumped Parameter Model

Patil *et al.* (1977) modified the seven-DOF biodynamic lumped parameter model developed by Muskian and Nash (1974) by adding an additional lumped mass representing the seat pan. The seat pan was connected to the pelvis by another set of a spring and a damper as shown in Figure 3.6. The model consisted of seven mass segments with pelvis, abdomen, diaphragm, thorax, torso, back and head, which were formulated as nonlinear mechanical models comprising of masses M_i interconnected with springs with stiffness K_i and dampers with viscous damping constants C_i for i=1-7 respectively. In addition, the torso was linked to occupant's back by a spring of stiffness K_{56} and a damper with viscous damping C_{56}. The parameters with asterisk in Figure 3.6 determined nonlinear forces between two related lumped segments (Patil *et al.*, 1977). The displacements of seat pan and the lumped parameters of biodynamic model were defined by coordinates z_i, for i=0-7 respectively, where z_i was defined positive upwards similar to Liu's biodynamic model. The biodynamic parameters are listed in Table 3.2.

The governing equations of motion for the biodynamic lumped parameter model of a compliant occupant are given as follows

$$M_1 \ddot{z}_1(t) = -F_{K_{1,0}} - F_{C_{1,0}} + F_{K_{6,1}} + F_{C_{6,1}} + F_{K_{2,1}}^* + F_{C_{2,1}}^* \tag{3.11}$$

$$M_2 \ddot{z}_2(t) = -F_{K_{2,1}}^* - F_{C_{2,1}}^* + F_{K_{3,2}}^* + F_{C_{3,2}}^* \tag{3.12}$$

$$M_3 \ddot{z}_3(t) = -F^*_{K_{3,2}} - F^*_{C_{3,2}} + F^*_{K_{4,3}} + F^*_{C_{4,3}} \tag{3.13}$$

$$M_4 \ddot{z}_4(t) = -F^*_{K_{4,3}} - F^*_{C_{4,3}} + F^*_{K_{5,4}} + F^*_{C_{5,4}} \tag{3.14}$$

$$M_5 \ddot{z}_5(t) = -F^*_{K_{5,4}} - F^*_{C_{5,4}} + F^{**}_{K_{56}} + F^{**}_{C_{56}} \tag{3.15}$$

$$M_6 \ddot{z}_6(t) = -F_{K_{6,1}} - F_{C_{6,1}} + F_{K_{7,6}} + F_{C_{7,6}} - F^{**}_{K_{56}} - F^{**}_{C_{56}} \tag{3.16}$$

$$M_7 \ddot{z}_7(t) = -F_{K_{7,6}} - F_{C_{7,6}} \tag{3.17}$$

with linear forces given as

$$F_{K_{i,j}} = K_i \left(z_i(t) - z_j(t) \right) \tag{3.18}$$

$$F_{C_{i,j}} = C_i \left(\dot{z}_i(t) - \dot{z}_j(t) \right) \tag{3.19}$$

and nonlinear forces evaluated as

$$F^*_{K_{i,j}} = K^*_i \left(z_i(t) - z_j(t) \right) + K^*_i \left(z_i(t) - z_j(t) \right)^3 \tag{3.20}$$

$$F^*_{C_{i,j}} = C^*_i \left(\dot{z}_i(t) - \dot{z}_j(t) \right) + C^*_i \left(\dot{z}_i(t) - \dot{z}_j(t) \right)^3 \tag{3.21}$$

and

$$F^{**}_{K_{56}} = K^*_{56} \left(z_6(t) - z_5(t) \right) + K^*_{56} \left(z_6(t) - z_5(t) \right)^3 \tag{3.22}$$

$$F^{**}_{C_{56}} = C^*_{56} \left(\dot{z}_6(t) - \dot{z}_5(t) \right) + C^*_{56} \left(\dot{z}_6(t) - \dot{z}_5(t) \right)^3 \tag{3.23}$$

The initial conditions for each lumped parameter under consideration were identical and given as

$$z_i(0) = 0; \; \dot{z}_i(0) = -v_0 \quad \forall \, i = [0 - 7] \tag{3.24}$$

3.5.1. Patil's Biodynamic Model Response

The biodynamic responses were obtained in a similar fashion as for Liu's biodynamic model by simulating the seat pan exactly as ACAP pilot's seat pan shown in Figure 3.1. The lumbar loads were evaluated by multiplying mass of the lumped segment representing back with its deceleration. From the biodynamic responses plotted in Figure 3.7, it is clear that Patil's biodynamic model significantly under-predicted the biodynamic decelerations and the lumbar loads due to the fact that Patil's model was relatively more compliant than Liu's model. In other words, the linear and nonlinear springs in Patil's model were softer than that of Liu's model. Patil's model predicted the maximum lumbar compression forces of 1.25 kN when compared to ACAP pilot's lumbar loads of 8.46 kN, an under-prediction of 85.22%. Similar to Liu's model, the response of Patil's model was also delayed. Based on the similar reasoning of negative deceleration of seat pan for up to 90 ms and a softer spring between pelvis and seat pan resulted in large extension between the related lumped segments. Therefore, the response of the biodynamic model could not respond instantaneously by incurring sudden compression. As can be seen from Figure 3.8, the relative displacement between pelvis and seat pan incurred extension (i.e. negative relative displacement) causing such a lagged biodynamic response. Since the spring stiffnesses were relatively small, the relative displacements between

lumped segments were higher compared to Liu's biodynamic model. The compression of lumbar spine was considered as the relative displacement between torso and pelvis. The peak spinal compression value was close to 200 mm, which appears impractical.

3.6. Proposed Biodynamic Lumped Parameter Model

The motivation was to develop a new biodynamic lumped parameter model of a seated occupant exposed to crash in order to predict theoretical biodynamic response as accurately as possible. A nonlinear four-DOF biodynamic lumped parameter model corresponding to a 50th percentile male exposed to high-speed vertical impacts was proposed as shown in Figure 3.9. The biodynamic model consisted of four lumped mass segments, similar to Liu's biodynamic model, with pelvis, viscera, chest and head represented by masses M_i, for i=1-4 respectively. These rigid masses were connected via nonlinear springs and dampers. The viscera was connected to chest and pelvis as well, unlike Liu's model. The lumbar spine was represented as a stiff nonlinear spring and a damper connecting the chest to the pelvis. The displacements of the seat pan and the biodynamic degrees of freedom were defined by coordinates z_i, for i=0-4 respectively, where z_i was defined positive upwards. The occupant was assumed to be seated in a perfect upright position, i.e., the seat suspension did not support the weight of the legs and therefore lumped mass for legs was not considered (Hiemenz *et al.*, 2007; Liu *et al.*, 1998). The occupant was assumed to undergo pure vertical displacement i.e. *z* direction only and the motion in forward direction and sideways was not considered. The governing equations of motion for the proposed biodynamic model are given as follows:

$$M_1\ddot{z}_1(t) = -F_{K_{1,0}} - F_{C_{1,0}} + F_{K_{2,1}} + F_{C_{2,1}} + F_{K_{3,1}} + F_{C_{3,1}} \tag{3.25}$$

$$M_2\ddot{z}_2(t) = -F_{K_{2,1}} - F_{C_{2,1}} + F_{K_{3,2}} + F_{C_{3,2}} \tag{3.26}$$

$$M_3\ddot{z}_3(t) = -F_{K_{3,2}} - F_{C_{3,2}} - F_{K_{3,1}} - F_{C_{3,1}} + F_{K_{4,3}} + F_{C_{4,3}} \tag{3.27}$$

$$M_4\ddot{z}_4(t) = -F_{K_{4,3}} - F_{C_{4,3}} \tag{3.28}$$

where, subscript K and C represent nonlinear spring and damper forces, respectively.

$$F_{K_{i,j}} = K_{i,j}\left(z_i(t) - z_j(t)\right) \tag{3.29}$$

$$F_{C_{i,j}} = C_{i,j}\left(\dot{z}_i(t) - \dot{z}_j(t)\right) \tag{3.30}$$

The spring stiffnesses and damper constants were obtained based on the relative displacements and velocities between two lumped segments respectively.

$$K_{i,j} = \alpha_{i,j} + \beta_{i,j}\|z_i(t) - z_j(t)\|^{\gamma_{i,j}} \tag{3.31}$$

$$C_{i,j} = \phi_{i,j} + \chi_{i,j}\|\dot{z}_i(t) - \dot{z}_j(t)\|^{\psi_{i,j}} \tag{3.32}$$

The parameters that define nonlinear spring stiffness and damping constants were determined by minimizing the least squared error between experimental measurements and simulated biodynamic responses. The occupant as well as the seat suspension, impacts the ground at the sink rate, which determines the initial condition for the numerical analysis.

$$z_i(0) = 0; \ \dot{z}_i(0) = -v_0 \quad \forall \, i = [0 - 4] \tag{3.33}$$

3.6.1. Parametric Identification of Proposed Biodynamic Model

Parametric optimization techniques based on stochastic search methods, which in this case is Genetic Algorithm developed by the Mathworks Inc. (MATLAB, R2010b), were applied in order to determine the spring stiffnesses and damping values of the biodynamic model. The cost function was defined as the least square error between the experimental measurements and predicted pilot ATD response using simulation. There were five sets of springs and dampers with six unknown variable per set. The masses of the lumped segments were taken from Hybrid II 50th percentile male dummy specifications by Humanetics ATD (Table 3.3). The upper torso and lower torso were clumped to form a single lumped segment representing chest. The masses were also considered as design variables to be optimized with ± 10% variation from the baseline values. Viscera was not a part of Hybrid II 50th percentile male dummy by Humanetics ATD and therefore it was given lower and upper bound of 1 and 6 kg respectively.

The least square error was evaluated based on a simple error function, $er[f]$, defined as

$$er[f] = \sqrt{\sum_{i=1}^{N}\left(\frac{f_i - \hat{f}_i}{\bar{f}}\right)^2}$$

(3.34)

where N is the number of data points, f is the experimental ACAP response with $\bar{f}$ as peak value and $\hat{f}$ is corresponding to the biodynamic model response.

The objective function for parametric identification was defined as

$$Min : \sum_{j=1}^{4} er\left[f_j\right]$$

(3.35)

where f_j for j=1-4 were corresponding to pelvic deceleration, lumbar load, chest and head deceleration respectively.

3.6.2. Proposed Biodynamic Model Response

The optimal parameters that minimized the cost function given by Eq. (3.35) are presented in Table 3.3. Figure 3.10 shows the comparison between model and experimental responses obtained from Sikorsky ACAP helicopter experiment (Jackson *et al.*, 2004) for different biodynamic parts under consideration. The peak pelvic decelerations as per model and experimental response were found to be 43.74g and 40.49g so the model predicted 8.03% higher pelvic deceleration. The peak compressive spinal lumbar load as simulated by lumped parameter model was 8.55 kN when compared to 8.46 kN based on experiment. Hence, the model prediction was close to the experimental measurement with only 1.06% over-prediction. The chest and head responses from model and experiment were not as good a match as pelvic or lumbar responses. The model based peak chest and head deceleration estimations were 26.67% and 53.63% higher than experimental values respectively. The experimental head responses were characterized by oscillations in forward, sideways and vertical direction and therefore the data was not as smooth as for pelvis or lumbar response resulting in large over-prediction by the biodynamic model. Moreover, the interaction of nonlinearities of different body parts escalate since the impact energy and the biodynamic response is channelized from pelvis to

101

head for a pure vertical impact commencing from the floor of a seat suspension. Unlike Liu's and Patil's biodynamic model, the proposed biodynamic model resulted in instantaneous response without any delay.

The relative displacements between different biodynamic body parts are shown in Figure 3.11. It was observed that the relative displacements were of the order of few millimeters. Therefore, the optimal parameters configure the biodynamic model close to a rigid body. However, the biodynamic model has compliance and damping in a nonlinear manner and therefore the biodynamic response might differ to that of a rigid body. Such low relative displacements in a biodynamic model could have been a result of confining the response in a vertical direction only whereas the experimental ATD incurs multidirectional displacements in reality.

3.7. Comparison of the Biodynamic Models

A quantitative comparison was carried out for each biodynamic model response with respect to the experimental response obtained from ACAP crash test (Jackson *et al.*, 2004). The goodness of fit was dependent on the least square error given by Eq. (3.34), low values of least square error were favorable. The least square error values for pelvic deceleration f_1, lumbar loads f_2, chest deceleration f_3, and head deceleration, f_4 are listed in Table 3.4. When compared to Liu's model, the error values were lower for Patil's model even though neither models was able able to predict an accurate response. The under-predicted values by Patil's model were not as far as over-predicted values by Liu's model when compared to ACAP pilot's experimental response leading to such an outcome.

The proposed biodynamic model least square error values were significantly lower when compared to Liu's and Patil's model for pelvic, lumbar and chest response. However, the head response from the proposed model was not as low as for other biodynamic parts due to the reasons described earlier. Overall, the proposed model was able to predict the biodynamic responses better than other two models.

3.8.   Validation of Proposed Biodynamic Model

The proposed biodynamic model required validation in order to estimate biodynamic responses for a random shock. Fasanella and Jackson (2004) conducted an experiment on crashworthy composite fuselage (CCF) section with two 50th percentile male Hybrid II type ATDs subjected to vertical impact. The two ATDs were seated side by side (referred as left and right ATD) on their respective Jungle Aviation and Radio Service (JAARS) energy absorbing seats. The fuselage section was dropped from a height of 3.05 m (10 feet) on a rigid surface resulting in vertical velocity of 7.62 m/s (25 ft/s) approximately. During the impact, the seat pan experienced vertical as well as rotational displacements. Since the seat pan of the biodynamic model was restricted to stroke vertically for the analytical analysis, it was difficult to simulate multi-directional experimental seat pan response. However, vertical pelvic decelerations were utilized to ascertain the corresponding lumbar loads for model validation for both left and right ATD as shown in Figure 3.12.

The experimental peak lumbar load for the left ATD was 7.02 kN approximately. It was observed that peak compressive lumbar load for left ATD was found to be 6.73 kN from simulation with an under-prediction of 4.13%. The compressive lumbar load profile obtained from simulations could not capture the true

experimental profile but the peak lumbar load was close to peak experimental value as shown in Figure 3.13a. The simulated and experimental lumbar loads for the right ATD were 7.17 kN and 6.56 kN respectively. Hence, the biodynamic model over-predicted the peak lumbar load by 9.29%. In comparison to the left ATD lumbar loads simulation, the right ATD lumbar loads profile roughly mimicked the experimental lumbar loads profile as plotted in Figure 3.13b. FEM simulations conducted by Fasanella and Jackson (2004) by precisely modeling the multi-directional experimental crash predicted the overall shape and pulse duration. Similarly in this analysis, the proposed biodynamic model was able to predict the peak magnitude, response shape and response duration when compared to experimental CCF dummy responses. The envelope for the simulated response was obtained by fitting a spline through the peak values of the response along with start and end values. Another important observation is that the proposed model, when compared to CCF experiment, did not result in a lagged response similar to the case of ACAP experiment.

The relative displacements between chest and pelvis or equivalently the compression of lumbar spine for both left and right ATD are shown in Figure 3.14. Similar to simulation based on ACAP experiment, the biodynamic model's relative displacement is of the order of millimeters.

3.9. Conclusions

In this study, two existing biodynamic lumped parameter models developed by Liu *et al.* (1998) (four-DOF) and Patil *et al.* (1977) (seven-DOF) were considered to compare biodynamic response with the experimental response of a Hybrid II 50th

percentile male pilot ATD obtained from ACAP experiment. Liu's model exhibited large discontinuities in lumbar response due to piecewise modeling of spring connecting upper torso with pelvis. The model highly over-predicted the peak lumbar load by 120% when compared with the experimental observations. The biodynamic model response was also delayed due to absence of spring stiffness for relative extensional displacement between pelvis and seat pan.

Patil's model also showed a delayed response similar to Liu's model due to a soft spring connecting pelvis and seat pan. Overall, the model was relatively more compliant with soft springs when compared to Liu's model resulting in large under-prediction of biodynamic response in comparison with experimental observations from ACAP experiment. Due to this, the spinal compression, represented by relative displacement between torso and pelvis, were higher. Patil's model response was also delayed similar to Liu's model due to a very soft spring that connected pelvis with seat pan.

In order to accurately predict the biodynamic response, a nonlinear four-DOF biodynamic lumped parameter model of a seated 50th percentile male occupant subjected to high-speed vertical impact was developed. The biodynamic forces were modeled using nonlinear spring and damper forces that were dependent on the relative displacements and velocities between different isolated lumped mass segments. Anthropomorphic test dummy (ATD) responses from full-scale crash testing of Sikorsky ACAP helicopter formed basis for the biodynamic model parametric identification. Least squares were minimized using genetic algorithm

between experimental and simulated responses to extract the optimal biodynamic parameters.

The seat pan of the biodynamic model was simulated as per the experimental measurement of the pilot ATD's seat pan. The optimized biodynamic model over-predicted peak pelvic deceleration and lumbar loads by 8.03% and 1.06% respectively compared to pilot's ATD response in Sikorsky ACAP helicopter experiment. For the same ACAP experiment, chest and head responses from biodynamic model had large over-predictions of 26.67% and 53.63% respectively because of interaction of motion in forward direction and sideways. Unlike Liu's and Patil's model, the response from proposed model was instantaneous in comparison with the experimental observations. Compared to Liu's and Patil's model, the proposed biodynamic model was significantly more accurate.

The optimized biodynamic model was further validated by comparing simulated responses to the crashworthy composite fuselage (CCF) experiment for two different 50th percentile Hybrid II ATDs (left and right dummy) responses. The pelvic deceleration of the biodynamic model was matched to the pelvic decelerations of both left and right ATD and the simulated biodynamic response was compared to the experiments. The peak lumbar loads from simulated biodynamic model were under-predicted by 4.13% for left ATD and over-predicted by 9.29% for right ATD when compared to the experimental measurements. The proposed model response was able to predict shape, peak magnitude and response duration of the experimental response.

References

Fasanella E L and Jackson K E 2004 Impact Testing and Simulation of a Crashworthy Composite Fuselage Section with Energy-Absorbing Seats and Dummies *Journal of the American Helicopter Society,* Vol. 49, No. 2, pp. 140-148.

Fice J B and Cronin D S 2012 Investigation of Whiplash Injuries in the Upper Cervical Spine Using a Detailed Neck Model *Journal of Biomechanics*, Vol. 45, No. 6, pp. 1098-1102.

Hiemenz G J, Choi Y-T and Wereley N M 2007 Semi-Active Control of Vertical Stroking Helicopter Crew Seat for Enhanced Crashworthiness *AIAA Journal of Aircraft*, Vol. 44, No. 3, pp. 1031-1034.

Huang S-C 1998 Analysis of Human Body Dynamics in Simulated Rear-End Impacts *Human Movement Science*, Vol. 17, No. 6, pp. 821-838.

HUMANETICS, Last accessed Oct 15, 2013. http://www.humaneticsatd.com/crash-test-dummies/frontal-impact/hybrid-ii-50th

Jackson K E, Fasanella E L, Boitnott R, McEntire J and Lewis A 2004 Occupant Responses in a Full-Scale Crash Test of the Sikorsky ACAP Helicopter *Journal of the American Helicopter Society*, Vol. 49, No. 2, pp. 127-139.

Kapoor T, Altenhof W, Wang Q A and Howard A 2006 Injury Potential of a Three-year-old Hybrid III Dummy in Forward and Rearward Facing Positions Under CMVSS 208 Testing Conditions *Accident Analysis and Prevention*, Vol. 38, No. 4, pp. 786-800.

Liang C C and Chiang C F 2006 A Study on Biodynamic Models of Seated Human Subjects Exposed to Vertical Vibration *International Journal of Industrial Ergonomics*, Vol. 36, pp. 869-890.

Linder A 2000 A New Mathematical Neck Model for a Low-Velocity Rear-End Impact Dummy: Evaluation of Components Influencing Head Kinematics *Accident Analysis and Prevention*, Vol. 32, No. 2, pp. 261-269.

Liu X X, Shi J, Li G, Le X, Zhao B, Yue M, Liu J, Bai G and Ke W 1998 Biodynamic Response and Injury Estimation of Ship Personnel to Ship Shock Motion Induced by Underwater Explosion *Proceedings of the 69th Shock and Vibration Symposium, Shock and Vibration Information Analysis Center*, Richmond, VA, Vol. 18,pp. 1–18.

Lopik D W V and Acar M 2007 Development of a Multi-Body Computational Model of Human Head and Neck *Proceedings of the Institution of Mechanical Engineers Part K-Journal of Multi-body Dynamics*, Vol. 221, No. 2, pp. 175-197.

MATLAB, R2010b, The Mathworks Inc.

Muksian R and Nash C D 1974 A Model for the Response of Seated Humans to Sinusoidal Displacements of the Seat *Journal of Biomechanics*, Vol. 7, pp. 209-215.

Patil M K, Palanichamy M S and Ghista D N 1977 Dynamic Response of Human Body Seated on a Tractor and Effectiveness of Suspension Systems *Society of Automobile Engineers,* No. 770932, pp.755-792.

Potula S R, Solanki K N, Oglesby D L, Tschopp M A and Bhatia M A 2012 Investigating Occupant Safety Through Simulating the Interaction Between Side Curtain Airbag Deployment and an Out-of-Position Occupant *Accident Analysis and Prevention*, Vol. 49, pp. 392-403.

Qassem W, Othman M O and Abdul-Majeed S 1994 The Effects of Vertical and Horizontal Vibrations on the Human Body *Medical Engineering Physics*, Vol. 16, pp. 151-161.

Suggs C W, Abrams C F and Stikeleather L F 1969 Application of a Damped Spring-Mass Human Vibration Simulator in Vibration Testing of Vehicle Seats *Ergonomics*, Vol. 12, No. 1, pp. 79-90.

Teng T L, Chang F A, Liu Y S and Peng C P 2008 Analysis of Dynamic response of Vehicle Occupant in Frontal Crash Using Multibody Dynamics Method *Mathematical and Computer Modeling*, Vol. 48, No. 11-12, pp. 1724-1736.

Xingqiao D, Potula S, Grewal H, Solanki K N, Tschopp M A and Horstemeyer M F 2013 Finite Element Analysis of Occupant Head Injuries: Parametric Effects of the Side Curtain Airbag Deployment Interaction with a Dummy Head in a Side Impact Crash *Accident Analysis and Prevention,* Vol. 55, pp. 232-241.

Zong Z and Lam K Y 2002 Biodynamic Response of Shipboard Sitting Subject to Ship Shock *Journal of Biomechanics,* Vol. 35, No. 1, pp. 35-43.

Table 3.1. Biodynamic model parameters (Liu *et al.*, 1998)

Biodynamic Parameter		Mass (kg)		Spring Constant (kN/m)		Damping Ratio (-)
Pelvis	M_1	29	K_1	Eq. (3.8)	ζ_1	0.25
Upper Torso	M_2	21.8	K_2	Eq. (3.9)	ζ_2	0.11
Viscera	M_3	6.8	K_3	2.83	ζ_3	0.5
Head	M_4	5.5	K_4	202.3	ζ_4	0.1

Table 3.2. Biodynamic model parameters (Patil *et al.*, 1977)

Biodynamic Parameter		Mass (kg)		Spring Constant (N/m)		Viscous Damping (N-s/m)
Pelvis	M_1	27.23	K_1	25500	C_1	371
Abdomen	M_2	5.921	K_2^*	877	C_2^*	292
Diaphragm	M_3	0.455	K_3^*	877	C_3^*	292
Thorax	M_4	1.362	K_4^*	877	C_4^*	292
Torso	M_5	32.76	K_5^*	877	C_5^*	292
--	--	--	K_{56}^*	52600	C_{56}^*	3580
Back	M_6	6.808	K_6	52600	C_6	3580
Head	M_7	5.45	K_7	52600	C_7	3580

Table 3.3. Proposed Biodynamic Model Parameters

Biodynamic Parameter	M* (kg)	α (N/m)	β (N/m$^{1+\gamma}$)	γ (-)	ϕ (N-s/m)	χ (N-s$^{1+\psi}$/m$^{1+\psi}$)	ψ (-)
Seat pan	M_0 --	$\alpha_{1,0}$ 105	$\beta_{1,0}$ 3.32e+6	$\gamma_{1,0}$ 0.816	$\phi_{1,0}$ 110	$\chi_{1,0}$ 112	$\psi_{1,0}$ 2.034
Pelvis	M_1 16.7	$\alpha_{2,1}$ 4.88e+6	$\beta_{2,1}$ 5.62e+6	$\gamma_{2,1}$ 3.962	$\phi_{2,1}$ 104	$\chi_{2,1}$ 1.51e+4	$\psi_{2,1}$ 1.145
Viscera	M_2 1.4	$\alpha_{3,1}$ 2.45e+6	$\beta_{3,1}$ 9.09e+6	$\gamma_{3,1}$ 0.489	$\phi_{3,1}$ 3.76e+3	$\chi_{3,1}$ 6.99e+3	$\psi_{3,1}$ 1.195
Chest	M_3 33.7	$\alpha_{3,2}$ 9.77e+6	$\beta_{3,2}$ 1.47e+6	$\gamma_{3,2}$ 4.279	$\phi_{3,2}$ 104	$\chi_{3,2}$ 1.23e+4	$\psi_{3,2}$ 1
Head	M_4 5.1	$\alpha_{4,3}$ 5.12e+6	$\beta_{4,3}$ 101	$\gamma_{4,3}$ 1.658	$\phi_{4,3}$ 102	$\chi_{4,3}$ 103	$\psi_{4,3}$ 5.592

*Hybrid II 50th percentile male dummy data from http://www.humaneticsatd.com/crash-test-dummies/frontal-impact/hybrid-ii-50th. Last accessed on October 15, 2013

Table 3.4. Goodness of fit of biodynamic model responses to ACAP experimental response.

Error Function	Liu's Model	Patil's Model	Proposed Model
$er[f_1]$	21.19	24.49	8.45
$er[f_2]$	47.83	21.36	10.73
$er[f_3]$	31.62	25.71	7.82
$er[f_4]$	56.60	42.65	30.67
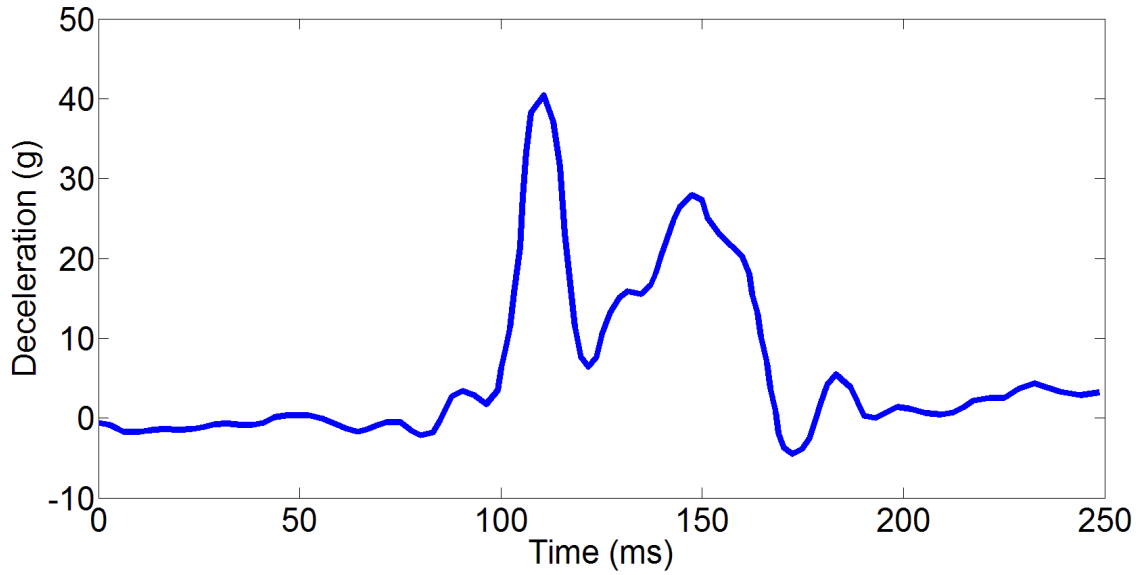
Figure 3.1. Pilot's seat pan deceleration from Sikorsky ACAP helicopter (Jackson *et al.*, 2004).
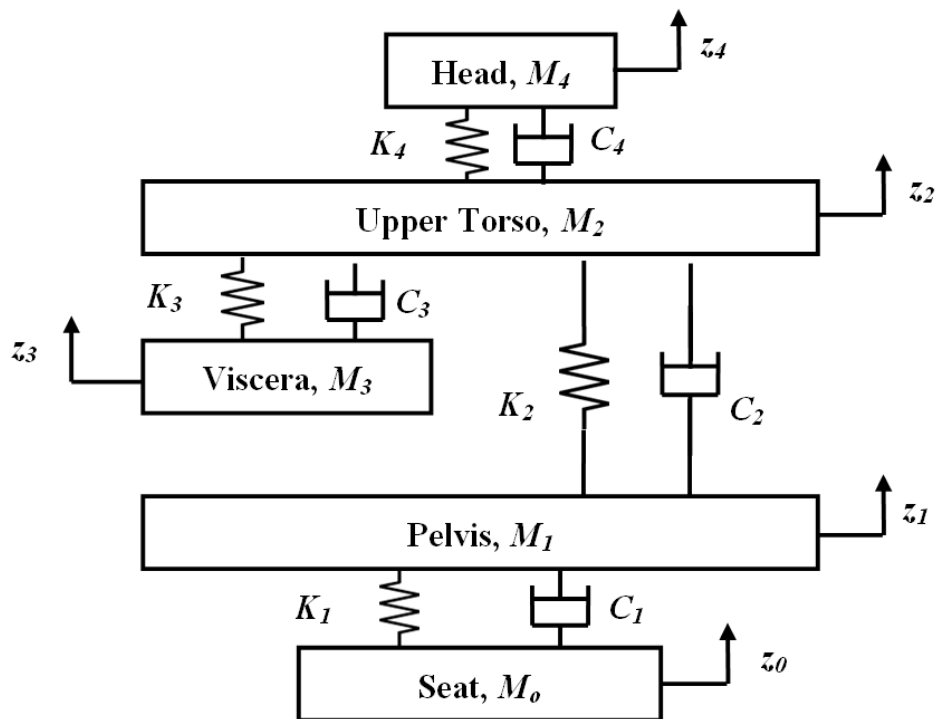
Figure 3.2. Four-DOF biodynamic model of a seated occupant (Liu *et al.*, 1998).

(a) Pelvis

(b) Spine

(c) Chest

(d) Head
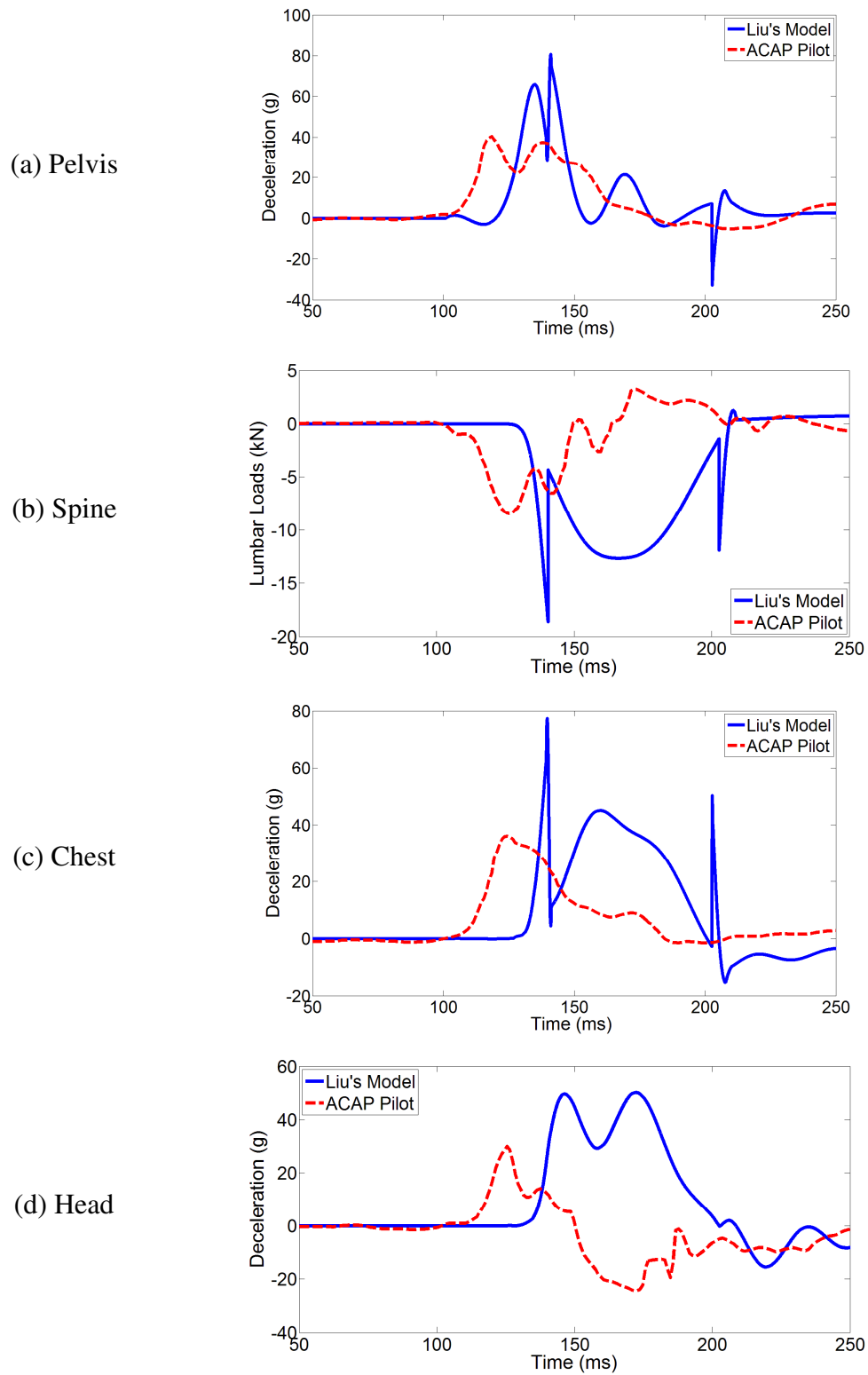
Figure 3.3. Experimental and Liu's biodynamic model response comparison.
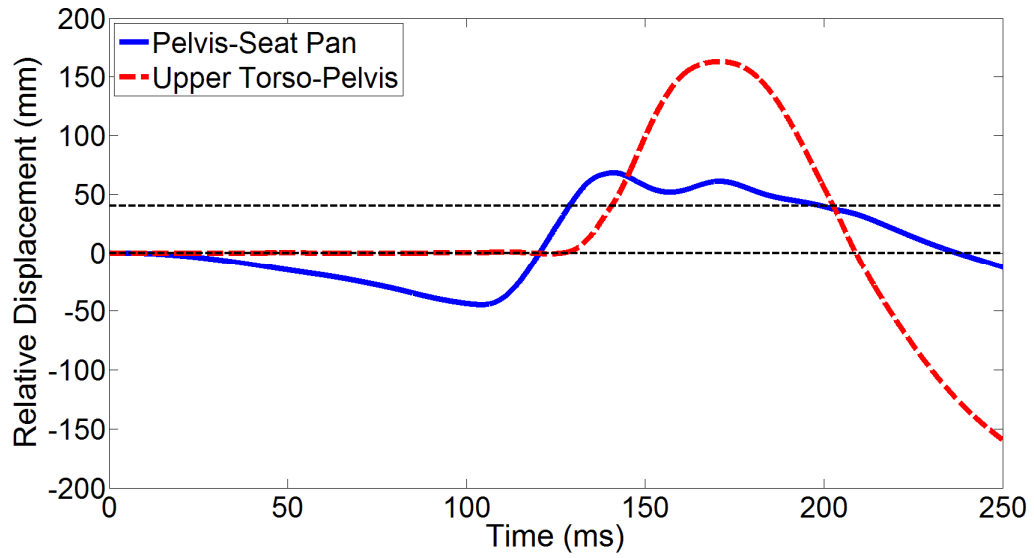
Figure 3.4. Time history of relative displacement from Liu's biodynamic model.
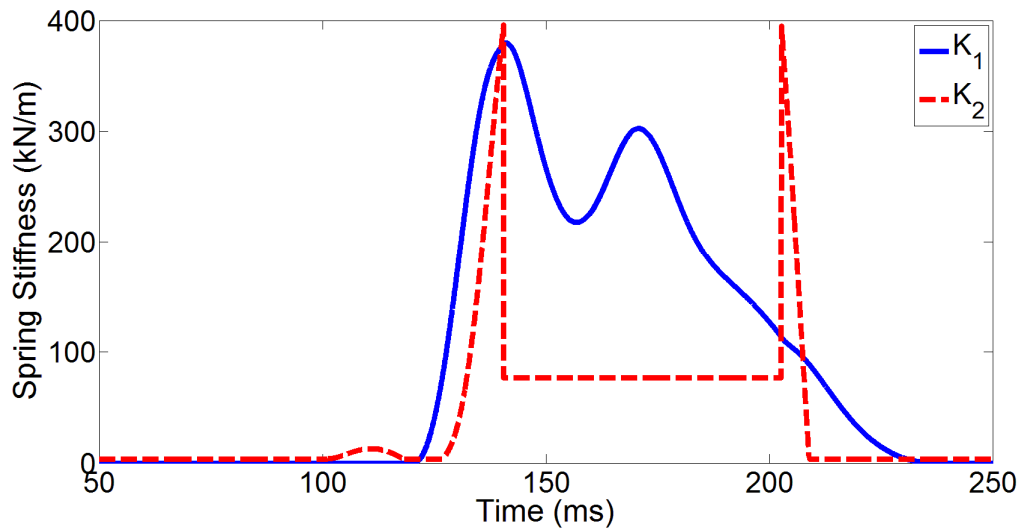
Figure 3.5. Time history of spring stiffness from Liu's biodynamic model.

114
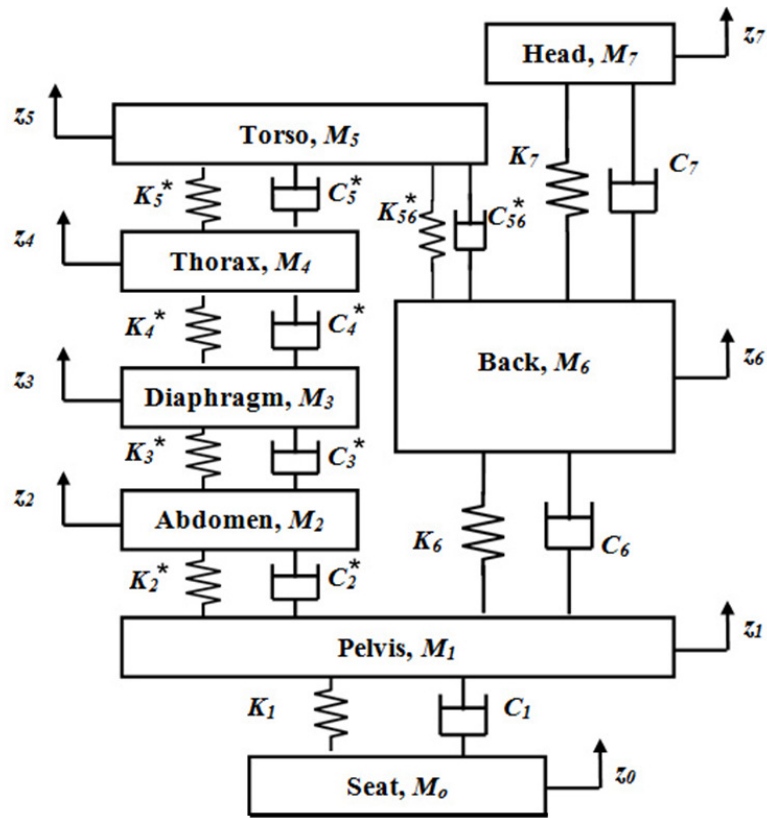
Figure 3.6. Seven-DOF biodynamic model of a seated occupant developed by Patil *et al.* (1977).

(a) Pelvis

(b) Spine

(c) Chest

(d) Head
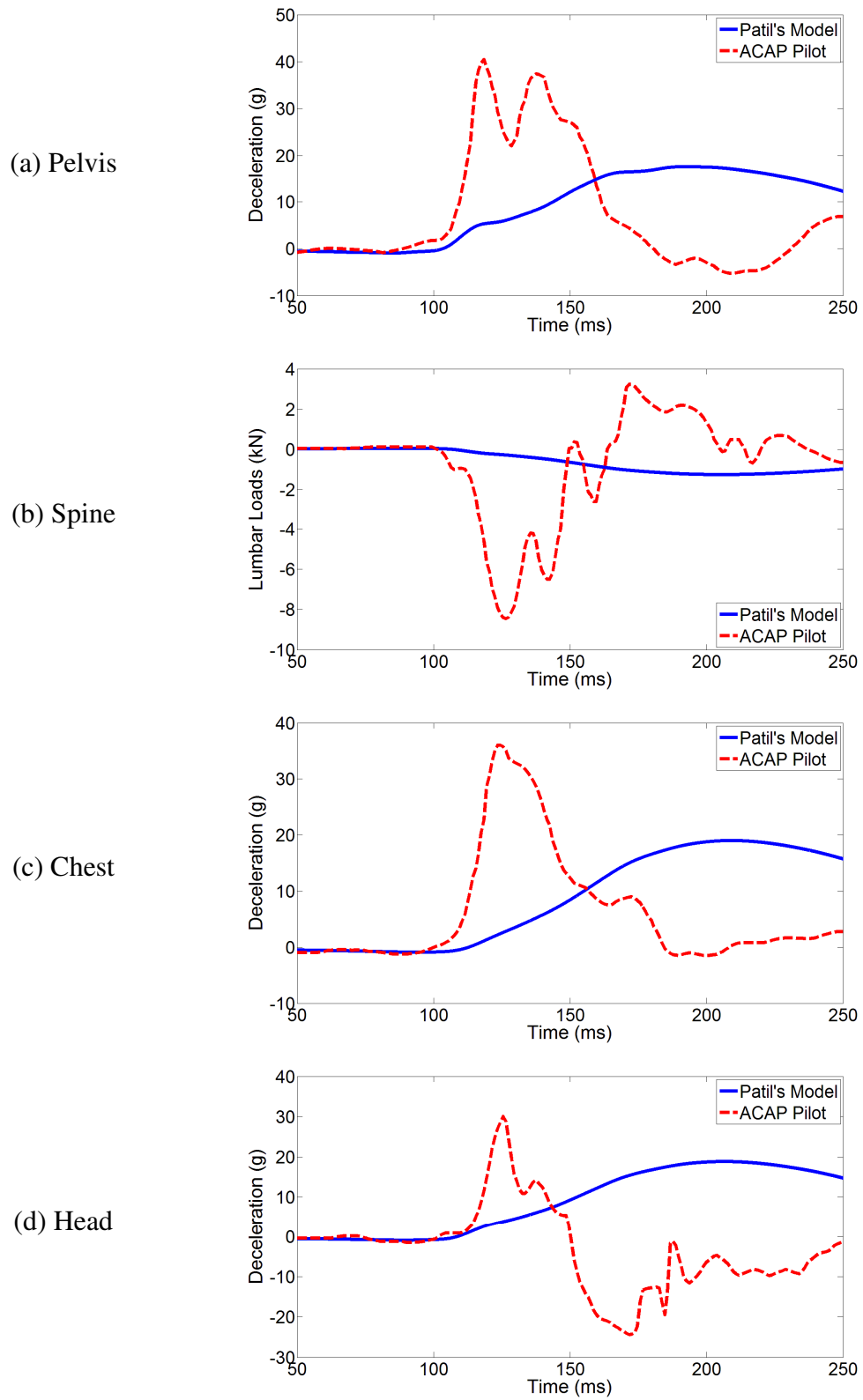
Figure 3.7. Experimental and Patil's biodynamic model response comparison.
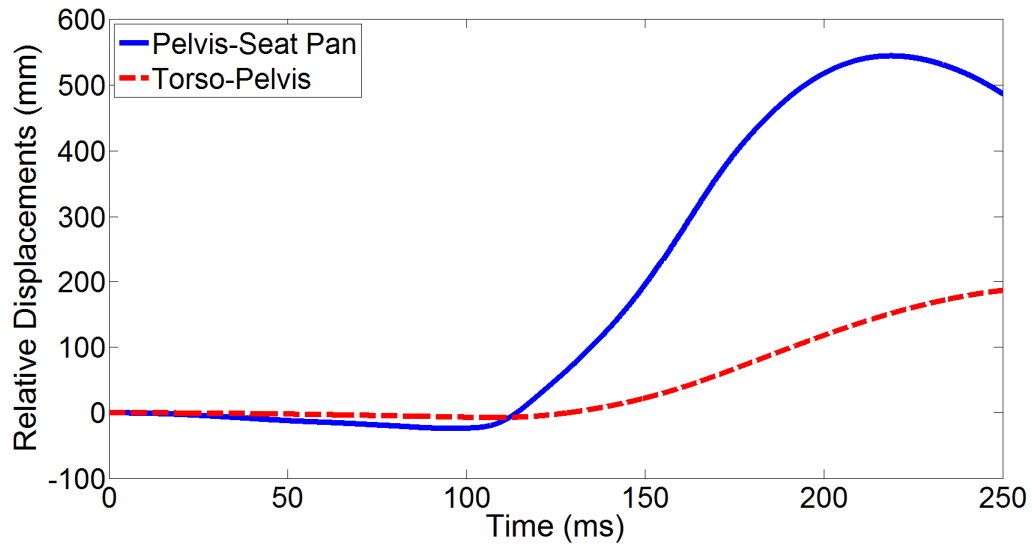
Figure 3.8. Relative displacement time history from Patil's biodynamic model.
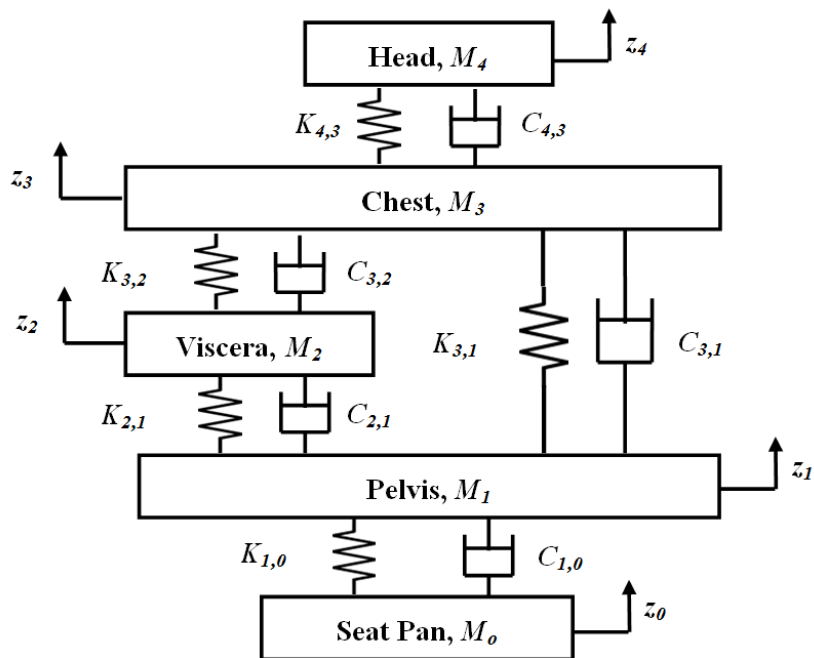
Figure 3.9. Proposed four-DOF biodynamic model of a seated occupant.

(a) Pelvis

(b) Spine

(c) Chest

(d) Head
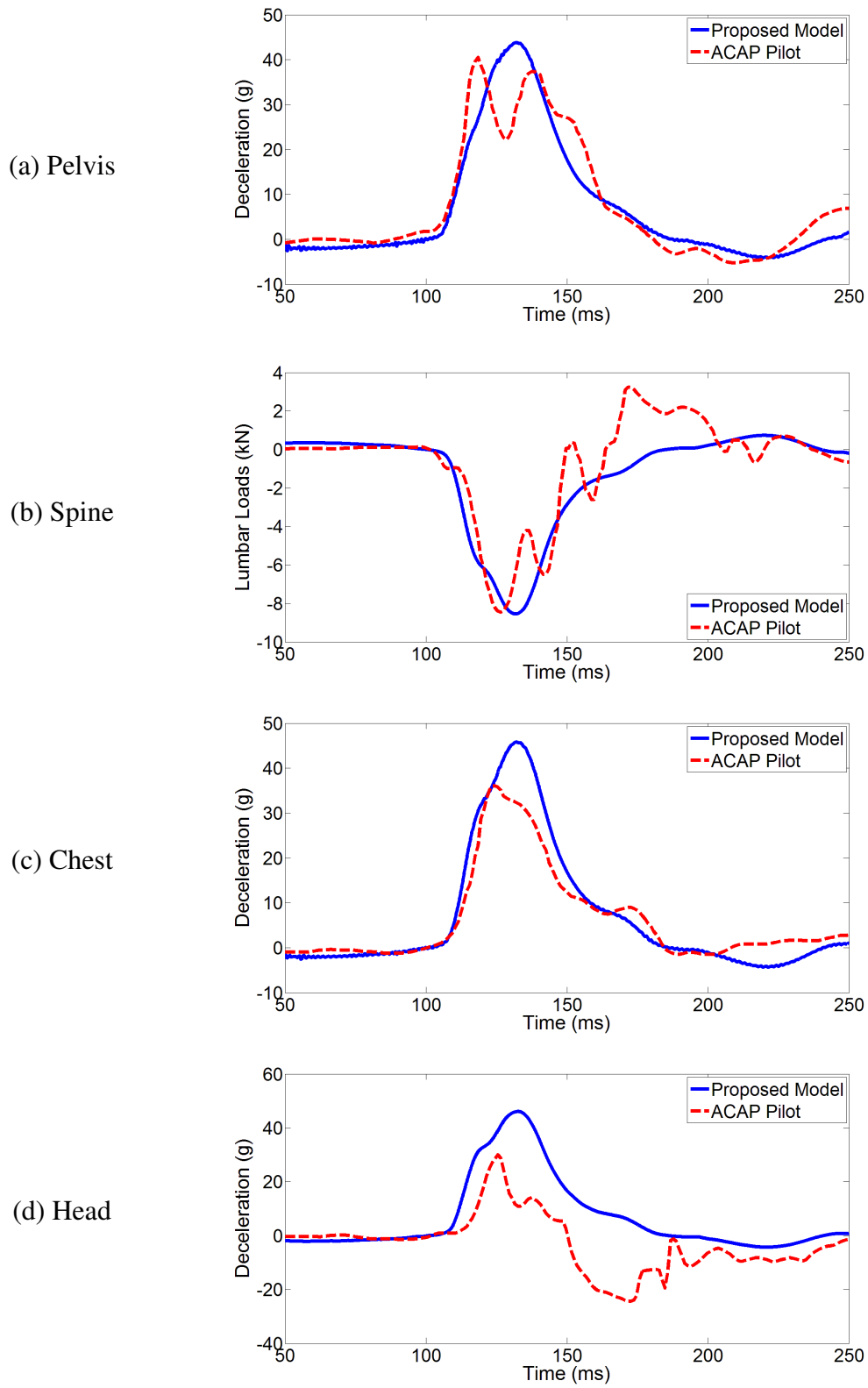
Figure 3.10. Experimental and optimized biodynamic model response comparison.
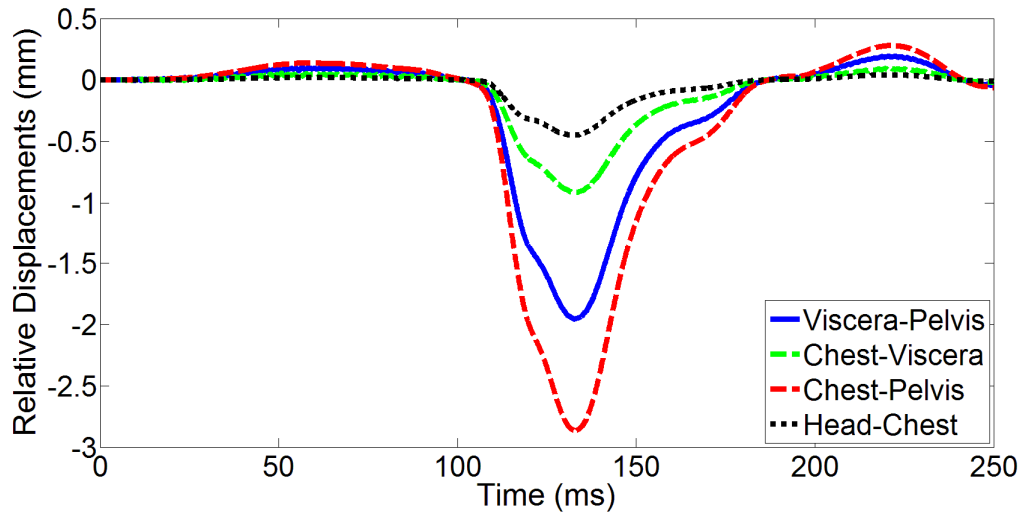
Figure 3.11. Relative displacements between lumped masses of proposed biodynamic model.
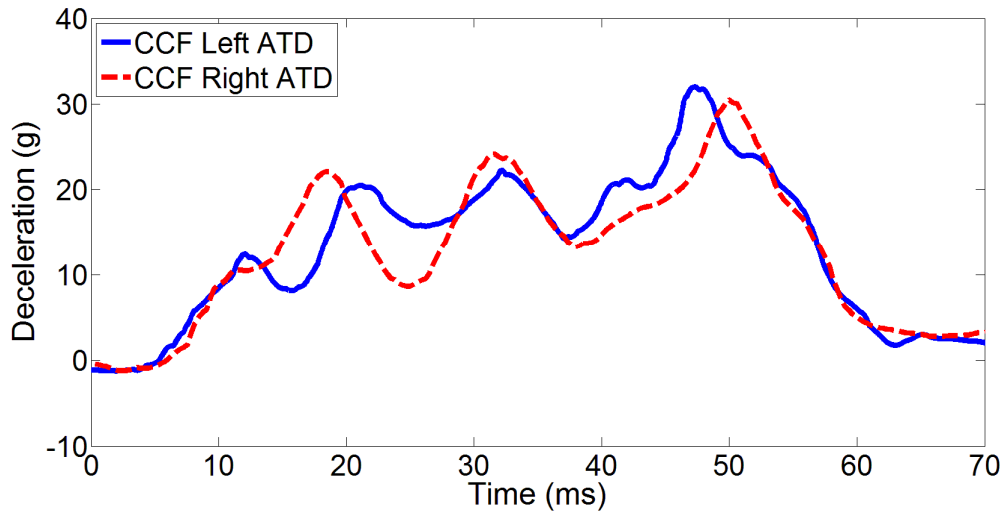
Figure 3.12. Pelvic deceleration of left and right ATD in CCF experiment (Fasanella and Jackson, 2004).

(a) Left ATD
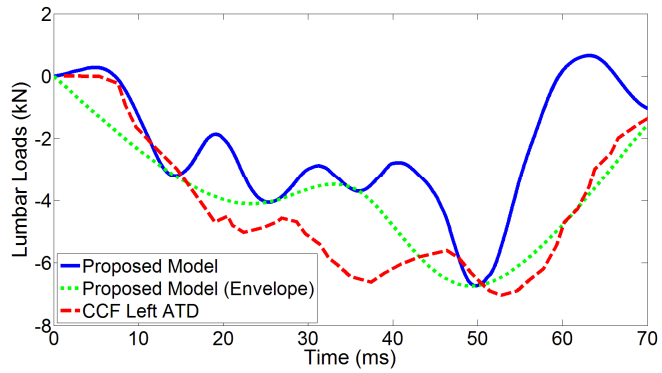
(b) Right ATD
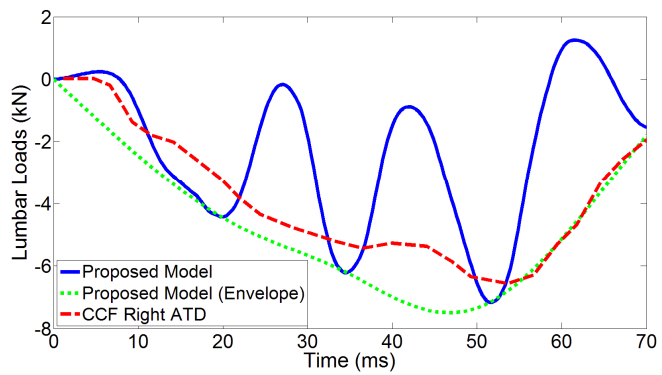
Figure 3.13. Lumbar loads comparison of model with CCF experiment.
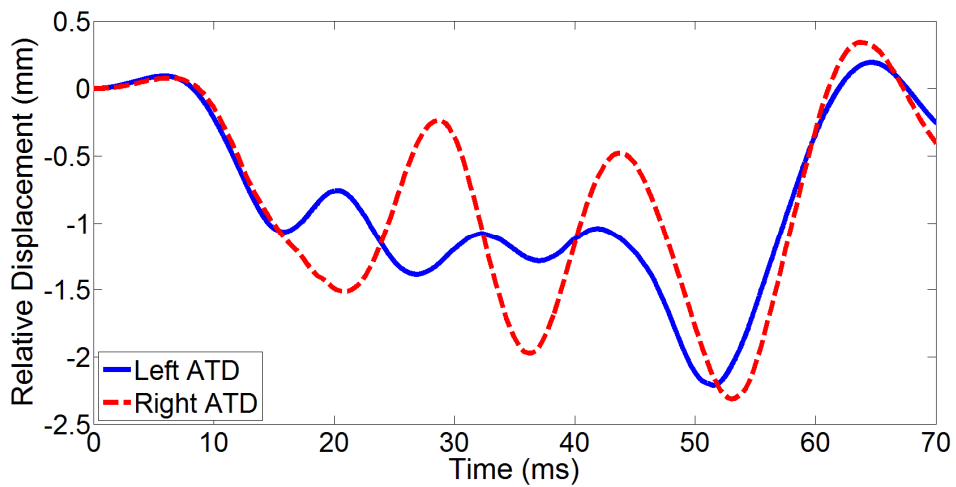
Figure 3.14. Relative lumbar spine compression of left and right ATD from model simulations.

Chapter 4

Influence of Occupant Compliance on Performance of an Adaptive Seat Suspension

4.1. Abstract

This study addresses the effects of compliance of an occupant seated in an adaptive seat suspension equipped with magnetorheological energy absorber (MREA) and exposed to intense vertical shocks. A 50th percentile male occupant exposed to shock conditions characterized by sink rates varying from 5 to 10 m/s was considered. Compliance effects were examined by comparing the response of a multiple degree-of-freedom biodynamic lumped parameter model derived from the response of a Hybrid II anthropomorphic test dummy representing a compliant occupant model (COM) to the response of an equivalent rigid occupant model (ROM) under the same shock conditions. An experimentally validated nonlinear mathematical model of an MREA was integrated with both compliant and rigid model of the occupants. In addition, three different control techniques were investigated based on controlling the onset of MREA stroking load: constant stroking load control, terminal trajectory control, and optimal control. The internal damping of a compliant occupant proved to be a crucial parameter in determining the

biodynamic response for all control techniques. An assessment of potential of injury was conducted based on established injury criteria for compliant occupants in order to evaluate the applicability of the control techniques.

4.2.   Introduction

Minimization of shock load-induced injury to a seated occupant as a result of hard or crash landing is a key issue to consider when designing a seat suspension for helicopters, armored vehicles, automobiles and fast boats. Shock events tend to result in lumbar load transmissions that may be sufficiently high to induce pelvic and spinal injuries (Choi and Wereley, 2005a; Hiemenz *et al.*, 2007; Singh and Wereley, 2011; Singh and Wereley, 2013b). The potential for injuries can be significantly moderated by employing state-of-the-art adaptive crashworthy seat suspensions that control the transmission of impact loads to the occupant by applying stroking load appropriate to the weight of seated occupant (Choi and Wereley, 2005b; Choi and Wereley, 2005c).

Seat suspensions employing semi-active devices such as magnetorheological energy absorbers (MREAs) render desirable performance for varying shock conditions because of their capability of adapting load-stroke profile. MREAs combine the best features of passive energy absorbers (EAs) such as fixed-load energy absorbers (FLEAs) (Rakheja *et al.*, 1994) and active energy absorbers such a electro-pneumatic EAs (Stein, 1997). An MREA is similar to a conventional passive EA in that a fluid is pushed through an orifice due to piston motion in a hydraulic cylinder (Cook *et al.*, 2007; Mao *et al.*, 2014). MREAs employ magnetorheological (MR) fluid consisting of 0.3-10 micrometer diameter carbonyl iron particles

suspended in hydrocarbon based carrier fluid (Guo *et al.*, 2012). The magnetic induction between these suspended particles can be controlled using an electromagnet housed in the piston of MREA. The controllability of magnetic induction between iron particles provide adaptive load-stroke profile which can be manipulated electronically, rapidly and reversibly, therefore, making it suitable for varying shock conditions (Mao *et al.*, 2014). In this study, the MREA was analyzed using a nonlinear mathematical model called Bingham-plastic model with minor losses (BPM model) for smooth annular valve as described in Chapter 2. The MREA forces were obtained by evaluating pressure drops corresponding to the controllable MR effect, as well as passive viscous losses and passive minor losses due to fluid undergoing sudden expansion and contraction.

Researchers have developed several biodynamic models, which are based on detailed experimental work, in order to study human subjects exposed to shock loads and vibrations. These biodynamic models can be classified into three categories according to the applied modeling techniques: finite element models, multi-body models and lumped parameter models (Liang and Chiang, 2006). Among these, lumped-parameter models have been implemented rigorously to study the biodynamic response. Several lumped parameter models of a seated occupant with various degrees-of-freedom (DOFs) ranging from single- to multiple-DOFs including linear and nonlinear systems have been formulated (Liang and Chiang, 2006). The lumped parameter model divides the human body into lumped mass segments isolated by springs and dampers that can be linear or nonlinear. Coermann (1962) developed a single-DOF model and measured driving point mechanical

impedance of a human in sitting and standing positions. A two-DOF lumped parameter model was established by Suggs *et al.*(1969) based on experiments using mechanical simulator for a human body subjected to vibrations. Two-DOF (Muksian and Nash, 1976) and six-DOF (Muksian and Nash, 1974) biodynamic mechanical models were analyzed using nonlinear springs and dampers to model the physical properties of humans. Patil *et al.* (1977) modified the six-DOF biodynamic model developed by Muksian and Nash (1974) by adding another lumped parameter under the human pelvis. The model was further simplified by neglecting the internal body forces. Qassem *et al.* (1994) developed an eleven-DOF model in order to study the biodynamic response of an occupant to horizontal and vertical vibrations. Similar vibrations effects were investigated for a pregnant seated female occupant by Qassem and Othman (1996).

Current analyses investigate a lumped parameter based biodynamic model of a 50th percentile male occupant derived on the basis of a response of Hybrid II anthropomorphic test dummy for intense shocks (Chapter 3). The shock conditions were modeled as an initial velocity impact corresponding to sink rates varying from 5 to 10 m/s. The effect of occupant compliance was investigated by comparing the seat suspension response for a multiple-DOF biodynamic model to an equivalent single-DOF rigid model response. The comparison was extended for three different control techniques for mitigating shock. These control techniques were based on constant EA stroking load (Desjardins *et al.*, 1989), terminal trajectory (Singh and Wereley, 2013c; Wereley *et al.*, 2011) and optimized control (Singh and Wereley, 2013a).

Injury assessment criteria for body components (lumped masses) of the occupant were drawn from the scientific literature on vertical impact (AGARD, 1996; Desjardins *et al.*, 1989; Dept. of Army, 2000). The criteria were established from landmine testing of tactical ground vehicles and from injury assessment reference values (IARVs) for hybrid III type adult dummies for crash and escape systems testing. The potential for body injuries was evaluated based on the selected injury criteria for a compliant occupant model for the best control approach.

4.3.   MREA-based Seat Suspension

The configurations of an MREA-based seat suspension with a seated compliant occupant and rigid occupant model are presented in Figure 4.1. The occupant/seat suspension was isolated from the shock using an MREA with a total stroking load (EA force), F_D, which is a summation of passive viscous force, F_V, (off-state MREA force) and MR yield force, F_{MR},(controllable MREA force). The MREA stroke, S, and seat pan mass, M_0,were selected as 16 inches and 13.5 kg, respectively (Hiemenz *et al.*, 2007).

4.3.1. Compliant Occupant Model (COM)

A seated compliant occupant subjected to shock was modeled using lumped parameters as shown in Figure 4.1a. The biodynamic model consisted of four lumped segments connected by nonlinear springs and dampers. The biodynamic model comprised of pelvis, viscera, chest and head, with masses M_i interconnected with springs with stiffness K_i and dampers with viscous damping constants C_i for i=1-4 respectively. The spring stiffness and damping constant were dependent on the

relative displacements and relative velocities between two lumped segments respectively. The displacements of seat pan and the lumped segments of biodynamic model were defined by co-ordinates z_i, for i=0-4 respectively, where z_i was defined positive upwards. All lumped parameters were assumed to be descending at the same sink rate, v_o, in the negative z direction before undergoing impact. The occupant was assumed to be seated in a perfect upright position and therefore the biodynamic model neglected additional degrees of freedom corresponding to the legs because the weight of legs was not supported by the seat suspension.

The governing equations of motion for the MREA-based seat suspension coupled with the biodynamic model of a compliant occupant are given as follows:

$$M_0 \ddot{z}_0(t) = -F_D sgn[\dot{z}_0(t)] + F_{K_{1,0}} + F_{C_{1,0}} - M_0 g \tag{4.1}$$

$$M_1 \ddot{z}_1(t) = -F_{K_{1,0}} - F_{C_{1,0}} + F_{K_{2,1}} + F_{C_{2,1}} + F_{K_{3,1}} + F_{C_{3,1}} - M_1 g \tag{4.2}$$

$$M_2 \ddot{z}_2(t) = -F_{K_{2,1}} - F_{C_{2,1}} + F_{K_{3,2}} + F_{C_{3,2}} - M_2 g \tag{4.3}$$

$$M_3 \ddot{z}_3(t) = -F_{K_{3,2}} - F_{C_{3,2}} - F_{K_{3,1}} - F_{C_{3,1}} + F_{K_{4,3}} + F_{C_{4,3}} - M_3 g \tag{4.4}$$

$$M_4 \ddot{z}_4(t) = -F_{K_{4,3}} - F_{C_{4,3}} - M_4 g \tag{4.5}$$

where, subscript K and C represent nonlinear spring and damper forces, respectively.

$$F_{K_{i,j}} = K_{i,j} \left(z_i(t) - z_j(t) \right) \tag{4.6}$$

$$F_{C_{i,j}} = C_{i,j} \left(\dot{z}_i(t) - \dot{z}_j(t) \right) \tag{4.7}$$

The spring stiffnesses and damper constants were obtained based on the relative displacements and velocities between two lumped segments respectively.

$$K_{i,j} = \alpha_{i,j} + \beta_{i,j}\|z_i(t) - z_j(t)\|^{\gamma_{i,j}} \qquad (4.8)$$

$$C_{i,j} = \phi_{i,j} + \chi_{i,j}\|\dot{z}_i(t) - \dot{z}_j(t)\|^{\psi_{i,j}} \qquad (4.9)$$

The occupant as well as the seat suspension, impacts the ground at the sink rate, which determines the initial condition for the numerical analysis.

$$z_i(0) = 0; \ \dot{z}_i(0) = -v_0 \quad \forall \ i = [0 - 4] \qquad (4.10)$$

The total stroking load of MREA is given as

$$F_D = F_V + F_{MR} \qquad (4.11)$$

4.3.2. Rigid Occupant Model (ROM)

The rigid occupant model (ROM) assumed a single rigid payload by consolidating all of compliant occupant's lumped segments and the seat pan. The rigid payload was isolated from the shock using the same MREA as for the compliant occupant model (COM) as shown in Figure 4.1b. The governing equation of motion for the rigid occupant model is given as

$$\left(\sum_{i=0}^{4} M_i\right)\ddot{z}_0(t) = -F_D sgn[\dot{z}_0(t)] - \sum_{i=0}^{4} M_i g \qquad (4.12)$$

4.4. MREA Controllers

Two different types of controllers were classified based on compliant and rigid occupant models. The rigid controller (RC) was developed for controlling the MREA stroking load by assuming the occupant/seat pan as a single rigid payload, i.e. the linear and nonlinear springs and dampers of the biodynamic model had no

contribution to the MREA-based seat suspension response. On the other hand, the compliant controller (CC) considered the occupant compliance according to the established biodynamic model.

1. Rigid Controller (RC): Controller assuming occupant/seat as a single rigid payload.

2. Compliant Controller (CC): Controller assuming occupant as compliant biodynamic model.

Initially, the MREA response for a RC with a rigid occupant model (ROM) was ascertained for a given crash condition and that pre-determined MREA load-stroke profile based on RC was implemented for a compliant occupant model (COM) and the biodynamic response was evaluated. Afterwards, the response was compared with the compliant occupant employing CC. In other words, the response was evaluated for the following cases:

- Rigid occupant model (ROM) with rigid controller (RC).

- Compliant occupant model (COM) with rigid controller (RC).

- Compliant occupant model (COM) with compliant controller (CC).

4.5. MREA Design

A linear stroking MR damper was analyzed using Bingham-plastic model incorporating minor losses for smooth flow channel as described in Chapter 2. An optimization methodology similar to optimizing the stroking load profile of MREA was considered for lower passive viscous forces and higher MREA yield forces with 5 electromagnetic coils.

The passive viscous or off-state force and maximum controllable MREA yield force are shown in Figure 4.2, which were obtained using the parameters listed in Table 4.1. The maximum controllable yield force of $F_{MR} = 10.5$ kN was obtained at maximum yield stress of $\tau_{MR} = 45$ kPa.

4.6.   Constant Stroking Load Control

A constant MREA stroking load control approach for evaluating the biodynamic response mitigation was employed based on dynamic limit load of an energy absorber. The dynamic limit load was determined based on the maximum permissible vertical load the occupant could endure during the impact, i.e. the total stroking force of energy absorber and frictional forces in the seat suspension. A limit load factor of $14.5g$ was selected for sizing the energy absorber for a 50th percentile male. In other words, the total force of energy absorber was designed not to exceed 14.5 times the effective weight (80% of total weight) of 50th percentile male subjected to a crash condition (Desjardins *et al.*, 1989).

$$F_{D_L} = 14.5 \left(\sum_{i=0}^{4} M_i\, g \right) = 10 \text{ kN} \tag{4.13}$$

Therefore, the corresponding controllable MREA yield force was varied as

$$F_{MR} = F_{D_L} - F_V \tag{4.14}$$

In order to analyze the implementation of constant stroking load control (CSLC), a50[th] percentile male occupant seated on a MREA-based seat suspension

with a stroke of S=16 inches was considered at crash corresponding to sink rate of 10 m/s with rigid (RC) as well as compliant controller (CC).

4.6.1. Seat Pan Response

The seat pan displacements of a 50th male for rigid and compliant controller implementations based on ROM and COM are shown in Figure 4.3a. When considering the rigid occupant model, the payload utilized 14.87 inches of stroke for a rigid controller. For a compliant occupant employing RC based MREA load-stroke profile, the seat pan utilized slightly larger stroke and was found to be 15.17 inches. The response of a compliant occupant with compliant controller revealed that when subjected to constant stroking load, the seat pan required comparatively smaller MREA stroke of 13.86 inches. The reason for such variation in the stroke utilized by ROM and COM is based on the additional component of damping arising from biodynamic model. The internal damping also mitigated a part of shock energy and affected the corresponding stroking load of the MREA.

The seat pan velocities for the cases under consideration are plotted in Figure 4.3b. The velocity of seat pan of rigid occupant was same as the velocity of the entire payload because all mass segments were lumped into a single mass and connected rigidly. Compared to rigid occupant, the velocity profiles of compliant occupant had fluctuations arising from internal nonlinear compliance. The subsequent fluctuations in the seat pan deceleration of a compliant occupant were higher in magnitude for a compliant controller when compared to the response based on a rigid controller. The effect of compliance was observed to be significantly dominant because even though

the initial velocity was same for compliant occupant with RC and CC, the respective difference in total stroke utilized was 1.31 inches.

4.6.2. MREA Response

An occupant at a particular crash condition had a definite amount of kinetic energy which was the same for both the compliant and rigid occupant model. For a rigid occupant, the shock energy was expended entirely by controllable MREA yield force and passive viscous force because of absence of internal damping in a rigid payload. On the other hand, for a compliant occupant, the energy was dissipated by MREA yield force, passive viscous force and internal biodynamic damping due to occupant compliance, which was modeled using nonlinear dampers. The internal compliant damping was determined by relative velocity between two lumped segments. Therefore, the internal damping could vary from small to large values depending upon the relative velocities between different lumped masses.

The MREA yield force, passive viscous force and total MREA stroking load variation with respect to the displacement of the seat pan is presented in Figure 4.4. It is observed from Figure 4.4a that the variation of MREA yield force for ROM and COM with RC was exactly same with the only difference in stroke utilized by a compliant occupant. In case of COM utilizing lesser stroke with RC, the MREA yield force profile was exactly followed as obtained by ROM with RC. However, for the cases when COM with RC stroked larger than ROM with RC, the end-value of MREA yield force was kept constant afterwards as can be seen in Figure 4.4a for a small fraction of the stroke utilized. When compared to the MREA yield force

required to maintain a constant stroking load for a rigid occupant, the MREA yield force corresponding to a compliant occupant had large fluctuations.

Observing the variation of the passive viscous force with respect to the seat pan displacement presented in Figure 4.4b, there was a linear decay of the viscous force for ROM with RC that led to linear build up of the MREA yield force as observed in Figure 4.4a. In a similar fashion, the fluctuations in the viscous force for a COM with CC led to the fluctuations in the variation of the MREA yield force.

The total stroking load of the MREA depicted that a constant stroking load was sustained for a rigid occupant with a rigid controller. However, when that rigid controller was implemented for a compliant occupant, there existed significant fluctuations varying from a minimum stroking load of 6.45 kN to a maximum value of 11.28 kN violating the objective of the control scheme. A compliant occupant employing a compliant controller maintained the stroking load that was constant during the entire operation as can be seen in Figure 4.4c.

The variation in the stroking load of the MREA was compared by estimating the amount of energy dissipated as obtained by the following equation.

$$E_D = \int_0^{t_s} F_D \, dz_0(t)$$

(4.15)

where E_D is the energy dissipated by the MREA during the entire operation and t_s represents the time at which the seat pan came to a complete halt after the impact.

Since the constant stroking load was maintained for both ROM with RC and COM with CC, the energy dissipated by MREA for COM with CC was slightly lesser when compared to ROM with RC. The difference between the energy dissipated by MREA was mitigated by the internal biodynamic damping. The energy

dissipated by ROM with RC was estimated to be 3.78 kN-m, whereas for COM with CC the dissipated energy was about 3.53 kN-m. For the case of COM with RC, the stroke utilized was slightly larger compared to other cases but due to internal biodynamic damping the energy dissipated by the MREA was smaller than ROM with RC and estimated to be 3.62 kN-m.

4.7. Terminal Trajectory Control

The second approach was based on optimal terminal trajectory control (TTC) and was implemented with the goal of maximizing biodynamic shock attenuation by adopting two key goals (Wereley *et al.*, 2011). The first goal was to utilize the available MREA stroke completely such that the kinetic energy of the occupant was dissipated over the entire stroke. The second goal was to avoid the potentially injurious end-stop impact, i.e. the condition when the energy absorber runs out of its stroke and transmits large impact loads to the seated occupant. In order to achieve these goals and to maintain soft landing, the MREA yield force had to be controlled accordingly. The optimal MREA yield force should always satisfy the terminal conditions given as:

$$z_0(t_s) = -S \; ; \; \dot{z}_0(t_s) = 0 \qquad (4.16)$$

The simplicity of this approach was based on the fact that a constant MREA yield force could achieve the terminal trajectory goals. In other words, the MREA yield force was tuned to a constant value throughout the impact.

4.7.1. Seat Pan Response

Similar to CSLC, the response of a50th male was evaluated at sink rate of 10 m/s for TTC. The seat pan displacements and decelerations are presented in Figure 4.5. The rigid occupant with RC utilized the energy absorber stroke of 16 inches completely. However, when RC was implemented for a compliant occupant, the seat pan required slightly larger stroke of 16.25 inch than available, so that the compliant occupant incurred a minor end-stop impact and, therefore, resulted in an infeasible response. On the other hand, compliant occupant with CC rendered a desirable response with soft landing similar to ROM with RC. However, the time-history of seat pan displacement for all of the three cases was almost similar.

The seat pan velocity for a rigid occupant with RC smoothly decayed with time. The compliant occupant with RC and CC experienced much larger oscillations similar to the response when employing CSLC. Overall, the rigid and compliant controller behaved similarly for a compliant occupant for a terminal trajectory control with minor differences in stroke utilized.

4.7.2. MREA Response

The variation of MREA yield force with the seat pan displacement was same for compliant and rigid occupant with RC as shown in Figure 4.6a. The compliant occupant, however, experienced a minor end-stop impact with constant MREA yield force based on RC because the total stroke utilized was beyond permissible limit of 16 inches. The reason for such a phenomenon is underlying in the variation of passive force and the corresponding total MREA stroking load. It is noticeable from Figure 4.6c that the energy dissipated by the total stroking load for COM with RC

was much lower than that of ROM with RC. The MREA yield force and viscous force facilitated in dissipating majority of kinetic energy associated with the occupant. The internal biodynamic damping could not have been sufficient to mitigate the non-dissipated kinetic energy and because of that the occupant experienced an end-stop impact. Therefore, compliant occupant required a slightly higher MREA yield force to mitigate the leftover kinetic energy and to achieve soft landing by implementing CC as shown in Figure 4.6a.

The energy dissipated by the MREA for ROM with RC, COM with RC and COM with CC were estimated around 3.80, 3.62 and 3.61 kN-m. The increase in MREA yield force for COM with CC to 5.39 kN compared to COM with RC with 5.29 kN resulted in increased biodynamic damping that further led to dissipate the leftover kinetic energy within 16 inches of stroke and avoiding any end-stop impact. Subsequently, the increased biodynamic damping providing enhanced dissipation led to a slight decrease in the energy dissipated by the MREA from 3.62 to 3.61 kN-m.

4.8.   Optimal Control

The seat pan was subjected to a constant MREA stroking load with CSLC approach and, therefore, there was a flat onset of MREA force from the beginning of the impact till the end. However, such an approach did not govern full stroke utilization that resulted in minimizing the energy dissipation per unit stroke. On the other hand, TTC provided a constant MREA yield force throughout the operation such that the available stroke was fully utilized by the seat pan but that did not guarantee that constant MREA yield force provide the best response.

The seat suspension response could improve significantly if the MREA yield force was optimally tuned during the shock event. Therefore, another approach was formulated based on optimizing the MREA yield force profile throughout the impact such that the occupant/seat pan experienced appropriate onset of MREA forces.

4.8.1. Optimal Control Formulation

The biodynamic response optimization was established using design-optimization based techniques (Singh and Wereley, 2013a).The potential for injuries to different lumped parameters of the biodynamic model was minimized if the operation of MREA was optimally controlled. In other words, the variation of MREA yield force should be determined during the shock event such that the decelerations for seat pan and different body parts and the potential for injury were minimized. One way of achieving such a response is to minimize the peak stroking load of the MREA during the impact.

Cost Function

The cost function seeks to minimize the peak MREA total stroking load during the crash event:

$$Min: Max[F_D] \qquad\qquad (4.17)$$

Minimization of peak MREA stroking load was considered because optimal stroking load leads to reduction in seat pan deceleration and corresponding reductions in biodynamic decelerations so that the occupant maintained a sufficient level of protection.

Design Variables

The design variables involved with the optimization formulation determined the variation of MREA yield force with respect to the seat pan displacement during the shock event. A cubic polynomial curve was fitted with four unknown design variables in order to define the MREA yield stress and the corresponding yield force variation with the seat pan displacement.

$$\tau_{MR} = p_1 \|z_0(t)\|^3 + p_2 \|z_0(t)\|^2 + p_3 \|z_0(t)\| + p_4 \tag{4.18}$$

where, p_1, p_2, p_3 and p_4 are the unknown design variables.

Constraint: Seat Pan Displacement

An important constraint was defined for the seat pan displacement because the seat pan displacement could not exceed available MREA stroke of S=16 inches, or else potentially injurious end-stop impact would occur. For a particular sink rate, the kinetic energy of the payload (i.e. seat plus occupant mass) must be dissipated completely by the seat suspension in order to minimize the biodynamic decelerations. Therefore, the energy should be dissipated within the permissible stroke.

$$\|z_0(t_s)\| \leq S \tag{4.19}$$

Constraint: MREA Yield Force

The MREA yield force is proportional to the yield stress, which was a maximum when magnetization reached the saturation point of magnetic particles dispersed in the fluid. The upper bound on MREA yield force was selected based on the operating yield stress providing maximum yield force for the MREA

configuration. Moreover, in the absence of magnetic field, the yield force was zero. Therefore, the MREA yield force could be either zero or positive.

$$0 \le F_{MR} \le 10.5 \, kN \qquad (4.20)$$

4.8.2. Seat Pan Response

Similar to CSLC and TTC, a 50th male exposed to crash condition corresponding to sink rate of 10 m/s was analyzed using optimization-based technique (Singh and Wereley, 2013a). An inbuilt optimization methodology in MATLAB known as *Genetic Algorithm* was utilized to couple the optimizer with differential equations governing the biodynamic response. A major advantage of *Genetic Algorithm* was that it generated a population which was mutated for subsequent generations (i.e. assigning values to the unknown design variables) and evaluated the response to find multiple local optima. By doing so, the possibility of capturing the global optimum or best design point increased significantly and was mainly dependent on the population size and generations.

The seat pan displacements and velocities are plotted in Figure 4.7. The rigid occupant with RC smoothly utilized the entire stroke of 16 inches. The optimizer converged to full stroke utilization even when the constraint on the seat pan was relaxed to take any value between 0 and 16 inches. When a compliant occupant implemented the RC, the seat pan slightly over-utilized the stroke and stopped after 16.26 inches. On the other hand, a compliant occupant with CC also converged to full stroke utilization of 16 inches without violating any constraint. Ignoring the infeasible response of over-utilized stroke, the responses of ROM with RC and COM with CC were almost similar.

The seat pan velocity for ROM with RC reveal that minimizing the total stroking load of the MREA resulted in velocity profile similar to what was observed for CSLC. These seat pan velocities obtained by employing optimal control were similar for compliant occupant with RC and CC because of approximately same seat displacements as shown in Figure 4.7a.

4.8.3. MREA Response

The MREA yield force, viscous force and total stroking load are presented in Figure 4.8. It is observed that the variation of MREA yield force for ROM and COM with RC was same but average passive viscous force for COM with RC was lower resulting in lower average total stroking load of the MREA and correspondingly, lower energy dissipation by the MREA. The internal compliance damping along with controllable MREA yield force and passive viscous force assisted in dissipating a part of the kinetic energy but resulted in an over-utilized stroke that was infeasible. In order to achieve a desirable and feasible response within the permissible MREA stroke, the compliant occupant required CC.

The total stroking load variation with the seat pan displacement shows that for a rigid occupant with RC, the total MREA stroking load was almost constant throughout the operation. The peak stroking load for COM with CC was marginally higher than with RC. The slight increased stroking load resulted in stopping the seat pan within the limited MREA stroke of 16 inches. The energy dissipated by the MREA stroking load was around 3.80, 3.64 and 3.64 kN-m for ROM with RC, COM with RC and CC respectively. Since the energy dissipated was same from COM with

RC and CC, the internal biodynamic damping would have been the same for these particular cases given that the occupant was subjected to same shock conditions.

4.9.   Comparison of Control Schemes

The comparison of different schemes based on constant stroking load, terminal trajectory and optimal control was carried out for a compliant 50th percentile male employing compliant controller (CC) subjected to the crash conditions corresponding to sink rates varying from 5 to 10 m/s. Since compliance had moderate to significant role on the control schemes as observed in previous sections, the focus was drawn mainly towards COM with CC.

The peak seat pan displacements are plotted in Figure 4.9. It was observed that terminal trajectory and optimal control converged to full stroke utilization for varying sink rates. The constraint of full stroke utilization was tighter in terminal trajectory control resulting in such an outcome. For optimal control, the constraint was relaxed using an inequality but minimization of the total stroking load led to complete stroke utilization. On the other hand, the CSLC offered same level of stroking load irrespective of the variation in sink rate resulting in lower seat pan displacements for lower sink rates and vice versa. Such phenomenon was based on the fact that the lower sink rate instilled lower kinetic energy to the occupant compared to higher sink rates. The 16 inches of stroke limit was not violated for any control scheme.

4.10. Injury Assessment Criteria and Evaluation

The potential for injuries to the biodynamic segments was evaluated using injury assessment criteria established on the basis of scientific literature. The injury criteria were based on landmine testing experiments and vertical drop tests on Hybrid III type adult anthropomorphic test devices. The peak biodynamic decelerations for pelvis, chest and head, and lumbar loads are presented in Figure 4.10.

4.10.1. Pelvis

The recommended injury criteria from landmine testing based on pelvic deceleration were determined as 15, 18 and 23 g for low, medium and high risk injuries respectively (Department of Army, 2000). Ladkany (2009) suggested that the maximum pelvic deceleration be limited to 15 g. The US army research established that complete incapacitation occurred at 23 g (225 m/s^2) for more than 7 ms for vertical pelvic decelerations (Eiband, 1959). For the present study, the criteria based on pelvic deceleration were taken as 15 g for low risk injuries, 18 g for medium risk injuries and 23 g for more than 7 ms for high risk injuries. The summarized injury criteria based on pelvic decelerations is shown in Table 4.2. The thresholds were defined on Abbreviated Injury Scale (AIS).

From Figure 4.10a, it is clear that with increased shock intensity, the pelvic decelerations increased significantly for TTC and optimal control. The pelvic decelerations were almost constant for CLSC because the stroking load was tuned to a constant value irrespective of the sink rate.

The compliant occupant violated the threshold for medium risk injuries based on 18 g pelvic deceleration for the entire range of sink rates when implemented with CLSC scheme. TTC resulted in low risk injuries to pelvis set by threshold of 15 g peak deceleration for sink rates of 8 and 9 m/s. Further increasing the sink rate to 10 m/s resulted in medium risk injuries based on TTC scheme. On the other hand, optimal control only violated the threshold of low risk injuries at the highest sink rate of 10 m/s with peak pelvic deceleration around 17.4 g.

4.10.2. Lumbar Spine

The injury criteria established by the US army based on landmine testing are 3.8 kN for 30 ms or 6.67 kN for lumbar spine in compression (Eiband, 1959; Ladkany, 2009). Federal Aviation Regulation 29 determined the maximum allowable lumbar spine load to be 6.67 kN (Ladkany, 2009). Landmine injury criterion proposed by Axelsson *et al.* (2003) limited the lumbar loads from 6.67-8.0 kN. The injury criteria selected for current analyses for lumbar spine connecting pelvis with chest was 3.8 kN for 30 ms or maximum load of 6.67 kN for severe injuries.

The variation in peak compressive lumbar loads show that maximum load of around 4.46 kN was maintained by CSLC for sink rates varying from 5-10 m/s due to reasons explained earlier. Increased sink rates resulted in large lumbar loads transmissions for TTC and optimal control, however, no control scheme violated the threshold for severe injuries based on 6.67 kN. TTC resulted in peak lumbar load of 4.25 kN for highest sink rate of 10 m/s. In order to ascertain whether violating the threshold of 3.8 kN resulted in severe injuries, it was mandatory to look into the time history of the lumbar response to estimate the duration lumbar loads exceeding 3.8

kN. The time histories for lumbar responses are plotted in Figure 4.11 for the cases violating the threshold of 3.8 kN. The duration of lumbar loads exceeding 3.8 kN was around 8.5 ms for CLSC for all sink rates as shown in Figure 4.11a. When implementing TTC, the lumbar loads exceeded 3.8 kN for only 7.6 ms for the sink rate of 10 m/s. Therefore, injuries to lumbar spine were least likely to occur based on these observations.

4.10.3. Chest

Landmine testing experiments concluded that the injury criteria based on chest deceleration for high risk injury be 60 g for more than 3 ms or 40 g for more than 7 ms (Eiband, 1959). The injury assessment reference values (IARVs) for Hybrid III type adult dummies stated the injury criteria as 73, 60 and 54 g for small female, mid-size and large male respectively (AGARD, 1996; USA RDECOM, 2009). The injury criteria for the current analysis were selected as 40 g for more than 7 ms or 60 g for more than 3 ms for high risk injuries as mentioned in Table 4.2.

The peak chest decelerations followed the similar trend as for pelvis i.e. constant values CLSC and increased values for TTC and optimal control for increased sink rates as plotted in Figure 4.10c. The peak decelerations were almost of the same order for chest when compared to pelvis for a given sink rate. For any shock condition, the compliant 50th percentile male occupant with CC did not violate the established injury threshold of 40 g for more than 7 ms or 60 g for more than 3 ms.

4.10.4. Head

Head injuries were measured on a scale called Head Injury Criteria (HIC), which was determined as an averaged value of the resultant acceleration of center of gravity of the head and evaluated as defined by the following equation (Choi and Wereley, 2005a; Zong and Lam, 2002).

$$HIC = max\left\{(t_2 - t_1)\left[\frac{1}{g(t_2 - t_1)}\int_{t_1}^{t_2}\ddot{z}_4(t)dt\right]^{2.5}\right\} \qquad (4.21)$$

where t_1 and t_2 are the initial and final time of integration for head decelerations.

The landmine testing established HIC of 750 with 5% risk of brain injuries (Eiband, 1959). Axelsson *et al.* (2003) proposed HIC tolerance of 1000. Injury assessment reference values (IARVs) for Hybrid III type adult dummies state HIC criteria as 1113, 1000 and 957 for 15 ms duration for small female, mid-size and large male respectively (AGARD, 1996). Research by the US Army established the criteria on HIC scale as 700 for 15 ms time interval (USA RDECOM, 2009). For the present study, the reference values were chosen as 700 and 1000 for moderate and severe injuries respectively on HIC_{15} scale.

From Figure 4.10d, the maximum HIC_{15} value was obtained around 30 for CLSC scheme for all sink rates. The HIC_{15} values increased with sink rates for TTC and optimal control scheme but were relatively lower compared to CSLC. Therefore, there was a good level of protection for occupant's head for all shock conditions since the HIC_{15} values were significantly lower than the threshold values of 700.

4.11. Conclusions

In this study, the effect of occupant's compliant body was studied for vertical shock events corresponding to sink rates varying from 5 to 10 m/s. A nonlinear biodynamic model representing a 50th percentile seated male occupant was considered that had internal biodynamic compliance and damping. An equivalent rigid occupant model formulated by consolidating all lumped mass segments as a single rigid payload was compared with biodynamic model response for three different control techniques. These techniques were based on controlling the onset of MREA stroking load. A constant stroking load control (CSLC), in which the MREA stroking load was regulated to a constant value, was compared with a terminal trajectory control (TTC) with constant MREA yield force only. Another control approach was based on minimized MREA stroking load with constrained MREA performance and analyzed using design optimization-based techniques. Two controllers were implemented: one assuming the occupant as a compliant body, CC, and another assuming the seat pan/occupant as a single rigid payload without any internal damping, RC. It was observed that

1. The compliance of occupant was key factor in determining the internal biodynamic damping, which mitigated a fraction of total kinetic energy associated with the occupant subjected to shock.

2. The compliant occupant either slightly under-utilized the MREA stroke or experienced an end-stop impact (infeasible) when employing RC. However,

the response of a compliant occupant with RC was close to that of compliant occupant with CC for TTC and optimal control.

3. The constant stroking load control resulted biodynamic decelerations and lumbar loads independent of sink rate due to its inflexible MREA stroking load. In other words, the occupant was subjected to same loading conditions even for mild shock events. TTC and optimal control adapted the MREA stroking load such that 50th percentile male was subjected to lower loads at lower sink rates and vice versa. The difference in performance of three control schemes reduced for higher sink rates.

4. The 50th percentile male occupant experienced medium risk injuries based on $18g$ pelvic deceleration for CLSC for all shock conditions whereas low and medium risk injuries were estimated for optimal control and TTC for higher sink rates respectively.

5. Chest, lumbar spine and head maintained good level of protection for entire shock spectrum for all control schemes. Pelvis was more prone towards low to medium risk injuries due to vertical shock transmitting loads from pelvis to head.

6. The control approach based on optimization techniques proved better in minimizing the transmitted shock loads when compared to CSLC and TTC approaches.

References

AGARD 1996 Anthropomorphic Dummies for Crash and Escape System Testing *AGARD-AR-330*.

Axelsson H and Sundqvist O 2003 Mine Clearance Vehicles, Crew Safety Standard *The Swedish Defense Material Administration,* VoVC 14 910:1142/03.

Choi Y T and Wereley N M 2005a Mitigation of Biodynamic Response to Vibratory and Blast-induced Shock Loads Using Magnetorheological Seat Suspensions *Proc. IMechE Part D: Journal of Automobile Engineering*, Vol. 219, pp. 741-753.

Choi Y T and Wereley N M 2005b Biodynamic Response Mitigation to Shock Loads Using Magnetorheological Helicopter Crew Seat Suspensions *AIAA Journal of Aircraft*, Vol. 42, No. 5, pp. 1288-1295.

Choi Y T and Wereley N M 2005c Semi-Active Vibration Isolation Using Magnetorheological Isolators *AIAA Journal of Aircraft*, Vol. 42, No. 5, pp. 1244-1251.

Coermann R R 1962 The mechanical Impedance of the Human Body in Sitting and Standing Positions at Low Frequencies *Human Factors*, Vol. 4, No. 5, pp. 227-253.

Cook E, Hu W and Wereley N M 2007 Magnetorheological Bypass Damper Exploiting Flow Through a Porous Channel *Journal of Intelligent Material Systems and Structures,* Vol. 18, No. 12, pp. 1197-1203.

Department of Army 2000 Occupant Crash Protection Handbook for Tactical Ground Vehicles.

Desjardins S P, Zimmerman R E, Bolukbasi A O and Merritt N A 1989 Aircraft Crash Survival Design Guide *Aviation Applied Technology Directorate*, USAAVSCOM TR 89-D-22D, Fort Eustis, VA.

Eiband M A 1959 Human Tolerance to Rapidly Applied Accelerations: A Summary of the Literature *NASA Memo* 5-19-59E.

Guo C, Gong X, Xuan S, Zong L and Peng C 2012 Normal Forces of Magnetorheological Fluids Under Oscillatory Shear *Journal of Magnetism and Magnetic Materials,* Vol. 324, No. 6, pp. 1218-1224.

Hiemenz G J, Choi Y T and Wereley N M 2007 Semi-Active Control of Vertical Stroking Helicopter Crew Seat for Enhanced Crashworthiness *AIAA Journal of Aircraft*, Vol. 44, No. 3, pp. 1031-1034.

Ladkany G S 2009 Design and Characterization of a Shock and Vibration Mitigation Seat System *Masters Thesis in Mechanical Engineering*, University of Nevada, Las Vegas.

Liang C C and Chiang C F 2006 A Study on Biodynamic Models of Seated Human Subjects Exposed to Vertical Vibration *International Journal of Industrial Ergonomics,* Vol. 36, pp. 869-890.

Mao M, Hu W, Choi Y T, Wereley N M, Browne A L, and Ulicny J, 2014, Experimental validation of a magnetorheological energy absorber design analysis, *Journal of Intelligent Material Systems and Structures*, 25(3):352-363.

Muksian R and Nash C D 1974 A Model for the Response of Seated Humans to Sinusoidal Displacements of the Seat *Journal of Biomechanics,* Vol. 7, No. 3, pp. 209-215.

Muksian R and Nash C D 1976 On Frequency-Dependent Damping Coefficients in Lumped-Parameter Models of Human Beings *Journal of Biomechanics,* Vol. 9, No. 5, pp. 339-342.

Patil M K, Palanichamy M S and Ghista D N 1977 Dynamic Response of Human Body Seated on a Tractor and Effectiveness of Suspension Systems *Society of Automobile Engineers,* No. 770932, pp.755-792.

Qassem W, Othman M O and Abdul-Majeed S 1994 The effects of Vertical and Horizontal Vibrations on the Human Body *Medical Engineering Physics,* Vol. 16, pp. 151-161.

Qassem W and Othman M O 1996 Vibration Effects on Sitting Pregnant Women-Subjects of Various Masses *Journal of Biomechanics,* Vol. 29, No. 4, pp. 493-501.

Rakheja S, Afework Y and Sankar S 1994 An Analytical and Experimental Investigation of the Driver Seat Suspension System *Vehicle System Dynamics*, Vol. 23, No. 3, pp. 501-524.

Singh H J and Wereley N M 2011 Biodynamic Response Mitigation for Seat Suspension with Adaptive Energy Absorbers *AHS 67ᵗʰ Annual Forum*, Virginia Beach, VA, USA.

Singh H J and Wereley N M 2013a Adaptive Magnetorheological Seat Suspensions for Shock Mitigation *Proceedings of the SPIE*, San Diego, CA, USA.

Singh H J and Wereley N M 2013b Model-based Optimal Control of Biodynamic Response to Vertical Crash Loads for an Occupant Seated in a Helicopter *AHS 69ᵗʰ Annual Forum*, Phoenix, AZ, USA.

Singh H J and Wereley N M 2013c Adaptive Magnetorheological Shock Isolation Mounts for Drop-induced Impacts *Smart Materials and Structures*, Vol. 22, 122001.

Stein G J 1997 A Driver's Seat with Active Suspension of Electro-pneumatic Type *ASME Journal of Vibration and Acoustics,* Vol. 119, No. 2, pp. 230-235.

Suggs C W, Abrams C F and Stikeleather LF 1969 Application of a Damped Spring-Mass Human Vibration Simulator in Vibration Testing of Vehicle Seats *Ergonomics*, Vol. 12, No. 1, pp. 79-90.

U.S. ARMY RDECOM 2009 Preliminary Full Spectrum Rotary Wing Crashworthiness Criteria RDECOM TR 10-D-25.

Wereley N M, Choi Y T and Singh H J 2011 Adaptive Energy Absorbers for Drop-Induced Shock Mitigation *Journal of Intelligent Material Systems and Structures,* Vol. 22, No. 6, pp. 515-519.

White F M 1986 *Fluid Mechanics*, Second Edition, McGraw-Hill.

Zong Z and Lam K Y 2002 Biodynamic Response of Shipboard Sitting Subject to Ship Shock *Journal of Biomechanics,* Vol. 35, No. 1, pp. 35-43.

Table 4.1. MREA parameters

Parameter	Value
MR fluid Density (ρ)	3080 kg/m^3
MR fluid viscosity (η)	0.112 Pa-s
Maximum MR yield stress (τ_{MR})	45 kPa
Hydraulic cylinder inner diameter (D_{in})	2.36 in
Diameter of piston rod (D_r)	1 in
MR valve thickness (d)	3 mm
Coil gap thickness (d_c)	3 mm
Active length of MR valve (L_a)	1.5 in
Length of coil (L_c)	0.5 in
Number of coils (n)	5
Average pipe wall roughness (ϵ)	0.006 mm

Table 4.2. Biodynamic model tolerances on Abbreviated Injury Scale.

AIS Code	Injury Description	Pelvis *Acc.* (*g*)	Chest *Acc.* (*g*)	Lumbar Spine *Load* (kN)	Head *HIC$_{15}$* (s)
1	Minor	15	--	--	--
2	Moderate	18	--	--	700
3	Serious	--	--	--	--
4	Severe	23@7ms	40@7ms, 60@3ms	3.8@30ms, 6.67	1000
5	Critical	--	--	--	--
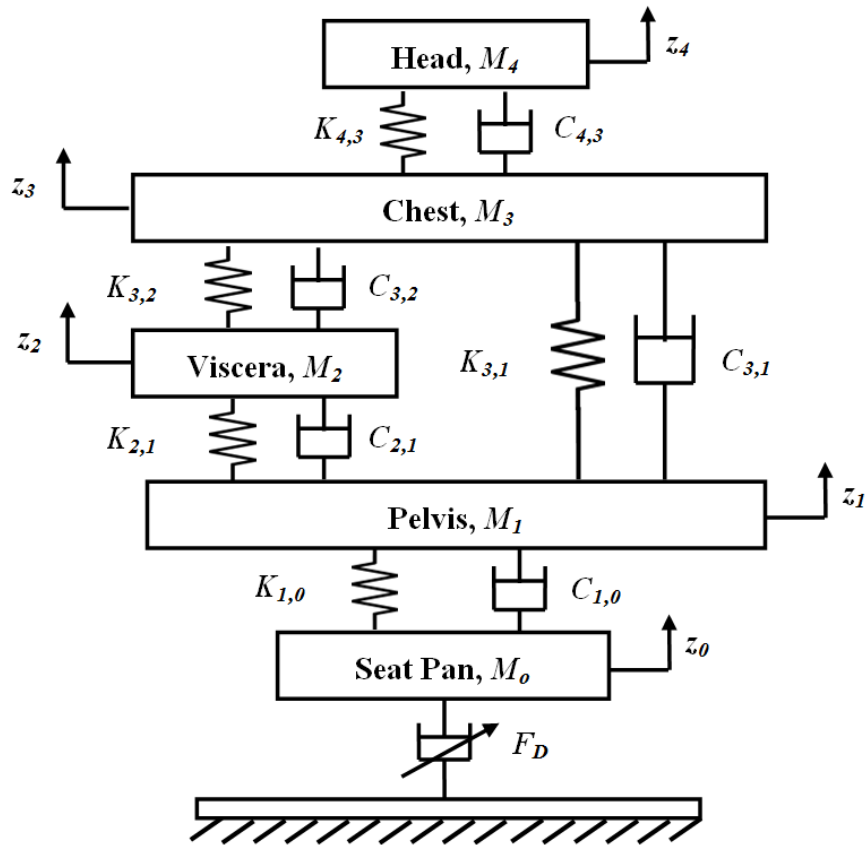
(a)
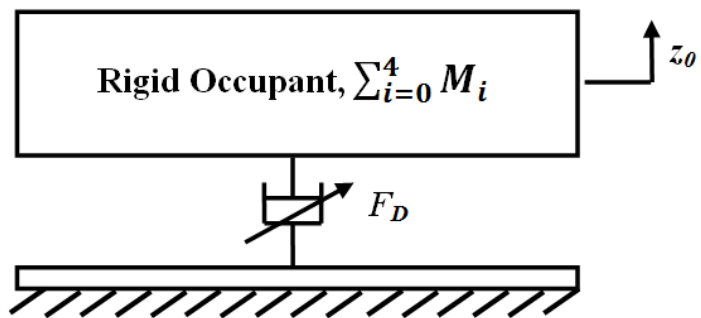
(b)

Figure 4.1. Configurations of MREA-based seat suspension with (a) compliant occupant model and (b) rigid occupant model.
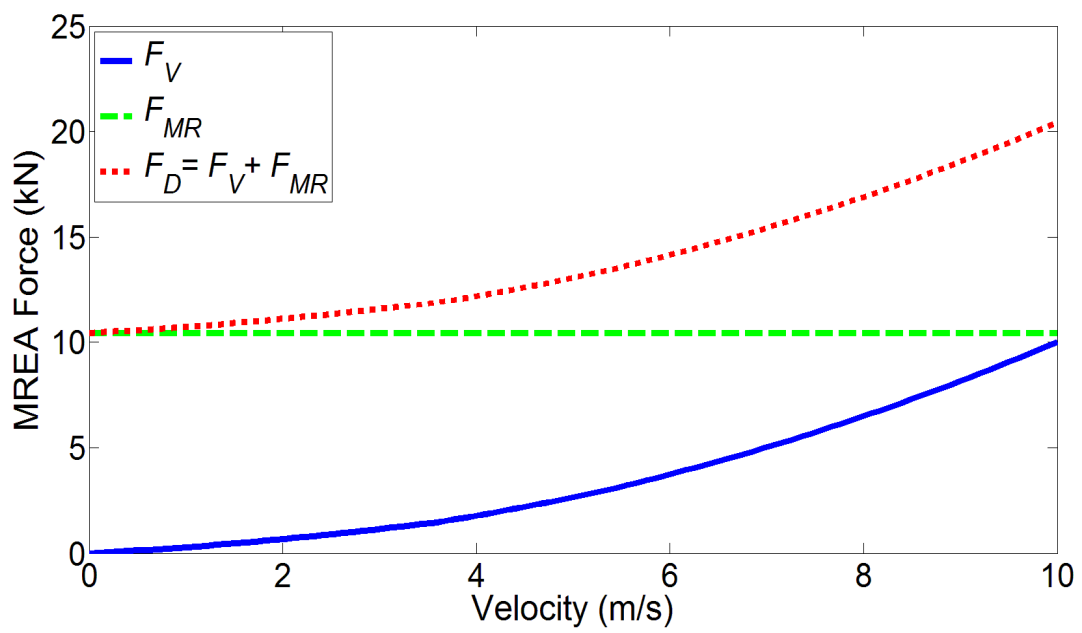
Figure 4.2. MREA force variation with velocity.
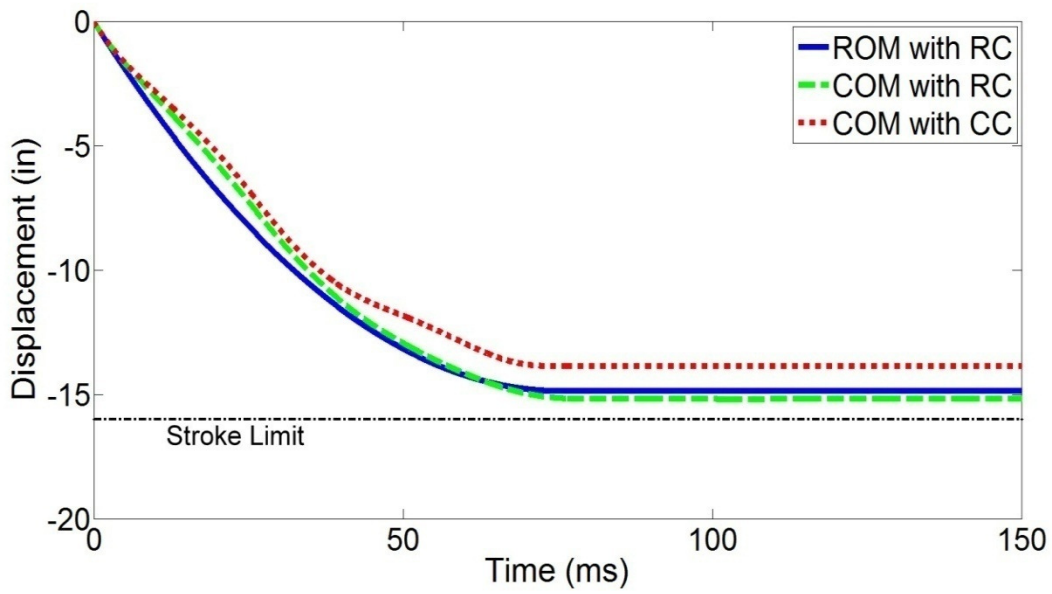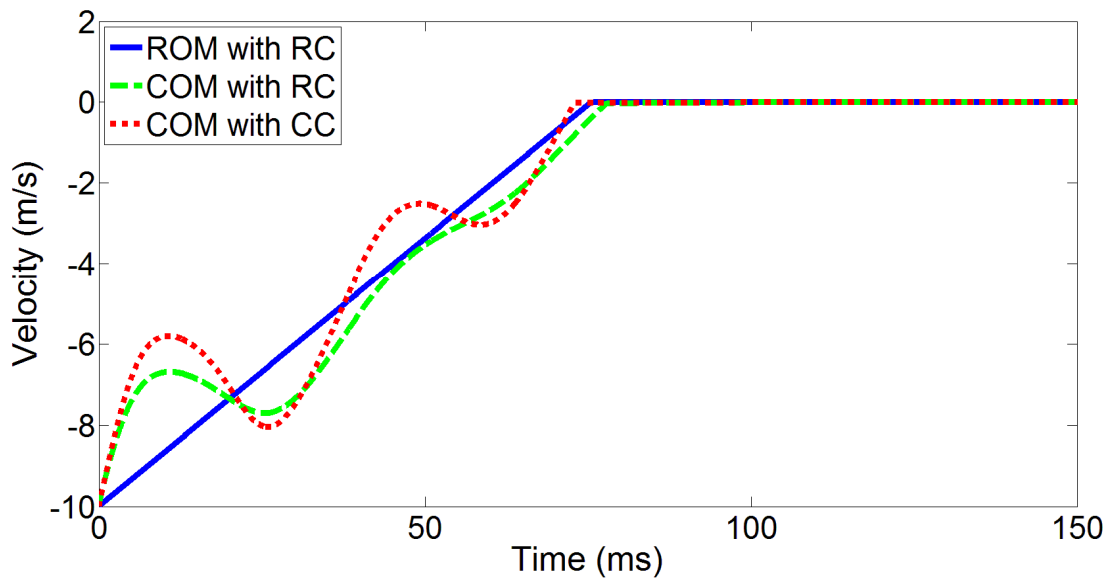
Figure 4.3. Seat pan (a) displacement and (b) velocity corresponding to sink rate of 10 m/s using CSLC.
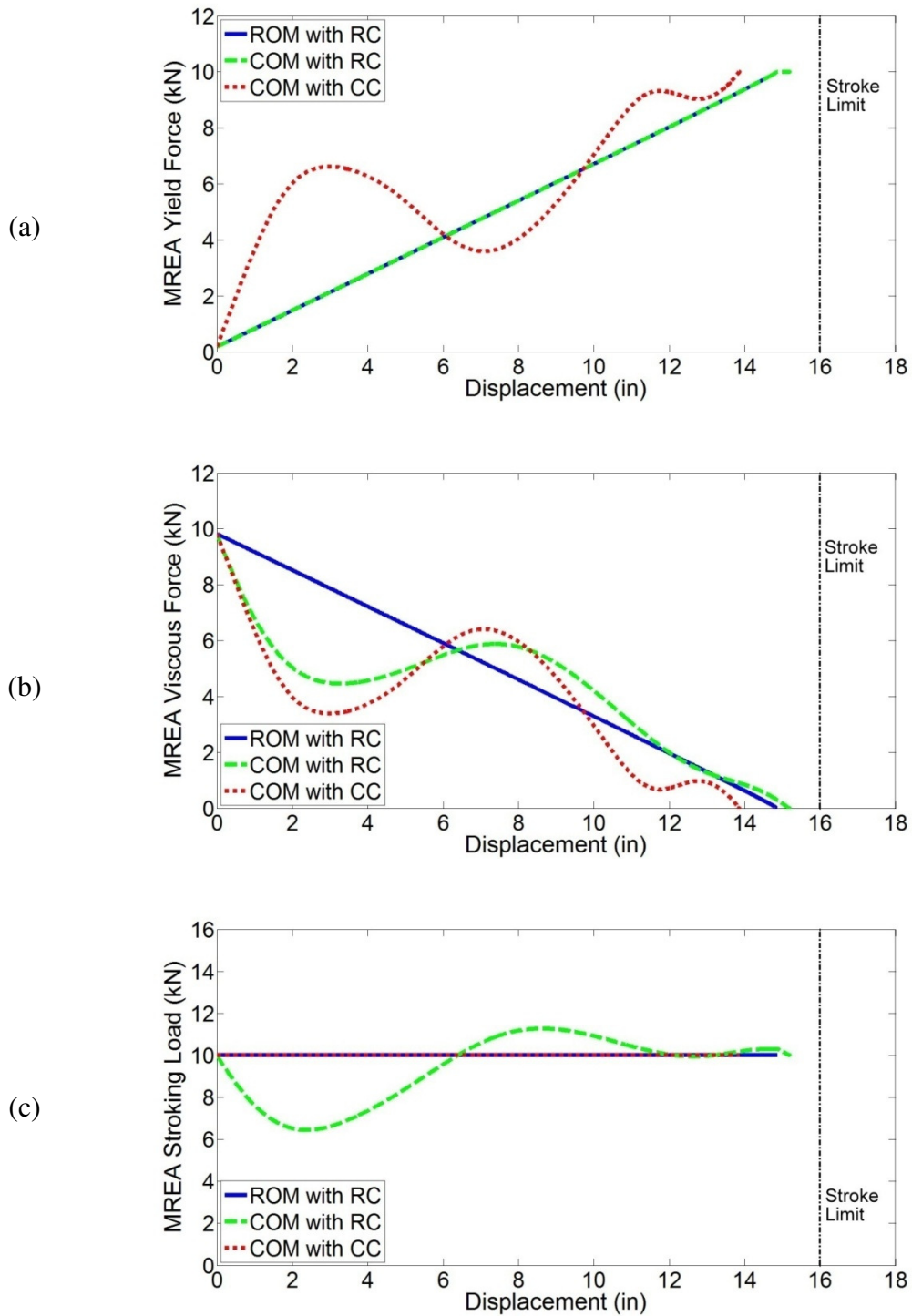
Figure 4.4. MREA (a) yield force, (b) viscous force and (c) stroking load corresponding to sink rate of 10 m/s using CSLC.
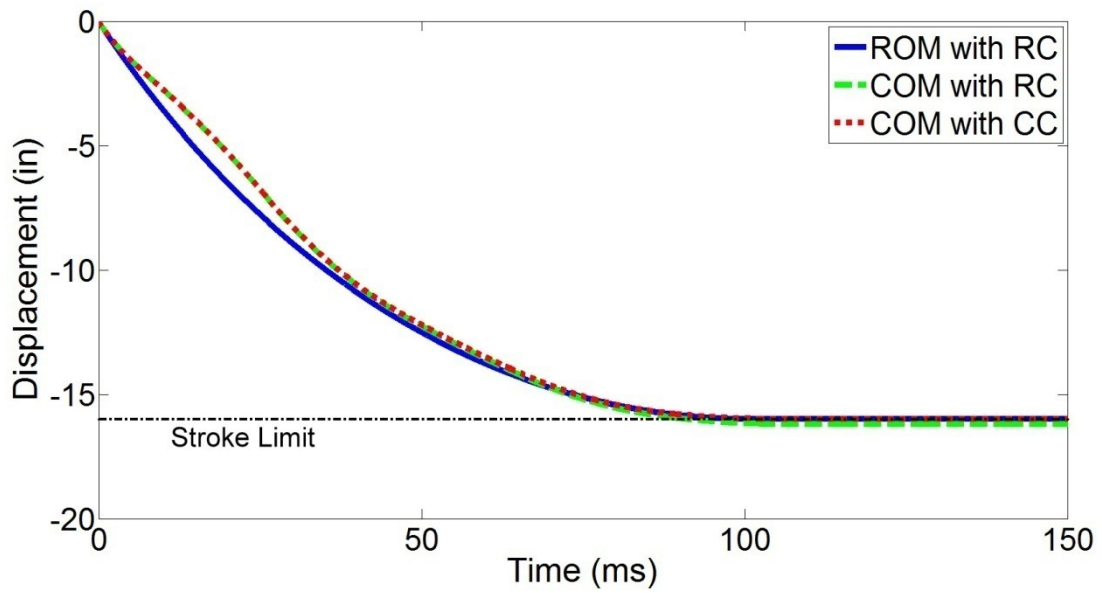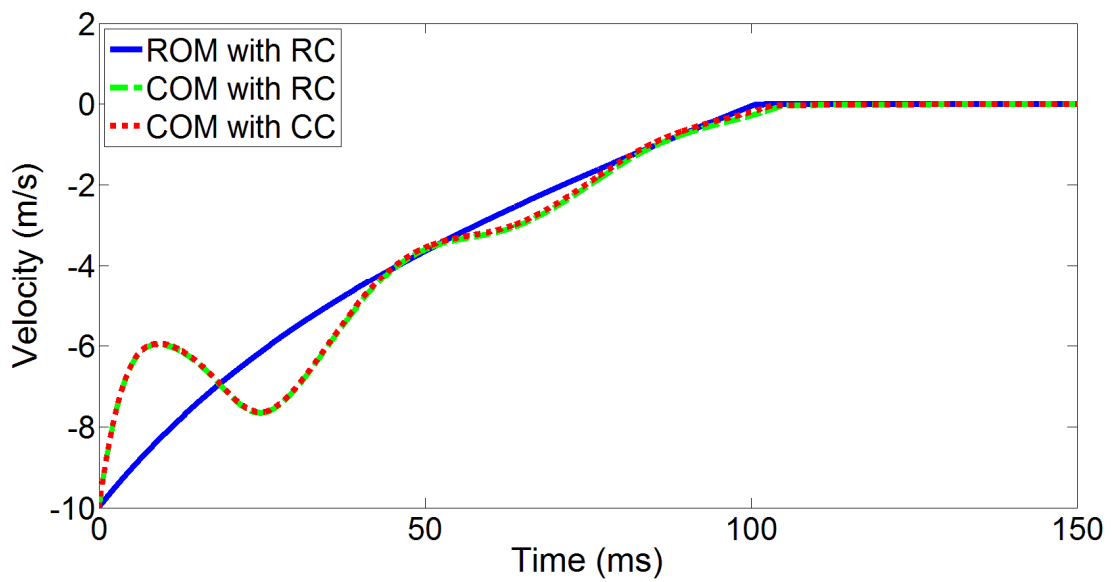
Figure 4.5. Seat pan (a) displacement and (b) velocity corresponding to sink rate of 10 m/s using TTC.
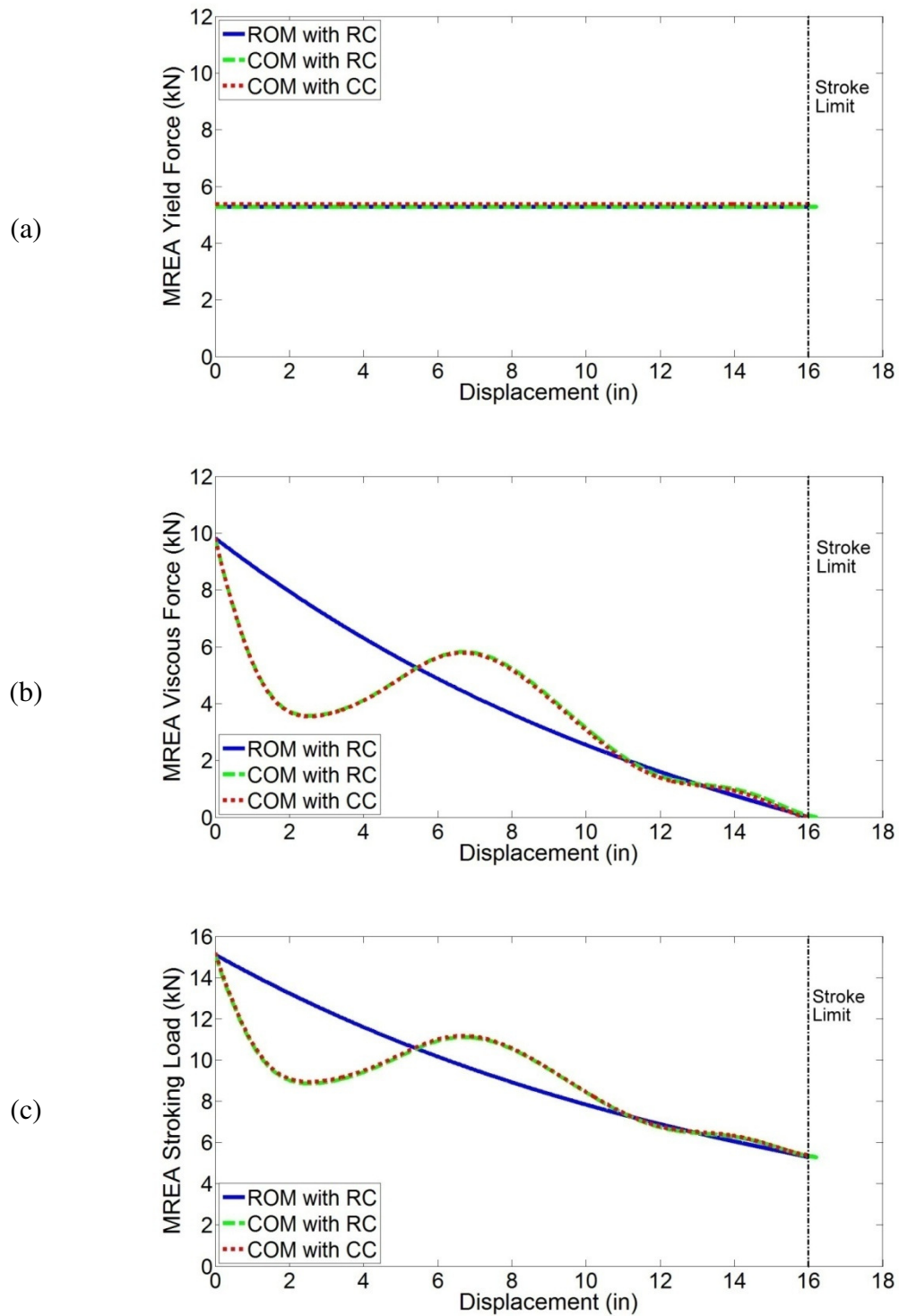
Figure 4.6. MREA (a) yield force, (b) viscous force and (c) stroking load corresponding to sink rate of 10 m/s using TTC.
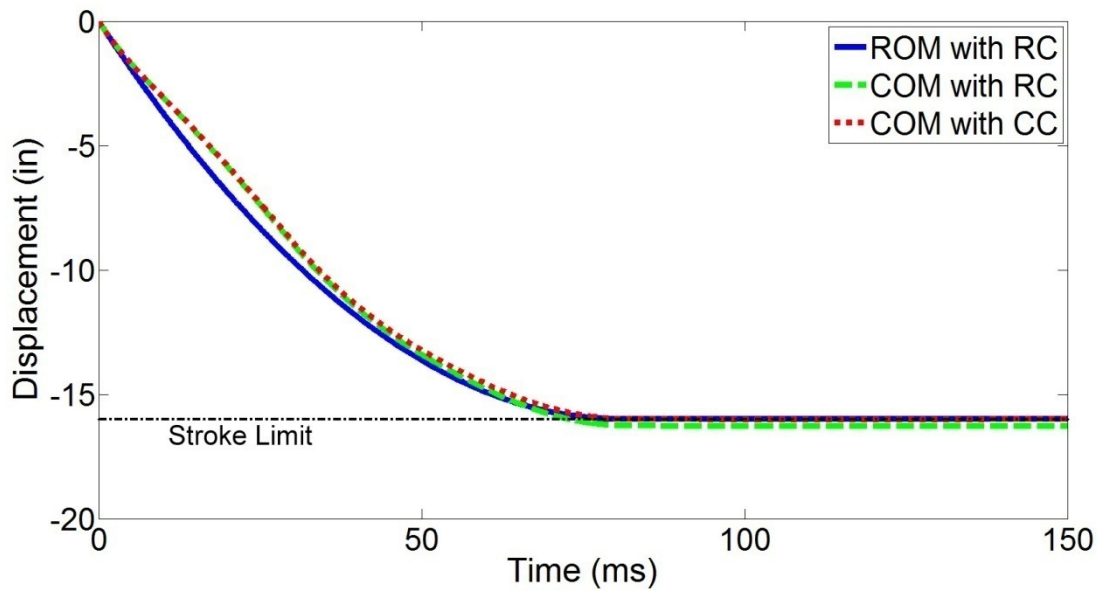
(a)
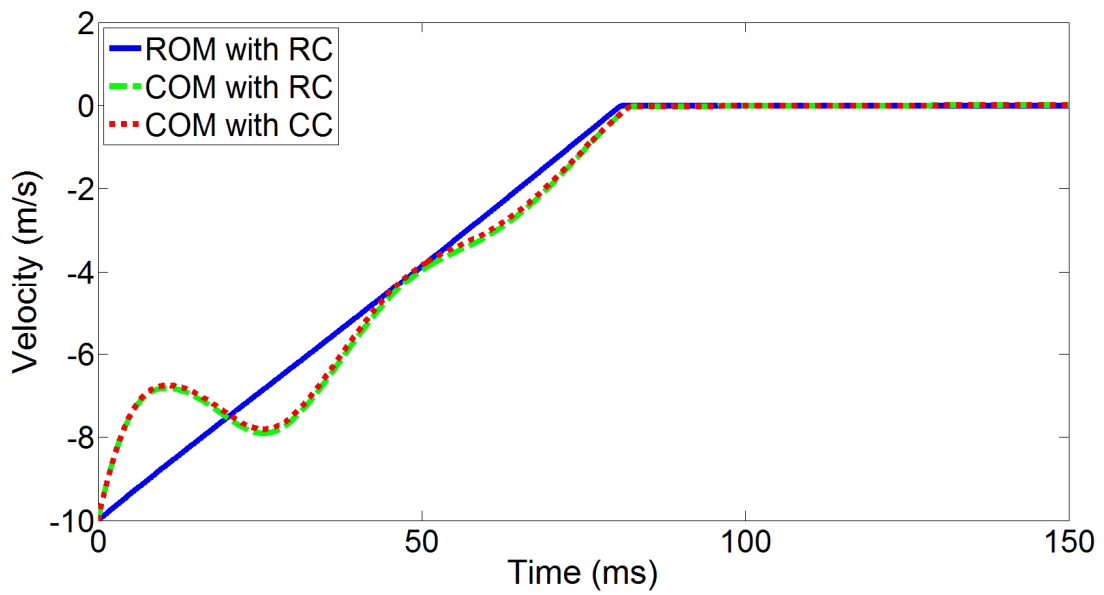
(b)

Figure 4.7. Seat pan (a) displacement and (b) velocity corresponding to sink rate of 10 m/s using optimal control.
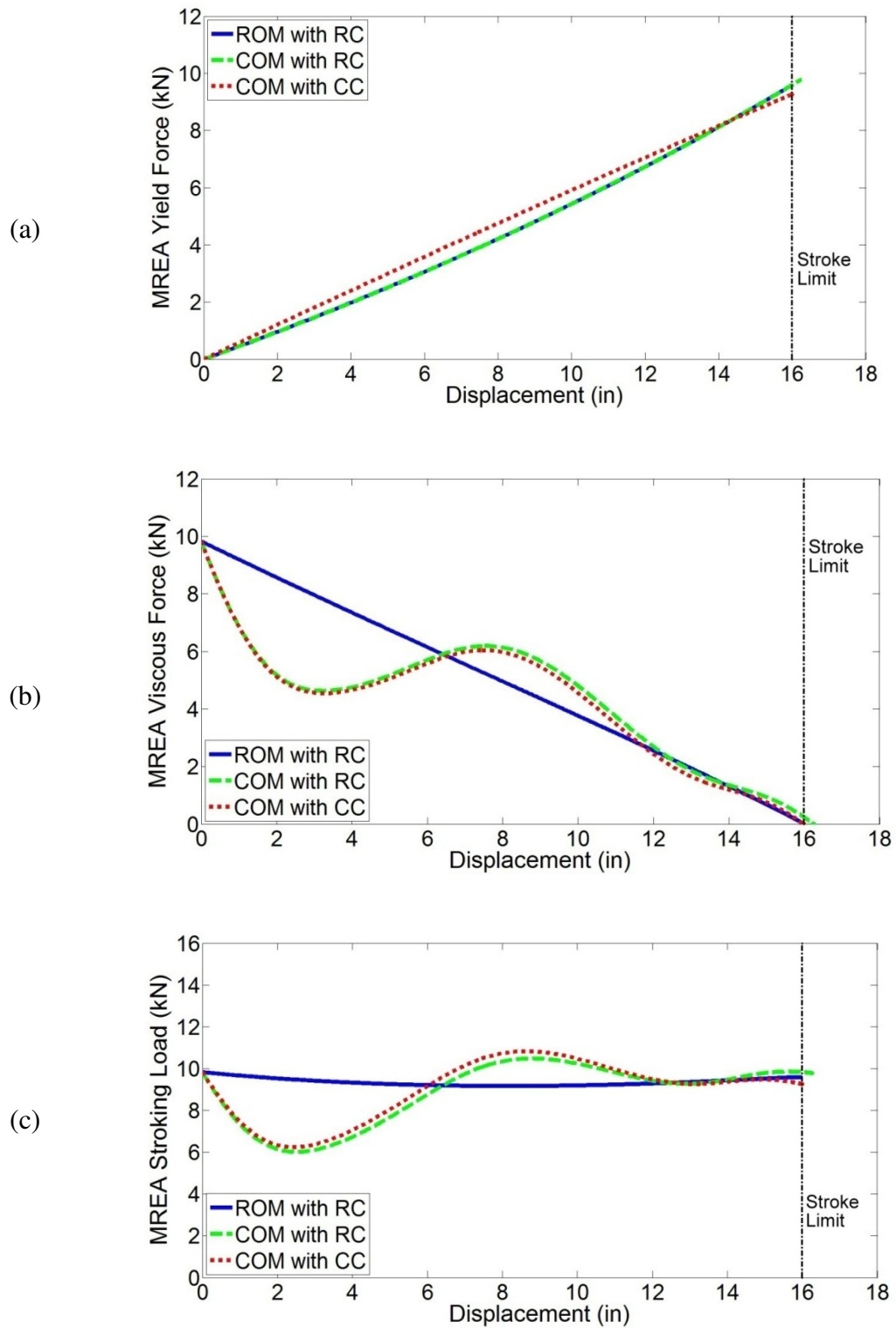
Figure 4.8. MREA (a) yield force, (b) viscous force and (c) stroking load corresponding to

sink rate of 10 m/s using optimal control.
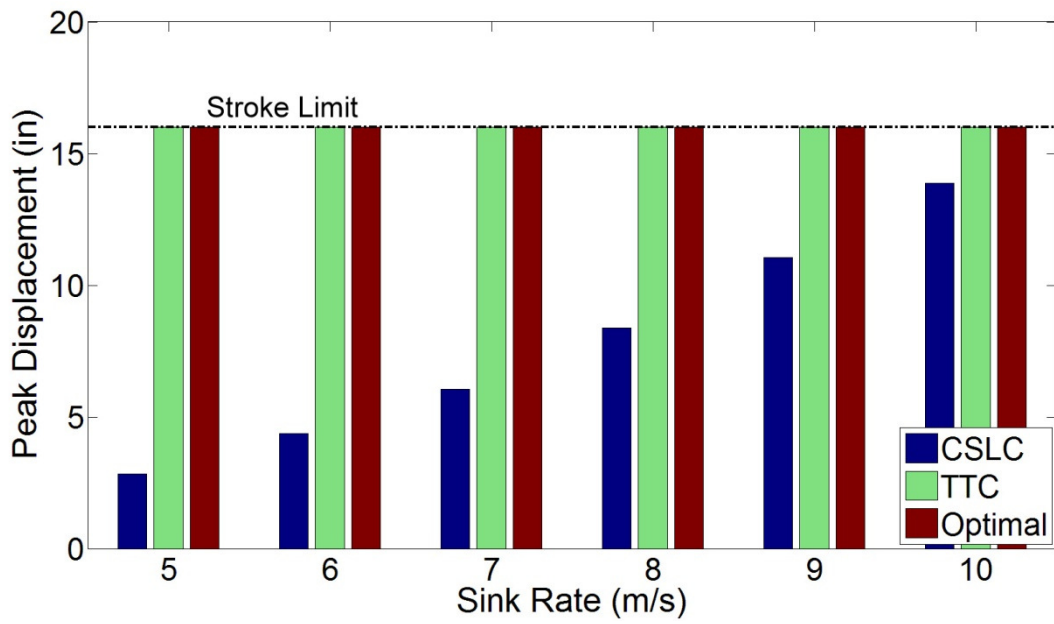
Figure 4.9. Peak seat pan displacement over the entire shock spectrum.

(a)

(b)

(c)

(d)
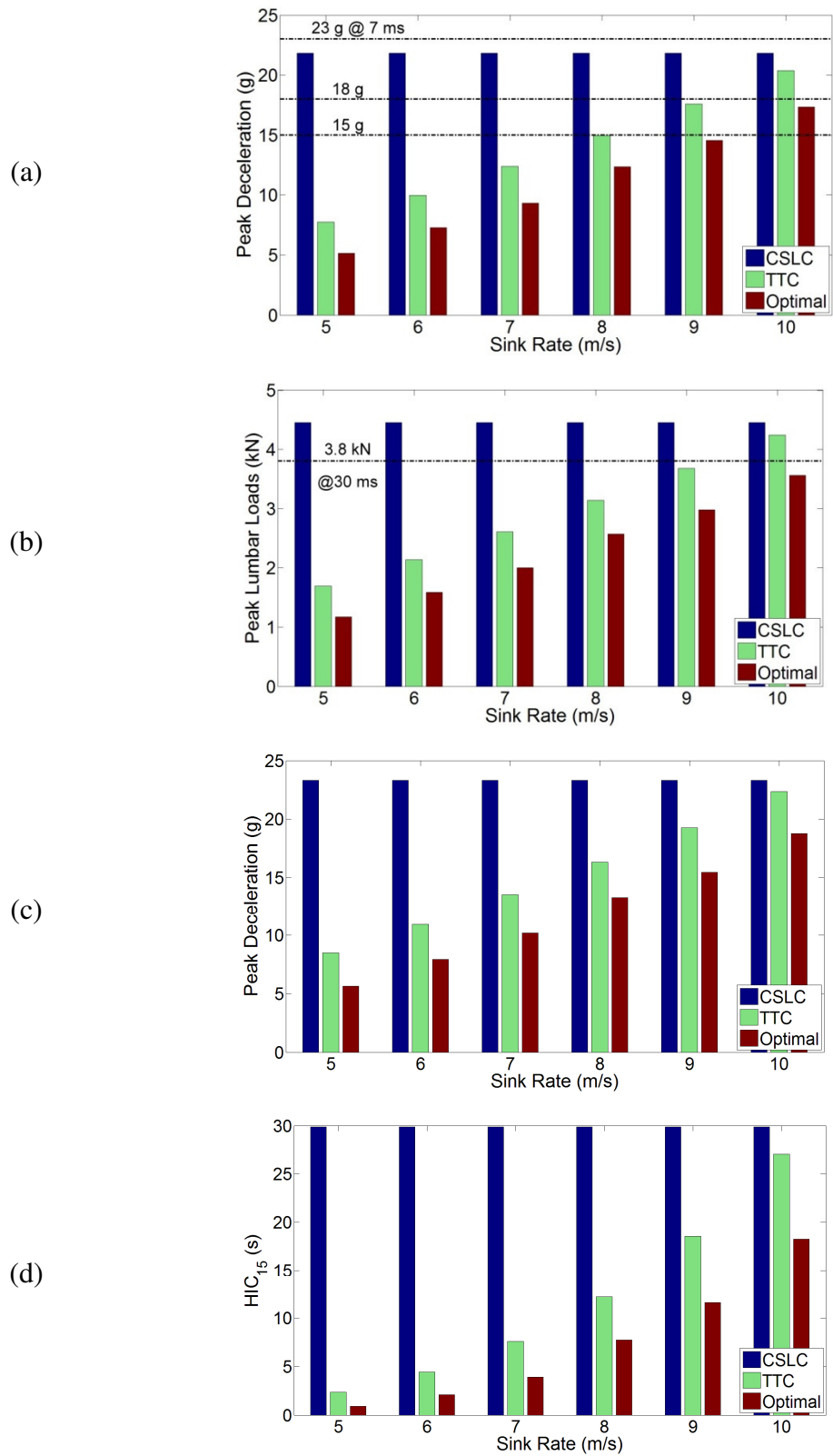
Figure 4.10. Peak biodynamic response for (a) pelvis, (b) lumbar spine, (c) chest and (d) head over the entire shock spectrum.

161
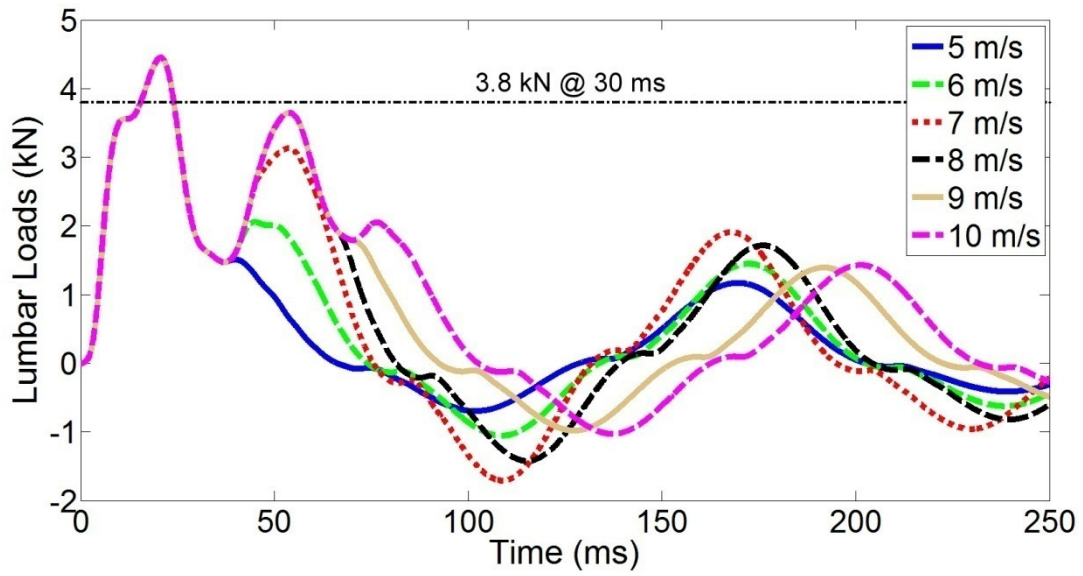
(a)
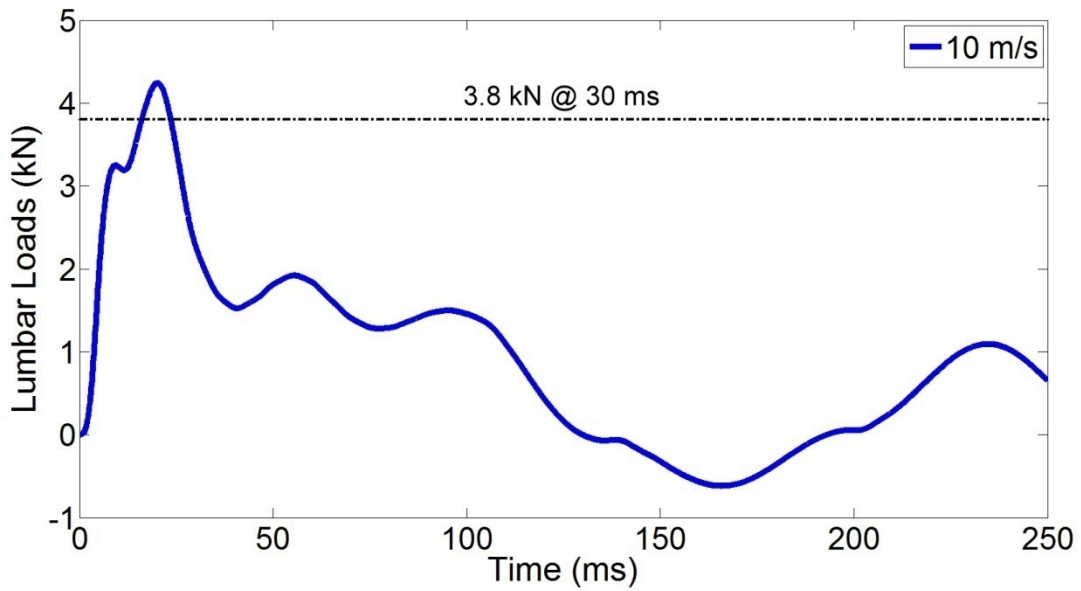
(b)

Figure 4.11. Time history of lumbar loads for (a) CSLC and (b) TTC.

Chapter 5

Control Schemes for Shock Mitigation

5.1.   Abstract

The effectiveness of three different control schemes for maximizing shock attenuation is evaluated in this study. The control schemes were based on regulating the stroking load of the magnetorheological energy absorber (MREA) that served as a shock absorption device. The first control scheme called constant stroking load control (CSLC) offered inflexible stroking load irrespective of varying shock intensity. The other two control schemes: terminal trajectory control (TTC) and optimal control (OC) adapted MREA stroking load as per the shock intensity. The control schemes were compared on the basis of their adaptability and ease of implementation to varying shock conditions. High-speed drop experiments were conducted by dropping two rigid payloads of 240 and 340 lb mass from heights of 35 and 60 inch to simulate different impact intensities.

5.2.   Introduction

Maximization of shock mitigation during intense impacts is a critical issue when designing a shock absorption system. The main goal of shock absorption system is to minimize the potential for damage to a rigid payload/electronics system

or body injuries to occupants seated in helicopters, automobiles, fast boats etc exposed to shock. Most shock mitigation systems utilize energy absorbers (EAs) such that the shock energy is dissipated and moderation of shock is achieved (Hiemenz *et al*., 2007; Rakheja *et al.* 1994; Swinbanks *et al*., 2005; Mao *et al*., 2014). Typically the energy absorbers are of passive nature and are designed for a narrow shock spectrum. In other words, the load stroke profile of passive energy absorbers are non-adaptive and for the same reason they are called fixed load energy absorbers (FLEAs) (Rakheja *et al*., 1994). For instance, FLEAs employed in crashworthy helicopter seats were designed for a 50th percentile male occupant even though the occupants belong to a wide range from a 5th percentile female to a 95th percentile male (Desjardins, 2003). Few mechanisms have been developed that add little flexibility in the load-stroke profile of passive EAs and those devices are called variable load energy absorbers (VLEAs) (Desjardins, 2003). In such devices, the load-stroke profile is manually adjusted a priori on the basis of predetermined shock conditions.

The passive EAs employ different shock mitigation concepts such as plastic deformation of material, hydraulic EAs etc. Energy absorption by crushing a tube or column made from aluminum or paper honeycomb is one simple but non-adaptive method for shock mitigation (Desjardins, 2003). Inversion tubes developed by General Motors Research Laboratories dissipated shock energy by inverting the metal tubing inside out under shock loads (Jackson *et* al., 2004; Kroell, 1962). The performance of inversion tubes is repeatable and reliable and applied to crashworthy seats of UH-60 Blackhawk (Desjardins, 2003). Similarly wire-bending is a

mechanism in which a metal wire is plastically deformed under impact by passing through series of rollers (Campbell, 1982). Trooper seats of installed in UH-60 Blackhawk use wire-bending shock mitigation mechanism. Metal cutting and slitting mechanisms using single point tool are also used as a shock absorption concept in landing gears (Desjardins, 2003). On the other hand, passive hydraulic EAs in which a piston pushes the fluid through a small channel (orifice) inside a hydraulic cylinder are a common application in automobiles for shock isolation. The variation in the load-stroke profile of a passive hydraulic EA can be achieved by integrating mechanical moving parts that change the orifice area. Hajihosseinloo *et al.* (1989) used such variable orifice area based hydraulic EA for minimization of gun recoil forces. Chen and Macagno (1979) analyzed the performance of hydraulic energy absorbers with variable orifice area mechanism that included the contribution of frictional forces.

The lack of adaptability of passive EAs led to the evolution of controllable or active EAs. An active seat suspension was developed by Swinbanks *et al*. (2005) for a marine platform with a look-ahead detection system. The look-ahead detection system had downward looking sensors for predicting the intensity of the shock. Active seat suspensions require large control authority and are mainly focused towards low-amplitude vibration isolation. Stein (1991) simulated electro-hydraulic active vibration control system (AVCS) for off-road vehicles. The AVCS system helped improve the vibration absorption as much as 3 times when compared with the passive seat suspensions but had a major drawback of large energy consumption.

Later on, Stein (1995) studied the electro-pneumatic active vibration control system (AVCS) that employed a pneumatic spring with transducers.

Seat suspensions employing semi-active devices such as magnetorheological energy absorbers (MREAs) combine features of both passive and active seat suspensions and deliver desirable performance (Mao *et al*., 2014; Choi and Wereley, 2005) as discussed in Chapter 2. The variable shock conditions can be easily accommodated by adapting the load-stroke profile of MREA. There exist various designs of MREA varying from simple (Hiemenz *et al.*, 2010) and easy to fabricate to more complicated designs (Bai *et al.,* 2012). An MREA is similar to a conventional passive EA in that a fluid is pushed through an orifice due to piston motion in a hydraulic cylinder (Cook *et al*., 2007; Mao *et al*., 2014). However, series of electro-magnets are installed in the piston of MREA that generate magnetic field when fed with current input. The magnetic field built by using electromagnets generates magnetic induction in the smart magnetorheological (MR) fluid that changes the apparent energy absorption capability of the MREA. MR fluids typically consisting of 0.3-10 micrometer diameter ferromagnetic particles suspended in carrier fluid (Guo *et al*., 2012, Hiemenz *et al*., 2007). Under magnetic field, the ferromagnetic particles form long chains and provide resistance to the fluid flow during shock events. The controllability of magnetic induction between iron particles provide adaptive load-stroke profile which can be manipulated electronically, rapidly and reversibly, therefore, making it suitable for varying shock conditions (Hiemenz *et al*., 2007; Mao *et al*., 2014). Furthermore, shock mitigation capacity of the MREA

can be enhanced by appropriately controlling the load-stroke profile (Wereley *et al.*, 2011; Singh and Wereley, 2013)

An MREA with a large load-stroke profile was designed, fabricated and tested in our prior work (Chapter 2). Under consideration are three different control schemes to evaluate shock mitigation performances: constant stroking load control (Desjardins, 2003; Desjardins *et al.*, 1989; Hiemenz *et al.*, 2007), terminal trajectory control (Wereley *et al.*, 2011) and optimal control. Drop experiments with varying shock intensities were conducted by dropping two different payload masses (240 and 340 lb) from two different drop heights (35 and 60 inch).

5.3.   Magnetorheological Energy Absorbers (MREAs)

A linear stroking MREA with a large dynamic range described in Chapter 2 served as a shock absorption device to study the effectiveness of different control schemes under impact conditions. MREA stroking load had two components: controllable yield force and passive viscous force. The yield force was adaptable by changing the current levels whereas passive viscous force was uncontrollable and were proportional to the piston velocities. The dynamic range of MREA is defined as the ratio of maximum achievable stroking load (i.e. stroking load at maximum current input) to the passive viscous force (Mao *et al.*, 2014). The dynamic range gives direct measure of effectiveness of adaptability of the MREA. In other words, it is desirable to achieve larger dynamic range at intense impact conditions.

$$DR = \frac{F_D}{F_V} = \frac{F_V + F_{MR}}{F_V} = 1 + \frac{F_{MR}}{F_V} \qquad (5.1)$$

where F_D is the MREA stroking load, F_V is the passive viscous force and F_{MR} is the controllable yield force.

Under these considerations, an MREA was designed, fabricated and tested for a dynamic range of 1.73 at piston velocity of 8 m/s in our earlier work (Chapter 2). A modified analytical Bingham-plastic model incorporating minor losses (BPM model) was implemented to estimate the MREA controllable yield force and viscous force. Computational fluid dynamics (CFD) studies and magnetic finite element analysis were conducted to verify the modified BPM model estimations followed by fabrication. The piston of MREA with 5 electromagnetic coils covered with insulating epoxy and fully assembled MREA are shown in Figure 2.16. Subsequent low-speed cyclic experiments were conducted on hydraulically powered MTS machine for different current inputs varying form 0-5.5 A. Increased current inputs generated increased MREA yield forces. High-speed experiments at zero-field (0 A) were also conducted to attain high piston velocities using 12 ft high drop tower in the Department of Aerospace Engineering at the University of Maryland.

The controllable MREA yield force variation with current input and passive viscous force variation with piston velocity are shown in Figure 2.23b and 2.25 respectively. The variation of MREA viscous force with piston velocity was quadratic in nature. For the sake of implementation of viscous force model into the control algorithms a quadratic curve was fitted to the experimental observations as given by the following equation:

$$F_V = 176.9\,V_P^2 + 429.6\,V_P \qquad\qquad (5.2)$$

where V_P is the piston velocity.

Similar quadratic estimation of the experiment based MREA yield force dependent on current input, I, was also carried out for the ease of implementation in the control algorithm.

$$F_{MR} = -129.9\,I^2 + 2856.1\,I$$

$$(5.3)$$

A complete MREA load-stroke profile was obtained when viscous and yield forces were combined together. In other words, a load-stroke profile delineates the performance of MREA at different piston velocities and current inputs as shown in Figure 2.26.

5.4. Testing Set-up

Three control schemes were implemented by conducting series of tests on MREA using the 12 ft tall high-speed drop test facility at the University of Maryland as shown in Figure 2.21a. The drop test facility comprised a carriage on which drop-weights/payload were installed and dropped from different heights to obtain varying impact conditions. The MREA set-up on the drop test facility is shown in detail in Figure 2.21b. MREA was mounted on the load cell installed on a base plate. At the other end of the shaft, a crown stand was mounted where either a thin honeycomb or a rubber pad was placed to avoid metal-to-metal contact that may cause ringing in the load cell. A linear variable differential transformer (LVDT) was installed on one side of the MREA to measure displacement and velocity of the piston. Two different

payloads of 240 and 340 lb were dropped from two different heights of 35 and 60 inch with MREA stroke limited to 10 inch because of maximum LVDT displacement measurement of 10 inch. However, the stroke utilization was restricted to 7 inch with safety margin of 3 inch. The test matrix is presented in Table 5.1. The accumulator of MREA was pressurized with compressed nitrogen gas to 450 psi in order to accommodate the volume change due to shaft motion inside the hydraulic cylinder under impact.

Experimental data using load cell and LVDT were recorded at a sampling rate of 2 kHz. Corresponding piston velocities were obtained by differentiating the LVDT data using data acquisition system. During the post processing, the recorded data were filtered by using CFC 60 (100 Hz cut-off frequency) for load cell and CFC 180 (300 Hz cut-off frequency) for LVDT (Huang, 2002).

5.5.   Controllers

Two control approaches were employed for the control schemes under consideration. Closed-loop approach was based on force-feedback and open-loop approach was based on pre-determined shock conditions.

5.5.1. Closed-Loop Approach

The closed-loop approach with force-feedback was implemented in order to achieve desirable and controllable performance of MREA. During the shock event, the MREA stroking load had to be adjusted as per the requirements. MREA stroking load comprised of two components: controllable yield force and uncontrollable viscous force as described earlier. Therefore, in order to tune the MREA to a particular stroking load, the yield force had to be precisely adjusted. The force-

170

feedback control approach is presented in Figure 5.1. The desirable MREA stroking load governed the predetermined current, I_{PRE}. Measured MREA stroking load was obtained from the load cell and then compared with the desired MREA stroking load. On the basis of comparison, the command current from the controller, I_{CMD}, was adjusted. The gains G_1 and G_2 were given values of 0.75 and 1.5 respectively.

5.5.2. Open-Loop Approach

The current inputs required for achieving desirable goals were estimated by modeling a single degree-of-freedom system shown in Figure 5.2a. The shock was represented as an initial velocity impact similar to studies conducted by Wereley *et al*. (2011). The initial velocity was determined by taking into consideration the drop height of the payload and energy dissipated by the honeycomb placed on the crown stand as shown in Figure 5.2b. The initial drop velocity was proportional to drop height, H. Assuming 10% reduction in velocity due to friction in carriage system such as drop mass rolling on the rail guides, the velocity is obtained as

$$v_i = 0.9\sqrt{2gH} \tag{5.4}$$

The kinetic energy of the drop mass, m, based on the initial velocity is obtained as

$$K.E. = \frac{1}{2}mv_i^2 \tag{5.5}$$

The energy dissipated by the honeycomb was estimated as

$$E_D^{HC} = P^{HC}V^{HC} \tag{5.6}$$

where P^{HC} and V^{HC} represent compressive strength and crushed volume (cross-section area multiplied by crush height) of honeycomb. The leftover energy was dissipated by MREA and corresponding impact velocity was obtained.

$$E_D^{MREA} = K.E. - E_D^{HC} \tag{5.7}$$

$$v_0 = \sqrt{\frac{2E_D^{MREA}}{m}} \tag{5.8}$$

Once the initial velocity was determined, the governing equation of motion for the payload subjected to initial conditions was solved.

$$m\ddot{z}_0(t) = -F_D sgn(\dot{z}_0(t)) - mg \tag{5.9}$$

$$z_0(0) = 0; \ \dot{z}_0(0) = -v_0 \tag{5.10}$$

A fixed point iteration algorithm was implemented with a MREA stroke of S=7 inch and required MREA yield forces were obtained (Wereley *et al.*, 2011). The required yield forces were converted into respective current values using the relation given by Eq. (5.3) and used as an input to the MREA.

5.6.   Constant Stroking Load Control

A constant stroking load control approach for shock mitigation was employed based on dynamic limit load of an energy absorber. Various existing crashworthy seats have employed such shock mitigation scheme (Desjardins, 2003) using different operating mechanisms such as plastic deformation of inversion tubes (Jackson *et al.*, 2004), wire-benders, metal cutters etc. The plastic deformation or cutting of metal under impact dissipates the shock energy. Such mechanisms are simple in operation and do not require any controller because of their passive nature. The major disadvantage of these concepts is their lack of adaptability for varying payload weight and impact conditions. In other words, no matter what the shock conditions or the payload weights are, these crashworthy concepts provide a constant stroking load to the payload.

Generally, the dynamic limit load was determined based on the maximum permissible vertical load the occupant/payload could endure during the impact, i.e. the total stroking force of energy absorber and frictional forces in the seat suspension. A limit load factor of $14.5g$ was selected for sizing the energy absorber for a 50th percentile male (Desjardins, 2003) for helicopter seat suspensions. In other words, the total force of energy absorber was designed not to exceed 14.5 times the effective weight (80% of total weight plus the seat pan weight) of 50th percentile male subjected to a crash condition (Desjardins *et al.*, 1989; Hiemenz *et al.*, 2007). Similar limited load approach was employed for evaluating performance of constant stroking load scheme with stroking load tuned to a 5th percentile female (120 lbs) with seat pan weight of 50 lbs.

$$F_{D_L} = 14.5g\left(0.8M_{5th} + M_{seat}\right) = 9.44 \text{ kN} \qquad (5.11)$$

Since, the MREA force had two components, i.e. passive viscous force and controllable yield force, the lack of control authority over passive viscous force led to the variation of MREA yield force as follows:

$$F_{MR} = F_{D_L} - F_V \qquad (5.12)$$

The feedback to determine the variation of current input and corresponding MREA yield force for CSLC was based on force feedback algorithm as described earlier.

5.6.1. Payload Response

The load cell forces for different shock conditions are presented in Figure 5.3a. As can be seen, the peak stroking load maintained a threshold of $14.5g$ whether it was a low impact (240 lb at 35 inch) or high impact condition (340 lb at 60 inch). Since the kinetic energy increased with either increase in payload or drop height, the stroking load pulse became wider for intense shocks while maintaining the same stroking threshold. During the shock, the kinetic energy of the payload was dissipated via MREA stroking load and MREA stroke was utilized. Increased stroke utilization was observed to accommodate increased kinetic energy as shown in Figure 5.3b. For low intensity case of 240 lb payload dropped from 35 inch height, the stroke utilized was around 1.26 inch. Such an outcome showed that the shock absorption system was too rigid for low intensity case. As the shock intensity increased, the stroke utilization also increased significantly with about 7.37 inch

stroke utilized for highest impact condition with 340 lb payload with 60 inch drop height. The usage of MREA stroke for 240 lb at 60 inch drop height and 340 lb at 35 inch height was almost similar showing that kinetic energy or the shock intensity for these two cases were almost of the same order.

Increased shock intensity also led to increase in piston velocity as can be seen in Figure 5.3c. As the velocity increased, the passive viscous forces dependent on velocity in a nonlinear fashion also increased. Increased viscous forces determined lower MREA yield forces and the corresponding current input for a constant limit load threshold as per Eq. (5.12). The current input from the controller is presented in Figure 5.3d. The larger the magnitudes of piston velocity, larger current drops were observed.

5.7.   Terminal Trajectory Control

The second control approach based on terminal trajectory control (TTC) was implemented with the goal of maximizing shock attenuation by adopting two key goals (Singh and Wereley, 2013; Wereley *et al*., 2011). The first goal was to utilize the available MREA stroke completely such that the kinetic energy of the payload was dissipated over the entire stroke. The second goal was to avoid intense end-stop impacts, i.e. the condition when the energy absorber runs out of its stroke and transmits large impact loads to the payload. In order to achieve these goals and to maintain soft landing, the MREA stroking load should be adapted according to the impact severity. The optimal MREA yield force should be controlled in a manner to satisfy the terminal conditions given as:

$$z_0(t_s) = -S \; ; \; \dot{z}_0(t_s) = 0 \tag{5.13}$$

where t_s is the stoppage time when the payload comes to rest and MREA available

stroke, S, was limited to 7 inch.

The simplicity of this approach was based on the fact that a constant MREA

yield force could achieve the terminal trajectory goals. In other words, the MREA

yield force was tuned to a constant value throughout the impact. One major

advantage of TTC over CSLC was its open-loop control, i.e. no feedback was

required since the current input was predetermined based on the known impact

conditions.

5.7.1. Payload Response

The time histories of stroking loads for different shock conditions for a

terminal trajectory control (TTC) are plotted in Figure 5.4a. Unlike the inflexible

stroking load offered by CSLC, the stroking load adapted according to the shock

intensity. In other words, the peak stroking load for low intensity shock with 240 lb

dropped from 35 inch height was lower when compared to high intensity shock with

340 lb dropped from 60 inch height. The biggest constraint on TTC was the stroke

utilization of $S= 7$ inch. So with increased kinetic energy, the stroking load had to be

adapted to increased levels to confine the payload within 7 inch of MREA stroke.

The adaptation of stroking load led to almost same stroking load pulse duration for

different shock intensities unlike CSLC. When comparing the stroking load

responses from CSLC and TTC, it can be easily observed that CSLC response was

characterized with chatter whereas the TTC response was relatively smooth. The

main reason behind such an outcome was open-loop algorithm for TTC that did not require any feedback and eliminated time delay between the command current and magnetic field build up in the electromagnet.

The displacements plot presented in Figure 5.4b show that the stroke utilized varied between 6-7.3 inch with varying shock conditions. The variation in the stroke utilized could have been reduced with accurate prediction of energy dissipated by the honeycomb. When comparing with TTC, CSLC based non-adaptive stroking load led to large variation in the stroke utilized because even for low intensity shock the stroking load was tuned to a large value. Figure 5.4c shows the piston velocities that increased with increase in shock intensities.

The current input were tuned to a constant value for a given shock condition but increased as the shock intensity increased by either incrementing payload weight or drop height. Since the increased kinetic energy of the payload necessitated large MREA yield force (controllable force) the required current levels increased. The current input for 240 lb at 60 inch was same as for 340 lb at 35 inch concluding that the shock intensity was almost identical. This is similar to what was observed earlier with almost same stroke utilization under fixed stroking load for CSLC.

5.8. Optimal Control

The seat pan was subjected to a constant MREA stroking load with CSLC approach and, therefore, there was a flat onset of MREA force from the beginning of the impact till the end. However, such an approach did not govern full stroke utilization that resulted in minimizing the energy dissipation per unit stroke. On the other hand, an open-loop TTC provided a constant MREA yield force throughout the

177

operation such that the available stroke was fully utilized. A third control scheme, hybrid of CSLC and TTC called optimal control, was developed in order to investigate if the shock mitigation performance could be enhanced.

The optimal control scheme should satisfy the terminal conditions as describer earlier for TTC while maintaining a constant stroking load threshold like CSLC. However, the constant stroking load threshold was adaptive and not fixed to $14.5g$. In other words, a g-level of constant stroking load threshold was adapted such that terminal conditions for smooth landing were achieved.

$$F_D = \Gamma g\left(0.8M_{5th} + M_{seat}\right) \qquad (5.14)$$

where Γ is the threshold level.

The optimal control also employed a force feedback closed-loop approach similar to CSLC.

5.8.1. Stroking Threshold Estimation

The energy dissipated by the MREA was obtained as per Eq. (5.7). Since the shock energy was required to be expended over a given MREA stroke, S, the energy dissipated by MREA is simply the product of stroking load and stroke utilized. The MREA limit load and stroking threshold were estimated as

$$F_D = \frac{E_D^{MREA}}{S} \qquad (5.15)$$

$$\Gamma = \frac{F_D}{g\left(0.8M_{5th} + M_{seat}\right)} \qquad (5.16)$$

5.8.2. Payload Response

Similar to CSLC and TTC, the stroking load time histories are plotted in Figure 5.5a for different shock intensities. The stroking loads were adapted according to the intensity of shock similar to TTC. The optimal control (OC) technique employed force feedback to maintain a constant stroking load threshold and experienced large chatter similar to CSLC response. The stroking load pulse durations were of the same order due to good adaptability of stroking load for varying shock conditions. Overall, the stroking load response by implementing OC was hybrid of CSLC (constant stroking load with large chatter) and TTC (adaptive stroking load).

MREA strokes utilized presented in Figure 5.5b were also within 6-8 inch for varying shock intensities similar to TTC. Adaptive stroking load was the main reason for utilizing almost same strokes under different impacts. A better estimation of energy dissipated by honeycomb could reduce the variation of stroke utilized. The piston velocities also show increased magnitudes with shock intensities in Figure 5.5c.

The variation in current input also depicted hybrid nature of OC as shown in Figure 5.5d. The current input also had sharp troughs corresponding increased piston velocities building high viscous forces and chatter like CSLC. In addition, the initial current level at $t = 0$ ms was adapted based on shock intensity similar to TTC. The current inputs for 240 lb at 60 inch and 340 lb at 35 inch were almost similar and corroborate the observations of same kinetic energy as explained for CSLC and TTC.

5.9. Comparison of Control Schemes

The three control schemes for shock mitigation are compared in this section for two extreme shock conditions: low intensity shock (240 lb at 35 inch) and high intensity shock (340 lb at 60 inch). The control schemes differed in their nature of operation with CSLC providing non-adaptable stroking load tuned to $14.5g$ threshold irrespective of shock intensity being low or high. TTC and OC adapted the stroking load based on the shock intensity employing open-loop and force feedback based closed-loop algorithm respectively.

The stroking loads and piston displacements for low intensity shock are plotted in Figure 5.6. The kinetic energy of payload of 240 lb dropped from 35 inch height was same for all the control schemes. The kinetic energy was dissipated over MREA stroke, therefore the product of stroking load with MREA stroke provided a rough estimate of the kinetic energy. The stroking load offered by CSLC was too high for low intensity shock and resulted in corresponding smaller stroke utilization of 1.26 inch. On the other hand, TTC and OC adapted the stroking load based on low impact conditions and therefore resulted in larger stroke utilization of around 6 inch for a particular kinetic energy of payload. Both TTC and OC provided almost similar response because of their adaptability. OC had a noisy response compared to TTC because of force-feedback. For a low intensity shock, TTC and OC performed better than CSLC because of low load transmissions to the payload.

The performance of all control schemes was comparable for the highest shock intensity corresponding to drop mass of 340 lb at 60 inch as presented in Figure 5.7. The stroking loads providing resistance to the payload motion were

180

similar for CSLC, TTC and OC with TTC providing chatter-free response. Since TTC and OC provided best response for a given shock condition and a similar CSLC response meant that CSLC was operating at its best condition. In other words, the designed operating condition of CSLC was corresponding to high shock intensity. Furthermore, such particular behavior shows that TTC and OC are capable of mimicking CSLC as well for extreme shock conditions. The MREA strokes utilized were also of the same order as shown in Figure 5.7. The loads transmitted to the payload using TTC and OC could have been reduced if the constrained available MREA stroke was relaxed to larger than 7 inch. In summary, all control schemes performed likewise with MREA stroke limited to 7 inch for high intensity shocks.

5.10. MREA Model Validation

MREA models for viscous force and yield force as given by Eqs. (5.2) and (5.3) were validated with respect to experiments. The experimental current inputs and piston velocities were utilized to determine MREA yield force and viscous force respectively. Both these components add up to determine the total stroking load of the MREA given by following equation.

$$F_D = (F_V + F_{MR})\|\tanh(\Psi V_P)\| \tag{5.17}$$

The hyperbolic tangent function was modeled in order to replicate the real system such that when there was no motion (stationary MREA piston), the load cell registered zero compressive force. The parameter Ψ was a constant and given a large value to estimate the MREA force magnitude accurately.

The model validation was conducted for all three control schemes for low (240 lb at 35 inch) and high (340 lb at 60 inch) intensity shock conditions. It can be

181

observed in Figures 5.8-5.10 that for all the control schemes at any given shock condition, the model predicted the stroking load with a significant delay for the initial phase of stroking load pulse. This is due to the fact that honeycomb placed on the crown stand was crushed initially before MREA got compressed under impact. Therefore, the load cell recorded the compressive force for the initial moments of honeycomb crushing when MREA piston had negligible velocity (negligible viscous force). The MREA model incorporated only the viscous and yield force and did not predict honeycomb crushing leading to such a delay. Quantitative comparison between experimental and model based stroking loads was carried out on the basis of three metrics: energy dissipation, peak MREA loads and stroking load pulse duration. The energy dissipated by MREA was obtained as

$$E_D^{MREA} = \int_0^{t_s} F_D \, dz_0(t)$$

(5.18)

The percentage errors for every shock condition and control scheme are plotted in Figure 5.11. The error values for any function were obtained as

$$er(fn) = \left\| \frac{fn - \widehat{fn}}{\widehat{fn}} \right\|$$

(5.19)

The quantity ($\widehat{}$) represents experimental observation. For any error metric, the percentage errors were generally under 20% with a few outliers. Therefore, it can be concluded that MREA viscous and yield force models predicted experiments with reasonable accuracy on the basis of these observations.

5.11. Conclusions

Three control schemes for shock mitigation: constant stroking load control (CSLC), terminal trajectory control (TTC) and optimal control (OC) were studied for varying shock conditions. The shock intensities were varied by dropping different payload masses from different drop heights. Two payloads of 240 and 340 lb were dropped from height of 35 and 60 inch using a vertical drop test facility.

CSLC was tuned to $14.5g$ stroking load threshold of 5th percentile female irrespective of the shock intensity. Such inflexible stroking load led to poor shock attenuation at low impacts since the stroking load was relatively high compared to the kinetic energy of the payload. Force feedback closed loop algorithm was implemented and resulted in noisy response.

On the other hand, TTC and OC adapted the MREA stroking load according to the shock intensity. In other words, lower MREA resistance was offered to payload at low intensities. The MREA stroke utilized varied between 6-8 inch for TTC and OC. Also, TTC and OC emulated CSLC for intense impact of 340 lb dropped from 60 inch height. Compared to OC implementing force feedback, TTC experienced a noise-free response because of open-loop algorithm.

MREA viscous and yield force models were validated against the experiments for all control schemes. Honeycomb placed on the crown stand of MREA eliminated ringing in the load cell but led to a time delay in model-based response in comparison with experiments. The comparison was carried out on the basis of three characteristics: energy dissipated, peak MREA loads and stroking load pulse duration. Overall, the errors were well within 20% with a few outliers.

References

Bai X-X, Wereley N M, Hu W and Wang D-H, 2012 A Bidirectional Controllable Magnetorheological Energy Absorber for Shock and Vibration Isolation Systems *ASME Conference on SMASIS* doi:10.1115/SMASIS2012-8250

Campbell R F 1982 Vehicle Crashworthy Seat *US Patent* 4,358,154.

Chen C J, and Macagno E O, 1979, Fluid and thermodynamic characteristics of compressible recoil mechanisms Report DAAG 29-78-G-0120, US Army Research Office by Energy Division, Iowa Institute of Hydraulic Research, Iowa University.

Choi Y T and Wereley N M 2005 Mitigation of Biodynamic Response to Vibratory and Blast-induced Shock Loads Using Magnetorheological Seat Suspensions *Proc. IMechE Part D: Journal of Automobile Engineering*, Vol. 219, pp. 741-753.

Cook E, Hu W and Wereley N M 2007 Magnetorheological Bypass Damper Exploiting Flow Through a Porous Channel *Journal of Intelligent Material Systems and Structures,* Vol. 18, No. 12, pp. 1197-1203.

Desjardins S P, Zimmerman R E, Bolukbasi A O and Merritt N A 1989 Aircraft Crash Survival Design Guide *Aviation Applied Technology Directorate*, USAAVSCOM TR 89-D-22D, Fort Eustis, VA.

Desjardins S P 2003 The Evolution of Energy Absorption Systems for Crashworthy Helicopter Seats *59th Annual AHS Forum*, Phoenix, AZ, May 6-8.

Guo C, Gong X, Xuan S, Zong L and Peng C 2012 Normal Forces of Magnetorheological Fluids Under Oscillatory Shear *Journal of Magnetism and Magnetic Materials,* Vol. 324, No. 6, pp. 1218-1224.

Hajihosseinloo M A, Hooke CJ, and Walton D 1989 Gun recoil system performance-measurement and prediction*Proc. IMechE Part C: J. Mech. Eng. Sci.*, Vol. 203, pp. 85-92.

Hiemenz G J, Choi Y T and Wereley N M 2007 Semi-Active Control of Vertical Stroking Helicopter Crew Seat for Enhanced Crashworthiness *AIAA Journal of Aircraft*, Vol. 44, No. 3, pp. 1031-1034.

Hiemenz G J, Hu W, Ngatu G, and Wereley N M, 2010, Rotary vane magnetorheological energy absorber U.S. Patent US2010/0300819 A1.

Huang M, 2002, Vehicle crash mechanics *CRC Press*, Dearborn, MI.

Jackson K E, Fasanella E L, Boitnott R, McEntire J, and Lewis A, 2004 Occupant Responses in a Full-Scale Crash Test of the Sikorsky ACAP Helicopter *Journal of the American Helicopter Society*, Vol. 49, No. 2, pp. 127-139.

Kroell C K 1962 A Simple, Efficient, One Shot Energy Absorber *Bulletin No. 30, Shock, Vibration and Associated Environments, Part III, General Motors Research Laboratory*, Warren, MI

Mao M, Hu W, Choi Y T, Wereley N M, Browne A L, and Ulicny J, 2014, Experimental validation of a magnetorheological energy absorber design analysis, *Journal of Intelligent Material Systems and Structures*, 25(3):352-363.

Rakheja S, Afework Y and Sankar S 1994 An Analytical and Experimental Investigation of the Driver Seat Suspension System *Vehicle System Dynamics*, Vol. 23, No. 3, pp. 501-524.

Singh H J and Wereley N M 2013 Adaptive Magnetorheological Shock Isolation Mounts for Drop-induced Impacts *Smart Materials and Structures*, Vol. 22, 122001.

Stein G J 1991 Active Vibration Control System for the Drivers Seat for Off-road Vehicles *Vehicle System Dynamics,* Vol. 20, No. 2, pp. 57-78.

Stein G J 1995 Results of Investigation of an Electropneumatic Active Vibration Control System for a Drivers Seat *Proceedings IMechE Part D: Journal of Automobile Engineering,* Vol. 209, No. 3, pp. 227-234.

Swinbanks M A, Simon D E, Holford J M and Napoletano JR. F M 2005 Active Suspension for a Marine Platform *US Patent Application Publication* US 2005/0278094 A1

Wereley N M, Choi Y T and Singh H J 2011 Adaptive Energy Absorbers for Drop-Induced Shock Mitigation *Journal of Intelligent Material Systems and Structures,* Vol. 22, No. 6, pp. 515-519.

Table 5.1. Drop test matrix for each control scheme

Drop Height (inch)	Drop Mass (lb)	
	240	340
35	x	x
60	x	x
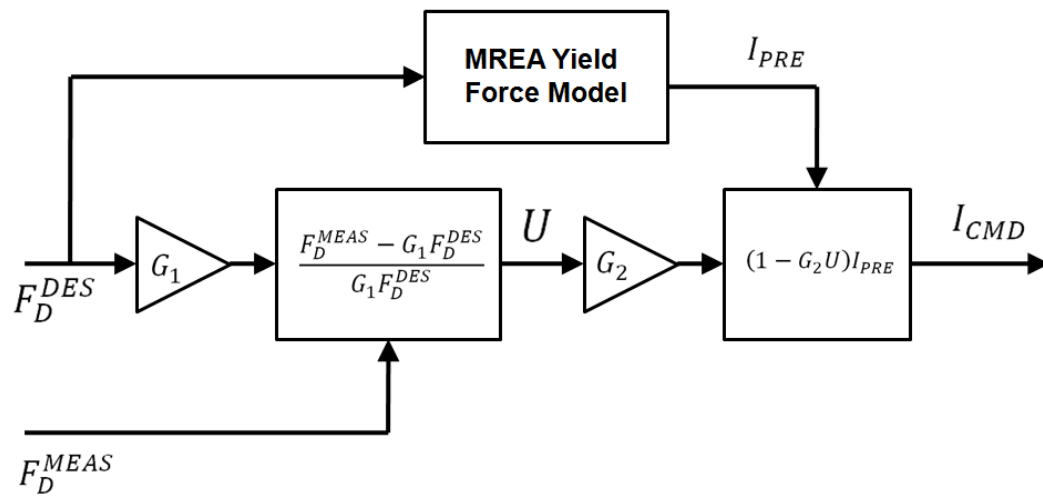
Figure 5.1. Force feedback closed-loop algorithm.
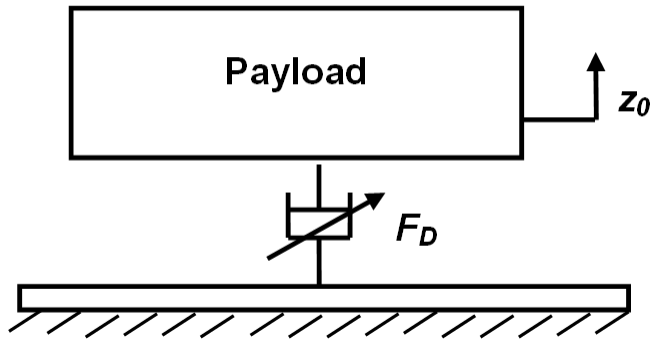
(a)
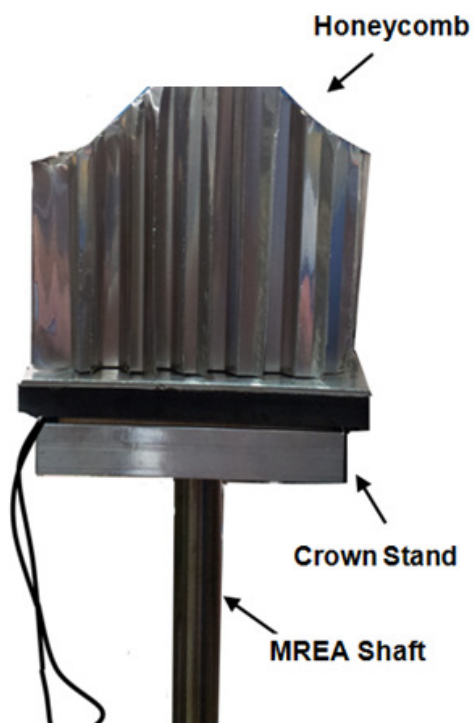
(b)

Figure 5.2. Schematic of (a) single-DOF model and (b) honeycomb placed on crown stand of MREA to avoid ringing in load cell.

(a)

(b)

(c)

(d)
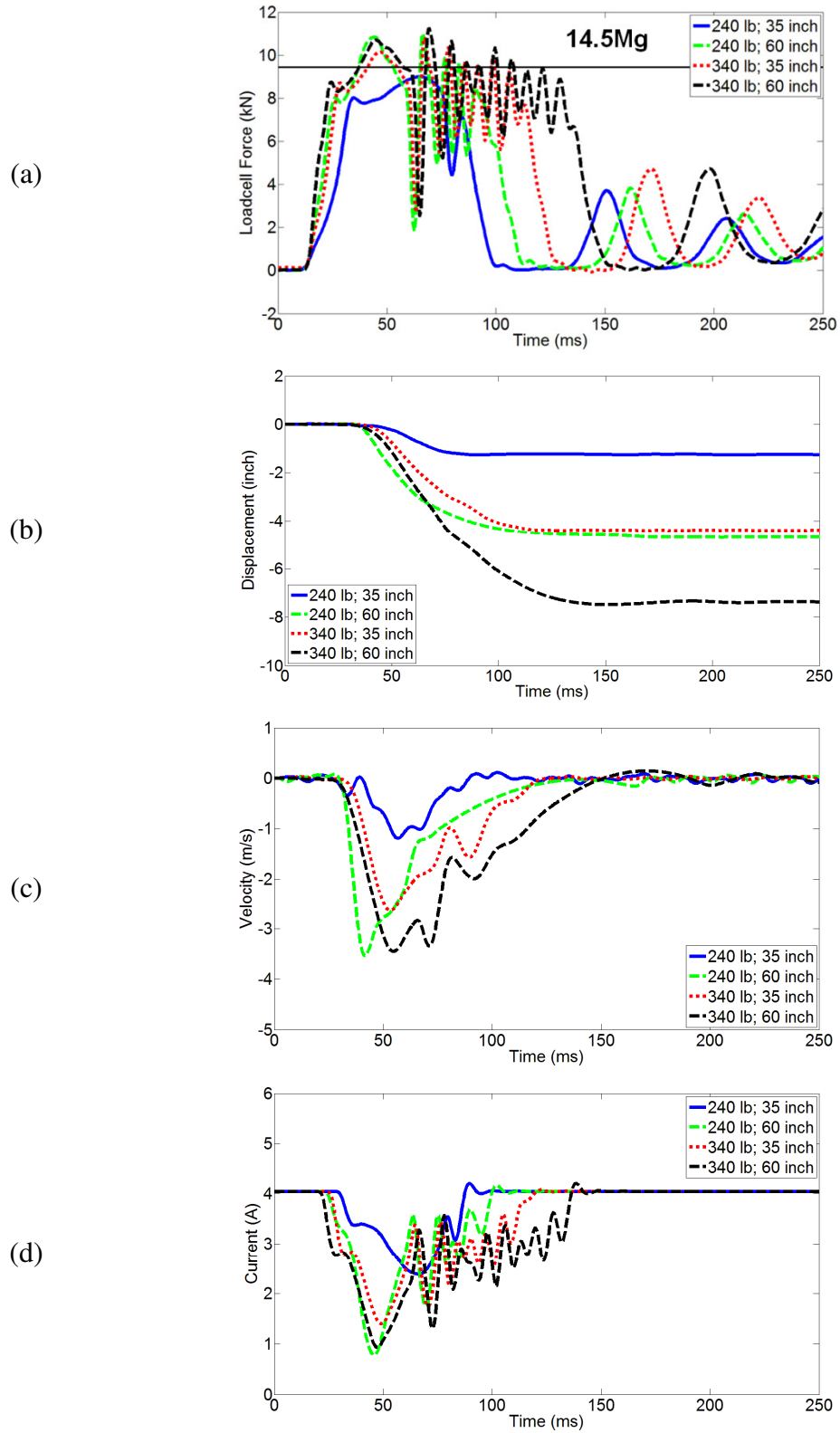
Figure 5.3. Constant stroking load control (CSLC) based (a) load cell force, (b) piston displacement, (c) piston velocity and (d) current input.

(a)

(b)

(c)

(d)
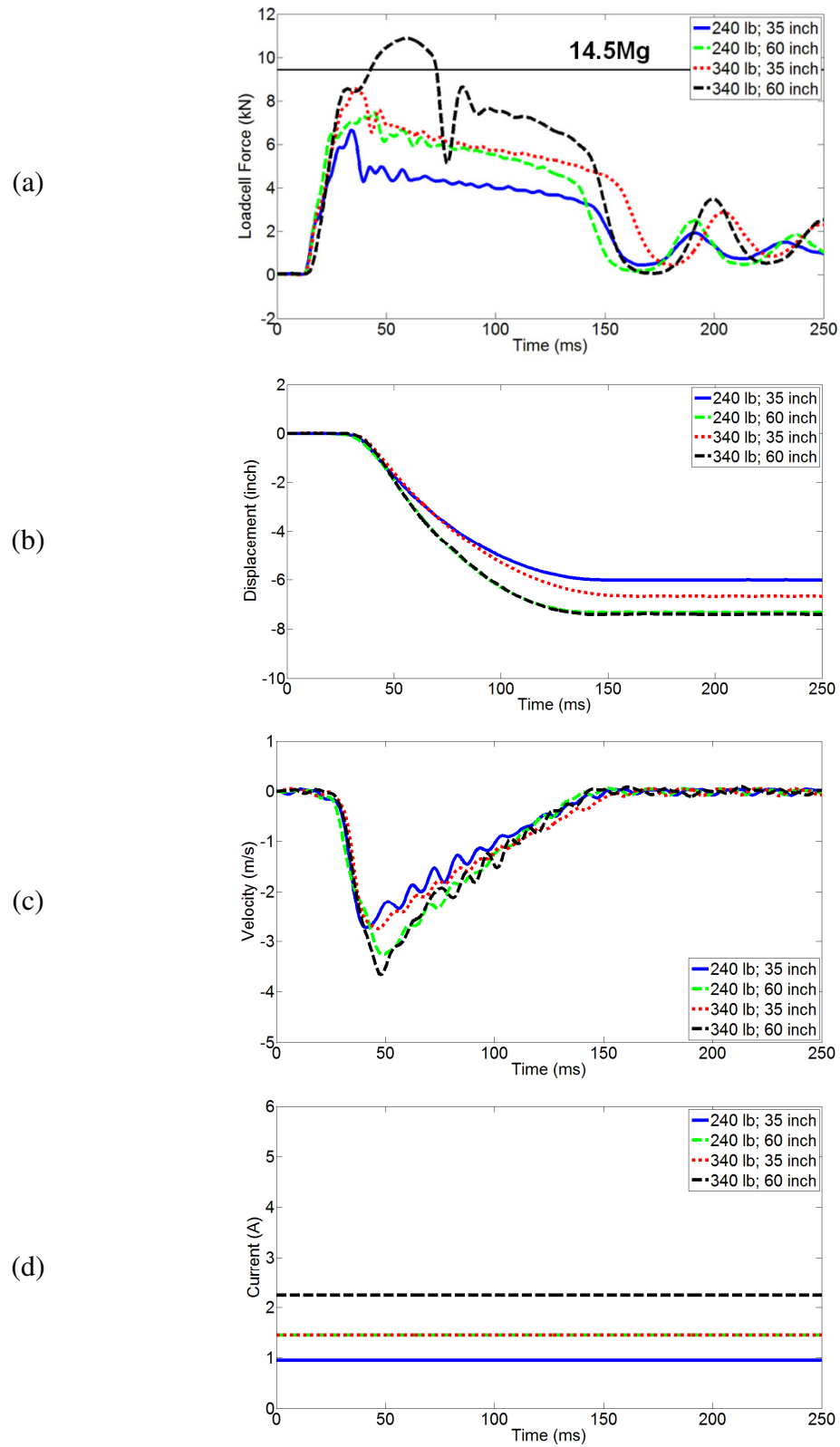
Figure 5.4. Terminal trajectory control (TTC) based (a) load cell force, (b) piston displacement, (c) piston velocity and (d) current input.

(a)

(b)

(c)

(d)
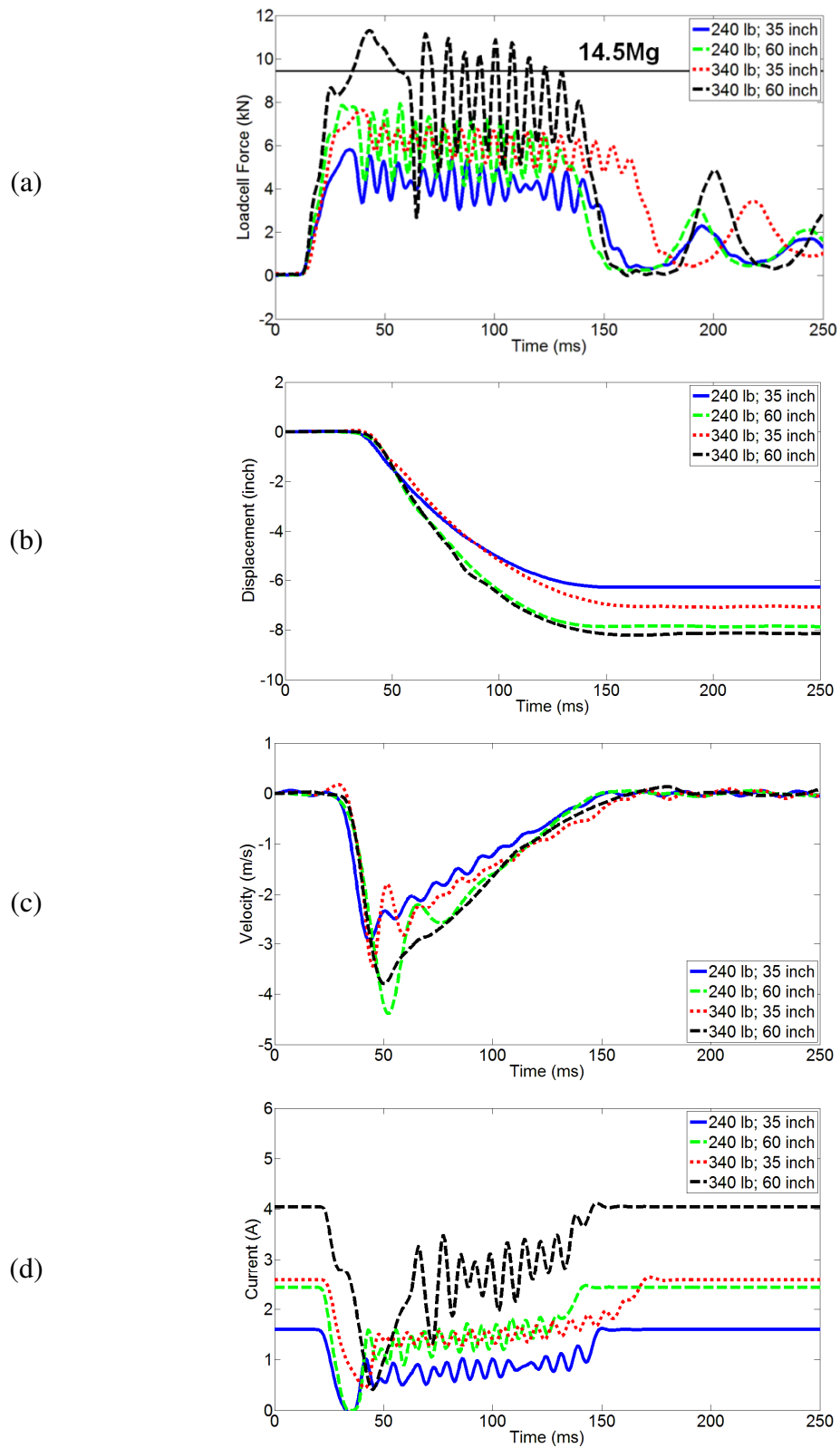
Figure 5.5. Optimal control (OC) based (a) load cell force, (b) piston displacement, (c) piston velocity and (d) current input.
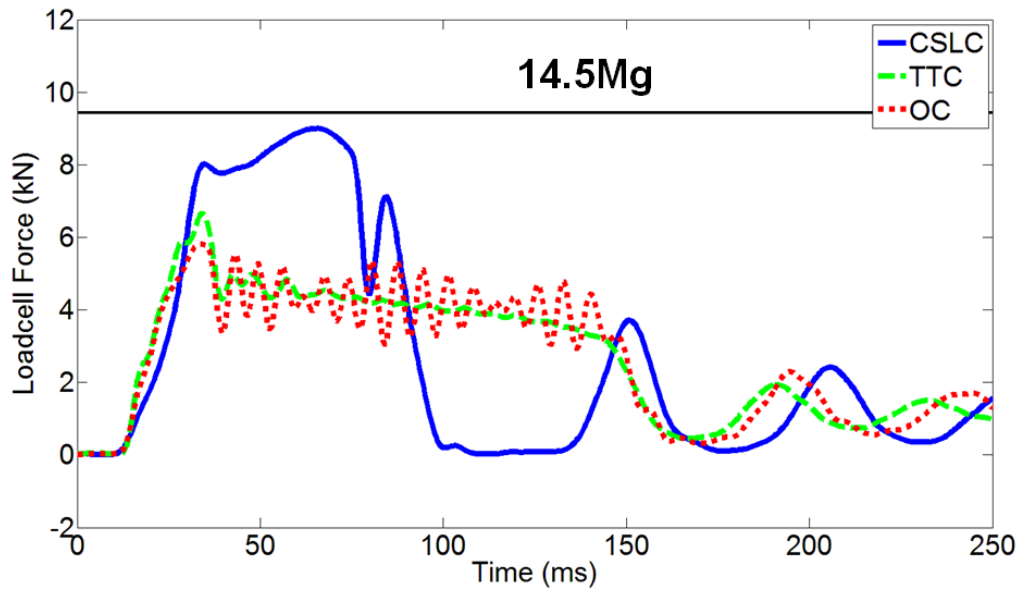
(a)
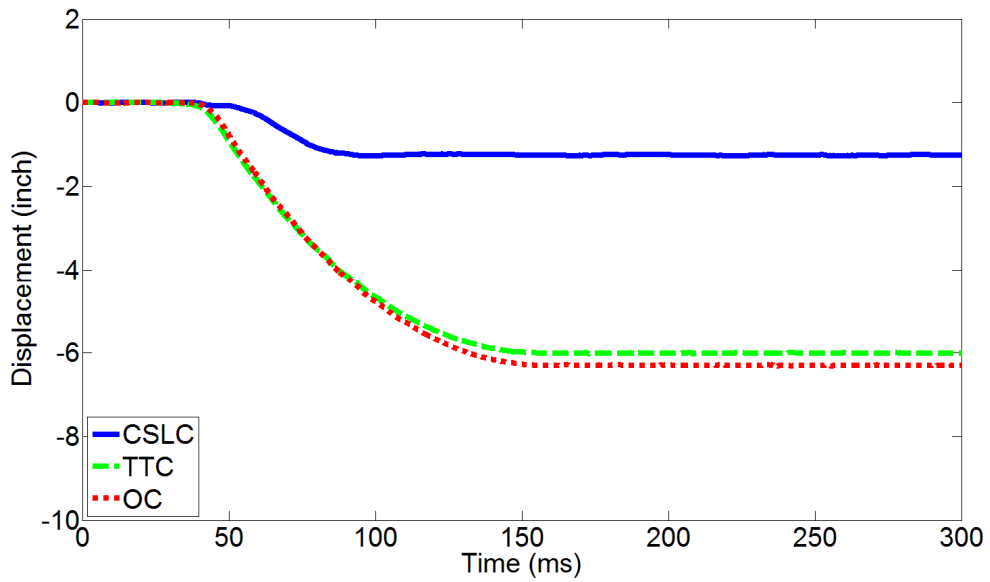
(b)

Figure 5.6. Comparison of control schemes at low intensity shock (240 lb at 35 inch).
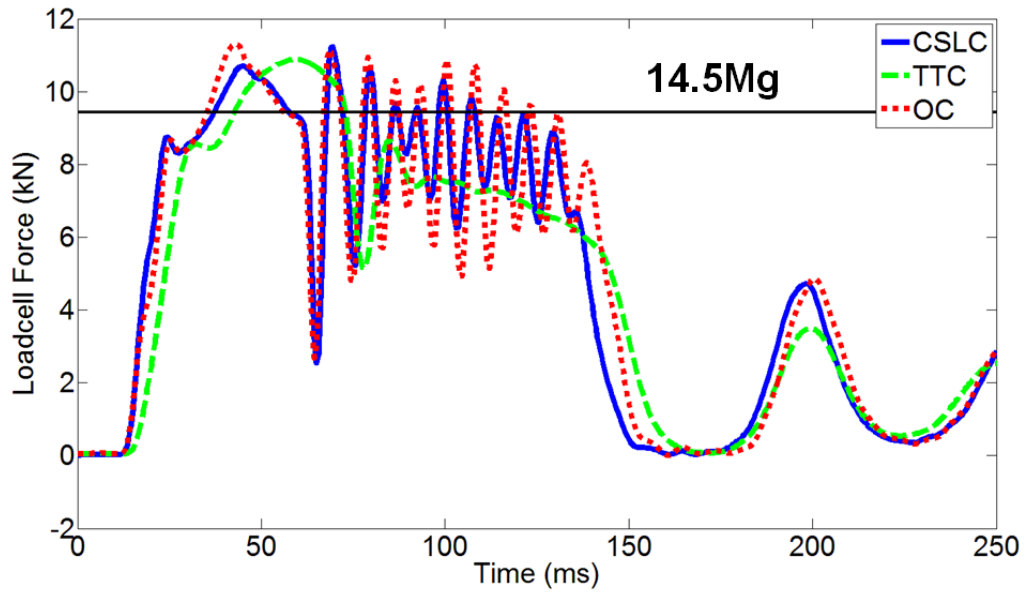
(a)
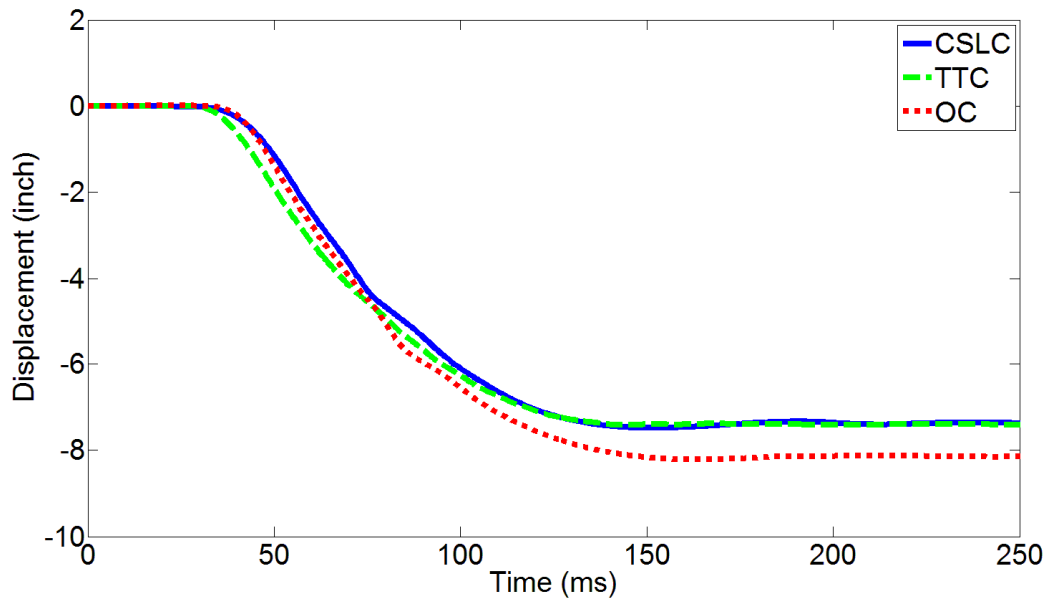
(b)

Figure 5.7. Comparison of control schemes at high intensity shock (340 lb at 60 inch).
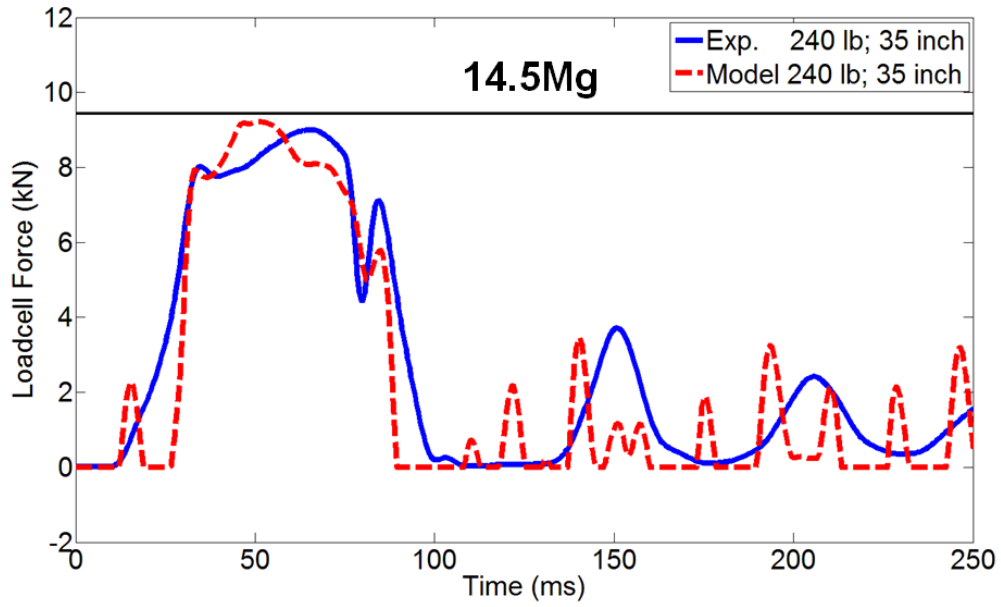
(a)
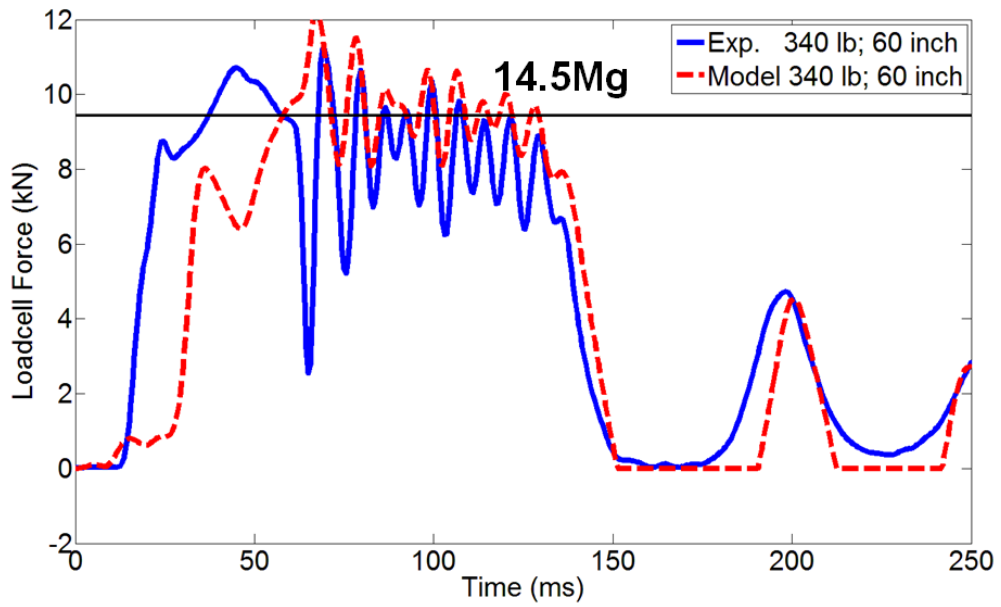
(b)

Figure 5.8. Comparison of MREA model with experiments at low and high intensity shock for CSLC.
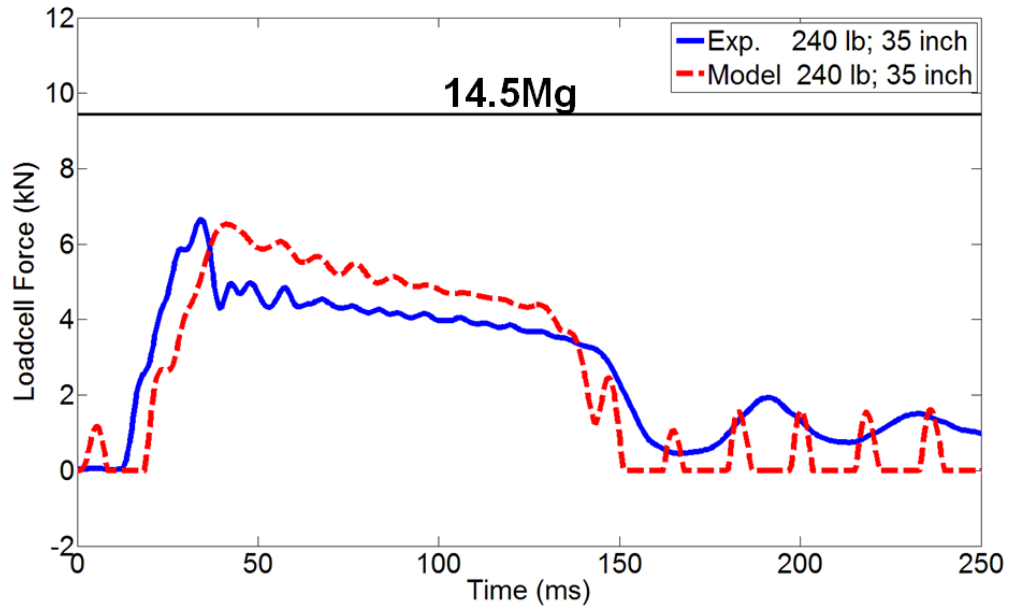
(a)
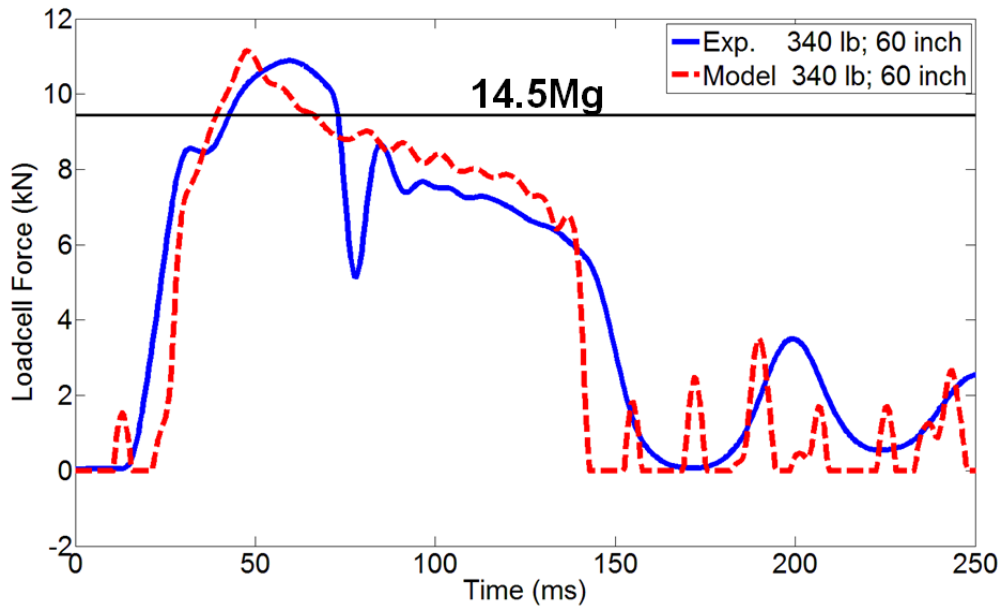
(b)

Figure 5.9. Comparison of MREA model with experiments at low and high intensity shock for TTC.
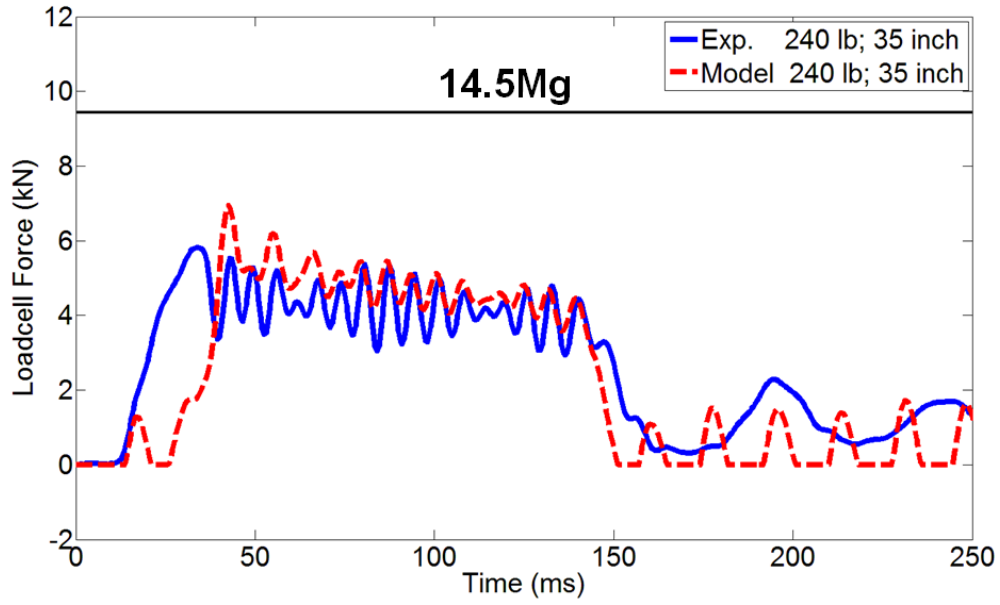
(a)
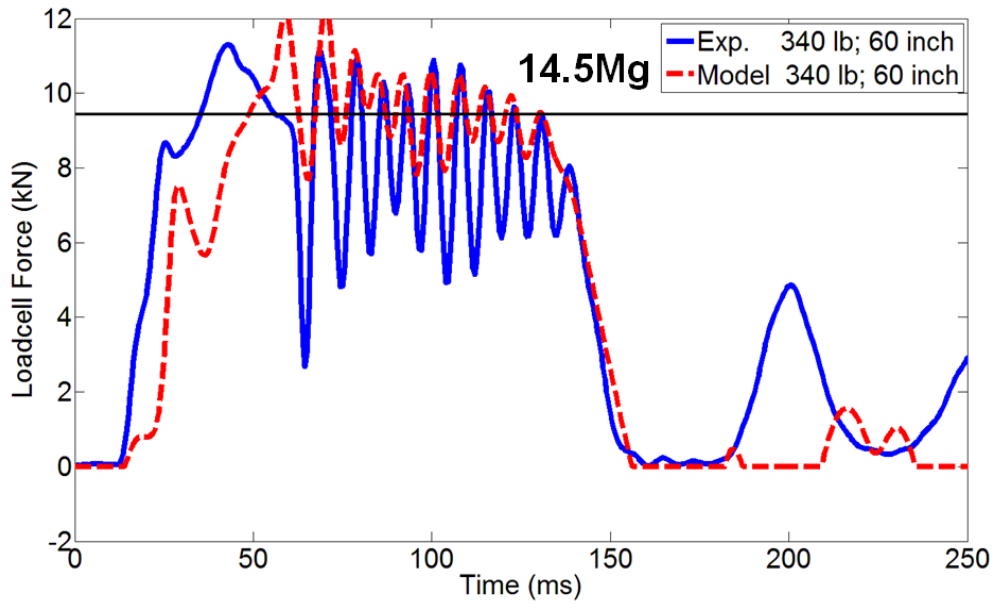
(b)

Figure 5.10. Comparison of MREA model with experiments at low and high intensity shock for OC.
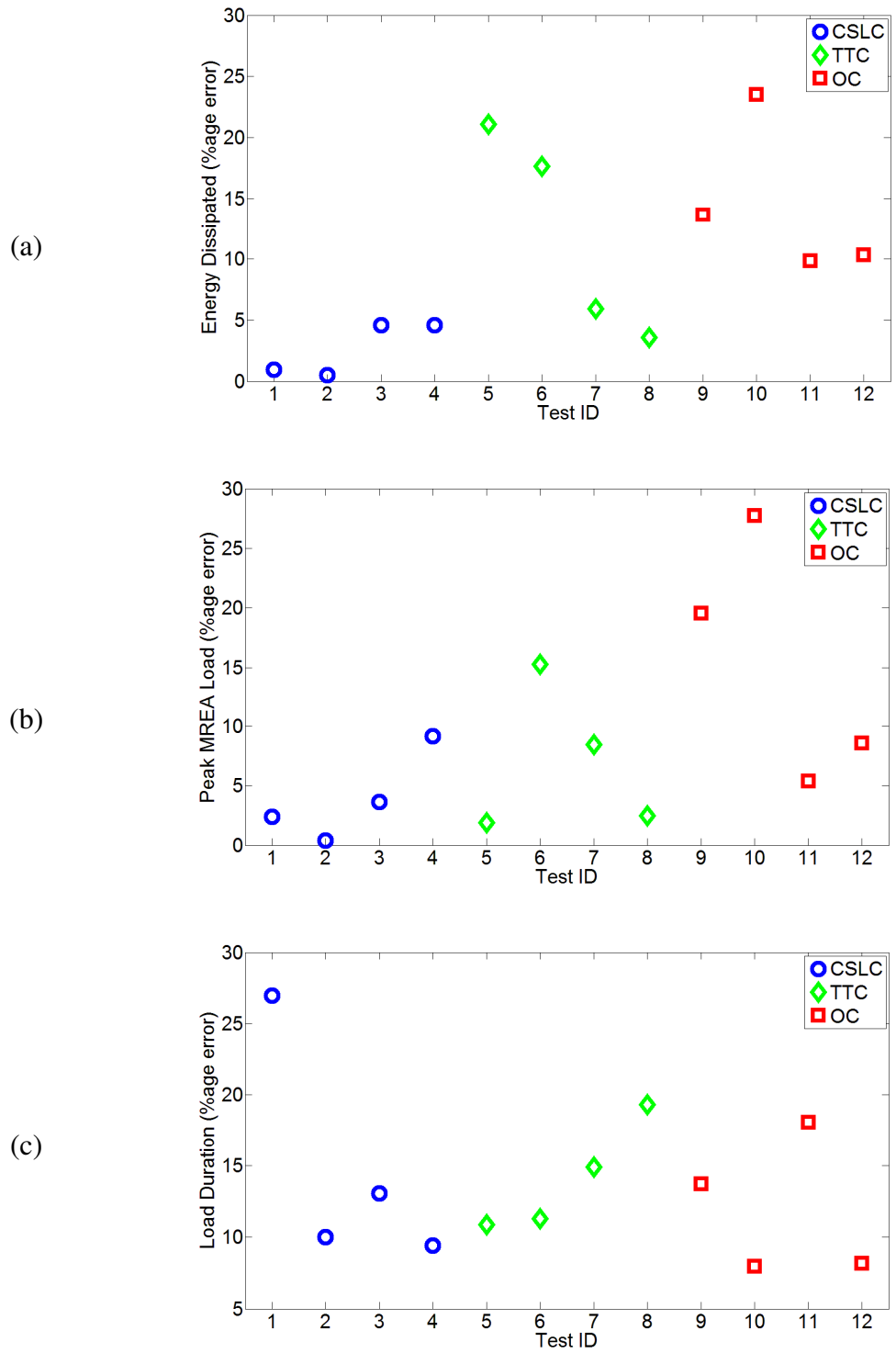
Figure 5.11. Percentage errors for (a) energy dissipated, (b) peak MREA load and (c) stroking load pulse duration for comparing MREA model with experiments.

Chapter 6

Testing a Hybrid III 50th Percentile Male ATD Using a Horizontal Accelerator Facility

6.1.   Abstract

A nonlinear four degrees-of-freedom (DOF) biodynamic model with lumped mechanical segments was validated against high-speed impact testing on a Hybrid III 50th percentile male occupant anthropomorphic test device (ATD). A total of 16 impact tests were conducted with two acceleration pulses by impacting the floor of the crash emulator on a horizontal accelerator. A semi-active magnetorheological energy absorber was employed in the crash emulator for shock mitigation and constant stroking threshold of $14.5g$ was maintained for both impact conditions. Quantitative comparison of lumbar loads obtained from impact testing and biodynamic model simulation was carried out. The biodynamic model predicted the peak lumbar loads with a mean error of 11.65% over 16 impact tests.

6.2.   Introduction

Performance of crashworthy seats in helicopters, armored vehicles and automobiles is evaluated through full-scale impact testing on differently sized and

types of seated anthropomorphic test devices (ATDs). Over the decades, ATDs have evolved with state-of-the art instrumentation that help in assessing injuries that an occupant experiences during a crash. The impact tests on ATDs are conducted in different manners such as vertical drop testing (Polanco and Littell, 2011), drop tests of ATDs installed in a subsection of vehicle/aircraft (Fasanella and Jackson, 2004), full-scale crash testing of entire vehicle/aircraft fitted with ATDs (Jackson *et al.*, 2004).

Polanco and Littell (2011) conducted 14 vertical impact tests on Hybrid II and Hybrid III 50th percentile male ATDs based on different spinal configurations. Hybrid III was configured with a curved lumbar spine compared to Hybrid II with straight section lumbar spine. Two different impact conditions were generated by using different type of honeycomb blocks in the drop tower and lumbar responses of both ATDs were compared. A vertical drop test on a subsection of a composite fuselage with two 50th percentile male Hybrid II ATDs was conducted by Fasanella and Jackson (2004). The test generated an impact corresponding to drop velocity of 25 ft/s. Lumbar and pelvic responses of both ATDs were assessed and compared with the responses obtained from finite-element (FE) simulations. A full-scale test was performed by Jackson *et al*. (2004) by crashing Sikorsky advanced composite airframe program (ACAP) helicopter outfitted with four ATDs. All ATDs were 50th percentile male occupants representing pilot, co-pilot and two crew members. Pilot and two crew members were Hybrid II dummies and co-pilot was Hybrid III dummy with additional body worn weight. Injuries were evaluated based on lumbar loads, pelvis, chest and head accelerations and compared with injury prediction models.

Beeman *et al.* (2013) quantified kinetic and kinematic data based on testing on post mortem human surrogates (PMHS) and Hybrid III 50th percentile male ATD for high-speed frontal automotive collisions. Hybrid III ATD's limitations were explored under loading conditions when compared to PHMS responses. In earlier study, Beeman *et al.* (2012) tested on five human volunteers of approximately 50th percentile weight and height, Hybrid III 50th percentile male ATD and three male PMHS for low-speed frontal impacts. Side impact testing was conducted by Yoganandan *et al.* (2013) on ATD that represented human surrogates and peak biomechanical deflections were evaluated to characterize the effects of impact loading and for deriving injury criteria. Sled tests were conducted for three different velocities varying from 3.4 to 7.5 m/s and time varying deflections/contours were determined.

The impact testing is not limited to 50th percentile male ATD's response and injury evaluation based on vehicle/aircraft crash. Bartsch *et al.* (2012) studied the response of Hybrid III ATD to head impacts and evaluated athletic helmet protection in a series of front, oblique front and lateral head impacts. In a similar fashion, injury potential and biodynamic response evaluations have been conducted on Hybrid III three-year old ATD in forward and rearward facing child restraint seats in frontal collisions (Kapoor *et al.*, 2006) .

For the outcome of impact tests to be as accurate as a real crash situation, advanced instrumentation, ATDs representing true human body and modeling of real crash environment are necessary. A complicated fully simulated crash scenario modeled in a laboratory could be very expensive. In order to reduce experimentation

costs, various researchers have developed finite-element models, multi-body models and lumped parameter models to study the response of an occupant under different crash situations using computational means. A finite-element model discretizes the human body into small elements and represents the human body properties such as stiffness, damping and mass. Fasanella and Jackson (2004) compared the responses of finite element model with that of vertical drop test of two 50th percentile male Hybrid II dummies. Xingqiao *et al.* (2013) evaluated the head injuries resulting from side curtain airbag impacts in automobiles using large scale finite element simulations.

Multi-body models connect rigid bodies by pins or ball and socket joints to model human dynamics. Linder (2000) modeled neck for low-velocity rear end impact using a multi-body model, MADYMO 2D, to assess soft tissue injuries. Teng *et al.* (2008) studied the response of human body using multi-body model in a frontal crash collision and assessed the injuries to pelvis, chest and head.

Lumped parameter models employ rigid lumped masses connected via spring and dampers that can be linear or non-linear. Lumped parameter models can vary from a very simple one degree-of-freedom (DOF) linear model to complicated multi-DOF nonlinear models (Liang and Chiang, 2006). Mostly the lumped parameter models are limited to unidirectional analysis. Liu *et al.* (1998) developed a biodynamic model based on dynamic tensile testing. Zong and Lam (2002) evaluated the response of human subjected exposed to ship shock using Liu's biodynamic lumped parameter model. In Chapter 3, a four-DOF biodynamic model with lumped

parameter approach was developed for a 50th percentile male occupant using data from full-scale crash testing of Sikorsky ACAP helicopter.

In the present study, the validation of four-DOF biodynamic model of a 50th percentile male is extended on the basis of high-speed impact testing using a semi-active crash emulator. Sixteen high speed impact tests were conducted on Hybrid III 50th male ATD on a horizontal accelerator available at the U.S. Naval Air Warfare Center (NAVAIR) at Patuxent River. The tests were mainly restricted to sled acceleration of $30g$ amplitude at 30 ft/s velocity (low impact) and $40g$ amplitude at 40 ft/s velocity (high impact). The horizontal accelerator was installed with crash emulator that consisted of a semi-active magnetorheological energy absorber (MREA) and a seat bucket on which the ATD was placed. A linear stroking MREA designed and tested in our prior work (Chapter 2) was employed in the crash emulator. An MREA consists of piston in a hydraulic cylinder that displaces the hydraulic fluid through an orifice similar to conventional passive energy absorber (Cook *et al*., 2007; Mao *et al*., 2014). However, the piston houses copper wire windings as electro-magnets that generate magnetic field when current is fed to an MREA. Increased current inputs generate increased magnetic fields and that changes the apparent viscosity of the smart magnetorheological (MR) fluid inside the hydraulic cylinder. MR fluids typically consisting of 0.3-10 micrometer diameter ferromagnetic particles suspended in a hydrocarbon based carrier fluid (Guo *et al*., 2012, Hiemenz *et al*., 2007). Under magnetic field, the ferromagnetic particles form long chains and provide resistance to the fluid flow displaced by piston motion. The controllability of magnetic induction between ferromagnetic particles provide

adaptive MREA load-stroke profile which can be manipulated electronically, rapidly and reversibly (Hiemenz *et al*., 2007; Mao *et al*., 2014).

6.3. Magnetorheological Energy Absorbers (MREAs)

A linear stroking magnetorheological energy absorber (MREA) with an adaptive load-stroke profile served as a shock absorption device for testing on Hybrid III 50th percentile male ATD under impact conditions. MREA stroking load comprised of two components: controllable yield force and passive viscous force. The yield force was controllable by changing the current levels whereas passive viscous force was uncontrollable and was proportional to the piston velocities. The higher the current level, larger will be MREA yield force until saturation of magnetorheological fluid.

The MREA employed for full-scale impact testing was designed, fabricated and tested and provided a large dynamic range of 1.73 at piston velocity of 8 m/s (Chapter 2). The piston of MREA with 5 electromagnetic coils covered with insulating epoxy and fully assembled MREA are shown in Figure 6.1. These electromagnetic coils consisted of 24 AWG copper wire with electric resistance of 12 Ω and when fed with current input generated magnetic field. Subsequent low-speed cyclic experiments were conducted on hydraulically powered MTS machine for different current inputs varying form 0-5.5 A. Increased current inputs generated increased MREA yield forces. High-speed experiments at zero-field (0 A) were also

conducted to attain high piston velocities using 12 ft high drop tower at Alfred Gessow Rotorcraft Center (AGRC), University of Maryland.

The passive viscous force variation with piston velocity and controllable MREA yield force variation with current input are shown in Figure 6.2. The variation of MREA viscous force with piston velocity was quadratic in nature. For the sake of implementation of the viscous force model into the control algorithms a quadratic curve was fitted to the experimental observations as given by the following equation:

$$F_V = 176.9\,V_P^2 + 429.6\,V_P \tag{6.1}$$

where V_P is the piston velocity.

Similar quadratic estimation of the experiment based MREA yield force dependent on current input, I, was also carried out for the ease of implementation in the control algorithm.

$$F_{MR} = -129.9\,I^2 + 2856.1\,I \tag{6.2}$$

A complete MREA load-stroke profile was obtained when viscous and yield forces were combined together. In other words, a load-stroke profile delineates the performance of MREA at different piston velocities and current inputs as shown in Figure 6.3.

6.4. Impact Testing Set-up

A test bed integrated to the U.S. Naval Air Warfare Center's (NAVAIR's) horizontal accelerator was fabricated for the high speed impact testing. The test bed

comprised of a seat bucket, MREA and two rail guides. The seat bucket with a seated and fully instrumented ATD was able to slide on the rail guides under the impact. The sliding motion of seat bucket was controlled by the energy absorption capacity of the MREA as shown in Figure 6.4.

Figure 6.5 shows testing set-up before the impact with test bed integrated to the NAVAIR's horizontal accelerator. The experiments were conducted on a seated 50th percentile male Hybrid III ATD instrumented with load cell in ATD to measure the lumbar loads during the impact. Another shear pin load cell was also employed to measure the MREA stroking load. Accelerometers were also placed on the seat bucket to measure seat bucket acceleration under the impact conditions. Two string potentiometers were used to measure the seat displacement/MREA compression during impact testing. The string potentiometers were installed on the each side of the seat with the sensor body fixed to the rigid wall and the string was connected to the seat structure. As the seat bucket stroked, the string was pulled out of the body and string displacement was converted to corresponding voltage signal, giving a measurement of the linear position of the seat bucket or MREA shaft displacement. Experimental data were recorded at a sampling rate of 2 kHz. Corresponding piston velocities were obtained by differentiating the string potentiometers data using data acquisition system. During the post processing, the recorded data were filtered by using CFC 60 (100 Hz cut-off frequency) for load cell and CFC 180 (300 Hz cut-off frequency) for string potentiometers (Huang, 2002).

The MREA was in compressed state before the impact i.e. the entire MREA shaft was fully accommodated inside the hydraulic cylinder of the MREA as can be

seen in Figure 6.4a and 6.5. The seat floor was impacted from right to left direction as shown in Figure 6.5 and the shock loads were transmitted to the seated occupant causing the seat bucket to stroke from left to right. Such operation led to the motion of piston inside the hydraulic cylinder which extracted MREA shaft from the hydraulic cylinder. A schematic of mode of operation of MREA before and after impact is presented in Figure 6.6. Since the hydraulic cylinder had to accommodate the volume change due to the motion of shaft inside the hydraulic cylinder, an accumulator with compressed nitrogen gas was installed. In other words, extra volume required when the shaft moved inside the hydraulic cylinder was generated by compressing the pressurized accumulator and vice versa. For the experiments, the accumulator was charged with nitrogen gas to a low pressure of 50 psi. Low accumulator pressure was favorable because the MREA had to be positioned in a fully-compressed state before the impact and if the pressure was too high then compressing the MREA would have been difficult.

6.4.1. NAVAIR Horizontal Accelerator

The horizontal accelerator consisted of three major components: acceleration actuator, test sled and a set of rail guides. The acceleration actuator employed a cylinder that was divided into front and rear chambers, and a reaction mass. The rear chamber in the cylinder contained compressed air and the front chamber contained pressurized nitrogen. The compressed air fired the thrust piston and the compressed nitrogen provided a braking force. A metering pin located between the two chambers controlled the acceleration-time pulse shape applied to the sled.

The test bed was attached to the rail guides that allowed it to slide away from the accelerator with minimum friction. After the accelerating stroke was completed, caliper brakes mounted on the sled were automatically deployed to decelerate the test bed smoothly. The total length of the rail was 100 ft. The horizontal accelerator was capable of generating maximum acceleration $50g$ and maximum velocity 100 ft/s with a maximum payload 5000 lb for variable acceleration pulse shape. The high speed data acquisition system ranged from portable single channel analog systems through a 96-channel, high-frequency and high sample rate digital system.

6.4.2. Constant Stroking Load Control

Crashworthy seats in helicopters typically employ a constant stroking load concept in which the seat suspension is subjected to a fixed load under impact. The stroking load threshold is generally based on the maximum permissible shock load a human can sustain also known as dynamic limit load. Many crashworthy seats have employed constant stroking load based shock mitigation scheme (Desjardins, 2003) by plastically deforming the inversion tubes (Jackson *et al.*, 2004), bending a metal wire through series of rollers, cutting a metal using a pointed tool etc. All the shock energy is dissipated mainly by plastic deformation and/or cutting and slitting metal. These crashworthy concepts are simple in operation and do not require any active control. However, due to their passive nature these mechanisms are not adaptable and provide only one level of stroking load irrespective of varying occupant weight or shock conditions.

Similar constant stroking load control was intended to be emulated for the performance of existing crashworthy seats stroking at constant load. In other words,

208

the MREA was operated in such a fashion that stroking load level was maintained to a constant threshold. The dynamic limit load was determined based on the maximum permissible vertical load that an occupant could endure during the impact, i.e. the total stroking load of MREA and frictional forces in the seat suspension. A limit load factor of 14.5g was selected for a 50th percentile male (Desjardins, 2003). In other words, the total force of energy absorber was designed not to exceed 14.5 times the effective weight of 50th percentile male subjected to a crash condition. The effective weight comprised of 80% of occupant weight and weight of the seat bucket (Desjardins *et al.*, 1989; Hiemenz *et al.*, 2007). 80% of occupant weight was considered because seat bucket did not support leg weight. For the present study, the 50th percentile male occupant and seat bucket weighed 180 and 85 lbs.

$$F_{D_L} = 14.5g\left(0.8M_{50^{th}} + M_{seat}\right) = 14.81 \text{ kN} \qquad (6.3)$$

Since, the MREA stroking load had two components, i.e. passive viscous force and controllable yield force, the lack of control authority over passive viscous force led to the variation of MREA yield force as follows:

$$F_{MR} = F_{D_L} - F_V \qquad (6.4)$$

The feedback to determine the variation of current input and corresponding MREA yield force for CSLC was based on force feedback algorithm.

6.4.3. Force-Feedback Controller

The closed-loop approach with force-feedback was implemented in order to achieve desirable and controllable performance of MREA. During the shock event,

the MREA stroking load had to be adjusted as per the threshold requirements. MREA stroking load comprised of two components: controllable yield force and uncontrollable viscous force as described earlier. Therefore, in order to tune the MREA to a particular stroking load, the yield force had to be precisely adjusted. For instance, increased viscous forces led to lower MREA yield forces in order to maintain a constant stroking load threshold and vice versa.

The force-feedback control approach is presented in Figure 6.7. The desirable MREA stroking load governed the predetermined current, I_{PRE}, based on the MREA yield force model. Measured MREA stroking load, F_D^{MEAS}, was obtained from the load cell and then compared with the desired MREA stroking load, which is the limit load threshold. On the basis of comparison, the command current from the controller, I_{CMD}, was adjusted. The gains G_1 and G_2 were given values of 0.75 and 1.5 respectively for low impact (30 ft/s, $30g$) and 1 and 100 respectively for high impact (40 ft/s, $40g$). The gains were increased for high impact case in order to tune the MREA yield force quickly because high impact case was relatively faster compared to low impact case.

6.4.4. Experimental Observations

Two type of impacts were generated using the acceleration actuator on the NAVAIR's horizontal accelerator with $30g$ amplitude at 30 ft/s velocity and $40g$ amplitude at 40 ft/s. The sled acceleration inputs are shown in Figure 6.8. The profile of the input acceleration pulses were similar to half-cycle sinusoidal wave.

Constant stroking load control (CSLC) was implemented to generate constant MREA stroking load under impact. Figure 6.9a shows the variation of MREA

stroking load for two impact conditions. It is observable that for the initial moments, the MREA stroking load violated the threshold of $14.5g$ for both test conditions and afterwards maintained a level close to the desirable stroking threshold. The stroking load profile was almost similar for both test conditions because a constant stroking threshold was maintained to a same $14.5g$ level. The pulse duration of high impact (40 ft/s, $40g$) was slightly longer than low impact case (30 ft/s, $30g$) due to high kinetic energy of the occupant for high impact case. The increased kinetic energy also led to larger utilization of the MREA stroke for high impact condition as shown in Figure 6.9b. MREA stroke of 9.77 and 14.25 inch were utilized for low and high impact condition respectively. The respective peak piston velocities obtained were 5.77 and 6.91 m/s for low and high impact conditions.

The current profiles based on CSLC are presented in Figure 6.9d for two test conditions. As the piston velocities increased, the MREA viscous forces also increased and therefore low MREA yield forces were required in order to maintain a constant stroking load threshold. The sharp drops in MREA yield forces correspond to dips in the current profile. The current profile for low impact case (30 ft/s, $30g$) had more oscillations and the same were causing oscillations in the corresponding MREA stroking load as shown in Figure 6.9a.

The MREA force models given by Eqs. (6.1) and (6.2) were also examined to understand the reason behind sharp violation of stroking load threshold during the initial moments of the impact. The experimental piston velocity and current input were employed in MREA viscous force and yield force model given by Eqs. (6.1) and (6.2) respectively. The two model based forces were then added to obtain model

211

based MREA stroking load given by Eq. (6.5) and compared with the experimental observations as shown in Figure 6.10. The hyperbolic tangent function modeled the MREA force realistically such that when there was no motion (stationary piston), the load cell forces were zero. The parameters ψ was constant and given a large value to estimate MREA force magnitude accurately.

$$F_D = (F_V + F_{MR})\|\tanh(\psi V_P)\| \tag{6.5}$$

During the initial moments under impact conditions, the model based stroking load was much lower than experimental observations. One possible reason for such an outcome could be the sharp gradient of vacuum generated inside the MREA hydraulic cylinder due to sudden extraction of MREA shaft. The accumulator pressure inside MREA was as low as 50 psi and if the MREA shaft was displaced much faster than the expansion of accumulator to accommodate volume change, vacuum could have resulted over a period of a few milliseconds.

6.5. Biodynamic Model

A biodynamic lumped parameter model of a seated occupant appropriate to obtain biodynamic responses under crash was developed in Chapter 3. The biodynamic model was designed on the basis of experimental observations obtained from the full-scale crash testing of Sikorsky advanced composite airframe program helicopter (ACAP) (Jackson *et al.*, 2004). Under the impact, the ACAP helicopter attained 11.58 m/s (38 ft/s) vertical velocity and 9.91 m/s (32.5 ft/s) horizontal velocity, close to an intense real crash situation. The ACAP helicopter was equipped with four ATDs representing pilot, co-pilot and two troop members. Biodynamic model parameters were extracted using response data from pilot ATD, which was

50th percentile male Hybrid II dummy without any external body worn-equipment. The biodynamic responses of pelvis, chest, lumbar spine and head were compared against the responses obtained from two largely utilized biodynamic models developed by Patil *et al.* (1977) and Liu *et al.* (1998). The designed biodynamic model was validated against another experiment conducted on two Hybrid II ATDs (left and right ATDs) in a crashworthy composite fuselage impact conducted by Fasanella and Jackson (2004). The biodynamic model predicted the lumbar loads with 4.13% under-prediction and 9.29% over-prediction for left and right ATD respectively. The motivation of this comparison was to further validate the biodynamic model.

The biodynamic model is a nonlinear four-DOF lumped parameter model corresponding to a 50th percentile male exposed to high-speed impacts as shown in Figure 6.11. The biodynamic model consisted of four lumped mass segments corresponding to pelvis, viscera, chest and head represented by masses M_i, for i=1-4 respectively. These rigid masses were connected via nonlinear springs and dampers. The lumbar spine was represented as a stiff nonlinear spring and a damper connecting the chest to the pelvis. The displacements of the seat pan and the biodynamic degrees of freedom were defined by coordinates z_i, for i=0-4 respectively.

Originally, the biodynamic model was developed for vertical shocks in which the occupant was assumed to be seated in a perfect upright position, i.e., the seat suspension did not support the weight of the legs and therefore lumped mass for legs was not considered (Hiemenz *et al.*, 2007). In order to simulate the horizontal impact

213

conditions, same assumptions were applied because feet of the ATD were fixed to the seat suspension floor as shown in Figure 6.5. The occupant was assumed to undergo pure horizontal displacement i.e. z direction only and the motion in lateral direction and sideways was not considered. The governing equations of motion for the proposed biodynamic model are given as follows:

$$M_0 \ddot{z}_0(t) = -F_D sgn(\dot{z}_R(t)) + F_{K_{1,0}} + F_{C_{1,0}} \tag{6.6}$$

$$M_1 \ddot{z}_1(t) = -F_{K_{1,0}} - F_{C_{1,0}} + F_{K_{2,1}} + F_{C_{2,1}} + F_{K_{3,1}} + F_{C_{3,1}} \tag{6.7}$$

$$M_2 \ddot{z}_2(t) = -F_{K_{2,1}} - F_{C_{2,1}} + F_{K_{3,2}} + F_{C_{3,2}} \tag{6.8}$$

$$M_3 \ddot{z}_3(t) = -F_{K_{3,2}} - F_{C_{3,2}} - F_{K_{3,1}} - F_{C_{3,1}} + F_{K_{4,3}} + F_{C_{4,3}} \tag{6.9}$$

$$M_4 \ddot{z}_4(t) = -F_{K_{4,3}} - F_{C_{4,3}} \tag{6.10}$$

where, subscript K and C represent nonlinear spring and damper forces respectively and $\dot{z}_R(t)$ is the relative velocity of seat bucket with respect to its floor.

$$F_{K_{i,j}} = K_{i,j}\left(z_i(t) - z_j(t)\right) \tag{6.11}$$

$$F_{C_{i,j}} = C_{i,j}\left(\dot{z}_i(t) - \dot{z}_j(t)\right) \tag{6.12}$$

The spring stiffnesses and damper constants were obtained based on the relative displacements and velocities between two lumped segments respectively.

$$K_{i,j} = \alpha_{i,j} + \beta_{i,j}\|z_i(t) - z_j(t)\|^{\gamma_{i,j}} \tag{6.13}$$

$$C_{i,j} = \phi_{i,j} + \chi_{i,j} \left\| \dot{z}_i(t) - \dot{z}_j(t) \right\|^{\psi_{i,j}} \tag{6.14}$$

The parameters that define nonlinear spring stiffness and damping constants are presented in Table 6.1. The occupant as well as the seat suspension was subjected to impact at a particular sink rate, which determines the initial condition for the numerical analysis.

$$z_i(0) = 0; \; \dot{z}_i(0) = -v_0 \quad \forall \, i = [0 - 4] \tag{6.15}$$

6.5.1. Lumbar Load Response

Quantitative comparison of lumbar loads from biodynamic model and impact testing on Hybrid III 50th percentile male ATD was carried out. The experiment based MREA stroking load was used as an input to the biodynamic model as presented in Figure 6.9a. Biodynamic model based simulations were conducted for 16 tests corresponding to low (30 ft/s, $30g$) and high (40 ft/s, $40g$) impacts. Initial velocity of each lumped mass was obtained by integrating the acceleration pulse with respect to time as shown in Figure 6.8. Therefore, the initial velocities were 9.56 m/s (31.35 ft/s) and 12.72 m/s (41.72 ft/s) for horizontal accelerator impacts of 30 ft/s, $30g$ and 40 ft/s, $40g$ respectively.

As can be seen from Figure 6.12, that biodynamic model based lumbar loads were slightly over-predicted when compared to the experimental observations. One possible reason for such an outcome could be that the biodynamic model was derived from the response of Hybrid II 50th male whereas experimental responses are based on Hybrid III 50th male. Moreover, the biodynamic model lumbar response was more

oscillatory due to highly nonlinear compliance. The simulated biodynamic response for lumbar spine had two peaks. The peak with larger magnitude reflected lumbar loads due to impact and the lower magnitude peak represented subsequent oscillations between pelvis and chest leading to compression of lumbar spine.

The magnitude of error between peak lumbar loads obtained from biodynamic model and experiments is obtained as

$$er(LL) = \left\| 1 - \frac{\overline{LL}_{model}}{\overline{LL}_{exp}} \right\| \tag{6.16}$$

where the quantity $(^-)$ represents peak value and LL represents lumbar loads.

The percentage errors based on the comparison of lumbar loads between biodynamic model and impact testing on 50th percentile male ATD are presented in Figure 6.13. A total of 16 tests were conducted with a mix of low impact (30 ft/s, $30g$) and high impact (40 ft/s, $40g$) tests. The error values varied between 1.5%-19% with biodynamic model always over-predicting the lumbar load responses when compared to full-scale impact testing. For all the cases, the percentage errors were less than 20% with mean error value of 11.65% based on 16 comparison cases.

6.6.   Conclusions

High speed impact testing on 50th percentile male anthropomorphic test device (ATD) were conducted using a horizontal accelerator. The ATD was installed on a crash emulator employing semi-active magnetorheological energy absorber (MREA). Two test conditions in the form of half-cycle sinusoidal acceleration pulse were impacted on seat suspension floor corresponding to low impact (30 ft/s, $30g$)

and high impact (40 ft/s, 40g). A constant stroking load control (CSLC) of 14.5g was implemented to emulate existing crashworthy seat suspensions.

MREA was capable of maintaining a constant stroking threshold with momentarily bump in the initial phase of the impact. MREA stroking load profile for low and high impact test conditions were almost similar with CSLC. Since the stroking load threshold was same for both test conditions, larger MREA stroke was utilized for high impact test conditions (40 ft/s, 40g). The corresponding piston velocities were also larger with intense test conditions and related large current drops were observed to maintain constant stroking threshold.

Biodynamic model based responses were evaluated for both test conditions on the basis of experimental MREA stroking load. Lumbar loads were evaluated and compared with experimental observations. Model based peak lumbar loads were within 20% error when compared to experiments over 16 impact tests. The mean error was 11.65%. The model based response was relatively more oscillatory compared to experimental observations.

References

Bartsch A, Benzel E, Miele V, Morr D and Prakash V 2012 Hybrid III Anthropomorphic Test Device (ATD) Response to Head Impacts and Potential Implications for Athletic Headgear Testing *Accident Analysis and Prevention*, Vol. 48, pp. 285-291.

Beeman S M, Kemper A R, Madigan M L, Franck C T and Loftus S C 2012 Occupant Kinematics in Low-Speed Frontal Sled Tests: Human Volunteers,

Hybrid III ATD, and PMHS *Accident Analysis and Prevention*, Vol. 47, pp. 128-139.

Beeman S M, Kemper A R, Madigan M L and Duma S M 2013 Kinetic and Kinematic Responses of Post Mortem Human Surrogates and the Hybrid III ATD in High-Speed Frontal Sled Tests *Accident Analysis and Prevention*, Vol. 55, pp. 34-47.

Cook E, Hu W and Wereley N M 2007 Magnetorheological Bypass Damper Exploiting Flow Through a Porous Channel *Journal of Intelligent Material Systems and Structures,* Vol. 18, No. 12, pp. 1197-1203.

Desjardins S P, Zimmerman R E, Bolukbasi A O and Merritt N A 1989 Aircraft Crash Survival Design Guide *Aviation Applied Technology Directorate*, USAAVSCOM TR 89-D-22D, Fort Eustis, VA.

Desjardins S P 2003 The Evolution of Energy Absorption Systems for Crashworthy Helicopter Seats *59th Annual AHS Forum*, Phoenix, AZ, May 6-8.

Fasanella E L and Jackson K E 2004 Impact Testing and Simulation of a Crashworthy Composite Fuselage Section with Energy-Absorbing Seats and Dummies *Journal of the American Helicopter Society,* Vol. 49, No. 2, pp. 140-148.

Guo C, Gong X, Xuan S, Zong L and Peng C 2012 Normal Forces of Magnetorheological Fluids Under Oscillatory Shear *Journal of Magnetism and Magnetic Materials,* Vol. 324, No. 6, pp. 1218-1224.

Hiemenz G J, Choi Y T and Wereley N M 2007 Semi-Active Control of Vertical Stroking Helicopter Crew Seat for Enhanced Crashworthiness *AIAA Journal of Aircraft*, Vol. 44, No. 3, pp. 1031-1034.

Huang M, 2002, Vehicle crash mechanics *CRC Press*, Dearborn, MI.

Jackson K E, Fasanella E L, Boitnott R, McEntire J and Lewis A 2004 Occupant Responses in a Full-Scale Crash Test of the Sikorsky ACAP Helicopter *Journal of the American Helicopter Society*, Vol. 49, No. 2, pp. 127-139.

Kapoor T, Altenhof W, Wang Q A and Howard A 2006 Injury Potential of a Three-year-old Hybrid III Dummy in Forward and Rearward Facing Positions Under CMVSS 208 Testing Conditions *Accident Analysis and Prevention*, Vol. 38, No. 4, pp. 786-800.

Liang C C and Chiang C F 2006 A Study on Biodynamic Models of Seated Human Subjects Exposed to Vertical Vibration *International Journal of Industrial Ergonomics*, Vol. 36, pp. 869-890.

Linder A 2000 A New Mathematical Neck Model for a Low-Velocity Rear-End Impact Dummy: Evaluation of Components Influencing Head Kinematics *Accident Analysis and Prevention*, Vol. 32, No. 2, pp. 261-269.

Liu X X, Shi J, Li G, Le X, Zhao B, Yue M, Liu J, Bai G and Ke W 1998 Biodynamic Response and Injury Estimation of Ship Personnel to Ship Shock Motion Induced by Underwater Explosion *Proceedings of the 69th Shock and Vibration Symposium, Shock and Vibration Information Analysis Center*, Vol. 18, pp. 1–18.

Mao M, Hu W, Choi Y T, Wereley N M, Browne A L and Ulicny J 2014
Experimental validation of a magnetorheological energy absorber design
analysis, *Journal of Intelligent Material Systems and Structures*, Vol. 25, No. 3,
pp. 352-363.

Patil M K, Palanichamy M S and Ghista D N 1977 Dynamic Response of Human
Body Seated on a Tractor and Effectiveness of Suspension Systems *Society of
Automobile Engineers,* No. 770932, pp.755-792.

Polanco M A and Littell J D 2011Vertical Drop Testing and Simulation of
Anthropomorphic Test Devices *67th AHS Annual Forum,* Virginia Beach, VA.

Singh H J, Hu W, Wereley N M and Glass W 2014 Design Optimization and
Experimental Validation of Magnetorheological Energy Absorber with Large
Dynamic Range *Smart Materials and Structures*, submitted.

Singh H J and Wereley N M 2014 Biodynamic Model of a Seated Occupant Exposed
to Intense Impacts *AIAA Journal*, submitted.

Teng T L, Chang F A, Liu Y S and Peng C P 2008 Analysis of Dynamic response of
Vehicle Occupant in Frontal Crash Using Multibody Dynamics Method
Mathematical and Computer Modeling, Vol. 48, No. 11-12, pp. 1724-1736.

Xingqiao D, Potula S, Grewal H, Solanki K N, Tschopp M A and Horstemeyer M F
2013 Finite Element Analysis of Occupant Head Injuries: Parametric Effects of
the Side Curtain Airbag Deployment Interaction with a Dummy Head in a Side
Impact Crash *Accident Analysis and Prevention*, Vol. 55, pp. 232-241.

Yoganandan N, Humm J R, Pintar F A and Maiman D J 2013 Determination of Peak

    Deflections from Human Surrogates Using Chestbands in Side Impact Tests

    Medical Engineering & Physics, Vol. 35, No. 8, pp. 1181-1187.

Zong Z and Lam K Y 2002 Biodynamic Response of Shipboard Sitting Subject to

    Ship Shock *Journal of Biomechanics,* Vol. 35, No. 1, pp. 35-43.

Table 6.1. **Biodynamic Model Parameters**

Biodynamic Parameter	M^* (kg)		α (N/m)		β (N/m$^{1+\gamma}$)		γ (-)		ϕ (N-s/m)		χ (N-s$^{1+\psi}$/m$^{1+\psi}$)		ψ (-)
Seat pan	M_0	--	$\alpha_{1,0}$	105	$\beta_{1,0}$	3.32e+6	$\gamma_{1,0}$	0.816	$\phi_{1,0}$	110	$\chi_{1,0}$	112	$\psi_{1,0}$ 2.034
Pelvis	M_1	16.7	$\alpha_{2,1}$	4.88e+6	$\beta_{2,1}$	5.62e+6	$\gamma_{2,1}$	3.962	$\phi_{2,1}$	104	$\chi_{2,1}$	1.51e+4	$\psi_{2,1}$ 1.145
Viscera	M_2	1.4	$\alpha_{3,1}$	2.45e+6	$\beta_{3,1}$	9.09e+6	$\gamma_{3,1}$	0.489	$\phi_{3,1}$	3.76e+3	$\chi_{3,1}$	6.99e+3	$\psi_{3,1}$ 1.195
Chest	M_3	33.7	$\alpha_{3,2}$	9.77e+6	$\beta_{3,2}$	1.47e+6	$\gamma_{3,2}$	4.279	$\phi_{3,2}$	104	$\chi_{3,2}$	1.23e+4	$\psi_{3,2}$ 1
Head	M_4	5.1	$\alpha_{4,3}$	5.12e+6	$\beta_{4,3}$	101	$\gamma_{4,3}$	1.658	$\phi_{4,3}$	102	$\chi_{4,3}$	103	$\psi_{4,3}$ 5.592

*Hybrid II 50th percentile male dummy data from http://www.humaneticsatd.com/crash-test-dummies/frontal-impact/hybrid-ii-50th. Last accessed on October 15, 2013

(a)

(b)

Figure 6.1. Fabricated (a) piston guide assembly and (b) full assembly of MREA.
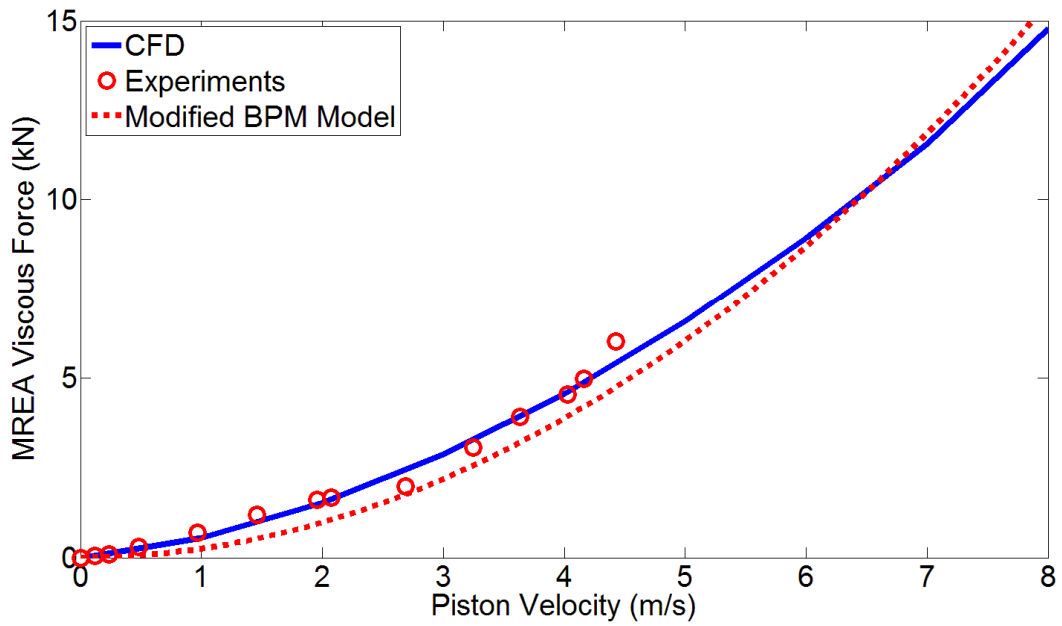
(a)
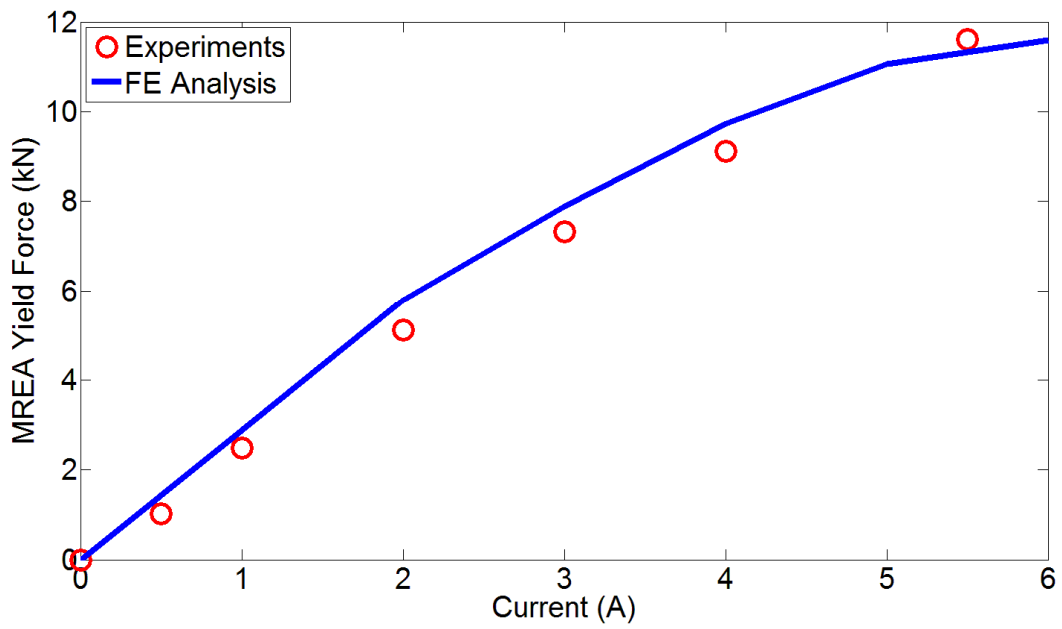
(b)

Figure 6.2. Analytical model and experiment based MREA (a) viscous force and (b) yield force.
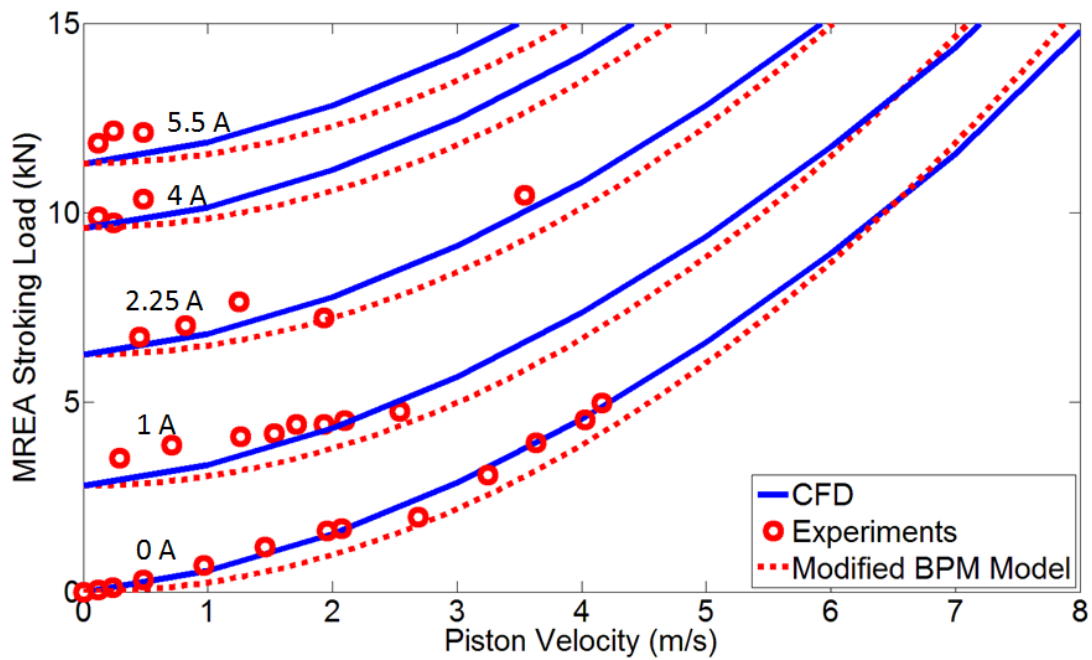
Figure 6.3. Load-stroke profile of MREA for different current inputs and piston velocities.
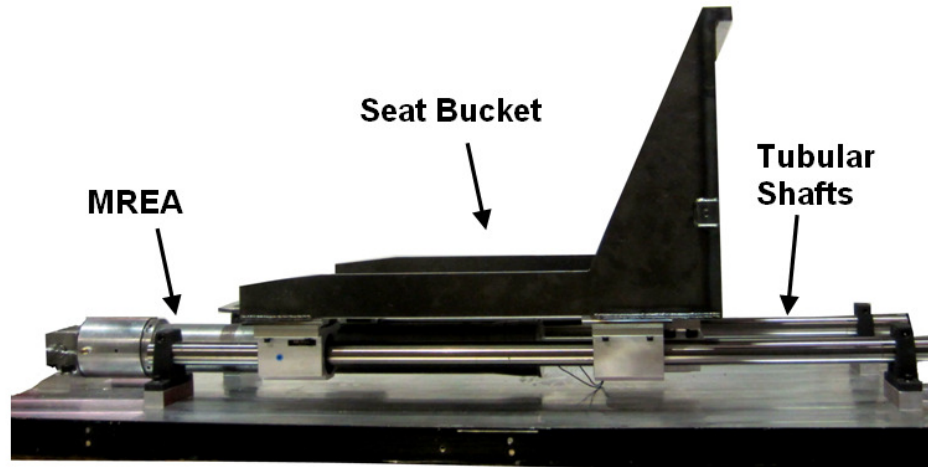
(a)
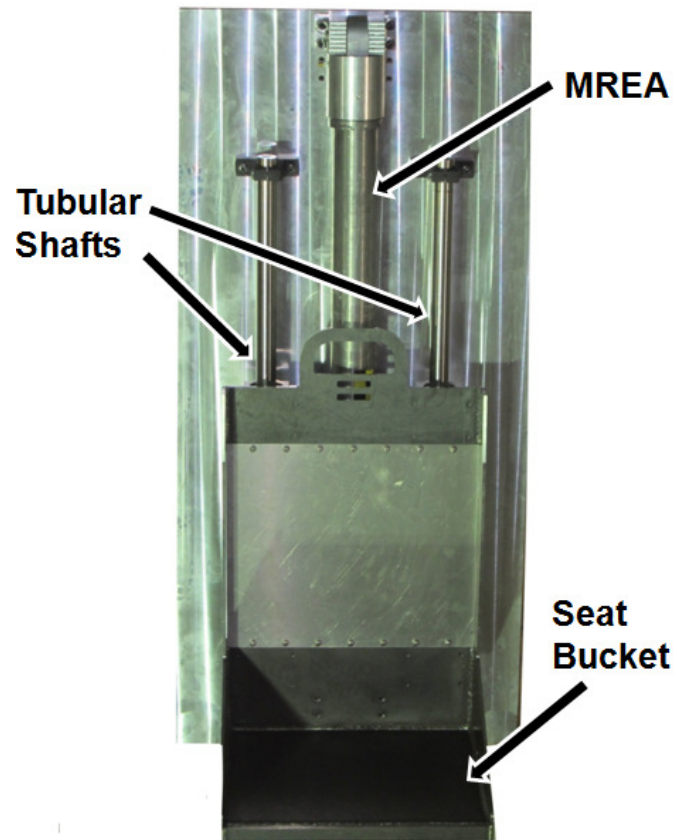
(b)

Figure 6.4. Seat bucket and MREA assembly installed on test bed (a) side view and

(b) top view.
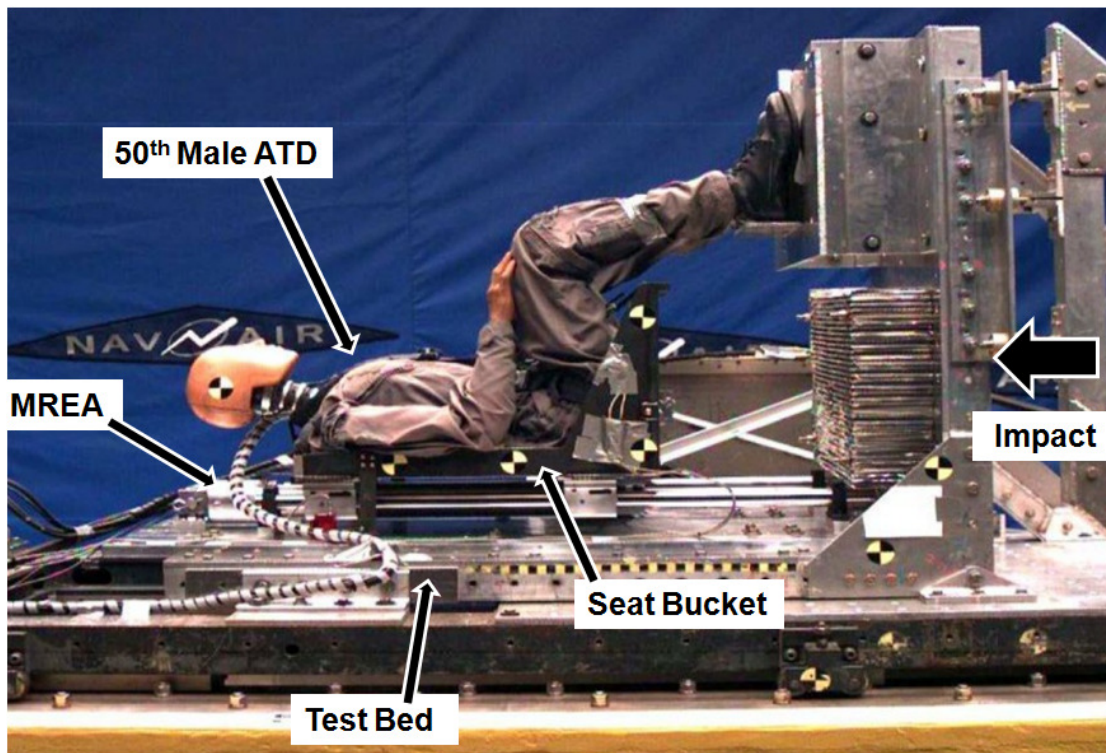
Figure 6.5. Hybrid III 50th percentile male instrumented ATD seated on the test bed
and integrated to the NAVAIR horizontal accelerator before impact.
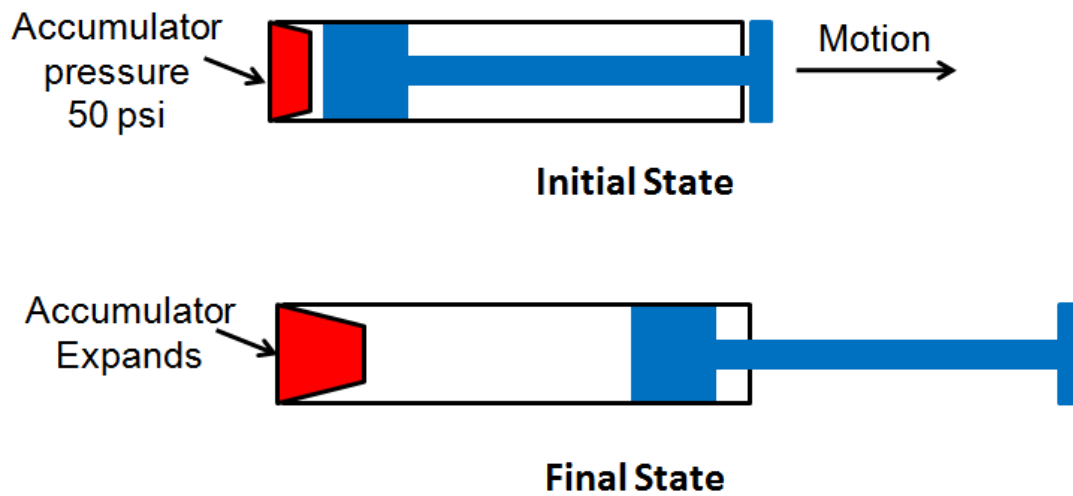
Figure 6.6. Mode of operation of MREA under impact.
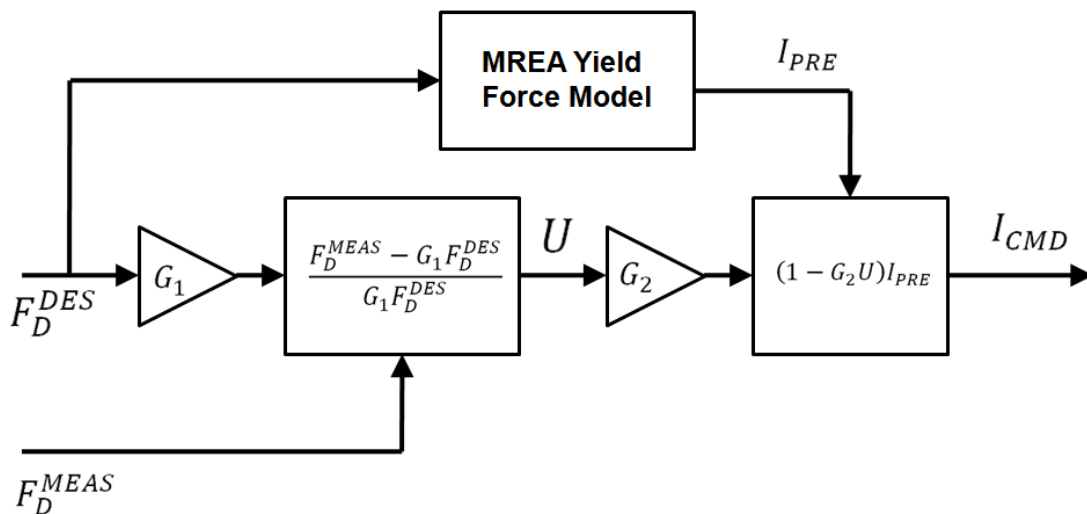
Figure 6.7. Force feedback closed-loop algorithm.
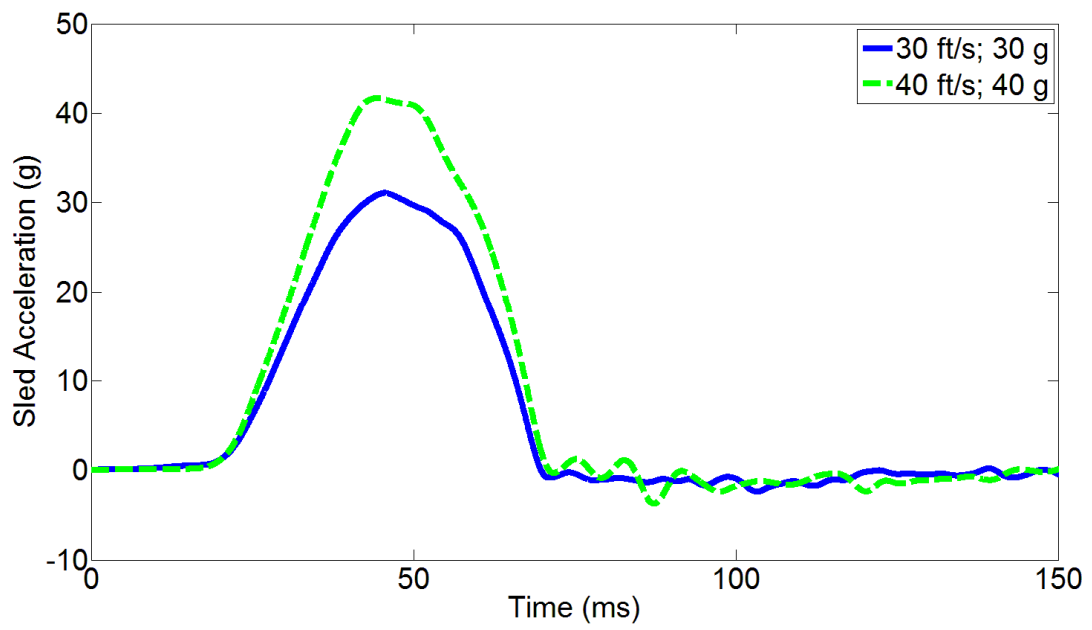
Figure 6.8. Sled input acceleration pulses to simulate impacts.

(a)

(b)

(c)

(d)
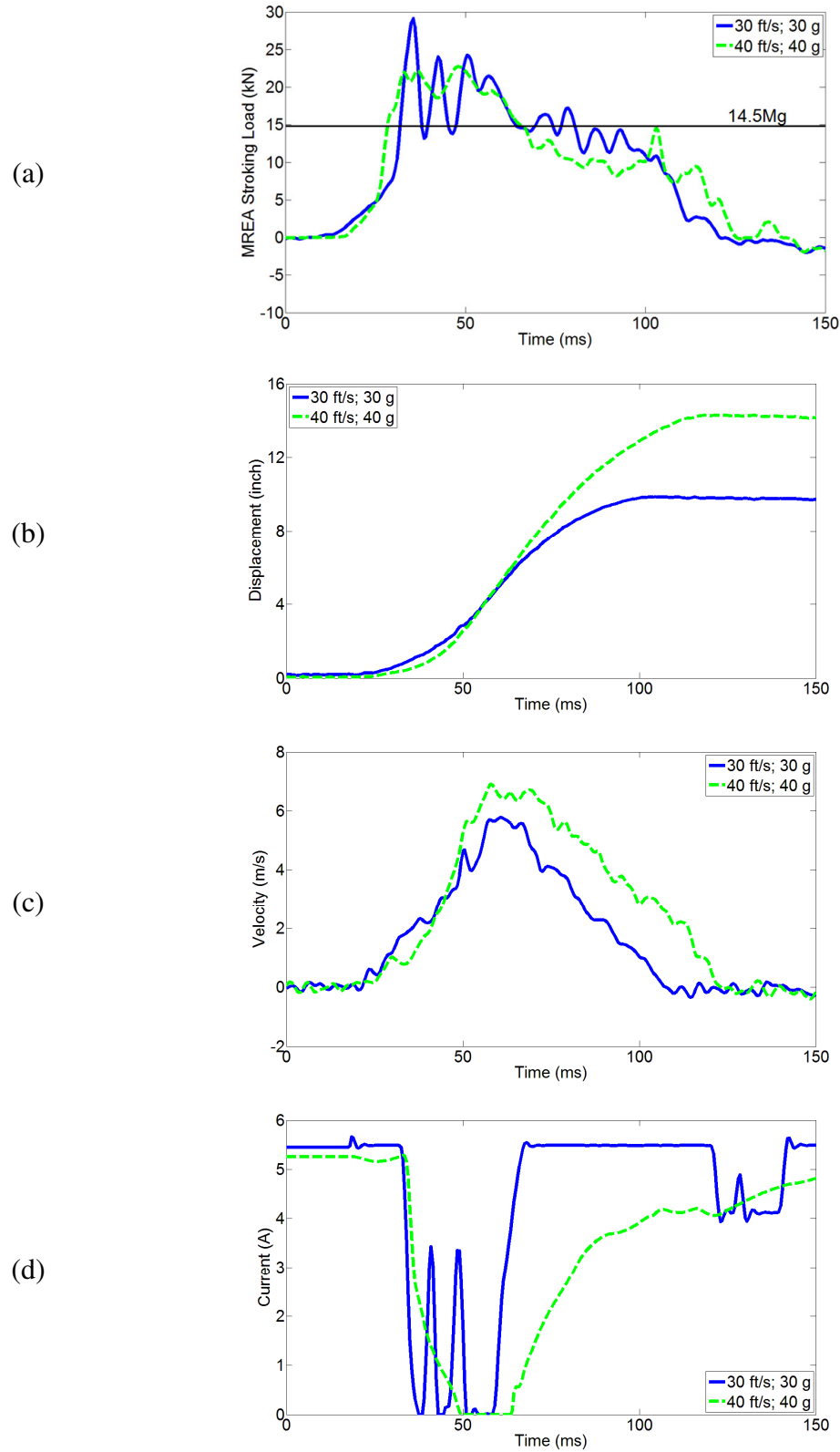
Figure 6.9. Constant stroking load control (CSLC) based (a) MREA stroking load, (b) piston displacement, (c) piston velocity and (d) current input.
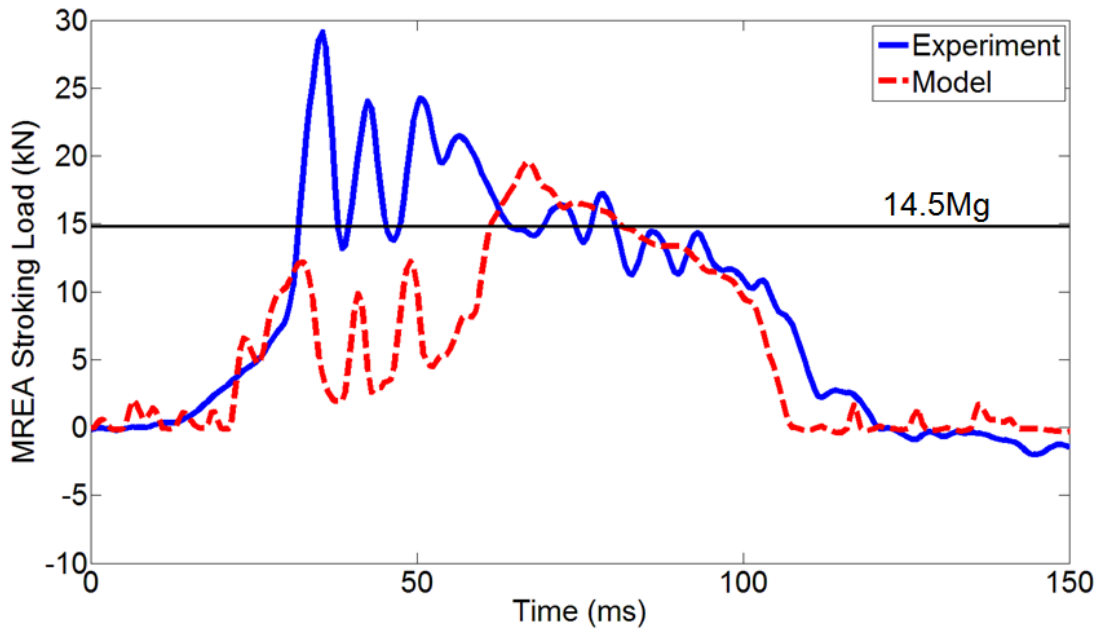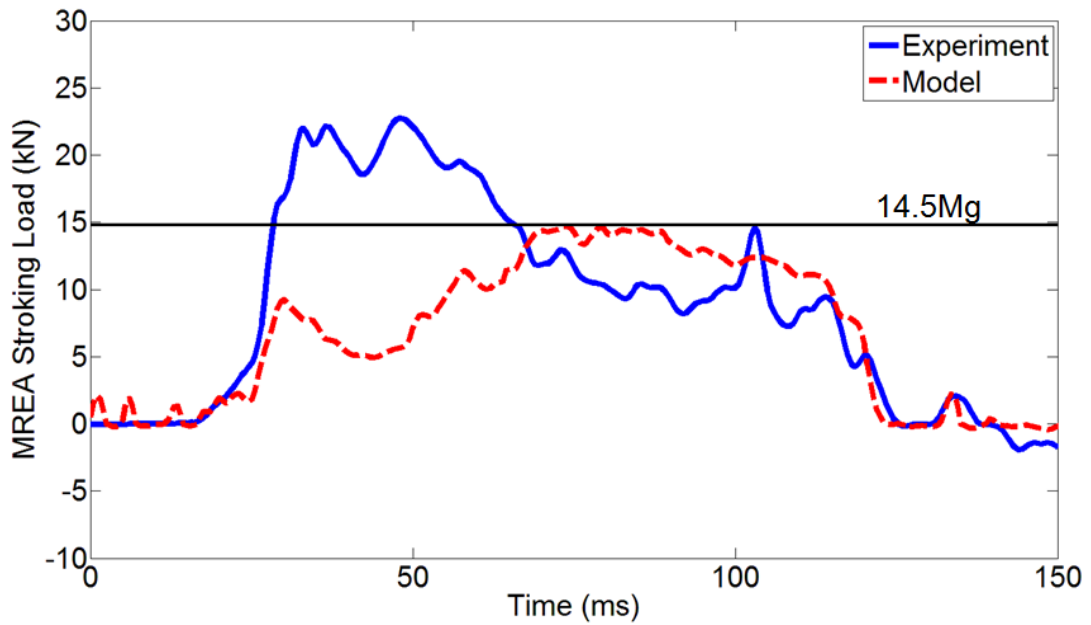
Figure 6.10. Comparison of MREA model with experiments for (a) 30 ft/s, 30g and (b) 40 ft/s, 40g impact.
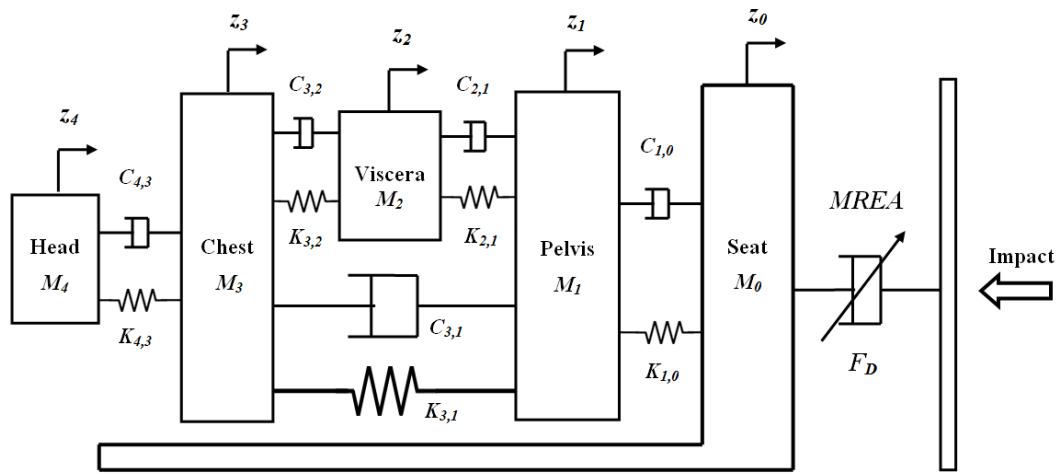
Figure 6.11. Biodynamic model integrated to the MREA based seat suspension model.
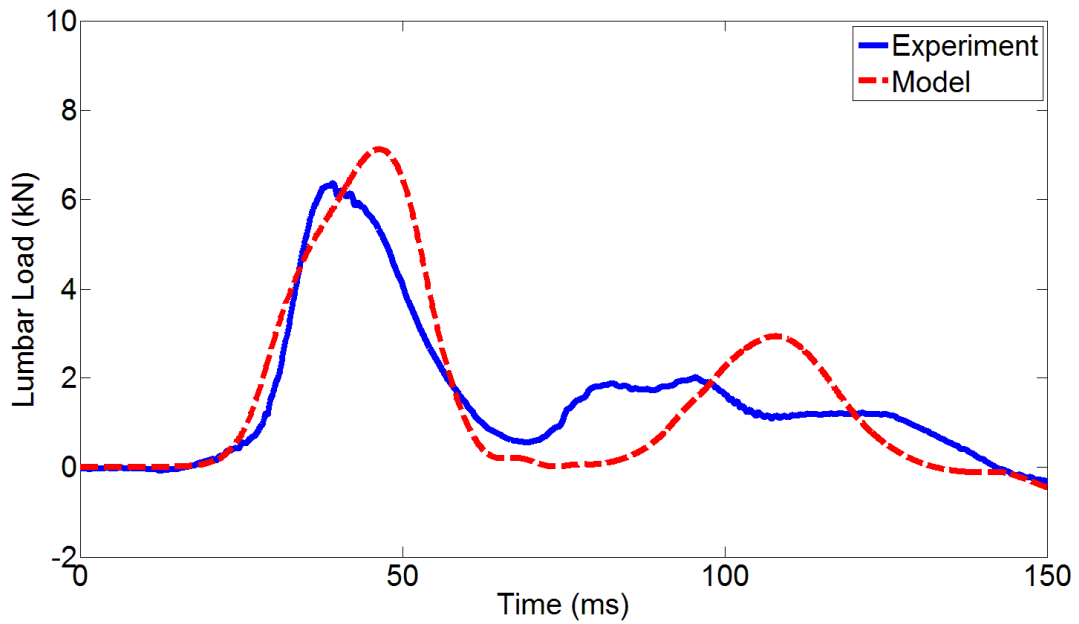
(a)
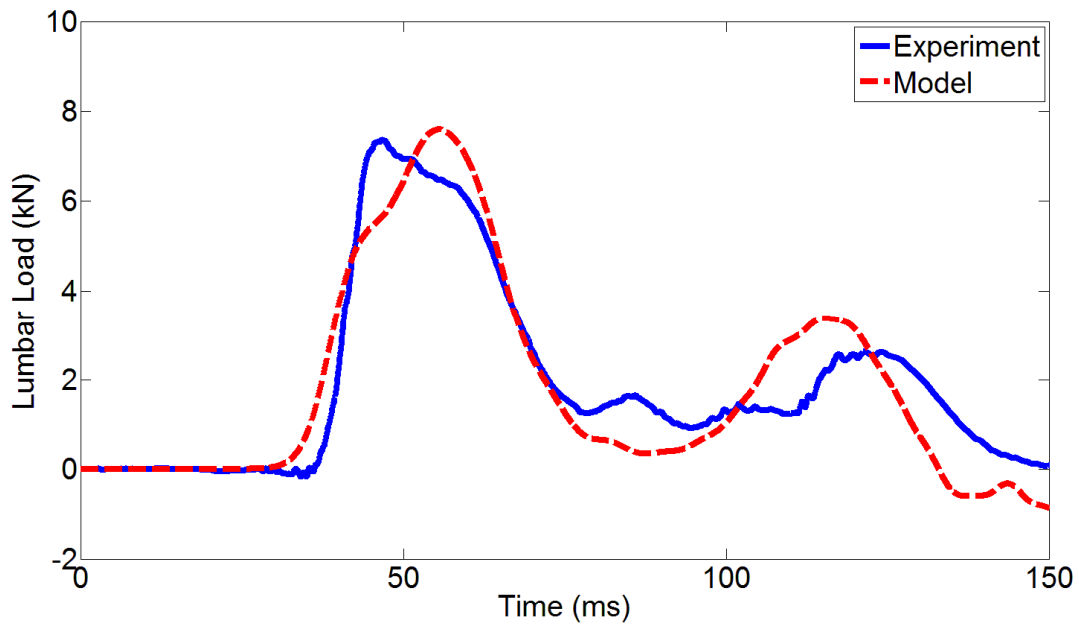
(b)

Figure 6.12. Comparison of biodynamic model and experiment based lumbar loads for (a) 30 ft/s, 30g and (b) 40 ft/s, 40g impact.
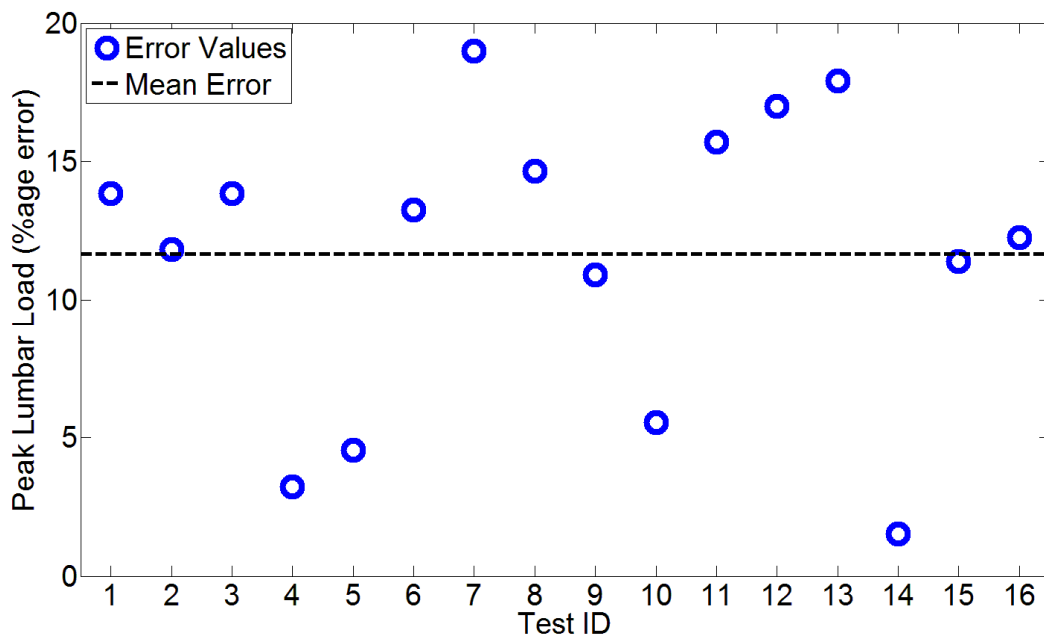
Figure 6.13. Percentage error between experiment and biodynamic model based observations for peak lumbar loads.

Chapter 7

Conclusions

This research was focused on the development and testing of semi-active magnetorheological energy absorber (MREA) based crashworthy seat suspension for enhanced occupant protection while operating in harsh environments such as hard vertical landings or crash. The performance of current state-of-the-art crashworthy systems is limited because of non-adaptive mode of operation with respect to varying occupant weight and impact severity. In other words, the existing crashworthy systems operate optimally for a narrow range of occupants and shock intensities. The motivation to extend optimal occupant protection for wide variation in occupant weight such as 5th percentile female to 95th percentile male exposed to shocks ranging from low impacts of 30 ft/s to high impacts of 40 ft/s sink rate led to the development of adaptive crashworthy seat suspension.

7.1. Summary of Research and Original Contributions

The development of adaptive crashworthy seat suspension employing semi-active MREA was delineated into a few segments. The first was the design analysis, fabrication and laboratory experiments based characterization of MREA.

235

Subsequently, a biodynamic model for a 50th percentile male seated occupant was developed using lumped parameters and its influence on crashworthy seat performance was evaluated. Afterwards, laboratory experiments were conducted to test adaptive control schemes for varying shock conditions and performance was compared against control schemes employed in existing crashworthy seat suspensions. High impact testing was conducted on Hybrid III 50th percentile male occupant using horizontal accelerator to evaluate crashworthy seat suspension performance at the U.S. Naval Air Warfare Center (NAVAIR), Patuxent River, MD.

7.1.1. Magnetorheological Energy Absorber with Large Dynamic Range

An MREA with large dynamic range of 1.73 at peak velocity of 8 m/s was designed, fabricated and tested in the laboratory. The design methodology included optimizing the stroking load profile of MREA using optimization techniques followed by refinements to geometrical parameters via finite element (FE) simulations. Stroking load profile optimization was a multi-objective problem with trade-off between controllable yield force and passive viscous force. MREA was assembled with Lord MRF-132DG fluid after optimizing the geometry and experiments were conducted. Cyclic testing for low speeds and impact testing for speeds as high as 4.5 m/s were conducted using MTS machine and 12 ft drop test tower at Alfred Gessow Rotorcraft Center, University of Maryland. The dynamic range based on experiments was around 2.93 at piston velocity of 4.5 m/s operated at maximum current of 5.5 A.

The analytical Bingham-plastic model incorporating minor losses (BPM model) was refined based on experimental observations. Surface roughness of piston

body forming flow channel proved to be the most critical factor in predicting MREA forces based on analytical BPM model.

This semi-active MREA has the largest dynamic range when compared to other existing linear stroking magnetorheological devices.

7.1.2. Biodynamic Lumped Parameter Model for Intense Shocks

A nonlinear four degrees-of-freedom (DOF) biodynamic model was developed with lumped mass segments on the basis of full-scale crash testing of Sikorsky ACAP helicopter with 50th percentile male anthropomorphic test devices (ATDs) (Jackson *et al.*, 2004). The biodynamic model parameters that defined nonlinear biodynamic compliance and damping were extracted using optimization algorithms corresponding to the response of seated Hybrid II 50th percentile male occupant in Sikorsky ACAP helicopter. The developed biodynamic model performance was compared with two biodynamic models from the literature.

The validation of the biodynamic model was conducted by comparing the simulated responses to the crashworthy composite fuselage (CCF) experiment in which two seated Hybrid II 50th percentile male ATDs were dropped from a particular height (Fasanella and Jackson, 2004). The peak lumbar loads obtained by biodynamic model simulations were within 10% when compared to the experimental measurements.

The biodynamic model was further validated against impact testing of Hybrid III 50th percentile male ATD using horizontal accelerator at NAVAIR. Series of 16 impacts tests were performed for low and high shock intensities. The biodynamic model mostly over-predicted the lumbar loads but the peak values were within the

237

20% error when compared to experiments with mean error of 11.65%. One probable reason for over-prediction could be that biodynamic model was developed from Hybrid II ATD and experiments were conducted on Hybrid III ATD.

The nonlinear four-DOF lumped parameter based biodynamic model is first biodynamic model developed for intense shocks. Existing lumped parameters based biodynamic models are limited to low amplitude vibration isolation only.

7.1.3. Adaptive Control Schemes

The control schemes validated via laboratory experiments for shock attenuation were based on variation of MREA stroking load during impact. The objective of studying different control schemes was to observe the applicability of different control schemes under varying conditions such as impact severity and occupant weight.

The first control scheme was constant stroking load control (CSLC) in which MREA was tuned to a fixed level of stroking load irrespective of seated occupant weight or impact severity. The non-adaptable nature of MREA stroking load in CSLC led to unnecessarily severe biodynamic response at low impacts because the stroking load was too high.

The second control scheme called terminal trajectory control (TTC) was based on full MREA stroke utilization for impacts varying from low to high intensities. The simplicity of TTC was that the control scheme was open-loop and therefore MREA was tuned to a respective current level based on the shock intensity and occupant weight. Such behavior led to a noise free response and good shock

mitigation at all shock conditions which was validated experimentally on a 12 ft drop test facility at AGRC, University of Maryland.

The third control scheme was hybrid of CSLC and TTC called optimal control (OC). The control scheme performed similarly to TTC in terms of utilizing the MREA stroke completely when under shock but by maintaining a constant stroking load. In other words, this scheme was maintaining constant MREA stroking load to a level such that full stroke was exploited. However, the response using OC was noisy because of closed-loop feedback when compared to TTC.

TTC and OC schemes are adaptable and could be implemented without much complexity. OC and TTC tune the MREA such that good level of protection is maintained irrespective of occupant weight and impact severity. In contrast, existing crashworthy seat suspensions employ passive energy absorbers that provide shock attenuation similar to CSLC and are unsuitable for varying occupant weight and shock intensities.

7.2. Future Work

While the research topics covered in this dissertation has shown the feasibility of adaptive crashworthy seat suspension in conjunction with biodynamic model to varying shock intensities, a few suggestions for future research are addressed in this section that expand upon the present research. The challenges faced and the scope of improvement in this research are presented with the aim of devising innovative concepts, compact devices and better shock response evaluation.

7.2.1. Compact MREA Designs

For an MREA, the dynamic range gives direct measure of performance and is inversely proportional to the passive viscous force which grows sharply as the piston velocity increases. In order to achieve large dynamic range of MREA for accommodating wide variation in occupant weight and shock intensity, the size of a linear stroking MREA device becomes large. A few innovative concepts related to MREA design tend to make MREA more compact without compromising with the dynamic range.

MREAs operating in shear mode have low passive force component because the passive force is generated by shearing the fluid. The relative linear or rotational translation between two parallel plates forms the flow channel where the fluid is sheared. This shearing action develops the viscous forces which are proportional to translational velocity, $F_V \propto V_P$, similar to Couette flow. The linear stroking MREA operating in flow mode generates viscous forces that are proportional to square of piston velocity, $F_V \propto V_P^2$. Therefore, shear mode based MREAs provide lower viscous forces with good control authority. Figure 1a shows rotary vane MR based device operating in shear mode (Hiemenz *et al.*, 2010). A schematic of operation of shear mode based MREA is shown in Figure 1b. Yazid *et al.* (2014) quasi-statically tested a mixed mode MR damper with shear and squeeze mode as shown in Figure 2. The energy absorption capacity of MR damper was tested in three different modes: (1) shear mode, (2) squeeze mode and (3) mixed shear and squeeze mode. When combined with shear and squeeze mode, higher damping was achieved than in any other single mode. Similarly, numerous innovative MREA design concepts are

coming forth with better performance that employ various modes of operation and are compact.

Shear mode based MREA operate at high shear rates when subjected to crash conditions. Care must be taken to design transmission mechanism that connects the seat pan with linear motion to the rotation of MREA piston operating with rotational motion. These transmission mechanisms could be racket and pinion, pulleys etc.

7.2.2. Biodynamic Model for 5th Female and 95th Male Occupants

Biodynamic model corresponding to a seated 50th percentile male occupant was developed in this study. The biodynamic model incorporated lumped mass segments isolated with nonlinear spring and dampers. The parameters were derived from experimental observations of Hybrid II 50th male occupant seated in Sikorsky ACAP helicopter. Typically, majority of crash testing is conducted on 50th percentile male ATDs and the crashworthy seats are designed for optimal protection of a 50th percentile male occupant subjected to intense crash situations. The experimental data for 5th percentile female and 95th percentile male ATDs are almost non-existent. If the biodynamic models for 5th female and 95th male are developed on the basis of experimental data then crashworthy seat suspension analysis can be easily extended for enhanced protection.

Another important consideration is that ATDs do not emulate true compliance of a human body because they are designed for durability. Researchers have developed a few biodynamic models that represent human body e.g. Total Human Model for Safety (THUMS) developed by Toyota (JSOL Corporation, 2014). THUMS models are developed for seated occupants (5th female to 95th male)

exposed to frontal crash as shown in Figure 1.11. Therefore, THUMS model could be utilized for vertical crash and a lumped parameter biodynamic model can be developed for 5th female and 95th male occupant accordingly.

7.2.3. Impact Testing for 5th Female and 95th Male Occupants

The performance of developed crashworthy system could be evaluated for 5th percentile female occupant and 95th percentile male occupant for different control schemes. Based on laboratory tests, terminal trajectory control proved to be beneficial because of its simplicity, open-loop control algorithm, noise-free response and adaptability (Chapter 5). Also the performance of terminal trajectory control was comparable with optimal control algorithm. Therefore, impact testing of 5th female and 95th male occupant could be conducted with a terminal trajectory control under crash conditions. The lumbar loads obtained from impact testing can be then compared with the injury assessment criteria established in Chapter 4 to evaluate injury potential.

References

Fasanella E L and Jackson K E 2004 Impact Testing and Simulation of a Crashworthy Composite Fuselage Section with Energy-Absorbing Seats and Dummies *Journal of the American Helicopter Society,* Vol. 49, No. 2, pp. 140-148.

Jackson K E, Fasanella E L, Boitnott R, McEntire J, and Lewis A, 2004 Occupant Responses in a Full-Scale Crash Test of the Sikorsky ACAP Helicopter *Journal of the American Helicopter Society*, Vol. 49, No. 2, pp. 127-139.

JSOL Corporation Total Human Model for Safety (THUMS), 2014, http://ls-dyna.jsol.co.jp/en/thums/modelDetail.html Last accessed: Mar 24, 2014.

Hiemenz G J, Hu W, Ngatu G, and Wereley N M 2010 Rotary vane magnetorheological energy absorber U.S. Patent US2010/0300819 A1.

Yazid I I M, Mazlan S A, Kikuchi T, Zamzuri H and Imaduddin F 2014 Design of Magnetorheological Damper with a Combination of Shear and Squeeze Modes *Materials and Design*, Vol. 54, pp. 87-95.

Wereley N M, Cho J U, Choi Y T and Choi S B 2008 Magnetorheological Dampers in Shear Mode *Smart Materials and Structures*, Vol. 17, 015022.
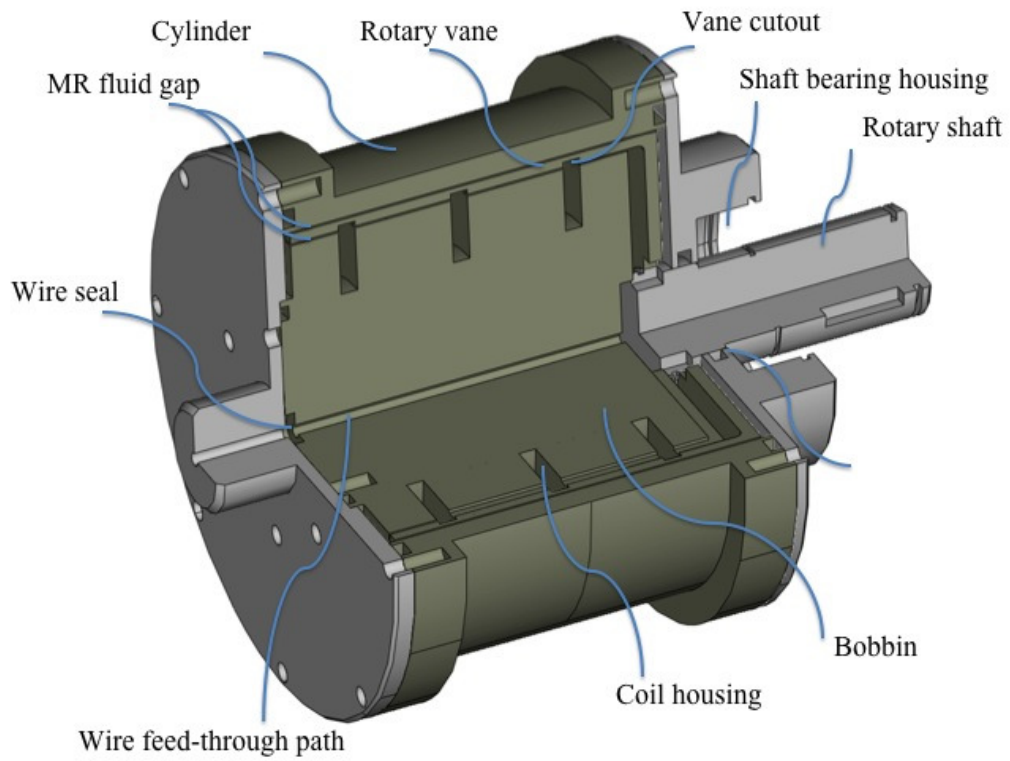
(a) (Hiemenz *et al.*, 2010)
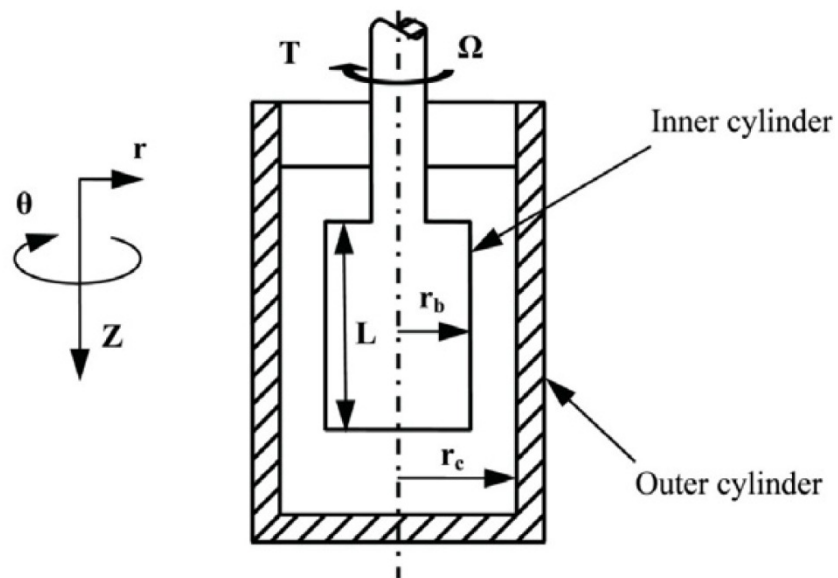
(b) (Wereley *et al.*, 2010)

Figure 7.1. Rotary vane magnetorheological energy absorber.
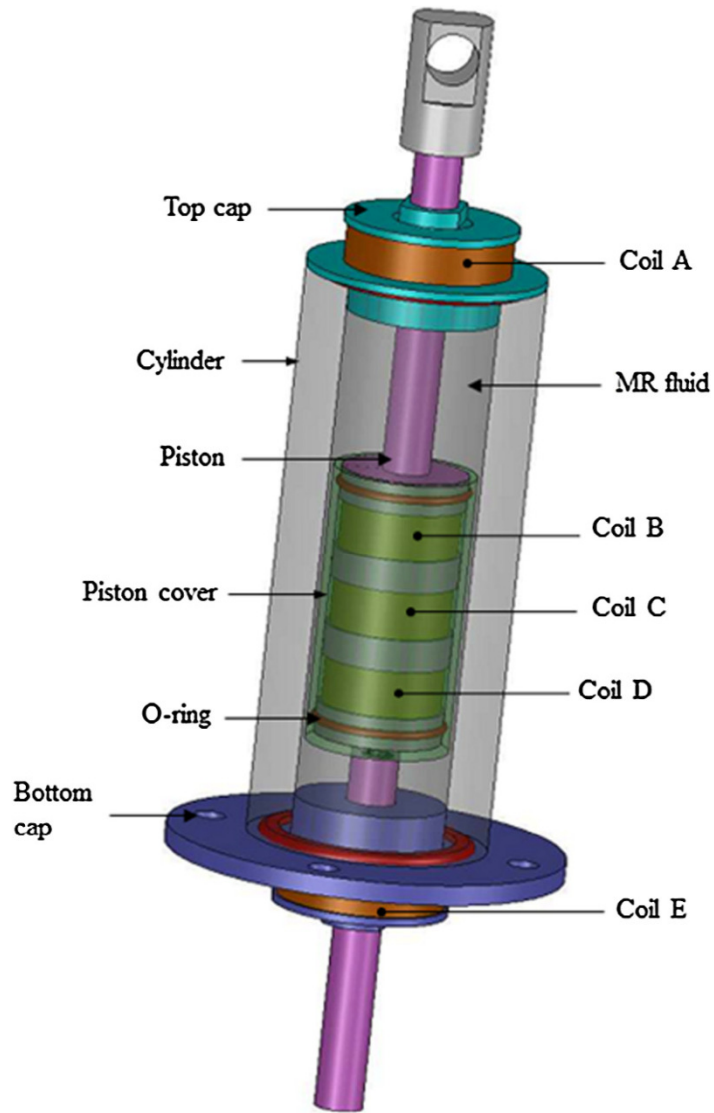
Figure 7.2. Illustration of mixed mode based MR damper (Yazid *et al.*, 2014).

Figure 7.3. Aerospace anthropomorphic test devices (ATD) from 5th female to 95th

male by Humanetics Innovative Solutions.

Last accessed on Mar 27, 2014; http://www.humaneticsatd.com/crash-test-

dummies/aerospace-military/aerospace

Appendix A

Adaptive Magnetorheological Energy Absorbing Mounts for Shock Mitigation

A.1. Abstract

Analysis of adaptive magnetorheological energy absorbers (MREAs) based mounts for drop-induced shock mitigation is addressed in this study. The governing equation of motion of a single degree of freedom payload isolated from the shock by employing an MREA was derived. Terminal trajectory optimal control was employed for the minimization of load transmissions to the payload. The optimal Bingham number was selected to achieve a soft landing, that is, the payload comes to rest after utilizing available MREA stroke. The optimal Bingham number is computed based on drop velocity, payload mass, viscous damping force, which enabled the payload to utilize the entire MREA stroke with and minimize the stroking load. The optimal responses for different MREA design configurations and drop velocities are illustrated.

A.2. Introduction

Intense shock loads resulting from harsh operating environments in vehicles, or high sink rate landings or crashes in helicopters, have the potential to cause severe

injuries to seated operators as well as crew members (Desjardins, 2003; Hiemenz *et al.*, 2007). Such intense impacts can be significantly attenuated if the seat suspension is outfitted with a simple passive energy absorber (EA) with a prescribed stroking load. However, a passive EA with a fixed stroking load cannot mitigate the variety of shock pulses, sink rates, and seated occupant weights that would be encountered. Thus, passive EAs, also known as fixed load energy absorbers (FLEAs), cannot optimally protect occupants under varying impact conditions. To provide adequate protection for the expected variation in impact events, variable load energy absorber (VLEA) is needed.

Magnetorheological energy absorbers (MREAs) are a type of VLEA that can provide adaptive stroking load capabilities to achieve shock mitigation and crashworthiness for vehicles, high-speed boats, and helicopters. MREAs have attractive features, such as rapidly adjustable stroking load in response to an applied current input. An MREA is similar to a conventional hydraulic shock absorber in that the fluid is pushed through an orifice by the motion of piston inside the hydraulic cylinder (Cook *et al.*, 2007; Mao *et al.*, 2009). However, the orifice is typically integrated with an electromagnet housed in the piston. MREAs employ magnetorheological (MR) fluids, which are typically composed of 0.3-10 micron diameter carbonyl iron particles suspended in a hydrocarbon-based fluid (Cha *et al.*, 2010; Jeon and Koo, 2012). The magnetic field generated by feeding current into the electromagnetic coil induces magnetic induction between the carbonyl particles and thereby changes the apparent viscosity of the MR fluid, further, enabling adjustment of the MREA stroking load. Another major advantage of MREAs is low power

consumption. Unlike systems that use force generators or actuators in conjunction with active feedback control, instabilities such as control spillover can be avoided eliminated because MREAs are inherently dissipative devices.

Under consideration is the optimal control of a single degree of freedom system representing a rigid payload descending at a prescribed drop velocity. The MREA isolates the payload from the shock, and the energy dissipated is related to the area under the load-displacement curve. A key goal is to exploit the entire EA stroke during the shock event such that the payload energy is dissipated over the entire stroke, and payload deceleration is minimized and the potential for damage to the payload is minimized. If the MREA stroking load is too large, then the payload would come to rest before utilizing the available EA stroke and payload decelerations would be larger than necessary. On the other hand, if the MREA stroking load is too small, then there will be insufficient stroke, and the MREA will bottom out, thus, producing an undesirable severe end-stop impact. However, the MREA stroking load can be optimally selected for a given payload mass and impact (or drop) velocity or sink rate, such that the suspension payload comes to rest after fully utilizing the available MREA stroke, that is, a soft landing. The optimal stroking load of the MREA, characterized by a unique optimal Bingham number, enables the optimal control of the terminal trajectory of the payload mass. This chapter describes the procedure by which such an optimal Bingham number, which depends on payload mass, drop velocity and EA stroke, can be selected to optimally control payload to achieve a soft landing, that is, the payload comes to rest after fully utilizing the available stroke of the MREA.

A.3. Magnetorheological Energy Absorbers (MREAs)

The configuration of a single degree of freedom system employing an MREA for drop-induced shock mitigation is shown in Figure A.1 with the payload mass, m, subjected to initial drop velocity, v_0. The available EA stroke before the impact is S.

The governing equation of motion is

$$m\ddot{z}(t) = -f_d - mg \tag{A.1}$$

The MREA damping force is a combination of viscous damping (passive) and MR yield force (controllable) and given as follows

$$f_d = c\dot{z}(t) + f_y sign\{\dot{z}(t)\} \tag{A.2}$$

with the initial conditions given by

$$z(0) = S; \quad \dot{z}(0) = -v_0 \tag{A.3}$$

Here, f_d is the total MREA force, c is the viscous damping constant of the MREA, $z(t)$ is the displacement of the MREA from the reference line, f_y is the MR yield force and g is the acceleration due to gravity.

The governing equation, Eq. (A.1) can be rewritten in terms of the velocity, $\dot{z}(t) = v(t)$.

$$\dot{v}(t) = -\frac{c}{m}v(t) - \frac{f_y}{m}sign\{v(t)\} - g \tag{A.4}$$

Integrating Eq. (A.4) and using the initial condition for velocity given by Eq. (A.3) we obtain

$$\dot{z}(t) = v(t) = -v_0 \left\{ \left[1 - \frac{f_y sign\{-v_o\}}{cv_0} - \frac{mg}{cv_0} \right] e^{-\frac{ct}{m}} \right.$$

$$\left. + \frac{f_y sign\{v(t)\}}{cv_0} + \frac{mg}{cv_0} \right\}$$

(A.5)

The Bingham number, Bi, is defined as the ratio of the MR yield force (controllable) to the viscous damping force (passive).

$$Bi = \frac{f_y}{cv_0}$$

(A.6)

The Bingham number can be interpreted as the nondimensional yield force, or the *control variable*. Note that $v(t)$ is negative during the shock event because the payload moves downward, therefore, *Signum* function attains a value of -1. Using the Bingham number in Eq. (A.6), the payload velocity in Eq. (A.5) can be rewritten as follows

$$\dot{z}(t) = v(t) = -v_0 \left\{ \left[1 + Bi - \frac{mg}{cv_0} \right] e^{-\frac{ct}{m}} - Bi + \frac{mg}{cv_0} \right\}$$

(A.7)

By integrating Eq. (A.7) again and using the initial condition given by Eq. (A.3), we obtain the displacement given as

$$z(t) = \frac{mv_0}{c} \left(1 + Bi - \frac{mg}{cv_0} \right) \left(e^{-\frac{ct}{m}} - 1 \right) + v_0 t \left(Bi - \frac{mg}{cv_0} \right) + S$$

(A.8)

The deceleration of the MREA is obtained by differentiating Eq. (A.7).

$$\ddot{z}(t) = \frac{cv_0}{m} \left[1 + Bi - \frac{mg}{cv_0} \right] e^{-\frac{ct}{m}}$$

(A.9)

A.4. Terminal Trajectory Control

The terminal trajectory control seeks to maximize the shock attenuation by adopting two key goals (Wereley *et al.*, 2011). The first goal is to utilize the entire EA stroke such that the kinetic energy of the payload is dissipated over the entire stroke. In other words, the energy dissipation per unit EA stroke is minimized. The second goal is to eliminate end-stop impact, i.e., the condition when the MREA runs out of stroke. These two control objectives are the terminal conditions given as follows

$$z(t_e) = 0$$

$$\dot{z}(t_e) = 0 \tag{A.10}$$

where t_e is the time at which the payload comes to a complete halt after the shock event. The simplicity of this approach lies in the fact that a constant Bingham number for a given shock intensity achieves these terminal conditions.

To calculate the optimal Bingham number, the Bingham number satisfying the velocity terminal condition and the displacement terminal condition are evaluated separately using Eqs. (A.7), (A.8) and (A.10) (Wereley *et al.*, 2011). The time at which the Bingham numbers corresponding to the displacement and velocity terminal condition coincide is the stoppage time. At this coinciding point all the terminal conditions are satisfied. The optimal Bingham number, Bi_o, is given by the following equation (Wereley *et al.*, 2011).

$$Bi_o = \frac{mg}{cv_0} - \frac{1}{1 + e^{\left\{\frac{cS}{mv_0} - 1 - W\left[e^{\left(\frac{cS}{mv_0} - 1\right)}\left(\frac{cS}{mv_0} - 1\right)\right]\right\}}} \tag{A.11}$$

where, $W[\cdot]$ is the Lambert W Function or product log function (Corless *et al.*, 1996).

A.5. Optimal Bingham Number

The optimal Bingham number, Bi_o, varies with viscous damping constant, c, anddrop velocities as shown in Figure A.2. In this case, the EA stroke was taken as S = 15 cm, and payload mass as m = 30 kg. From this chart, the optimal Bingham number, Bi_o, decreases as viscous damping constant increases. Because the viscous forces in the MREA are directly proportional to the viscous damping constant, reducing the viscous damping implies a reduction in the Bingham number in Eq. (A.6). Moreover, the total MREA stroking load is the sum of the passive viscous force and the controllable MR yield force as defined by Eq. (A.2). Therefore, absorbing a given amount of kinetic energy corresponding to a particular drop velocity is a trade-off between viscous damping force and MR yield force (or choice of Bingham number as the control variable). In other words, kinetic energy is dissipated by two stroking load components of the MREA i.e. passive viscous force and MR yield force. If the passive force is relatively low, then a high MR yield force or optimal Bingham number is required to reach the terminal conditions in Eq. (A.10). In contrast, if the passive force is relatively high, then a lower MR yield force or optimal Bingham number is required to reach the terminal conditions in Eq. (A.10). Figure A.2 depicts this design trade-off for an MREA, and a particular design

can be selected based on the requirements of viscous damping constant and the optimal Bingham number.

A second key observation is that if the drop velocity increases, then so too does the required MR yield force or optimal Bingham number. If the drop velocity increases, then the kinetic energy that must be absorbed by the shock isolation mount also increases, which implies that the stroking load must also increase for the available stroke. Because the viscous damping force is fixed for a particular MREA, the increase in kinetic energy is dissipated by an increase in the MR yield force or optimal Bingham number.

A.6. Optimal Time Response of MREA

Different MREA responses based on optimal and non-optimal Bingham numbers for drop-induced shock mitigation is shown in Figure A.3 for a payload mass of m = 30 kg. The optimal Bingham number was found to be Bi_o = 0.78 corresponding to a viscous damping constant, c = 400 Ns/m, and drop velocity, v_o = 5 m/s. The end-stop impact was modeled using a very stiff spring, k_i = 3000 kN/m, and damping ratio c_i = 7500 Ns/m, as shown in Figure A.1 (Wereley et $al.$, 2011)

It is clear from Figure A.3a that the payload utilized the complete EA stroke without experiencing an end-stop impact only when the optimal Bingham number control was implemented, that is, $Bi = Bi_o$. If the Bingham number is less than the optimal Bingham number, or $Bi < Bi_o$, then the payload completes the EA stroke with a non-zero velocity and incurs an end-stop impact. On the other hand, if $Bi > Bi_o$, then the payload did not fully utilize the EA stroke because the MR yield

force is too high.

Figure A.3b presents the deceleration of the payload mass for different Bingham numbers. The payload incurred large peak deceleration due to an end-stop impact when $Bi < Bi_o$. Such excessive deceleration and corresponding loads may result in potential payload damage and are, therefore, undesirable. For cases where $Bi > Bi_o$, the maximum deceleration was much less than the peak decelerations experienced for end-stop impacts. However, the maximum payload decelerations were greater than that for optimal Bingham number control because the MREA stroke was not fully utilized, which led to excessive energy dissipation per unit stroke.

A.7.   Optimal Time Response of MREA for Varying Shocks

This section compares the optimal responses of the payload mass incurred for sink rates of v_o = 5 and 10 m/s. Two different MREA designs are also compared for the same payload mass and MREA stroke, where the designs varied based on choice of viscous damping constants, either c = 100 or c = 700 Ns/m. The optimal Bingham number for each case is tabulated in Table A.1.

The displacement vs. time (Fig. A.4a) and deceleration vs. time (Fig. A.4b), achieved using optimal Bingham control, are shown for the two MREA designs. For all cases utilizing optimal Bingham number control, the payload exhibited a soft landing for either different drop velocities or different viscous damping constants, and satisfied the optimal terminal conditions, as shown in Figure A.4a.

For the high drop velocity case, v_o = 10 m/s, the payload under two MREA designs using optimal Bingham number control rapidly achieved the soft landing and

utilized the available MREA stroke. The low viscous damping case achieved soft landing faster than the high viscous damping case. But, the low viscous damping case required higher optimal Bingham number than the high viscous damping case. This implies that the low viscous damping case needs to more rely on MR yield force over viscous force than the high viscous damping case so as to achieve soft landing. As seen in Fig, A.4b, the initial deceleration of the payload for the low viscous damping case is lower than that for the high viscous damping case. In addition, the deceleration for the low viscous damping case decreased more moderately than that for the high viscous damping case. The duration of the deceleration for the low viscous damping case was slightly shorter than that for the high viscous damping case. The reason is that the high viscous damping case used much more viscous damping than MR yield force for energy absorption of the payload.

For the low drop velocity case, v_o = 5 m/s, the payload under two MREA designs using optimal Bingham number control could achieve the soft landing again. However, the low drop velocity case required smaller optimal Bingham number than the high drop velocity case. In addition, different from the high drop velocity case, the low drop velocity case showed that the duration of the deceleration for the low viscous damping case was much shorter than that for the high viscous damping case. The reason is that, for the high viscous damping case, since its stroking load for dissipating the energy of the payload is dominated by the viscous force, the magnitude of the stroking load becomes small when the damper velocity becomes small. In addition, the damper velocity for the low drop velocity case is smaller than that for the high drop velocity case when the payload reaches close to the rest.

Based on these results, it is advantageous to implement an MREA with low viscous force and high MR yield force, because energy dissipated per unit of stroke can be maximized. This implies that an MREA capable of achieving the largest possible Bingham number would be best for MR shock isolation, as long as the maximum allowable deceleration of the payload is not violated.

A.8.   Conclusions

The drop-induced shock mitigation of a single degree of freedom system employing an adaptive MREA was theoretically analyzed. Terminal trajectory control achieved via selection of an optimal Bingham number was demonstrated via analysis. This optimal Bingham number control algorithm avoided end-stop impact and enabled the payload to utilize the entire MREA stroke for energy absorption. Sub-optimal Bingham numbers resulted in either end-stop impact $(Bi < Bi_o)$ or under-utilization of MREA stroke $(Bi > Bi_o)$, in which sub-optimal solutions led to higher payload decelerations than necessary, thereby increasing probability of damage to the payload. The optimal Bingham number increased as drop velocity, v_o, increased. Therefore, if the impact becomes more intense, then higher yield force is necessary to mitigate the shock load. Also, as viscous damping, c, increased, then the optimal Bingham number decreased, which implies that an MREA design trade-off exists between viscous damping and MR yield force.

By analyzing MREAs with different viscous damping constants, it was shown that is advantageous to implement an MREA with low viscous force and high MR yield force, because energy dissipated per unit of stroke is maximized. An MREA capable of achieving the largest possible Bingham number should be used for

MR shock isolation, as long as the maximum allowable deceleration of the payload is not violated.

References

Cha G, Ju Y S, Ahure L A, and Wereley N M, 2010, Experimental characterization of thermal conductance switching in magnetorheological fluids *Journal of Applied Physics,* Vol. 107, No. 9, 09B505.

Cook E, Hu W and Wereley N M 2007 Magnetorheological Bypass Damper Exploiting Flow Through a Porous Channel *Journal of Intelligent Material Systems and Structures,* Vol. 18, No. 12, pp. 1197-1203.

Corless R M, Gonnet G H, Hare D E G, Jeffrey D J and Knuth D E 1996 On the Lambert W Function *Advances in Computational Mathematics,* Vol. 5, pp. 329-359.

Desjardins S P 2003 The Evolution of Energy Absorption Systems for Crashworthy Helicopter Seats *59th Annual AHS Forum*, Phoenix, AZ, May 6-8.

Hiemenz G J, Choi Y T and Wereley N M 2007 Semi-Active Control of Vertical Stroking Helicopter Crew Seat for Enhanced Crashworthiness *AIAA Journal of Aircraft*, Vol. 44, No. 3, pp. 1031-1034.

Jafri S M M 2004 *Modeling of impact dynamics of a tennis ball with a flat surface*, Master Thesis, Texas A & M University.

Jeon J, and Koo S, 2012, Viscosity and dispersion state of magnetic suspensions *Journal of Magnetism and Magnetic Materials,* 324(4), pp. 424-429.

Mao M, Hu W, Choi, Y T and Wereley N M 2007, A magnetorheological damper with bifold valves for shock and vibration mitigation *Journal of Intelligent Materials and System Structures,* 18 1227-1232.

Mao M, Hu W, Wereley N M, Browne A L and Ulicny J 2009 A Nonlinear Analytical Model for Magnetorheological Energy Absorbers Under Impact Conditions *Proceedings of ASME Conference on SMASIS,* Oxnard, CA, USA.

Thomson W T 1988 *Theory of vibration with applications*, Prentice-Hall International, Inc., New Jersey.

Wereley N M, Choi Y T and Singh H J 2011 Adaptive Energy Absorbers for Drop-Induced Shock Mitigation *Journal of Intelligent Material Systems and Structures,* Vol. 22, No. 6, pp. 515-519.

Woo D, Choi S B, Choi Y T and Wereley N M 2007 Frontal Crash Mitigation Using MR Impact Damper for Controllable Bumper *Journal of Intelligent Material Systems and Structures*, 18:1227-1232.

Table A.1. Optimal Bingham Numbers, Bi_o

Viscous Damping Constant, c [Ns/m]	Drop Velocity, v_o [m/s]	Optimal Bingham Number, Bi_o
100	5	4.933
	10	9.633
700	5	0.229
	10	0.847
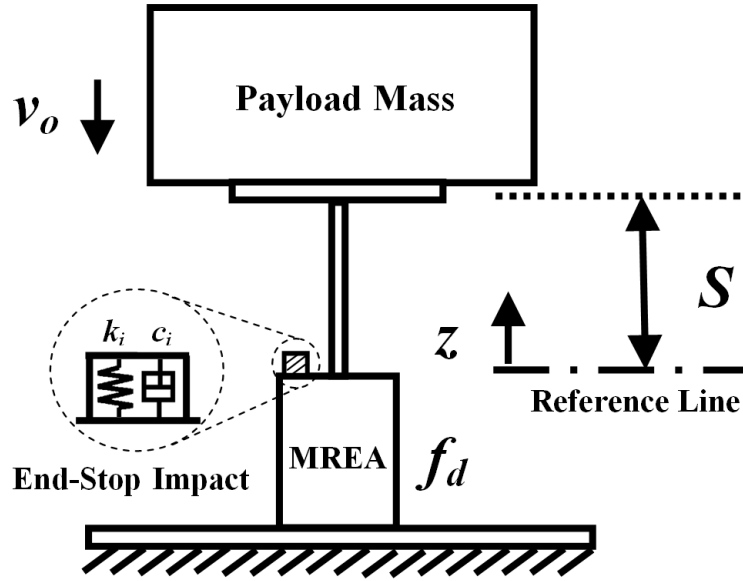
Figure A.1. Configuration of magnetorheological energy absorbing mounts for drop-induced shock mitigation.
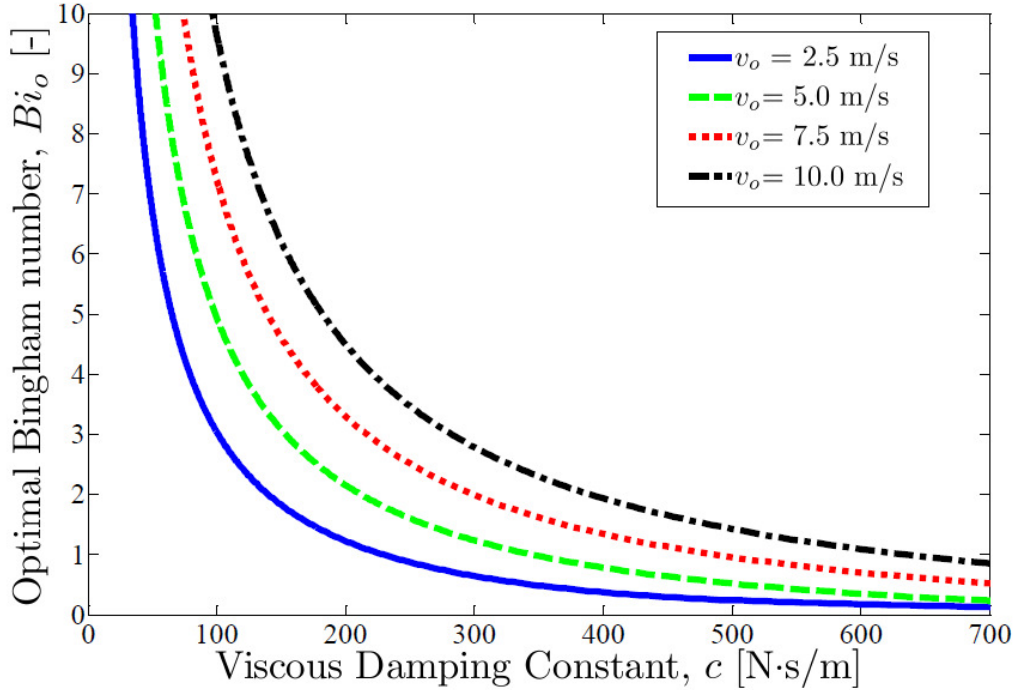
Figure A.2. Optimal Bingham number variation with viscous damping coefficients and drop velocities.
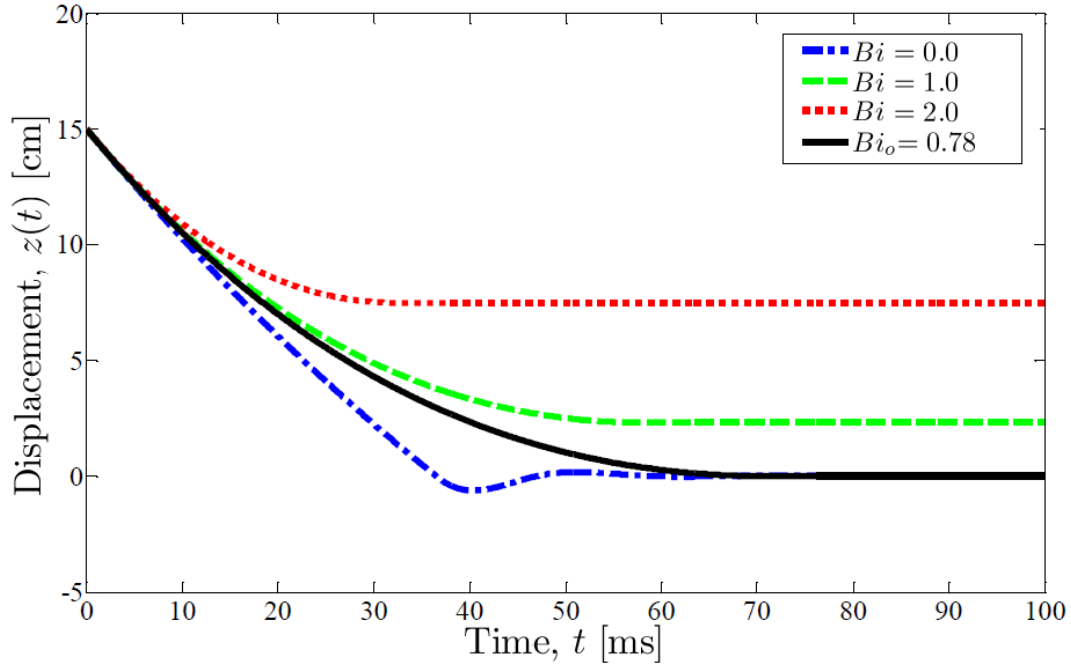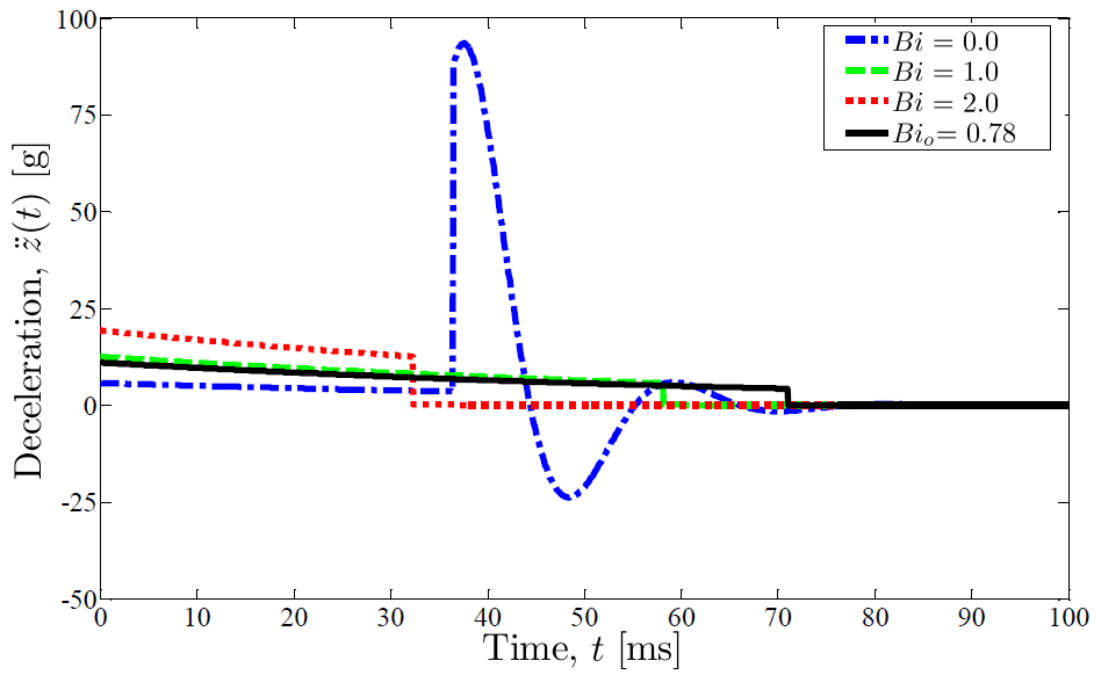
Figure A.3. Payload (a) displacement and (b) deceleration for optimal and non-optimal Bingham numbers.
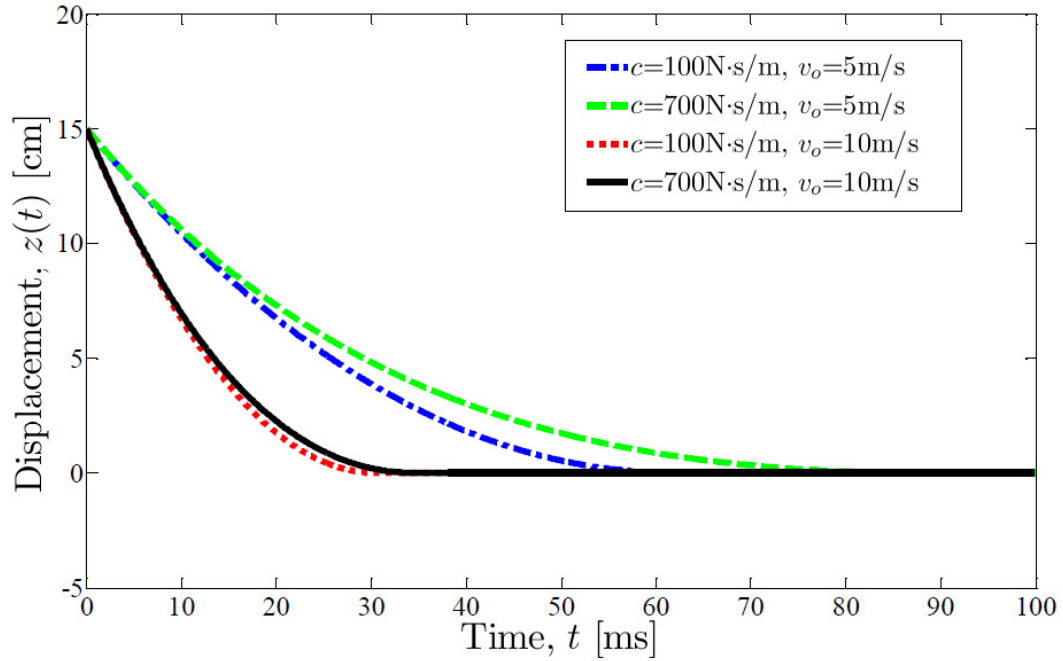
(a)
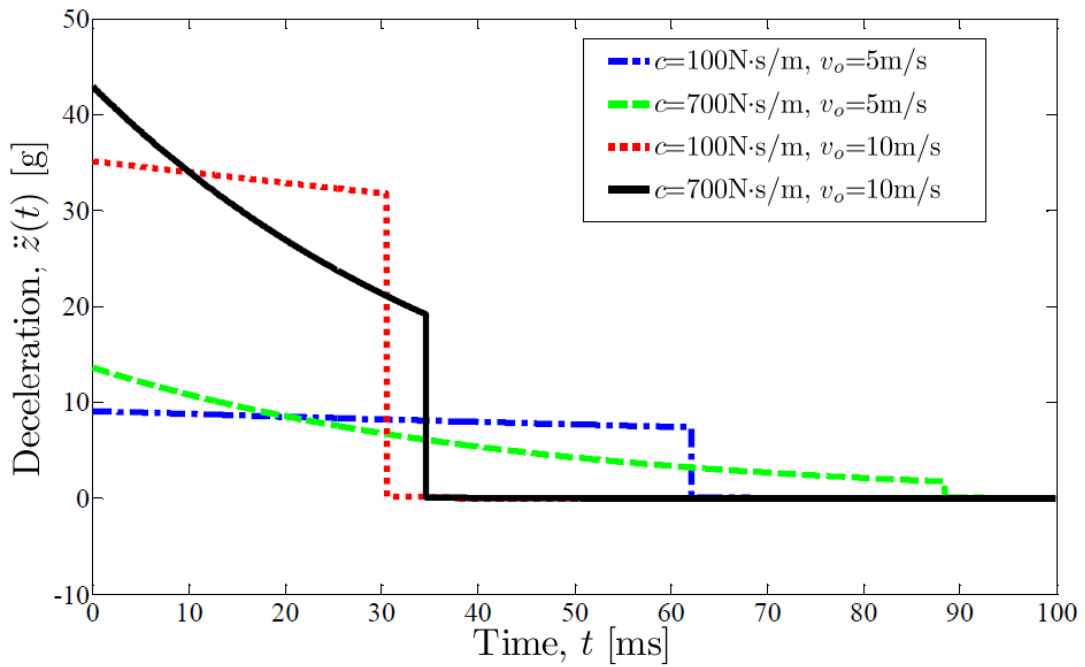
(b)

Figure A.4. Payload (a) displacement and (b) deceleration for varying damping coefficients and drop velocities for optimal Bingham numbers.

Appendix B

Adaptive Magnetorheological Shock Isolation Mounts for Drop-induced Impacts

B.1. Abstract

Nondimensional analysis and optimal control design of adaptive magnetorheological shock isolation (MRSI) mounts are addressed for drop-induced impacts. The governing equation of motion of a single degree-of-freedom under impact was derived, where a magnetorheological energy absorber (MREA), which has controllable stroking load and a passive linear spring, isolate the payload mass from the base that impacts the ground. During the impact event, the payload experiences both a compression and a rebound stroke. During the compression stroke, the payload descends as the MREA dissipates and the spring stores, the energy of impact. During the rebound stroke, the spring releases its stored energy under the control of the MREA. The Bingham number, defined as the ratio of the MREA yield force to its viscous force, is utilized as the control variable. A non-dimensional analysis was conducted using key parameters such as available MREA stroke and Bingham number. The first control objective was to ensure that the payload achieved a *soft landing* (i.e., comes to rest) at the end of the compression

stroke by fully utilizing the available stroke of the MREA. The second control objective was to completely recover the available MREA stroke during rebound, with no overshoot of the equilibrium point, i.e. dead-beat control. It is shown that the optimal MRSI control strategy implies the selection of two distinct Bingham numbers, one for the compression stroke and one for the rebound stroke, which achieve the control objectives.

B.2.   Introduction

Minimizing the load transmitted to a payload as the result of a drop-induced impact is the key performance criterion when designing shock isolation mounts (Hiemenz *et al.*, 2007; Choi and Wereley, 2003; Choi and Wereley, 2005a). When operating in harsh environments, tremendous shock loads can be transmitted to the payload, which is a major cause of concern because high intensity loads may result in payload damage (Choi and Wereley, 2005b; Brigley et al., 2008; Choi and Wereley, 2005c). Generally, shock isolation mounts are equipped with passive energy absorbers (EAs) that are designed on the basis of predetermined loading conditions. However, passive EAs, with their fixed load-stroke profile, are incompatible for real-time operating conditions because of varying impact load intensities. Due to such an incompatibility, adaptive magnetorheological energy absorbers (MREAs) are under consideration for shock mitigation applications (Wereley *et al.*, 2011; Choi and Wereley, 2008; Mao *et al.*, 2007). MREAs have the potential to adapt their load-stroke profile in order to accommodate varying impact conditions (Mao et al., 2007; Browne et al. 2009; Woo et al., 2007). MREAs are conformable to design optimization such that the load-stroke profile of the MREA

can be optimized electronically for a given dynamic range (Nguyen and Choi, 2009) and device volume (Nguyen et al., 2007; Rosenfeld and Wereley, 2004). The major attributes of MREAs are rapidly adjustable stroking load (Zhang et al., 2009; Hongsheng et al., 2009) in response to an applied current input without restoring to mechanical moving parts (Svoboda and Warrick, 1981). Moreover, MREA power consumption is fairly low compared to active feedback control and does not produce instabilities such as control spillover.

Magnetorheological shock isolation (MRSI) mounts are under consideration for a payload descending at a prescribed sink rate. MRSI mounts employ an MREA and a coil spring for isolating the payload from impact, such that, after the initial shock event is over, the suspension could be used either for vibration isolation or mitigation of subsequent impacts. Such suspensions have applications in occupant protection systems in high-speed boats and ground vehicles (Choi and Wereley., 2005a; McManus et al., 2002; Stelzer et al., 2003; Yu et al., 2006) where the nature of impact is repetitive.

A complete MRSI cycle of operation is characterized by two half cycles; first compression and then rebound. When subjected to drop-induced impacts, the payload strokes the damper in compression. The rebound stroke commences when the payload comes to a complete halt after the compression stroke is concluded. A fundamental goal is to utilize the entire EA stroke in order minimize load transmitted to the payload during the drop-induced impact (Wereley et al., 2011). An optimal adjustment of MREA stroking load enables the payload to achieve soft landing, that is, the payload comes to rest after fully utilizing available EA stroke with no end-

stop impact, which occurs when the MREA runs out of stroke. MREA stroking load that is too large causes the payload to stop before the MREA utilizes its available stroke, which induces payload decelerations that are greater than necessary. In contrast, a MREA stroking load that is too low causes the MREA to bottom out, that is, to experience an end-stop impact, which can cause damage to the payload.

Similar to the compression stroke, optimal adjustment of MREA stroking load during the rebound enables the payload to achieve dead-beat control, i.e. to return the payload to equilibrium smoothly while fully recovering the EA stroke. During the rebound stroke, MREA stroking loads that are smaller or larger than the optimal stroking can cause unnecessary payload oscillations or incomplete recovery of EA stroke, respectively.

The performance of MRSI mounts were analyzed, in this study, using key parameters such as EA stroke, time constant and Bingham number. The governing equations of motion were derived and non-dimensional analysis was carried out in order to determine under what conditions a soft landing and dead-beat control is feasible. The Bingham number is shown to be a parameter of utmost importance in effectively controlling the system response.

B.3. Magnetorheological Shock Isolation Mounts

Magnetorheological shock isolation (MRSI) mount for mitigating drop-induced impact is shown in Figure B.1. The payload is a rigid mass, m, isolated from the fastened base by employing a linear spring with stiffness, k, and magnetorheological energy absorber (MREA). The drop-induced impact is modeled as an initial velocity impact with sink rate, v_o, in the negative z direction. The

267

utilizable energy absorber stroke from the equilibrium is S, when the payload is stationary at equilibrium.

The governing equation of motion for the MRSI mount is given as

$$m\ddot{z}(t) = -f_d - kz(t) \tag{B.1}$$

where, f_d is the stroking load of the MREA which has two components. The passive or uncontrollable component of the stroking load is determined by the off-state (Newtonian) behavior of the MR fluid and is proportional to payload velocity, $c\dot{z}(t)$. The electronically controllable component of the stroking load is known as the MR yield force, f_y, so that the total stroking load is

$$f_d = c\dot{z}(t) + f_y sign\{\dot{z}(t)\} \tag{B.2}$$

Therefore, the governing equation of motion of the MRSI mount can be rewritten as

$$m\ddot{z}(t) = -c\dot{z}(t) - f_y sign\{\dot{z}(t)\} - kz(t) \tag{B.3}$$

where

$$sign\{\dot{z}(t)\} = \begin{cases} 1 & if \quad \dot{z}(t) > 0 \\ 0 & if \quad \dot{z}(t) = 0 \\ -1 & if \quad \dot{z}(t) < 0 \end{cases} \tag{B.4}$$

In general, compact MREAs are preferred in order to occupy smaller device volume while minimizing the suspension weight, such compact MREAs typically result in a system that is under-damped, therefore, the damping ratio, ζ, is small.

$$c = 2\,\zeta\sqrt{mk} \;\; ; \;\; \zeta < 1 \tag{B.5}$$

B.3.1. Compression Stroke

The compression stroke begins from the equilibrium point in the negative z direction when the rigid payload is subjected to the initial velocity impact. It is to be noticed that $\dot{z}(t)$ is negative during the compression stroke of the MRSI mount. With this consideration and using Eq. (B.3), the equation of motion for the compression stroke is determined as

$$m\ddot{z}(t) =- c\dot{z}(t) + f_{y_c} - kz(t) \tag{B.6}$$

where, f_{y_c} is the MR yield force of the MREA during the compression stroke. The governing equation of motion, Eq. (B.6), can also be written as follows

$$\ddot{z}(t) + 2\,\zeta\omega_n\dot{z}(t) + {\omega_n}^2\left(z(t) - \frac{f_{y_c}}{k}\right) = 0 \tag{B.7}$$

Assuming a solution of the form

$$z(t) = e^{-\zeta\omega_n t}(P_1 \cos\omega_d t + P_2 \sin\omega_d t) + \frac{f_{y_c}}{k} \tag{B.8}$$

where

$$\omega_n = \sqrt{\frac{k}{m}} \;\; ; \qquad \omega_d = \omega_n\sqrt{1 - \zeta^2} \tag{B.9}$$

Differentiating Eq. (B.8) with respect to time, the payload velocity is determined. The payload acceleration is obtained in a similar fashion by differentiating velocity equation.

$$\dot{z}(t) = \frac{d}{dt}z(t) = e^{-\zeta\omega_n t}[(P_2\omega_d - P_1\zeta\omega_n)\cos\omega_d t$$

$$- (P_1\omega_d + P_2\zeta\omega_n)\sin\omega_d t] \tag{B.10}$$

$$\ddot{z}(t) = \frac{d}{dt}\dot{z}(t) = e^{-\zeta\omega_n t}[(\zeta^2\omega_n^2 - \omega_d^2)(P_1\cos\omega_d t + P_2\sin\omega_d t)$$

$$+ 2\zeta\omega_n\omega_d(P_1\sin\omega_d t - P_2\cos\omega_d t)] \tag{B.11}$$

The constants, P_1 and P_2 are obtained using the initial conditions given as

$$z(0) = 0 \; ; \qquad \dot{z}(0) = -v_o \tag{B.12}$$

The displacement and velocity, Eqs. (B.8) and (B.10), along with the initial conditions determine the constants as

$$P_1 = -\frac{f_{y_c}}{k} \; ; \qquad P_2 = -\frac{f_{y_c}\zeta\omega_n + kv_o}{k\omega_d} \tag{B.13}$$

The compression stroke culminates when the payload comes to a complete stop. The controllability of the MR yield force is a key parameter that determines whether the payload completely utilized the available EA stroke. If the MR yield force is optimal during compression, then the payload would certainly achieve the terminal conditions. Terminal conditions refer to the full utilization of EA stroke with zero payload velocity at the completion of compression stroke.

$$z(t_{s_c}) = -S \; ; \qquad \dot{z}(t_{s_c}) = 0 \tag{B.14}$$

where t_{s_c} is the time at which the compression stroke is concluded. Mathematically, the stoppage time is obtained by equating payload velocity, Eq. (B.10), to zero.

B.3.2. Rebound Stroke

A schematic of one complete cycle of the MRSI mount in response to an impact is shown in Figure B.2. One complete MRSI cycle is comprised of a compression and a rebound stroke. The rebound stroke takes place after the compression stroke is completed. During the rebound, the payload moves in the positive z direction with a positive velocity. Therefore, similar to the compression stroke, the differential equation governing payload response during rebound can be written as

$$m\ddot{z}(t) = - c\dot{z}(t) - f_{y_r} - kz(t) \tag{B.15}$$

or

$$\ddot{z}(t) + 2\zeta\omega_n\dot{z}(t) + \omega_n{}^2\left(z(t) + \frac{f_{y_r}}{k}\right) = 0 \tag{B.16}$$

The MR yield force during rebound is denoted as f_{y_r}, which is distinct from the MR yield force determined for the compression stroke. The major consideration behind tuning a different MR yield force for the rebound stroke is to enable the payload to return to equilibrium with dead-beat control. The MR yield force during compression is determined by the initial conditions, Eq. (B.12), and hence the MREA has to dissipate energy mainly due to initial sink rate. Upon completion of the compression stroke, the energy due to initial sink rate is mitigated completely if controlled optimally. The rebound is determined by a different set of initial conditions, with the goal of the MREA stroking load to control the restoring force of the coil spring. The solution to the rebound equation of motion is of the form

$$z(t) = e^{-\zeta \omega_n t}(P_3 \cos \omega_d t + P_4 \sin \omega_d t) - \frac{f_{y_r}}{k} \qquad \text{(B.17)}$$

with P_3 and P_4 being constants determined from the initial conditions of the rebound stroke, which are the values of displacement and velocity of payload at the end of compression stroke. The velocity and acceleration for rebound stroke assume the same form as for the compression stroke given by Eqs. (B.10) and (B.11) with P_1 and P_2 replaced by P_3 and P_4 respectively.

$$\dot{z}(t) = \frac{d}{dt} z(t) = e^{-\zeta \omega_n t}[(P_4 \omega_d - P_3 \zeta \omega_n) \cos \omega_d t$$
$$- (P_3 \omega_d + P_4 \zeta \omega_n) \sin \omega_d t] \qquad \text{(B.18)}$$

$$\ddot{z}(t) = \frac{d}{dt} \dot{z}(t) = e^{-\zeta \omega_n t}[(\zeta^2 \omega_n^2 - \omega_d^2)(P_3 \cos \omega_d t + P_4 \sin \omega_d t)$$
$$+ 2\zeta \omega_n \omega_d (P_3 \sin \omega_d t - P_4 \cos \omega_d t)] \qquad \text{(B.19)}$$

If the compression stroke is optimally controlled then the initial conditions for the rebound stroke are the terminal conditions as given by Eq. (B.14). Otherwise, the payload would stop after under-utilizing or over-utilizing the EA stroke.

$$\begin{matrix} \text{Rebound} \\ \text{Initial} \\ \text{Conditions} \end{matrix} = \begin{cases} \begin{cases} z(t_{s_c}) = -S & \text{soft landing} \\ z(t_{s_c}) \neq -S & \text{otherwise} \end{cases} \\ \dot{z}(t_{s_c}) = 0 \end{cases} \qquad \text{(B.20)}$$

With this consideration, the constants P_3 and P_4 are obtained from the initial conditions as

$$P_3 = \frac{e^{\zeta \omega_n t_{s_c}}}{\omega_d} \left(\frac{f_{y_r}}{k} + z(t_{s_c}) \right) \left(\omega_d \cos \omega_d t_{s_c} - \zeta \omega_n \sin \omega_d t_{s_c} \right) \tag{B.21}$$

$$P_4 = \frac{e^{\zeta \omega_n t_{s_c}}}{\omega_d} \left(\frac{f_{y_r}}{k} + z(t_{s_c}) \right) \left(\omega_d \sin \omega_d t_{s_c} + \zeta \omega_n \cos \omega_d t_{s_c} \right) \tag{B.22}$$

The rebound stroke is completed when the payload comes to a stop again. It is desirable to have the payload return to equilibrium smoothly after a full cycle is completed. In other words, the rebound stroke has to be optimally controlled. Therefore, the terminal conditions for the rebound phase are

$$z(t_{s_r}) = 0 ; \qquad \dot{z}(t_{s_r}) = 0 \tag{B.23}$$

where, t_{s_r} is the time when rebound stroke is concluded. Similarly to the compression stroke, the stoppage time t_{s_r} can be obtained by equating the payload velocity during rebound stroke to zero or alternatively

$$t_{s_r} = t_{s_c} + \frac{\pi}{\omega_d} \tag{B.24}$$

B.4. Nondimensional Analysis

The governing equation of motion and its solution are normalized using parameters such as EA stroke, S, and time constant, τ. The Bingham number, Bi, is defined as the ratio of MR yield force to the viscous damping force of MREA. The non-dimensional quantities are denoted as $(\bar{\cdot})$ and the normalizing parameters are given as

$$\bar{z}(\bar{t}) = \frac{z(t)}{S}$$

$$\bar{t} = \frac{t}{\tau}$$

$$\tau = \frac{m}{c}$$

$$Bi = \frac{f_y}{cv_o} \tag{B.25}$$

B.4.1. Compression Stroke

Using the parameters defined in Eq. (B.25), we obtain the normalized displacement, velocity and acceleration from Eqs. (B.8), (B.10) and (B.11) respectively.

$$\bar{z}(\bar{t}) = (P_{1n} \cos \bar{\omega}_d \bar{t} + P_{2n} \sin \bar{\omega}_d \bar{t}) e^{\frac{-\bar{t}}{2}} + 4 Bi_c \bar{v}_o \, \zeta^2 \tag{B.26}$$

$$\dot{\bar{z}}(\bar{t}) = \frac{d}{d\bar{t}} \bar{z}(\bar{t}) = e^{\frac{-\bar{t}}{2}} \left[\left(P_{2n} \bar{\omega}_d - \frac{P_{1n}}{2} \right) \cos \bar{\omega}_d \bar{t} \right.$$

$$\left. - \left(P_{1n} \bar{\omega}_d + \frac{P_{2n}}{2} \right) \sin \bar{\omega}_d \bar{t} \right] \tag{B.27}$$

$$\ddot{\bar{z}}(\bar{t}) = \frac{d}{d\bar{t}} \dot{\bar{z}}(\bar{t}) = e^{\frac{-\bar{t}}{2}} \left[\left(\frac{1}{4} - \bar{\omega}_d{}^2 \right) (P_{1n} \cos \bar{\omega}_d \bar{t} + P_{2n} \sin \bar{\omega}_d \bar{t}) \right.$$

$$\left. + \bar{\omega}_d (P_{1n} \sin \bar{\omega}_d \bar{t} - P_{2n} \cos \bar{\omega}_d \bar{t}) \right] \tag{B.28}$$

where, Bi_c, is the Bingham number corresponding to the MR yield force during compression stroke and

$$\bar{\omega}_d = \frac{\sqrt{1-\zeta^2}}{2\zeta} \quad ; \quad \bar{v}_o = \frac{v_o}{S/\tau} \tag{B.29}$$

with constants

$$P_{1n} = \frac{P_1}{S} = -4Bi_c \bar{v}_o \, \zeta^2$$

$$P_{2n} = \frac{P_2}{S} = -\frac{1}{\bar{\omega}_d} (2Bi_c \bar{v}_o \, \zeta^2 + \bar{v}_o)$$

(B.30)

The terminal conditions for soft landing during compression stroke in a normalized form are given as

$$\bar{z}(\bar{t}_{s_c}) = -1; \quad \dot{\bar{z}}(\bar{t}_{s_c}) = 0$$

(B.31)

The optimal Bingham number for the compression stroke, Bi_c^o, is the Bingham number that satisfies the terminal conditions for a soft landing. In other words, if $Bi_c = Bi_c^o$ then the terminal conditions for the compression stroke are fulfilled. Using the non-dimensional velocity given by Eq. (B.27) and the normalized terminal condition for velocity given by Eq. (B.31), the non-dimensional time to complete the compression stroke is obtained.

$$\dot{\bar{z}}(\bar{t}_{s_c}) = e^{\frac{-\bar{t}_{s_c}}{2}} \left[\left(P_{2n} \bar{\omega}_d - \frac{P_{1n}}{2} \right) \cos \bar{\omega}_d \bar{t}_{s_c} - \left(P_{1n} \bar{\omega}_d + \frac{P_{2n}}{2} \right) \sin \bar{\omega}_d \bar{t}_{s_c} \right] = 0 \quad \text{(B.32)}$$

Rearranging,

$$\bar{t}_{s_c} = \frac{1}{\bar{\omega}_d} \tan^{-1} \left(\frac{2\bar{\omega}_d P_{2n} - P_{1n}}{2\bar{\omega}_d P_{1n} + P_{2n}} \right)$$

(B.33)

The completion time for compression stroke is a function of optimal Bingham number because the constants P_{1n} and P_{2n} are dependent on the optimal Bingham number. Therefore,

$$\bar{t}_{s_c} = f(Bi_c^o)$$

(B.34)

Terminal conditions also specify that at the instant when the compression stroke is finished, the EA stroke should also be completely utilized. Therefore, equating the nondimensional displacement to the terminal condition for compression stroke at the stoppage time, $\bar{t}_{s_c}$, we obtain

$$\bar{z}\left(\bar{t}_{s_c}\right) = \left(P_{1n} \cos \bar{\omega}_d \bar{t}_{s_c} + P_{2n} \sin \bar{\omega}_d \bar{t}_{s_c}\right)e^{\frac{-\bar{t}_{s_c}}{2}} + 4Bi_c^o \bar{v}_o\, \zeta^2 = -1 \qquad \text{(B.35)}$$

Rearranging, we obtain the equation for optimal Bingham number for soft landing which is solved numerically

$$Bi_c^o = -\frac{1}{4\,\bar{v}_o\zeta^2}\left[1 + \left(P_{1n} \cos \bar{\omega}_d \bar{t}_{s_c} + P_{2n} \sin \bar{\omega}_d \bar{t}_{s_c}\right)e^{\frac{-\bar{t}_{s_c}}{2}}\right] \qquad \text{(B.36)}$$

Eq. (B.36) is the equation for optimal Bingham number for soft landing during the compression stroke. This equation involves an unknown parameter, Bi_{o_c}, which is a function of itself. The optimal Bingham number is therefore determined using a simple numerical method called Fixed Point Iteration.

$$Bi_c^o = f(Bi_c^o) \qquad \text{(B.37)}$$

B.4.2. Rebound Stroke

The non-dimensional displacement, velocity and acceleration for the rebound stroke are obtained in a similar manner as for the compression stroke. The non-dimensional displacement is given as

$$\bar{z}(\bar{t}) = (P_{3n} \cos \bar{\omega}_d \bar{t} + P_{4n} \sin \bar{\omega}_d \bar{t})e^{\frac{-\bar{t}}{2}} - 4Bi_r \bar{v}_o\, \zeta^2 \qquad \text{(B.38)}$$

The normalized velocity and acceleration assume the same form as Eqs. (B.27) and (B.28) by replacing the constants P_{1n} and P_{2n} with P_{3n} and P_{4n} respectively. The constants for the rebound stroke are given as

$$P_{3n} = \frac{P_3}{S} = e^{\frac{\bar{t}_{sc}}{2}} \left(4Bi_r \bar{v}_o \, \zeta^2 + \bar{z}(\bar{t}_{sc}) \right) \left(\cos \bar{\omega}_d \bar{t}_{sc} - \frac{1}{2\bar{\omega}_d} \sin \bar{\omega}_d \bar{t}_{sc} \right) \tag{B.39}$$

$$P_{4n} = \frac{P_4}{S} = e^{\frac{\bar{t}_{sc}}{2}} \left(4Bi_r \bar{v}_o \, \zeta^2 + \bar{z}(\bar{t}_{sc}) \right) \left(\omega_d \sin \bar{\omega}_d \bar{t}_{sc} + \frac{1}{2\bar{\omega}_d} \cos \bar{\omega}_d \bar{t}_{sc} \right) \tag{B.40}$$

The terminal conditions for the rebound stroke are such that the payload returns to equilibrium smoothly and without any oscillations. The non-dimensional terminal conditions are satisfied only when the rebound stroke is determined by a different optimal Bingham number, $Bi_r = Bi_r^o$.

$$\bar{z}(\bar{t}_{sr}) = 0; \quad \dot{\bar{z}}(\bar{t}_{sr}) = 0 \tag{B.41}$$

The non-dimensional time when the payload completes the rebound stroke can be obtained similar to compression cycle by equating the normalized velocity to the terminal condition for rebound stroke. Alternatively,

$$\bar{t}_{sr} = \bar{t}_{sc} + \frac{\pi}{\bar{\omega}_d} \tag{B.42}$$

At this rebound completion time, the terminal condition for displacement should also be satisfied, i.e.

$$\bar{z}(\bar{t}_{sr}) = \left(P_{3n} \cos \bar{\omega}_d \bar{t}_{sr} + P_{4n} \sin \bar{\omega}_d \bar{t}_{sr} \right) e^{\frac{-\bar{t}_{sr}}{2}} - 4Bi_r^o \bar{v}_o \, \zeta^2 = 0 \tag{B.43}$$

Rewriting,

$$Bi_r^o = \frac{1}{4\,\bar{v}_o\zeta^2}\left(P_{3n}\cos\bar{\omega}_d\bar{t}_{s_r} + P_{4n}\sin\bar{\omega}_d\bar{t}_{s_r}\right)e^{\frac{-\bar{t}_{s_r}}{2}} \tag{B.44}$$

The optimal Bingham number for rebound stroke is also calculated via the same Fixed Point Iteration numerical approach as for the compression stroke because the solution assumes the same form as below:

$$Bi_r^o = f(Bi_r^o) \tag{B.45}$$

B.5. Results and Discussion

Analysis of the magnetorheological shock isolation mount was carried out for different Bingham numbers, i.e. different MREA stroking loads, for a shock modeled as initial velocity impact. The parameters of the MRSI mount are tabulated in Table B.1. Two approaches were analyzed based on adjusting MREA stroking load during each phase of the controlled impact response The first approach had the sole objective of achieving a soft landing during the compression stroke, and so used the same constant applied current (Bingham number) for the compression and rebound phase of the impact response. The second approach had the objective of achieving both a soft landing during the compression stroke and dead-beat control during the rebound stroke as the payload returns to the equilibrium point with no oscillation, so that the Bingham (or applied current) for the compression and rebound strokes are optimally tuned.

B.5.1. Objective 1: Soft Landing during Compression

The non-dimensional displacement, velocity and acceleration are plotted for the MRSI mount for an initial velocity impact of 5 m/s for three different MR yield forces (i.e. Bingham numbers) shown in Figure B.3. For a given case, the current

applied to the MREA was held constant throughout the complete cycle of MRSI mount (i.e. $Bi_c = Bi_r$) in order to determine the payload response during compression and rebound stroke for same controllable yield force. The optimum Bingham number for the compression stroke was found to be Bi_c^o=0.4356. The three different MR yield forces characterized by the Bingham numbers were selected as $Bi_c = Bi_r = 0.5Bi_c^o$, Bi_c^o and $1.5Bi_c^o$. It is observable from the non-dimensional displacements that for the Bingham number less then optimum, $Bi_c = 0.5Bi_c^o$, the payload experienced an end-stop impact as shown in the figure. In other words, the EA stroke for smaller Bingham number corresponding to smaller MR yield force was not sufficient and therefore resulted in an infeasible solution characterized by an end-stop impact.

The payload experienced smooth landing with full utilization of EA stroke and without an end-stop impact for optimum Bingham number, $Bi_c = Bi_c^o$, during the compression stroke. However, the payload could not reach the equilibrium after completing the rebound stroke when the rebound MR yield force was tuned to optimal compression Bingham number, $Bi_r = Bi_c^o$. The spring energy was not sufficient to overcome the resistance provided by optimal MR yield force for compression and, hence, the payload could not completely recover EA stroke and the equilibrium point was established at a new position.

When the yield force was increased above its optimum value, $Bi_c = 1.5Bi_c^o$, the payload could not utilize the available EA stroke completely during compression. The entire payload energy, which could have been dissipated over the available entire stroke, was expended over a shorter EA stroke. After the compression stroke

279

was finished, the spring restoring force pushed the payload towards the equilibrium. Since the MR yield force was extremely high for $Bi_r = 1.5 Bi_c^o$ when compared to the case of $Bi_r = Bi_c^o$, the recovery of EA stroke during rebound was even smaller.

Figures B.3b and B.3c correspond to the nondimensional velocity and acceleration of the payload for different controllable MR yield forces. It is quite discerning that the maximum acceleration for the payload increased with increase in Bingham number while ignoring the infeasible case when the payload experienced end-stop impact. The higher acceleration of payload was due to dissipation of payload energy over shorter EA stroke resulting in higher kinetic energy dissipation per unit stroke. Another important phenomenon to be noticed was the sudden change in the acceleration, known as jerk, during switching from compression to rebound stroke. The reason behind such a phenomenon was the abrupt variation in velocity profile from compression to rebound stroke i.e. the slopes of velocities were different between the end of compression stroke and the beginning of rebound stroke as shown in Figure B.3b.

The nondimensional forces experienced by payload, defined by Eq. (B.46), during the complete cycle were summation of spring resistive forces and MREA stroking load comprising of passive viscous forces and controllable yield forces as shown in Figure B.4. The motion of the payload is represented by the arrows on the plot. The payload forces were in accordance to the acceleration responses for different Bingham numbers. Disregarding the infeasible response for an end-stop impact for the case $Bi_c = Bi_r = 0.5 Bi_c^o$, the payload forces were observed to be high for larger Bingham number. The optimum Bingham number for the

compression stroke yielded a soft landing but was too high for rebound stroke such that the payload never reached the equilibrium point.

$$\bar{F}_P(\bar{t}) = \frac{m\ddot{z}(t)}{cv_o} = \frac{\ddot{\bar{z}}(\bar{t})}{\bar{v}_o}$$ (B.46)

The invariable MR yield force or the Bingham number, which was same for compression as well as rebound stroke, determined a feasible soft landing during compression for an optimal case but was undesirable for rebound stroke since the payload never recovered the EA stroke completely. This was due to the fact that nature of compression and rebound strokes were different because both were determined by different sets of initial conditions. The compression stroke was mainly defined by the initial sink rate which was entirely mitigated at the completion of compression stroke. However, the rebound stroke was governed by the end-conditions of compression stroke. Therefore, the payload response could be optimized for both compression and rebound stroke if the Bingham number was adjusted optimally for both half cycles.

B.5.2. Objective 2: Soft Landing during Compression and Dead-beat Control during Rebound

The optimal payload response for the compression as well as rebound stroke is plotted in Figure B.5. The Bingham numbers for compression and rebound stroke were tuned to their respective optimal values such that $Bi_c = Bi_c^o$ and $Bi_r = Bi_r^o$. Furthermore, the optimal Bingham number for the compression stroke was distinct from that for rebound stroke i.e. $Bi_c^o \neq Bi_r^o$.

The non-dimensional displacement shown in Figure B.5a reveals that the payload experienced smooth landing at the completion of compression stroke for the optimal Bingham number of Bi_c^o=0.4356 for the sink rate of 5 m/s. The rebound stroke was governed by a different optimal Bingham number enabling the payload to recover the EA stroke with no oscillations. The optimal Bingham number for the rebound stroke was estimated to be Bi_r^o=0.2041. It was observed that the optimal Bingham number for compression stroke was larger than that for the rebound stroke. In other words, the energy dissipated over the EA stroke during compression due to an initial velocity impact was greater than the energy dissipated during rebound stroke due to energy released by spring i.e. $Bi_c^o > Bi_r^o$.

The nondimensional velocity and acceleration are plotted in Figure B.5b and B.5c. The abrupt change in velocity between the termination of compression stroke and the commencement of rebound stroke caused the jerk as shown in acceleration plot. A relatively less intense jerk was observed at the end of rebound stroke due to slight smooth variation of velocity. The nondimensional payload force plot shows the optimal forces for compression as well as rebound stroke in Figure B.6.

The different optimal Bingham numbers for the compression and rebound stroke determined soft landing during compression and dead-beat control during rebound. The benefit of tuning the Bingham number optimally between the compression and rebound strokes was to enable the payload to reach the equilibrium point such that it could mitigate subsequent shock loads if any were to occur.

B.6.   Conclusions

In this study, magnetorheological shock isolation (MRSI) mounts, suitable for optimal compression and rebound performance, were theoretically analyzed for a rigid payload subjected to an initial velocity impact. The governing equations were normalized using parameters such as EA stroke, time constant and Bingham number. Nondimensional Bingham number was found to be the most important parameter governing the response of system for both compression and rebound stroke. Optimum Bingham numbers which satisfied the terminal conditions of soft landing for compression stroke and dead-beat control for rebound stroke were evaluated. Two different approaches were applied based on the optimal tuning of MR yield force defined by optimal Bingham numbers.

When the Bingham number for the compression stroke was identical to that of the rebound stroke, it was observed that suboptimal Bingham numbers resulted in either end-stop impact or under-utilization of EA stroke during compression stroke. It was determined that the optimal Bingham number for the compression led to a soft landing but that optimal Bingham number did not generally yield desirable response for the rebound, that is, deadbeat control to the payload's equilibrium point was not achieved.

In order to achieve the optimal response for compression as well as rebound stroke, a second approach was employed in which the Bingham numbers were tuned to the distinct optimal values for both compression and rebound stroke. By doing so, the soft landing was achieved for compression stroke and dead-beat control was observed for rebound stroke. In addition, the optimal Bingham number was found to

be higher for compression stroke because the kinetic energy associated with the payload due to initial velocity impact was relatively higher than energy released by the coil spring during rebound stroke.

References

Brigley M, Choi Y-T and Wereley N M 2008 Experimental and Theoretical Development of Multiple Fluid Mode Magnetorheological Isolators *Journal of Guidance, Control, and Dynamics*, 31:449-459.

Browne A L, McCleary J D, Namuduri C S and Webb S R 2009 Impact Performance of Magnetorheological Fluids *Journal of Intelligent Material Systems and Structures*, 20:723-728.

Choi Y-T and Wereley N M 2008 Shock Isolation Systems Using Magnetorheological Dampers *ASME Journal of Vibration and Acoustics*, Volume 130:024503.

Choi Y-T and Wereley N M 2005a Semi-Active Vibration Isolation Using Magnetorheological Isolators *Journal of Aircraft*, 42:1244-1251.

Choi Y-T and Wereley N M 2005b Mitigation of Biodynamic Response to Vibratory and Blast-induced Shock Loads Using Magnetorheological Seat Suspensions *Proc. IMechE Part D: J. Automobile Engineering*, 219:741-753.

Choi Y-T and Wereley N M 2005c Biodynamic Response Mitigation to Shock Loads Using Magnetorheological Helicopter Crew Seat Suspensions *Journal of Aircraft*, 42:1288-1295.

Choi Y-T and Wereley N M 2003 Vibration Control of a Landing Gear System Featuring Electrorheological/Magnetorheological Fluids *Journal of Aircraft*, 40:432-439.

Hiemenz G J, Choi Y-T and Wereley N M 2007 Semi-Active Control of Vertical Stroking Helicopter Crew Seat for Enhanced Crashworthiness *Journal of Aircraft*, 44:1031-1034.

Hongsheng H, Jiong W, Suxiang Q, Yancheng L and Xuezheng J 2009 Investigation on Controllability of a Magnetorheological Gun Recoil Damper *International Conference on Information and Automation*, 1044-1049 .

Mao M, Hu W, Choi Y-T and Wereley N M 2007 A Magnetorheological Damper with Bifold Valves for Shock and Vibration Mitigation *Journal of Intelligent Material Systems and Structures*, 18:1227-1232.

McManus S J, St. Clair K A, Boileau P E, Boutin J and Rakheja S 2002 Evaluation of Vibration and Shock Attenuation Performance of a Suspension Seat with a Semi-active Magnetorheological Fluid Damper *Journal of Sound and Vibration,* 253:313-327.

Meirovitch L 2001 *Fundamentals of Vibrations*, McGraw-Hill Companies, Inc., New York.

Nguyen Q-H and Choi S B 2009 Optimal Design of a Vehicle Magnetorheological Damper Considering Damping Force and Dynamic Range *Smart Materials and Structures*, 18:015013.

Nguyen Q-H, Han Y-M, Choi S B and Wereley N M 2007 Geometry Optimization of MR valves Constrained in a Specific Volume Using the Finite Element Method *Smart Materials and Structures*, 16:2242-2252.

Rosenfeld N and Wereley N M 2004 Volume-Constrained Optimization of Magneto- and Electro-rheological Valves and Dampers *Smart Materials and Structures*, 13:1303-1313.

Svoboda C M and Warrick J C 1981 *Design and Development of Variable Load Energy Absorber,* TR 3023.

Stelzer G J, Schulz M J, Kim J and Allemang R J 2003 A Magnetorheological Semi-Active Isolator to Reduce Noise and Vibration Transmissibility in Automobiles *Journal of Intelligent Material Systems and Structures*, 14:743-765.

Wereley N M, Choi Y-T and Singh H J 2011 Adaptive Energy Absorbers for Drop-induced Shock Mitigation *Journal of Intelligent Material Systems and Structures*, 22:515-519.

Woo D, Choi S B, Choi Y-T and Wereley N M 2007 Frontal Crash Mitigation Using MR Impact Damper for Controllable Bumper *Journal of Intelligent Material Systems and Structures*, 18:1227-1232.

Yu M, Liao C R, Chen W M and Huang S L 2006 Study on MR Semi-Active Suspension System and its Road Testing *Journal of Intelligent Material Systems and Structures*, 17:801-806.

Zhang L, Ma F and Wang J 2009 Study of Control System of Magnetorheological Dampers under Impact Load *International Conference on Intelligent Computation Technology and Automation*, 894-897 .

Table B.1. Parameters of MRSI mount

Parameter	Symbol	Value	Units
Payload Mass	m	30	*kg*
Spring Stiffness	k	20	*kN/m*
MREA Damping Constant	c	500	*N-s/m*
EA Stroke	S	10	*cm*
Sink Rate	v_o	5	*m/s*
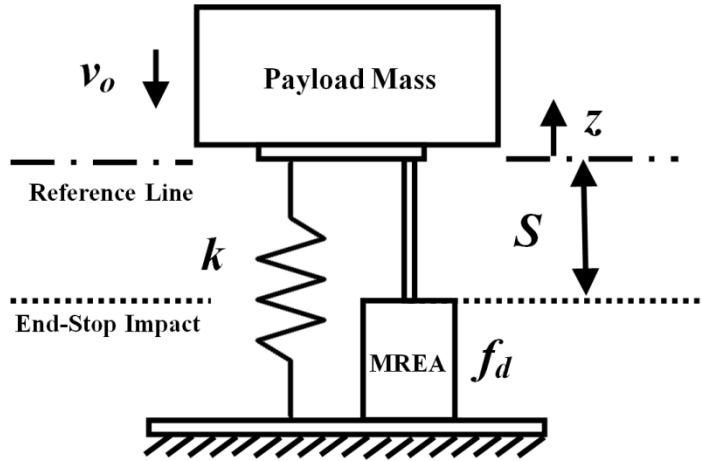
Figure B.1. Configuration of magnetorheological shock isolation (MRSI) mount.
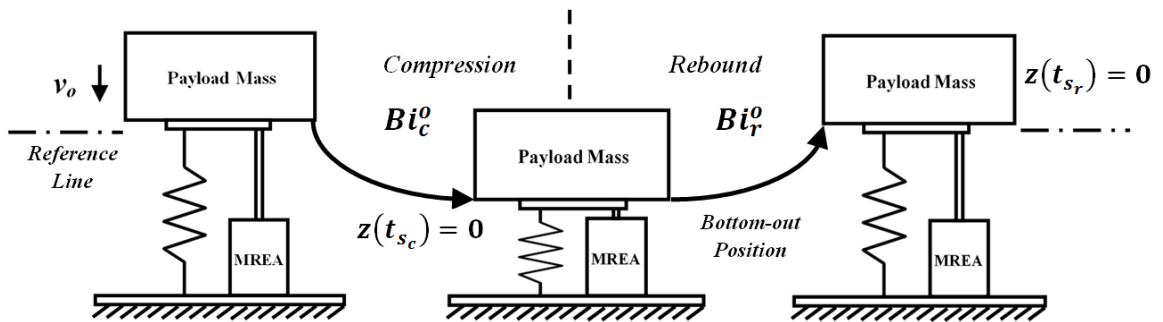
Figure B.2. Schematic of optimal performance of MRSI mount during a complete cycle.
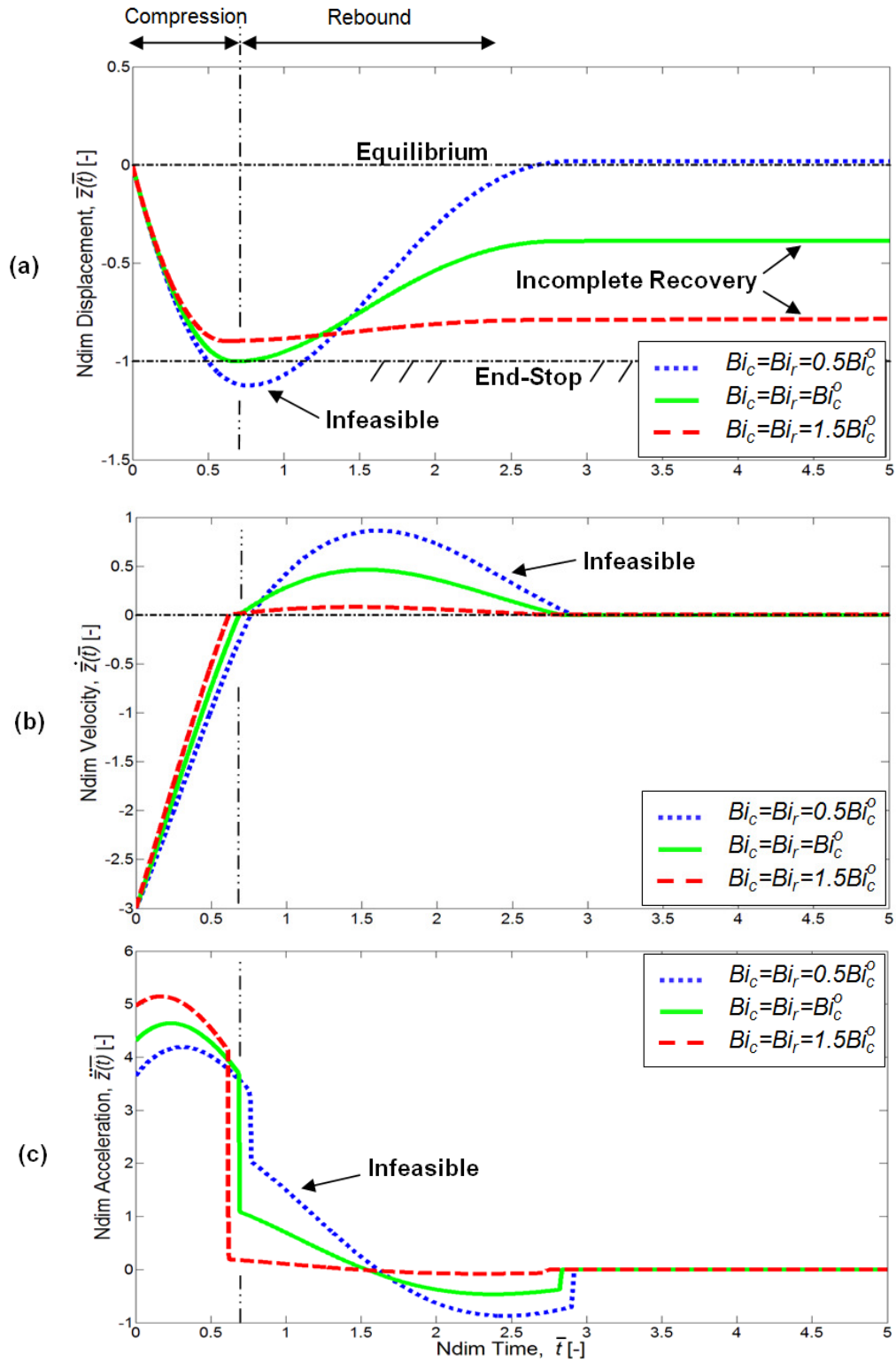
Figure B.3. Nondimensional (a) displacement, (b) velocity and (c) deceleration at

v_0= 5 m/s, Bi_c^o=0.4356.

Figure B.4. Nondimensional payload force at v_0= 5 m/s, Bi_c^o=0.4356.

Figure B.5. Optimal nondimensional (a) displacement, (b) velocity and (c) acceleration at $v_0 = 5$ m/s, $Bi_c^o = 0.4356$ and $Bi_r^o = 0.2041$.
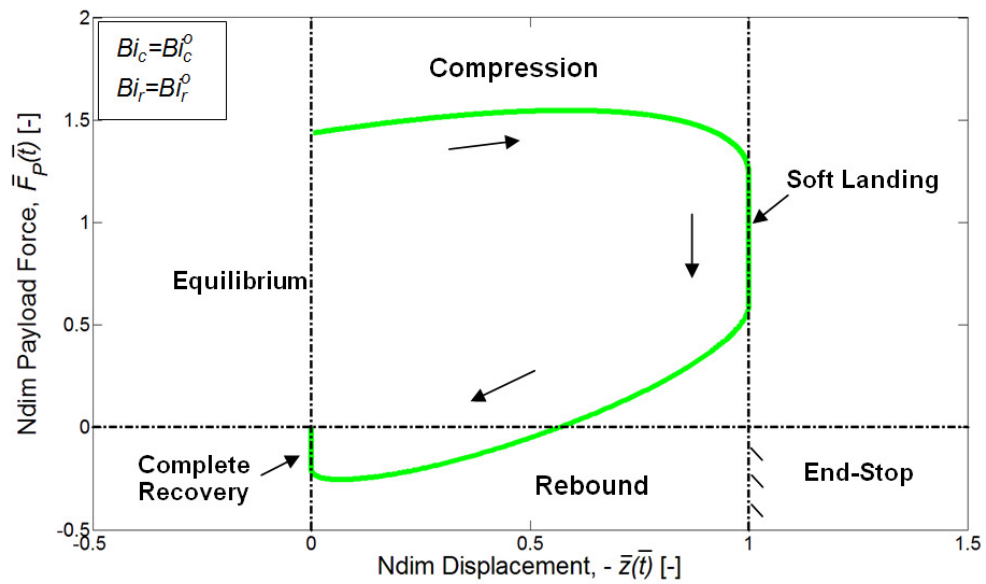
Figure B.6. Optimal nondimensional payload force at $v_0 = 5$ m/s, $Bi_c^o = 0.4356$ and $Bi_r^o = 0.2041$.

Bibliography

AGARD 1996 Anthropomorphic Dummies for Crash and Escape System Testing *AGARD-AR-330*.

Ahmadian M, and Poynor J C 2001 An evaluation of magneto-rheological dampers for controlling gun recoil dynamics *Shock and Vibration*, Vol. 8, pp. 147-155.
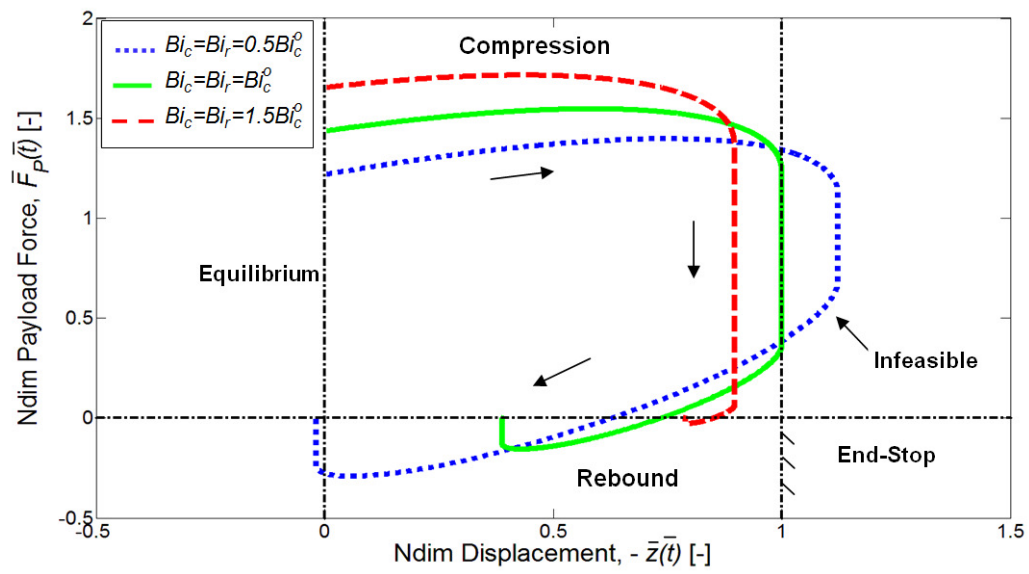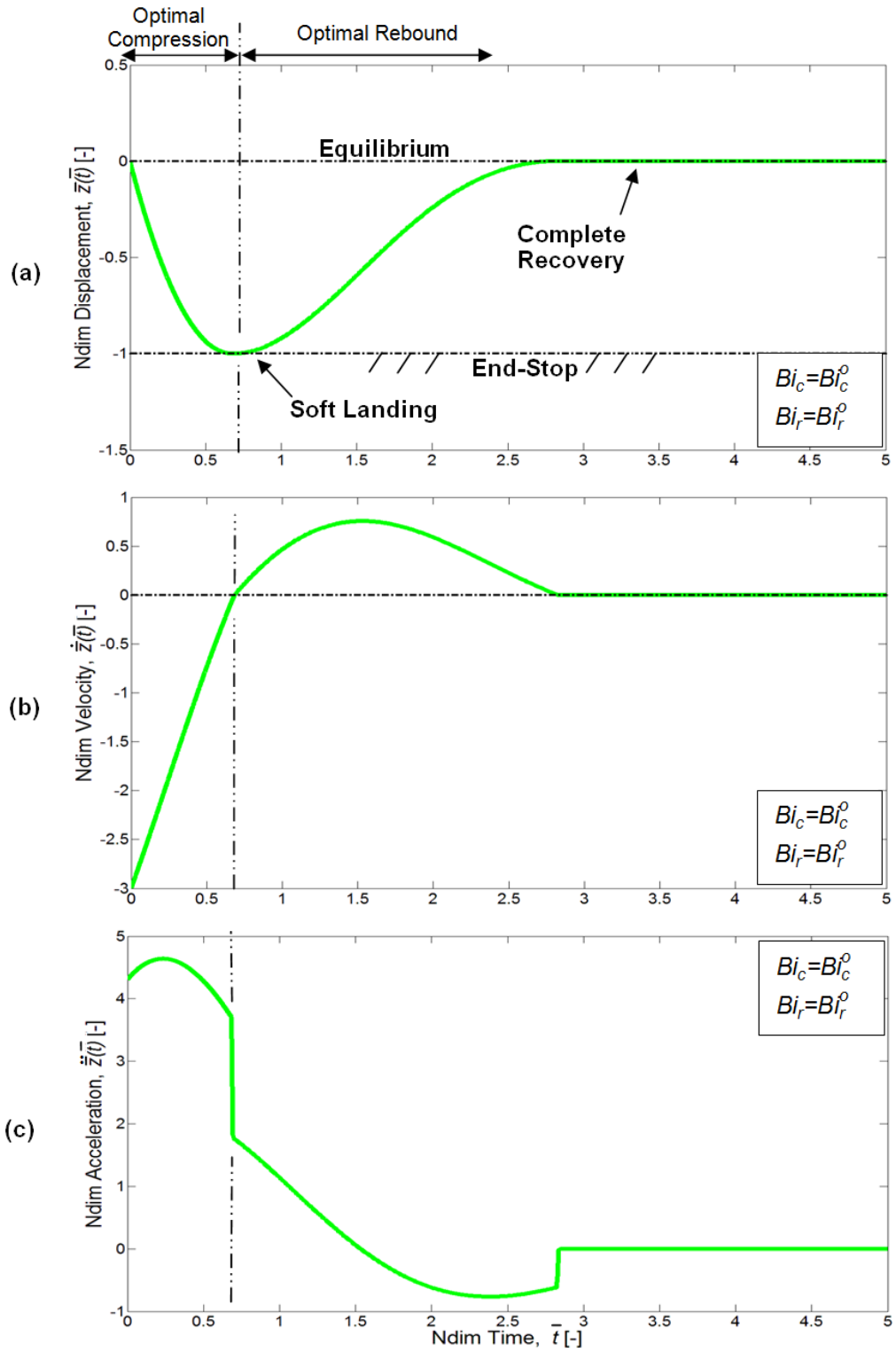
Ahmadian M, Appleton R, and Norris J A 2002 An analytical study of fire out of battery using magneto-rheological dampers *Shock and Vibration*, Vol. 9, pp. 129-142.

Ahmadian M, and Norris J A 2004 Rheological controllability of double-ended MR dampers subjected to impact loading *Proceeding of SPIE*, 5386:185-194.

Axelsson H and Sundqvist O 2003 Mine Clearance Vehicles, Crew Safety Standard *The Swedish Defense Material Administration,* VoVC 14 910:1142/03.

Bai X-X, Wereley N M, Hu W and Wang D-H 2012 A Bidirectional Controllable Magnetorheological Energy Absorber for Shock and Vibration Isolation Systems *ASME Conference on SMASIS* doi:10.1115/SMASIS2012-8250.

Bartsch A, Benzel E, Miele V, Morr D and Prakash V 2012 Hybrid III Anthropomorphic Test Device (ATD) Response to Head Impacts and Potential Implications for Athletic Headgear Testing *Accident Analysis and Prevention*, Vol. 48, pp. 285-291.

Batterbee D C, Sims N D, Stanway R and Rennison M 2007 Magnetorheological Landing Gear: Validation Using Experimental Data *Smart Materials and Structures,* Vol. 16, No. 6, pp. 2441-52.

Beeman S M, Kemper A R, Madigan M L, Franck C T and Loftus S C 2012 Occupant Kinematics in Low-Speed Frontal Sled Tests: Human Volunteers, Hybrid III ATD, and PMHS *Accident Analysis and Prevention*, Vol. 47, pp. 128-139.

Beeman S M, Kemper A R, Madigan M L and Duma S M 2013 Kinetic and Kinematic Responses of Post Mortem Human Surrogates and the Hybrid III ATD in High-Speed Frontal Sled Tests *Accident Analysis and Prevention*, Vol. 55, pp. 34-47.

Brigley M, Choi Y-T, Wereley N M and Choi S B 2007 Magnetorheological Isolators Using Multiple Fluid Modes *Journal of Intelligent Material Systems and Structures,* Vol. 18, No. 12, pp. 1143-48.

Browne A L, McCleary J, Namuduri C S, Webb S R, 2009, Impact performance of magnetorheological fluids *Journal of Intelligent Material Systems and Structures*, Vol. 20, pp. 723-728.

Campbell R F 1982 Vehicle Crashworthy Seat *US Patent* 4,358,154.

Carlson J D, Catanzarite D M and St. Clair K A 1996 Commercial Magnetorheological Fluid Devices *International Journal of Modern Physics B*, Vol. 10, No. 23, pp. 2857-65.

Cha G, Ju Y S, Ahure L A, and Wereley N M 2010 Experimental characterization of thermal conductance switching in magnetorheological fluids *Journal of Applied Physics,* Vol. 107, No. 9, 09B505.

Chen C J and Macagno E O 1979 Fluid and thermodynamic characteristics of compressible recoil mechanisms Report DAAG 29-78-G-0120, US Army Research Office by Energy Division, Iowa Institute of Hydraulic Research, Iowa University.

Chen P C, and Wereley N M 2004 Magnetorheological damper and energy dissipation method U.S. Patent 6,694,856. Filed: Feb. 22, 2002. Issued: Feb. 24, 2004.

Choi Y-T and Wereley N M 2003 Vibration Control of a Landing Gear System Featuring Electrorheological/Magnetorheological Fluids *Journal of Aircraft*, 40:432-439.

Choi Y-T and Wereley N M 2005a Mitigation of Biodynamic Response to Vibratory and Blast-induced Shock Loads Using Magnetorheological Seat Suspensions *Proceedings of the Institution of Mechanical Engineers Part D: Journal of Automobile Engineering,* Vol. 219, No. 6, pp. 741-53.

Choi Y T and Wereley N M 2005b Biodynamic Response Mitigation to Shock Loads Using Magnetorheological Helicopter Crew Seat Suspensions *AIAA Journal of Aircraft*, Vol. 42, No. 5, pp. 1288-1295.

Choi Y T and Wereley N M 2005c Semi-Active Vibration Isolation Using Magnetorheological Isolators *AIAA Journal of Aircraft*, Vol. 42, No. 5, pp. 1244-1251.

Choi Y-T and Wereley N M 2008 "Shock Isolation Systems Using Magnetorheological Dampers," *ASME Journal of Vibration and Acoustics*, Volume 130:024503.

Coermann R R 1962 The mechanical Impedance of the Human Body in Sitting and Standing Positions at Low Frequencies *Human Factors*, Vol. 4, No. 5, pp. 227-253.

Coltman J W, Van Ingen C, Johnson N B and Zimmerman R E 1989 Aircraft Crash Survival Guide Vol. II-Aircraft Crash Design Impact Conditions and Human Tolerance *Aviation Applied Technology Directorate,* USAAVSCOM TR89-D-22B, pp. 29-87.

Cook E, Hu W and Wereley N M 2007 Magnetorheological Bypass Damper Exploiting Flow Through a Porous Channel *Journal of Intelligent Material Systems and Structures,* Vol. 18, No. 12, pp. 1197-1203.

Department of Army 2000 Occupant Crash Protection Handbook for Tactical Ground Vehicles.

Desjardins S P, Zimmerman R E, Bolukbasi A O and Merritt N A 1989 Aircraft Crash Survival Design Guide *Aviation Applied Technology Directorate*, USAAVSCOM TR 89-D-22D, Fort Eustis, VA.

Desjardins S P 2003 The Evolution of Energy Absorption Systems for Crashworthy Helicopter Seats *59th Annual AHS Forum*, Phoenix, AZ, May 6-8.

Dong-won Y, Young-su S, Hee-chang P and Sang-kyu C 2009 Design of Novel MR Rotary Brake *World Congress on Computer Science and Information Engineering,* Los Angeles, CA, IEEE.

Eiband M A 1959 Human Tolerance to Rapidly Applied Accelerations: A Summary of the Literature *NASA Memo* 5-19-59E.

Fasanella E L and Jackson K E 2004 Impact Testing and Simulation of a Crashworthy Composite Fuselage Section with Energy-Absorbing Seats and Dummies *Journal of the American Helicopter Society,* Vol. 49, No. 2, pp. 140-148.

Fice J B and Cronin D S 2012 Investigation of Whiplash Injuries in the Upper Cervical Spine Using a Detailed Neck Model *Journal of Biomechanics*, Vol. 45, No. 6, pp. 1098-1102.

Genic S, Arandjelovic I, Kolendic P, Jaric M, Budimir N, and Genic V 2011 A review of explicit approximations of Colebrook's equation *FME Transactions,* Vol. 39, pp. 67-71.

Guo C, Gong X, Xuan S, Zong L and Peng C 2012 Normal Forces of Magnetorheological Fluids Under Oscillatory Shear *Journal of Magnetism and Magnetic Materials,* Vol. 324, No. 6, pp. 1218-1224.

Hajihosseinloo M A, Hooke CJ, and Walton D 1989 Gun recoil system performance-measurement and prediction*Proc. IMechE Part C: J. Mech. Eng. Sci.*, Vol. 203, pp. 85-92.

Hiemenz G J, Choi Y T and Wereley N M 2007 Semi-Active Control of Vertical Stroking Helicopter Crew Seat for Enhanced Crashworthiness *AIAA Journal of Aircraft*, Vol. 44, No. 3, pp. 1031-1034.

Hiemenz G J, Hu W, Ngatu G, and Wereley N M 2010 Rotary vane magnetorheological energy absorber U.S. Patent US2010/0300819 A1.

Hongsheng H, Jiong W, Suxiang Q, Yancheng L and Xuezheng J 2009 Investigation on Controllability of a Magnetorheological Gun Recoil Damper *International Conference on Information and Automation*, 1044-1049 .

Hu W and Wereley N M 2005 Magnetorheological Fluid and Elastomeric Lag Damper for Helicopter Stability Augmentation *International Journal of Modern Physics B*, Vol. 19, No. 7, pp. 1471-77.

Huang M 2002 Vehicle crash mechanics *CRC Press*, Dearborn, MI.

Huang S-C 1998 Analysis of Human Body Dynamics in Simulated Rear-End Impacts *Human Movement Science*, Vol. 17, No. 6, pp. 821-838.

HUMANETICS, Last accessed Oct 15, 2013. http://www.humaneticsatd.com/crash-test-dummies/frontal-impact/hybrid-ii-50th

Idelchik I E 2001a Handbook on Hydraulic Resistance: Stream intake in pipes and channels (resistance coefficients of inlet sections), Third Edition, CRC Begell House.

Idelchik I E 2001b Handbook on Hydraulic Resistance: Smooth velocity variation (resistance coefficients of diffusers), Third Edition, CRC Begell House.

Idelchik I E 2001c Handbook on hydraulic resistance: Variation of stream direction, Third Edition, CRC Begell House.

Jackson K E, Fasanella E L, Boitnott R, McEntire J, and Lewis A 2004 Occupant Responses in a Full-Scale Crash Test of the Sikorsky ACAP Helicopter *Journal of the American Helicopter Society*, Vol. 49, No. 2, pp. 127-139.

Jeon J, and Koo S 2012 Viscosity and dispersion state of magnetic suspensions *Journal of Magnetism and Magnetic Materials,* 324(4), pp. 424-429.

JSOL Corporation Total Human Model for Safety (THUMS), http://ls-dyna.jsol.co.jp/en/thums/modelDetail.html Last accessed: Mar 24, 2014.

Kapoor T, Altenhof W, Wang Q A and Howard A 2006 Injury Potential of a Three-year-old Hybrid III Dummy in Forward and Rearward Facing Positions Under CMVSS 208 Testing Conditions *Accident Analysis and Prevention*, Vol. 38, No. 4, pp. 786-800.

Kroell C K 1962 A Simple, Efficient, One Shot Energy Absorber *Bulletin No. 30 Shock Vibration and Associated Environments,* Part III, General Motors Research Laboratory, Warren, MI.

Ladkany G S 2009 Design and Characterization of a Shock and Vibration Mitigation Seat System *Masters Thesis in Mechanical Engineering*, University of Nevada, Las Vegas.

Li Z C, and Wang J 2012 Gun recoil system employing a magnetorheological fluid damper *Smart Mater. Struct.* 21105003 doi:10.1088/0964-1726/21/10/105003

Liang C C and Chiang C F 2006 A Study on Biodynamic Models of Seated Human Subjects Exposed to Vertical Vibration *International Journal of Industrial Ergonomics*, Vol. 36, pp. 869-890.

Linder A 2000 A New Mathematical Neck Model for a Low-Velocity Rear-End Impact Dummy: Evaluation of Components Influencing Head Kinematics *Accident Analysis and Prevention*, Vol. 32, No. 2, pp. 261-269.

Liu X X, Shi J, Li G, Le X, Zhao B, Yue M, Liu J, Bai G and Ke W 1998 Biodynamic Response and Injury Estimation of Ship Personnel to Ship

Shock Motion Induced by Underwater Explosion *Proceedings of the 69th Shock and Vibration Symposium, Shock and Vibration Information Analysis Center*, Richmond, VA, Vol. 18,pp. 1–18.

Lopik D W V and Acar M 2007 Development of a Multi-Body Computational Model of Human Head and Neck *Proceedings of the Institution of Mechanical Engineers Part K-Journal of Multi-body Dynamics*, Vol. 221, No. 2, pp. 175-197.

Mao M, Hu W, Choi, Y T and Wereley N M 2007, A magnetorheological damper with bifold valves for shock and vibration mitigation *J. Intell. Mater. Syst. Struct.*18 1227-1232.

Mao M, Hu W, Choi Y T, Wereley N M, Browne A L, and Ulicny J 2014 Experimental validation of a magnetorheological energy absorber design analysis, *Journal of Intelligent Material Systems and Structures*, 25(3):352-363.

MATLAB, R2010b, The Mathworks Inc.

Mavrotas G 2009 Effective implementation of the epsilon-constraint method in multi-objective mathematical programming problems *Applied Mathematics and Computation*, 213455-465.

McManus S J, St. Clair K A, Boileau P E, Boutin J and Rakheja S 2002 Evaluation of Vibration and Shock Attenuation Performance of a Suspension Seat with a Semi-active Magnetorheological Fluid Damper *Journal of Sound and Vibration,* 253:313-327.

Meirovitch L 2001 *Fundamentals of Vibrations*, McGraw-Hill Companies, Inc., New York.

Moody L F 1944 Friction factors for pipe flow *Transactions of the ASME*, 66(8), pp. 671-684.

Muksian R and Nash C D 1974 A Model for the Response of Seated Humans to Sinusoidal Displacements of the Seat *Journal of Biomechanics*, Vol. 7, pp. 209-215.

Muksian R and Nash C D 1976 On Frequency-Dependent Damping Coefficients in Lumped-Parameter Models of Human Beings *Journal of Biomechanics,* Vol. 9, No. 5, pp. 339-342.

Nguyen Q-H, Han Y-M, Choi S B and Wereley N M 2007 Geometry Optimization of MR valves Constrained in a Specific Volume Using the Finite Element Method *Smart Materials and Structures*, 16:2242-2252.

Nguyen Q-H and Choi S B 2009 Optimal Design of a Vehicle Magnetorheological Damper Considering Damping Force and Dynamic Range *Smart Materials and Structures*, 18:015013.

Patil M K, Palanichamy M S and Ghista D N 1977 Dynamic Response of Human Body Seated on a Tractor and Effectiveness of Suspension Systems *Society of Automobile Engineers,* No. 770932, pp.755-792.

Polanco M A and Littell J D 2011 Vertical Drop Testing and Simulation of Anthropomorphic Test Devices *67th AHS Annual Forum,* Virginia Beach, VA.

Potula S R, Solanki K N, Oglesby D L, Tschopp M A and Bhatia M A 2012

Investigating Occupant Safety Through Simulating the Interaction Between Side Curtain Airbag Deployment and an Out-of-Position Occupant *Accident Analysis and Prevention*, Vol. 49, pp. 392-403.

Qassem W, Othman M O and Abdul-Majeed S 1994 The Effects of Vertical and Horizontal Vibrations on the Human Body *Medical Engineering Physics*, Vol. 16, pp. 151-161.

Qassem W and Othman M O 1996 Vibration Effects on Sitting Pregnant Women-Subjects of Various Masses *Journal of Biomechanics*, Vol. 29, No. 4, pp. 493-501.

Rakheja S, Afework Y and Sankar S 1994 An Analytical and Experimental Investigation of the Driver Seat Suspension System *Vehicle System Dynamics*, Vol. 23, No. 3, pp. 501-524.

Rosenfeld N and Wereley N M 2004 Volume-Constrained Optimization of Magneto- and Electro-rheological Valves and Dampers *Smart Materials and Structures*, 13:1303-1313.

Singh H J and Wereley N M 2011 Biodynamic Response Mitigation for Seat Suspension with Adaptive Energy Absorbers *AHS 67th Annual Forum*, Virginia Beach, VA, USA.

Singh H J and Wereley N M 2013a Adaptive Magnetorheological Seat Suspensions for Shock Mitigation *Proceedings of the SPIE*, San Diego, CA, USA.

Singh H J and Wereley N M 2013b Model-based Optimal Control of Biodynamic Response to Vertical Crash Loads for an Occupant Seated in a Helicopter *AHS 69th Annual Forum*, Phoenix, AZ, USA.

Singh H J and Wereley N M 2013c Adaptive Magnetorheological Shock Isolation Mounts for Drop-induced Impacts *Smart Materials and Structures*, Vol. 22, 122001.

Stein G J 1991 Active Vibration Control System for the Drivers Seat for Off-road Vehicles *Vehicle System Dynamics,* Vol. 20, No. 2, pp. 57-78.

Stein G J 1995 Results of Investigation of an Electropneumatic Active Vibration Control System for a Drivers Seat *Proceedings IMechE Part D: Journal of Automobile Engineering,* Vol. 209, No. 3, pp. 227-234.

Stein G J 1997 A Driver's Seat with Active Suspension of Electro-pneumatic Type *ASME Journal of Vibration and Acoustics,* Vol. 119, No. 2, pp. 230-235.

Stelzer G J, Schulz M J, Kim J and Allemang R J 2003 A Magnetorheological Semi-Active Isolator to Reduce Noise and Vibration Transmissibility in Automobiles *Journal of Intelligent Material Systems and Structures*, 14:743-765.

Suggs C W, Abrams C F and Stikeleather L F 1969 Application of a Damped Spring-Mass Human Vibration Simulator in Vibration Testing of Vehicle Seats *Ergonomics*, Vol. 12, No. 1, pp. 79-90.

Svoboda C M and Warrick J C 1981 *Design and Development of Variable Load Energy Absorber,* TR 3023.

Swinbanks M A, Simon D E, Holford J M and Napoletano JR. F M 2005 Active Suspension for a Marine Platform *US Patent Application Publication* US 2005/0278094 A1

Tang X, Zhang X, Tao R and Rong Y 2000 Structure Enhanced Yield Stress of Magnetorheological Fluids *Journal of Applied Physics,* Vol. 87, No. 5, pp. 2634-38.

The Mathworks Inc., MATLAB, R2010b.

Teng T L, Chang F A, Liu Y S and Peng C P 2008 Analysis of Dynamic response of Vehicle Occupant in Frontal Crash Using Multibody Dynamics Method *Mathematical and Computer Modeling*, Vol. 48, No. 11-12, pp. 1724-1736.

U.S. ARMY RDECOM 2009 Preliminary Full Spectrum Rotary Wing Crashworthiness Criteria RDECOM TR 10-D-25.

Wang J, Meng G, Feng N and Hahn E J 2005 Dynamic Performance and Control of Squeeze Mode MR fluid Damper-Rotor System *Smart Materials and Structures,* Vol. 14, No. 4, pp. 11.

Wereley N M, Cho J U, Choi Y T and Choi S B 2008 Magnetorheological Dampers in Shear Mode *Smart Materials and Structures*, Vol. 17, 015022.

Wereley N M, Choi Y T and Singh H J 2011 Adaptive Energy Absorbers for Drop-Induced Shock Mitigation *Journal of Intelligent Material Systems and Structures,* Vol. 22, No. 6, pp. 515-519.

White F M 1998 Fluid mechanics: Viscous flow in ducts Fourth Edition, McGraw-Hill.

Woo D, Choi S B, Choi Y T and Wereley N M 2007 Frontal Crash Mitigation Using MR Impact Damper for Controllable Bumper *Journal of Intelligent Material Systems and Structures*, 18:1227-1232.

Xingqiao D, Potula S, Grewal H, Solanki K N, Tschopp M A and Horstemeyer M F

2013 Finite Element Analysis of Occupant Head Injuries: Parametric Effects of the Side Curtain Airbag Deployment Interaction with a Dummy Head in a Side Impact Crash *Accident Analysis and Prevention,* Vol. 55, pp. 232-241.

Yazid I I M, Mazlan S A, Kikuchi T, Zamzuri H, and Imaduddin F 2014 Design of magnetorheological damper with a combination of shear and squeeze modes *Materials and Design*, 54(2014), pp. 87-95.

Yoganandan N, Humm J R, Pintar F A and Maiman D J 2013 Determination of Peak Deflections from Human Surrogates Using Chestbands in Side Impact Tests *Medical Engineering & Physics*, Vol. 35, No. 8, pp. 1181-1187.

Yu M, Liao C R, Chen W M and Huang S L 2006 Study on MR Semi-Active Suspension System and its Road Testing *Journal of Intelligent Material Systems and Structures*, 17:801-806.

Zhang L, Ma F and Wang J 2009 Study of Control System of Magnetorheological Dampers under Impact Load *International Conference on Intelligent Computation Technology and Automation*, 894-897.

Zhang X J, Farjoud A, Ahmadian M, Guo K H and Craft M 2011 Dynamic Testing and Modeling of an MR squeeze Mount *Journal of Intelligent Material Systems and Structures,* Vol. 22, No. 15, pp. 1717-28.

Zong Z and Lam K Y 2002 Biodynamic Response of Shipboard Sitting Subject to Ship Shock *Journal of Biomechanics,* Vol. 35, No. 1, pp. 35-43.